Estimation of the near-surface air temperature and soil moisture from satellites and numerical modelling in New Zealand

A thesis

submitted in partial fulfilment of the requirements

for the degree of

Doctor of Philosophy in Environmental Science

By

M. Sohrabinia

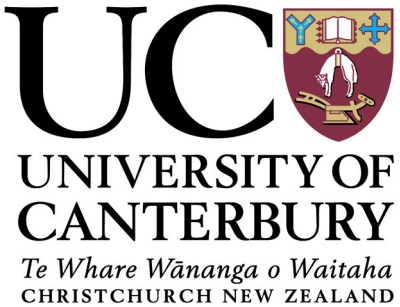

November 2013

Abstract

Satellite observations provide information on land surface processes over a large spatial extent with a frequency dependent on the satellite revisit time. These observations are not subject to the spatial limitations of the traditional point measurements and are usually collected in a global scale. With a reasonable spatial resolution and temporal frequency, the Moderate Resolution Imaging Spectroradiometer (MODIS) is one of these satellite sensors which enables the study of land-atmospheric interactions and estimation of climate variables for over a decade from remotely sensed data.

This research investigated the potential of remotely sensed land surface temperature (LST) data from MODIS for air temperature (T_a) and soil moisture (SM) estimation in New Zealand and how the satellite derived parameters relate to the numerical model simulations and the *in-situ* ground measurements. Additionally, passive microwave SM product from the Advanced Microwave Scanning Radiometer for the Earth Observing System (AMSR-E) was applied in this research.

As the first step, the MODIS LST product was validated using ground measurements at two test-sites as reference. Quality of the MODIS LST product was compared with the numerical simulations from the Weather Research and Forecasting (WRF) model. Results from the first validation site, which was located in the alpine areas of the South Island, showed that the MODIS LST has less agreement with the *in-situ* measurements than the WRF model simulations. It turned out that the MODIS LST is subject to sources of error, such as the effects of topography and variability in atmospheric effects over alpine areas and needs a careful pre-processing for cloud effects and outliers. On the other hand, results from the second validation site, which was located on the flat lands of the Canterbury Plains, showed significantly higher agreement with the ground truth data. Therefore, ground measurements at this site were used as the main reference data for the accuracy assessment of T_a and SM estimates.

Using the MODIS LST product, T_a was estimated over a period of 10 years at several sites across New Zealand. The main question in this part of the thesis was whether to use LST series from a single MODIS pixel or the series of a spatially averaged value from multiple pixels for T_a estimation. It was found that the LST series from a

single pixel can be used to model T_a with an accuracy of about ± 1 °C. The modelled T_a in this way showed $r \approx 0.80$ correlation with the *in-situ* measurements. The T_a estimation accuracy improved to about ± 0.5 °C and the correlation to $r \approx 0.85$ when LST series from spatially averaged values over a window of 9x9 to 25x25 pixels were applied. It was discussed that these improvements are due to noise reduction in the spatially averaged LST series. By comparison of LST diurnal trends from MODIS with T_a diurnal trends from hourly measurements in a weather station, it was shown that the MODIS LST has a better agreement with T_a measurements at certain times of the day with changes over day and night.

After estimation of T_a, the MODIS LST was applied to derive the near-surface SM using two Apparent Thermal Inertia (ATI) functions. The objective was to find out if more daily LST observations can provide a better SM derivation. It was also aimed to identify the potential of a land-atmospheric coupled model for filling the gaps in derived SM, which were due to cloud cover. The *in-situ* SM measurements and rainfall data from six stations were used for validation of SM derived from the two ATI functions and simulated by the WRF model. It was shown that the ATI function based on four LST observations has a better ability to derive SM temporal profiles and is better able to detect rainfall effects.

Finally, the MODIS LST was applied for spatial and temporal adjustment of the near-surface SM product from AMSR-E passive microwave observations over the South Island of New Zealand. It was shown that the adjustment technique improves AMSR-E seasonal trends and leads to a better matching with rainfall events. Additionally, a clear seasonal variability was observed in the adjusted AMSR-E SM in the spatial domain.

Findings of this thesis showed that the satellite observed LST has the potential for the estimation of the land surface variables, such as the near-surface T_a and SM. This potential is greatly important on remote and alpine areas where regular measurements from weather stations are not often available. According to the results from the first validation site, however, the MODIS LST needs a careful pre-processing on those areas. The concluding chapter included a discussion of the limitations of remotely sensed data due to cloud cover, dense vegetation and rugged topography. It was concluded that the satellite observed LST has the potential for SM and T_a estimations in New Zealand. It was also found that a land-atmospheric model (such as the WRF coupled with the Noah and surface model) can be applied for filling the gaps due to cloud cover in remotely sensed variables.

Deputy Vice-Chancellor's Office
Postgraduate Office

UNIVERSITY OF CANTERBURY
Te Whare Wānanga o Waitaha
CHRISTCHURCH NEW ZEALAND

Co-Authorship Form

This form is to accompany the submission of any thesis that contains research reported in co-authored work that has been published, accepted for publication, or submitted for publication. A copy of this form should be included for each co-authored work that is included in the thesis. Completed forms should be included at the front (after the thesis abstract) of each copy of the thesis submitted for examination and library deposit.

Please indicate the chapter/section/pages of this thesis that are extracted from co-authored work and provide details of the publication or submission from the extract comes:

Major contents of Chapter 3 (end of Sec. 3.1 to Sec. 3.9) of the thesis is published as a paper in the journal of Remote Sensing under the title "Analysis of MODIS LST Compared with WRF Model and in situ Data over the Waimakariri River Basin, Canterbury, New Zealand" in 2012 (DOI: 10.3390/rs4113501) with my supervisors, Dr. Wolfgang Rack and Dr. Peyman Zawar-Reza, as co-authors.

Please detail the nature and extent (%) of contribution by the candidate:

The PhD candidate was responsible for the computer modelling, data analysis and write-up of this paper (90%). The co-authors provided regular advice and feedback on the paper as it was developed (10%).

Certification by Co-authors:

If there is more than one co-author then a single co-author can sign on behalf of all

The undersigned certifys that:

- The above statement correctly reflects the nature and extent of the PhD candidate's contribution to this co-authored work
- In cases where the candidate was the lead author of the co-authored work he or she wrote the text

Name: *Peyman Zawar-Reza* Signature:  Date: *28/06/2013*

Deputy Vice-Chancellor's Office
Postgraduate Office

UNIVERSITY OF CANTERBURY
Te Whare Wānanga o Waitaha
CHRISTCHURCH NEW ZEALAND

Co-Authorship Form

This form is to accompany the submission of any thesis that contains research reported in co-authored work that has been published, accepted for publication, or submitted for publication. A copy of this form should be included for each co-authored work that is included in the thesis. Completed forms should be included at the front (after the thesis abstract) of each copy of the thesis submitted for examination and library deposit.

Please indicate the chapter/section/pages of this thesis that are extracted from co-authored work and provide details of the publication or submission from the extract comes:

The material in Chapter 4 of the thesis is under review as a paper in the journal of Theoretical and Applied Climatology under the title "Spatio-temporal analysis of the relationship between LST from MODIS and air temperature in New Zealand" with my supervisors, Dr. Peyman Zawar-Reza and Dr. Wolfgang Rack, as co-authors.

Please detail the nature and extent (%) of contribution by the candidate:

The PhD candidate was responsible for the computer modelling, data analysis and write-up of this paper (90%). The co-authors provided regular advice and feedback on the paper as it was developed (10%).

Certification by Co-authors:

If there is more than one co-author then a single co-author can sign on behalf of all

The undersigned certifys that:

- The above statement correctly reflects the nature and extent of the PhD candidate's contribution to this co-authored work
- In cases where the candidate was the lead author of the co-authored work he or she wrote the text

Name: *Peyman Zawar-Reza* Signature:  Date: *28/06/2013*

Deputy Vice-Chancellor's Office
Postgraduate Office

UNIVERSITY OF CANTERBURY
Te Whare Wānanga o Waitaha
CHRISTCHURCH NEW ZEALAND

Co-Authorship Form

This form is to accompany the submission of any thesis that contains research reported in co-authored work that has been published, accepted for publication, or submitted for publication. A copy of this form should be included for each co-authored work that is included in the thesis. Completed forms should be included at the front (after the thesis abstract) of each copy of the thesis submitted for examination and library deposit.

Please indicate the chapter/section/pages of this thesis that are extracted from co-authored work and provide details of the publication or submission from the extract comes:

The material in Chapter 5 of the thesis is under review as a paper for the second round in the journal of Applied Remote Sensing after acceptance with major revisions under the title "Soil moisture derived using two Apparent Thermal Inertia functions over Canterbury, New Zealand" with my supervisors, Dr. Wolfgang Rack and Dr. Peyman Zawar-Reza, as co-authors.

Please detail the nature and extent (%) of contribution by the candidate:

The PhD candidate was responsible for the computer modelling, data analysis and write-up of this paper (90%). The co-authors provided regular advice and feedback on the paper as it was developed (10%).

Certification by Co-authors:

If there is more than one co-author then a single co-author can sign on behalf of all

The undersigned certifys that:

- The above statement correctly reflects the nature and extent of the PhD candidate's contribution to this co-authored work
- In cases where the candidate was the lead author of the co-authored work he or she wrote the text

Name: *Peyman Zawar-Reza* Signature:  Date: *28/06/2013*

Deputy Vice-Chancellor's Office
Postgraduate Office

UNIVERSITY OF CANTERBURY
Te Whare Wānanga o Waitaha
CHRISTCHURCH NEW ZEALAND

Co-Authorship Form

This form is to accompany the submission of any thesis that contains research reported in co-authored work that has been published, accepted for publication, or submitted for publication. A copy of this form should be included for each co-authored work that is included in the thesis. Completed forms should be included at the front (after the thesis abstract) of each copy of the thesis submitted for examination and library deposit.

Please indicate the chapter/section/pages of this thesis that are extracted from co-authored work and provide details of the publication or submission from the extract comes:

The material in Chapter 6 of the thesis is compiled to be submitted soon for peer-review as a paper under the title "Spatio-temporal adjustment of AMSR-E soil moisture using the MODIS LST in New Zealand" with my supervisors, Dr. Wolfgang Rack and Dr. Peyman Zawar-Reza, as co-authors.

Please detail the nature and extent (%) of contribution by the candidate:

The PhD candidate was responsible for the computer modelling, data analysis and write-up of this paper (90%). The co-authors provided regular advice and feedback on the paper as it was developed (10%).

Certification by Co-authors:

If there is more than one co-author then a single co-author can sign on behalf of all

The undersigned certifys that:

- The above statement correctly reflects the nature and extent of the PhD candidate's contribution to this co-authored work
- In cases where the candidate was the lead author of the co-authored work he or she wrote the text

Name: *Peyman Zawar-Reza* Signature:  Date: *28/06/2013*

Acknowledgements

First, I would like to express special thanks to my supervisors: Dr. Peyman Zawar-Reza and Dr. Wolfgang Rack for their support, comments, ideas and expert advice which enabled me to complete this thesis. I would like to thank Professor Andy Sturman who also helped me from the initial stages until I developed my research proposal.

I appreciate the University of Canterbury (and New Zealand as a country) for providing me with a PhD scholarship which made it possible for me to come to New Zealand and finish my PhD. I would like to thank the Department of Geography and Gateway Antarctica in the University of Canterbury for supporting me to attend a conference in Australia.

Thanks for the field measurement staff in the Geography Department who helped me in the field measurements which were conducted as part of this research. My thanks also goes to the Geography administrative and technical staff who helped me when I needed. Thanks to the PhD students and post-doctoral fellows in the Department of Geography, who were friendly and at times very helpful with their ideas. I especially thank Sandipan for being a good office-mate in the Department of Geography and travel-mate during our occasional hiking in the mountains of New Zealand. I also thank Gateway Antarctica staff and PhD students who were always friendly and supportive.

I would like to thank the US NASA (National Aeronautics and Space Administration) and the USGS (US Geological Survey) for providing free access to their online satellite databases (Reverb and Earth Explorer, respectively), that I extensively used in this research. I thank the NIWA (National Institute of Water and Atmospheric research) in New Zealand for providing online access to their climate data via Cliflo, that I used in some parts of this research.

Contents

Abstract iii

Acknowledgements ix

1 Thesis Introduction 1
- 1.1 Introduction . . . 1
- 1.2 LST derivation and validation . . . 3
- 1.3 The relationship between LST and air temperature . . . 4
- 1.4 Soil moisture from remotely sensed LST . . . 6
- 1.5 Soil moisture from microwave satellite data . . . 8
- 1.6 Numerical modelling of air temperature and soil moisture . . . 9
- 1.7 Structure of the thesis . . . 10

2 Theoretical background, data and methods 11
- 2.1 LST retrieval from remotely sensed observations . . . 11
  - 2.1.1 Electromagnetic radiation in remote sensing . . . 11
  - 2.1.2 Atmospheric correction of remotely sensed data . . . 13
  - 2.1.3 Algorithms for the atmospheric correction . . . 14
  - 2.1.4 Uncertainty in LST retrievals . . . 17
  - 2.1.5 Validation versus inter-comparison . . . 20
- 2.2 Numerical modelling of land surface parameters . . . 20
  - 2.2.1 Components of the WRF modelling system . . . 21
  - 2.2.2 WRF physics . . . 22
  - 2.2.3 WRF Land surface schemes . . . 23
  - 2.2.4 Spatial analysis of the WRF simulations . . . 24
- 2.3 Geostatistical methods . . . 24
- 2.4 Statistical methods . . . 25
- 2.5 Data used in this research . . . 28
  - 2.5.1 Remotely sensed data . . . 28
  - 2.5.2 Ground measurements . . . 29
  - 2.5.3 Model simulations . . . 30

3 Validation of the MODIS LST over the study area **31**
3.1 Preface . . . 31
3.2 Introduction . . . 32
3.3 Study Area . . . 35
3.4 Data . . . 36
3.5 Methods . . . 41
3.5.1 LST Pre-Processing . . . 41
3.5.2 Spectral Unmixing . . . 42
3.5.3 Spatial Overlay of MODIS LST, WRF Simulations and *in situ* Points . . . 42
3.5.4 View Angle and Emissivity Analysis . . . 43
3.5.5 Geo-Statistical Analysis . . . 45
3.6 Results . . . 46
3.6.1 Time-Series of Spatially Averaged Datasets . . . 46
3.6.2 Land-Cover Based Time-series . . . 50
3.6.3 Comparison between Day and Night Measurements . . . 54
3.7 Discussion . . . 55
3.7.1 Site-Specific Characteristics . . . 55
3.7.2 Issues in LST Retrieval . . . 56
3.8 Conclusions . . . 58
3.9 Introduction to the second validation campaign . . . 60
3.10 Results from the 2nd measurement campaign . . . 60
3.11 Discussion ... 2nd validation campaign . . . 62

4 Air temperature and LST **65**
4.1 Preface . . . 65
4.2 Introduction . . . 66
4.3 Study area . . . 69
4.4 Data . . . 69
4.4.1 MODIS LST dataset . . . 69
4.4.2 Meteorological data . . . 71
4.4.3 Additional data . . . 72
4.5 Methods . . . 72
4.5.1 Temporal matching of Ta to LST observations . . . 72
4.5.2 Multiple LST window-size . . . 73
4.5.3 Day/Night analysis . . . 74
4.5.4 Statistical methods . . . 74
4.6 Results . . . 76
4.6.1 MODIS LST versus Ta time-series over a single pixel . . . 76
4.6.2 Effects of LST window-size . . . 79
4.6.3 Effects of distance . . . 83
4.6.4 Diurnal differences . . . 84

4.7 Discussion . . . 87
4.8 Conclusion . . . 88

5 Soil moisture retrieval from the MODIS LST 91
5.1 Preface . . . 91
5.2 Introduction . . . 92
5.3 Study Area . . . 94
5.4 Data . . . 94
5.5 Methods . . . 98
5.5.1 Thermal inertia approach for SM estimation . . . 98
5.5.2 Multi-temporal time-series analysis of SM from ATI method . . . 100
5.5.3 Statistical methods . . . 101
5.6 Results . . . 101
5.6.1 Short-term series: ATI results vs. WRF and *in-situ* SM . . . 101
5.6.2 Long-term analysis: ATI results vs. *in-situ* SM . . . 103
5.7 Discussion . . . 106
5.8 Conclusion . . . 109

6 Adjustment of the AMSR-E soil moisture 111
6.1 Preface . . . 111
6.2 Introduction . . . 112
6.3 Study area . . . 115
6.4 Data . . . 115
6.5 Methods . . . 117
6.5.1 Statistical methods . . . 117
6.5.2 Mixing matrix . . . 118
6.6 Results . . . 119
6.6.1 Comparison of the WRF simulations with the in-situ SM . . . 119
6.6.2 AMSR-E day and night SM time-series . . . 120
6.6.3 AMSR-E SM compared with the WRF simulations . . . 121
6.6.4 Adjustment of AMSR-E SM series . . . 124
6.6.5 Spatial domain . . . 124
6.7 Discussion . . . 127
6.8 Conclusion . . . 130

7 Summary, conclusion and outlook 131
7.1 Introduction . . . 131
7.2 An overview of key findings . . . 132
7.2.1 Paper 1. Validation of the MODIS LST over the study area . . . 132
7.2.2 Paper 2. Spatio-temporal variability of air temperature derived from the MODIS LST . . . 133
7.2.3 Paper 3. Soil moisture retrieval from the MODIS LST . . . 134

7.2.4 Paper 4. Adjustment of the AMSR-E soil moisture using the MODIS LST . . . 135
7.3 Discussion of the results and limitations . . . 136
7.4 Conclusion of the thesis . . . 138
7.5 Outlook for future research . . . 140

Bibliography **140**

List of Figures

1.1 Day and night LST–T_a differences... 5
1.2 Thermal inertia of wet and dry soils 7

2.1 Atmospheric windows 12
2.2 Sun, Earth and satellite zenith angles 19
2.3 WPS components 22

3.1 Cass validation site 36
3.2 GST minimum and maximum 38
3.3 GST over five land-cover types 39
3.4 Variability of emissivity over land-cover types 44
3.5 Variability of satellite viewing angle over the experiment period 44
3.6 Viewing angles versus emissivities 45
3.7 Comparison of LST hourly time-series 46
3.8 Comparison of LST subsampled time-series 48
3.9 Regression residuals from LST time-series 49
3.10 MODIS LST line-fits and outliers 51
3.10 MODIS LST line-fits and outliers *cont.* 52
3.11 Variability of regression results of five LC types 53
3.12 Day/night correlations over five LC types 55
3.13 Test-site over the Canterbury Plains 60
3.14 Scatterplot of Mixed Grass LC type in the Canterbury Plains 62

4.1 The study area and test-sites across New Zealand 70
4.2 Windroses in Christchurch and Darfield 71
4.3 Variability of MODIS daily four overpass times 73
4.4 LST-T_a scatterplots over four stations 77
4.5 Seasonal bootstraps of r at all sites 79
4.6 FFT filtering of LST and T_a 80
4.7 Errorbars and boxplots of LST from multiple windows 81
4.8 Variability of LST-T_a relationship at four MODIS overpass times 85
4.9 Diurnal variability of LST and T_a 86

5.1 Map of soil moisture measurement sites 95

5.2 Land-cover of soil moisture measurement sites 95
5.3 Temporal profile of ATI SM derivations in short-term 103
5.4 Temporal profile of ATI SM derivations in long-term 105
5.5 Spatial matching of the MODIS LST grid 107

6.1 Study area: AMSR-E 115
6.2 AMSR-E soil moisture FFT analysis 119
6.3 WRF (1x1 grid) vs. *in-situ* soil moisture 120
6.4 Variability of Euclidean dist. from the WRF soil... 120
6.5 Time-series of soil moisture from AMSR-E 121
6.6 AMSR-E & WRF soil moisture vs. rainfall 123
6.7 Adjusted AMSR-E soil moisture vs. WRF and rainfall 125
6.8 Adjusted AMSR-E soil moisture vs. rainfall 125
6.9 AMSR-E soil moisture grid over South Island 127
6.10 DTM and rainfall grid of South Island 128
6.11 Adjusted AMSR-E soil moisture grid over South Island 129

List of Tables

2.1 EMR energy subdivisions . . . 12
2.2 MODIS satellite and surface viewing angles . . . 20
2.3 WRF physics options . . . 23
2.4 List of satellite data . . . 29

3.1 Land-cover types of validation site . . . 38
3.2 Mixing ratios of land-cover types . . . 43
3.3 Basic statistics from LST time-series . . . 47
3.4 Regression statistics from LST time-series . . . 49
3.5 Regression statistics over five LC types . . . 53
3.6 Basic statistics from the second validation site . . . 61
3.7 Regression statistics from the 2nd validation site . . . 61

4.1 Regression statistics from multiple LST windows: Christchurch site . . . 82
4.2 Regression statistics from multiple LST windows: additional sites . . . 82
4.3 Fraction of explained variability over multiple windows . . . 83
4.4 Regression statistics considering wind effects . . . 84
4.5 Variability of LST-T_a relationship with overpass time . . . 86

5.1 List of SM measurement stations . . . 96
5.2 Statistics for the short-term analysis . . . 102
5.3 Statistics for the long-term analysis . . . 104
5.4 Summary table . . . 108

Nomenclature

ϵ emissivity

θ Satellite viewing angle

c_p specific heat capacity

d_E Euclidean distance

AMSR-E Advanced Microwave Scanning Radiometer for the Earth Observing System

ARW Advanced Research WRF

ATI Apparent Thermal Inertia

AVHRR Advanced Very High Resolution Radiometer

CLM Community Land Model

COLM Common Land Model

EMR ElectroMagnetic Radiation

FEV Fraction of Explained Variance

FFT Fast Fourier Transform

FNL Final Operational Global Analysis

GST Ground Surface Temperature

GSW Generalized Split-Window

HDF Hierarchical Data Format

iFFT inverse Fast Fourier Transform

IR Infra-Red

LC Land-cover

LSM Land Surface Model

LST Land Surface Temperature

MIR Middle Infra-Red

MODIS MODerate resolution Imaging Spectroradiometer

MW Microwave

NCEP National Centers for Environmental Prediction

NDVI Normalized Difference Vegetation Index

netCDF network Common Data Form

NIR Near Infra-Red

RT Radiative Transfer

SCA Single-Channel Algorithm

SMOS Soil Moisture and Ocean Salinity

SMSI Soil Moisture Saturation Index

SST Sea Surface Temperature

SVAT Soil Vegetation Atmosphere Transfer

SWIR Short-Wave Infra-Red

SWT Split-Window Technique

T_a Air Temperature

T_b brightness Temperature

T_s Surface Skin Temperature

TI Thermal Inertia

TIR Thermal Infra-Red

TOA Top Of the Atmosphere

TSK Skin Temperature in Kelvin

TVX Temperature/Vegetation indeX

VGF Vegetation Greenness Fraction

WPS WRF Preprocessing System

WRF Weather Research and Forecasting

Chapter 1

Thesis Introduction

1.1 Introduction

Satellite observations provide information on land surface processes over a vast spatial scale and a frequency which is controlled by the satellite revisit time and atmospheric conditions. Unlike traditional point measurements, these observations are collected with a standard area unit (or pixel size) from all over the globe regardless of logistical barriers, which can limit ground measurements. Regarding the availability of multi-decadal satellite observations from different platforms, these data can be used to analyse land-atmospheric processes and to derive global climate variables in the long-term and over a large spatial domain. For inter-comparison, cross-validation and to fill in the gaps (due to cloud cover, as an example), these data can be combined with the outputs of land-atmospheric models.

Through exchanges of water vapour, energy and atmospheric gases, the land surface influences climate on local, regional and global scales (Yang, 2004). Surface albedo, thermal capacity and heat conductivity are the main properties which contribute in the physical characteristics of the land surface (Dousset and Gourmelon, 2003). These properties vary across the landscape with the heterogeneity of the surface landcover (LC) types (see Lakhankar et al., 2009). Variability in thermal capacity and heat conductivity of the surface materials is captured by thermal infrared (TIR) remote sensing observations. TIR data are used to derive the land surface temperature (LST), which then can be used to estimate various properties of the surface such as moisture content of the near-surface soil. LST is an important quantity for estimation of water exchange between surface and atmosphere (Dash et al., 2002), which is used in numerical weather prediction, climate variability, hydrological, ecological and biogeochemical studies (Wan and Dozier, 1996). In numerical models, LST information is

necessary for parameterization of land surface energy budget (Sun and Pinker, 2004). It is one of the key variables required for characterization of the surface energy fluxes and water budgets, which can be described in a general form by Eq. 1.1 (Rigo and Parlow, 2007; Sheng et al., 2009):

$$Q^{\star} = Q_G + Q_E + Q_H \tag{1.1}$$

where $Q^{\star}$ is the net radiation, which is the sum of all incoming and outgoing radiation fluxes, Q_G is the ground or storage heat flux, Q_E is the turbulent latent heat flux, and Q_H is the convective sensible heat flux. LST influences the partitioning of energy into ground, sensible, and latent heat fluxes (Ghent et al., 2010).

If the net radiation is positive, energy can be transferred into turbulent heat fluxes (sensible and latent) and/or into the ground heat flux (Rigo and Parlow, 2007). Because TIR observations are indicative of net surface energy balance (Eq. 1.1), they are potentially an important source of terrestrial information (Prihodko and Goward, 1997) which can be used to derive several environmental parameters. Since LST influences the ambient air via convective sensible heat flux, it is used alongside LC data to approximate the near-surface air temperature (T_a). Several studies have attempted to derive maximum and minimum T_a from remotely sensed LST (Mostovoy et al., 2006; Vancutsem et al., 2010; Lin et al., 2012) and study the diurnal differences between LST and T_a (Jin and Dickinson, 2010). Similarly, LST can affect the moisture budget by influencing turbulent latent heat flux (Price, 1980). As a result, LST, alongside albedo information, can be used to approximate the near-surface SM. For the same reason, LST is assimilated into land surface models (LSMs) and coupled land-atmospheric models to determine the surface radiative properties and the surface to atmosphere fluxes of heat and water (Kumar and Kaleita, 2003; Huang et al., 2008; Meng et al., 2009; Ghent et al., 2010; Li et al., 2012b). In a global and regional climate model (GCM and RCM), LSM is coupled with the atmospheric model through exchanges of heat fluxes, water and momentum (Jin and Shepherd, 2005). The accuracy of LST parameterization, therefore, plays a key role in determining the predictive capability of hydrological and climatic models (Huang et al., 2008). The outputs of a state-of-the-art land-atmospheric coupled model, in turn, can be used for inter-comparison and cross-validation of the satellite derived variables over a large spatial domain.

The aim of this research is to exploit the great potential of remotely sensed LST data over a large spatial domain and a relatively long temporal period (~10 years) for T_a and SM estimation and improving the quality of an existing MW SM dataset. The surface skin temperature (T_s) and SM simulations in hindcasting mode from the

weather research and forecasting (WRF) model coupled with the Noah LSM will be used for comparison with the variables derived from satellite data after being validated based on the *in-situ* measurements. The main objectives of this research, therefore, can be summarized as follows:

- to validate remotely sensed LST data from the Moderate Resolution Imaging Spectroradiometer (MODIS) over varying topography as well as flat areas in New Zealand using the *in-situ* measurements in comparison with the WRF simulations;
- to estimate T_a from remotely sensed LST in the study area and to investigate the spatial variability of LST-T_a relationship by applying a varying window-size on the MODIS LST grid;
- to estimate the near-surface SM in the study area from the MODIS LST and evaluate the potential of using the WRF simulations for filling the gaps in SM derivations; and
- to apply the higher spatial details available from the MODIS LST to improve the lower resolution passive SM product from the Advanced Microwave Scanning Radiometer for the Earth Observing System (AMSR-E) in spatial and temporal domain.

A large part of the existing literature related to the applications and validation of LST is connected with the study of atmospheric and climate variability, numerical weather modelling, urban climate research and hydrological studies. A brief review of the existing research for validation and applications of LST for SM and T_a estimation is given below. This review covers the research related to numerical modelling and *in-situ* measurements for validation of satellite observed LST, with a primary focus on the MODIS LST which is used in this research.

1.2 LST derivation and validation

Traditionally, various interpolation methods have been used to generalize LST point measurements for regional and global ecosystem and water modeling, which is only possible when measurements are available at sufficient density (Hashimoto et al., 2008). Ground measurements of LST and other land surface data with widespread distribution for these models is costly and difficult, which justifies the need to derive these information from remotely sensed observations (Vandoninck et al., 2011). In that respect,

TIR remote sensing is the only cost effective and realistic source of data to retrieve LST in a regional to global scale with different spatial and temporal resolutions (Dash et al., 2002; Coll et al., 2005; Göttsche and Olesen, 2009).

Studies have shown that uncertainties exist in satellite-derived LST (e.g., Jackson et al., 2010). These uncertainties can vary with geographic location, weather conditions, LC (thus, emissivity), viewing angle and topography (see Trigo et al., 2008; Hulley et al., 2012). This implies that validation is a necessary step in order to determine the uncertainties of remotely sensed LST data and to understand their capabilities and limitations (Piters et al., 2011) in each region. LST is defined as the directional radiometric temperature of the surface based on radiance measurements (see Norman and Becker, 1995). Ground truth data used for validation of LST, on the other hand, are usually collected from point measurements. The most important factor for any LST validation site, therefore, is the homogeneity of its surface temperature, which can be minimized for regions with uniform LC and SM (Kabsch, 2009). Uniformity of LC types of field measurement sites for this research will be assessed based on the visible and near-infrared (NIR) observations (Landsat imagery) from the area. Homogeneity of surface temperature at validation site will be evaluated based on the differences between multiple ground measurement points on a similar LC type (Chapter 3).

1.3 The relationship between LST and air temperature

The standard meteorological T_a is measured in a shelter at ~2 m height (Brunel, 1989; Jin and Dickinson, 2010). It is an important descriptor of terrestrial environmental conditions across the earth (Prihodko and Goward, 1997). The spatial distribution of weather stations in many parts of the world, however, is often limited which restricts the use of T_a measurements over a large spatial domain (Vancutsem et al., 2010). LST, on the other hand, is measured in a global extent with significantly higher spatial coverage (Jin and Dickinson, 2010). The US National Research Council and the Intergovernmental Panel on Climate Change (IPCC) expressed the need for long-term remotely sensed LST data in global warming studies to overcome the limits of conventional surface T_a measurements (Jin, 2004). Remote sensing data have great potential to estimate spatio-temporal patterns of T_a which can further our knowledge on both climate and terrestrial biological processes at regional and global scales (Benali et al., 2012). Monitoring and understanding the trends of T_a and LST are crucial in the study of regional and global climate change (Yoo et al., 2011). These differences can be monitored and modelled from multiple daily satellite observations, such as the MODIS LST.

Studies have shown that LST can be used for linear regression estimates of daily minimum and maximum T_a at a local scale (Mostovoy et al., 2006; Vancutsem et al., 2010; Zhang et al., 2011a; Yoo et al., 2011; Evrendilek et al., 2012; Benali et al., 2012; Zhu et al., 2013). Cresswell et al. (1999) found an over and underestimation of T_a at day and night, respectively, from the Meteosat LST observations (Fig. 1.1). They attempted to correct these errors and produce a proxy of T_a by applying a solar zenith angle correction on the Meteosat geostationary observations. They achieved an accuracy within 3 °C for over 70% of the Meteosat temperatures. Similarly, Jin and Dickinson (2010) have studied the differences in the diurnal cycles of LST and T_a over a single site. Some studies (Florio et al., 2004) have used several statistical approaches that combine a simple AVHRR SWT with ground meteorological station measurements in the prediction of T_a. Other studies (Wloczyk et al., 2011) have used the Landsat LST data to derive T_a. They have attempted to assign the satellite-derived T_a to a certain height above the ground and have investigated the possibility of a simple correction for reference height. They also considered the link between T_a spatial pattern and the window-size of the Landsat LST pixels. Xu et al. (2012) used four empirical regression models to estimate the relationship between T_a measurements and the MODIS-Aqua LST and found different relationships between the two over different LC types. They also assessed the effect of the MODIS LST window-size on the agreement between the two variables and found that spatial averaging over multiple pixels improves the accuracy of T_a estimates. Other studies have used the temperature/vegetation index method (TVX) to derive T_a (Goward et al., 1985; Prihodko and Goward, 1997; Prince et al., 1998; Stisen et al., 2007; Nieto et al., 2011).

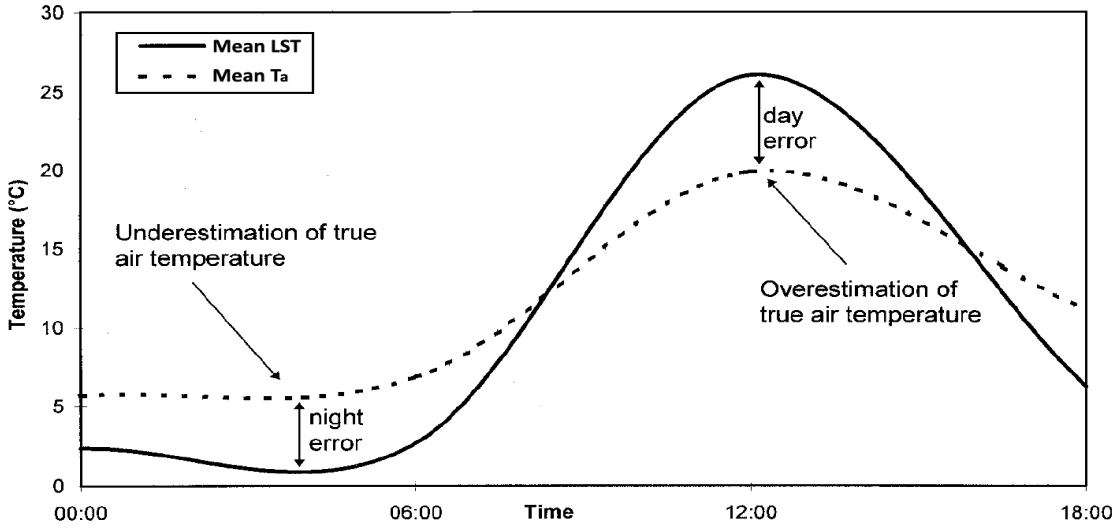

Figure 1.1: Day and night differences between satellite observed LST and screen T_a measurements at 2 m height (from Cresswell et al., 1999)

1.4 Soil moisture from remotely sensed LST

Thermal conductivity of soil varies with changes in moisture levels (Minacapilli et al., 2009; Vandoninck et al., 2011). These changes can be detected from remotely sensed LST data and, based on that, the near-surface SM can be estimated given all other soil properties constant over space or time (Vandoninck et al., 2011). The near-surface SM generally refers to the water contained in the upper 1-2 m of the soil, which can potentially evaporate into the atmosphere (Verstraeten et al., 2006). LST determines distribution of heat energy into the subsurface layer and consequently impacts associated water fluxes (Parinussa et al., 2011). Both observational and modeling studies provide evidence that surface SM plays a critical role in the partitioning of the available energy into latent and sensible heat fluxes (Bindlish et al., 2001). Consequently, as energy and water balance are preserved, changes in LST can affect SM and vice versa (Lakshmi and Zehrfuhs, 2002). For the same reason, remotely sensed LST is widely used to derive the near-surface SM over various spatial and temporal domains (Pratt and Ellyett, 1979; Verstraeten et al., 2006; Vandoninck et al., 2011; Zhao et al., 2012). The underlying principle used to determine SM from LST data is the ability to derive thermal inertia (TI) variability of the surface materials from multitemporal daily (typically once at day and once at night) TIR observations (Verstraeten et al., 2006; Carlson, 2007). TI is the resistance of the surface materials to changes in temperature (Sobrino and El-Kharraz, 1999a). The near-surface SM directly influences soil temperatures by increasing both specific heat and thermal conductivity, thus TI of soils (Moran et al., 2004). Specifically, TI method exploits the difference in heat capacity of dry and wet soils[1]. According to TI properties (Fig. 1.2), wet soils tend to hold heat for a longer period while warming and cooling in dry soils is faster (Hain et al., 2011). Two or more LST observations at cool and warm hours of the day (early morning, early afternoon) enables capturing the diurnal temperature differences (Price, 1980), which contain the information about TI of the surface.

TI mapping from airborne and spaceborne sensors has been known (Pratt and Ellyett, 1979) even before the ideas to exploit this property to derive the near-surface SM. A simple surrogate of TI is the apparent thermal inertia (ATI), which can be derived directly from multispectral remote sensing imagery (Wang and Qu, 2009). ATI has been used to derive the near-surface SM from daily LST observations, such as the MODIS LST daily product and Meteosat geostationary observations. This

[1]The specific heat capacity (c_p) of water, wet and dry soil are approximately 4.2, 1.48 and 0.8 J.g^{-1}.K^{-1}, respectively (see:
http://www.engineeringtoolbox.com/water-thermal-properties-d_162.html
and http://www.engineeringtoolbox.com/specific-heat-solids-d_154.html).

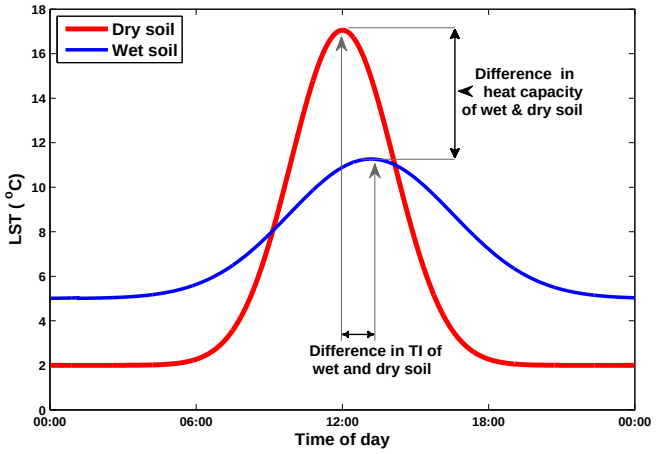

Figure 1.2: Diurnal variability of skin temperature under the effect of thermal inertia (TI) over wet and dry soils.

approach exploits LST differences at day and night (ΔLST) and albedo information from visible data to derive SM (Verstraeten et al., 2006). To account for the variation in sun angle, which affects albedo and surface temperature, the ATI output is adjusted for local latitude and day of the year. Verstraeten et al. (2006) used the ATI method to derive SM saturation index (SMSI) based on the difference between Meteosat day and night LST observations. Time-series of SM were then calculated by normalizing the remotely sensed SMSI to the long-term minimum and maximum measured SM in their study area. Vandoninck et al. (2011), on the other hand, used four LST observations from MODIS-Terra and MODIS-Aqua day and night overpasses to derive ATI values over Southern Africa. They investigated sources of error in ATI calculation over temporal and spatial domains. They also compared the ATI derived from the MODIS LST with the SM time-series from the AMSR-E SM product. Some of their experiment sites showed more consistency between the two dataset, whereas, some other sites showed considerable anomalies between the two. Matsushima et al. (2011) found that TI has the potential to estimate subsurface SM with a precision of $\pm$3%–4% over bare to sparsely vegetated areas. Chang et al. (2012), on the other hand, found a strong relationship between SM retrievals from the MODIS LST using ATI and the measurements at 10 cm, 100 cm and 200 cm depths with 0.80, 0.84 and 0.84 correlations, respectively, over a tropical area in northern Thailand.

Other methods to estimate SM from LST data also exist in the literature. Universal triangle method, which assumes a unique relationship among SM, the normalized difference vegetation index (NDVI) and the LST for a given region, is another technique to derive SM from a combination of TIR, visible and NIR data (Wang and Qu, 2009; Sun et al., 2012). This method is described with more detail in Carlson et al.

(1994) and Carlson (2007). Soil Vegetation Atmosphere Transfer (SVAT) is used to monitor root-zone SM based on a combination of visible, NIR and TIR remotely sensed observations (Crow et al., 2008).

Since precipitation is the dominant forcing of SM at atmospheric timescales (Draper et al., 2009), a strong spatial correlation is expected between the near-surface SM and rainfall. Hence, rainfall data alongside the *in-situ* SM will be used in this research to validate the near-surface SM derived from LST observations. After initial accuracy assessment, SM simulations from the WRF model coupled with Noah LSM will be compared remotely sensed SM derivations.

1.5 Soil moisture from microwave satellite data

The near-surface SM is also derived directly from satellite observations in microwave (MW) region, which rely on known dielectric properties of the soil and water (Jackson et al., 1996). The passive MW SM product from AMSR-E is one of these datasets. Compared with the TIR data, however, the spatial resolution of MW sensors is generally coarse (Hain et al., 2011). Several SM products are available from AMSR-E MW observations, which are derived using different algorithms. Draper et al. (2009) used AMSR-E SM product over Australia and compared this dataset with the *in-situ* SM measurements from 12 ground monitoring sites[2]. Jackson et al. (2010) compared the National Aeronautics and Space Administration (NASA) and Japan Aerospace Exploration Agency (JAXA) standard SM products with the ground network observations, along with two alternative SM products developed using the single-channel algorithm (SCA) and the land parameter retrieval model (LPRM). They found that each algorithm performs differently at each site. Neither the NASA nor the JAXA standard products provided reliable estimates for all the conditions represented by the four watershed sites, and both algorithms had a moderate to large bias in all cases. Similar results have been found by others, such as Choi and Hur (2012), where they have reported 10% to 17% bias between SM from AMSR-E MW observations and the *in-situ* measurements. They discussed that this anomaly is theoretically due to the spatial scaling mismatch and different measurement depth between the ground measurements and the AMSR-E SM. Therefore, they integrated the MODIS LST data with higher spatial resolution to improve the agreement between the *in-situ* measurements and AMSR-E product and reduce their error statistics. Many studies, therefore, have used AMSR-E data after careful filtering and validation for assimilation into numerical

[2]Their data can be accessed from International Soil Moisture Network via http://www.ipf.tuwien.ac.at/insitu/index.php/in-situ-networks.html

models (Reichle et al., 2007; Shi et al., 2009; Li et al., 2012a; Draper et al., 2012) and surface SM analysis (Draper et al., 2009; Zhang et al., 2011b). Li et al. (2010) have examined the potential benefits of simultaneously assimilating both near-surface SM estimates from MW and root-zone SM retrievals from TIR data into a soil water balance model. They have reported at least 35% improvement in the accuracy of SM simulations by integrating deeper-zone SM from TIR data. Others have used the MODIS LST for so called 'disaggregation' of L-band SM product from Soil Moisture and Ocean Salinity (SMOS), which has a lower spatial resolution of 40 km (Merlin et al., 2008, 2013). These studies shows that a better spatial resolution with adequate temporal abundance can be achieved if MW SM and LST data are combined. The MODIS LST dataset, therefore, is used in Chapter 6 to improve temporal and spatial profiles of AMSR-E SM product.

1.6 Numerical modelling of air temperature and soil moisture

Shortcomings of using only remotely sensed data is listed by Huang et al. (2008) as follows: (*i*) remote sensing observations are instantaneous missing the continuous variation of LST; (*ii*) optical and TIR sensors are influenced by atmospheric conditions such as cloud and water vapour; and finally, (*iii*), soil temperature beneath surface soil is not accessible by remote sensing. On the other hand, land-atmospheric models have uncertainties in approximation of surface physical processes due to the heterogeneity of the land surface, which can be improved using satellite based datasets (Ghent et al., 2010). These shortcomings can be partly resolved by combining simulations from numerical land-atmospheric models, which also provide continuous spatial fields of heat fluxes (Rigo and Parlow, 2007), with satellite-derived parameters. Meng et al. (2009) used remotely sensed LST data for assimilation into Common Land Model (COLM), originated from the state-of-the-art Community Land Model (CLM), to adjust the evaporative fraction of soil and canopy. They found that the COLM outputs compare well with the *in-situ* evapotranspiration observations after assimilation of LST. Huang et al. (2008) assimilated the MODIS LST into COLM LSM and found that their method significantly improves soil temperature profile estimation. Hain et al. (2011) compared SM from AMSR-E passive MW observations and TIR data with the Noah LSM simulations. On the other hand, AMSR-E SM product is used for assimilation into land (Reichle et al., 2007; Draper et al., 2012) as well as the coupled land-atmospheric models (Shi et al., 2009, 2010; Li et al., 2012a).

1.7 Structure of the thesis

This thesis is organized in seven chapters as follows:

1. Introduction to the thesis, expression of the research objectives and a review of the research background.

2. Description of the theoretical background which includes an overview of LST retrieval algorithms, a summary of the physics of numerical modeling of LST and SM by the WRF model and finally, a summary of spatial and statistical methods for LST data analysis, which will be used in this research.

3. Validation of the MODIS LST: this section describes the results from validation of the MODIS LST product based on the *in-situ* measurement and comparison of the results with the WRF model simulations over Cass test-site in the Waimakariri River Basin. Results from a second validation site located in the Canterbury Plains are also given in this chapter.

4. Spatio-temporal variability of LST-T_a relationship: the relationship between remotely sensed LST and T_a, which is strongly influenced by the local surface heat fluxes, is analysed by overlaying a spatial window of varying size on the MODIS LST grid.

5. Soil moisture retrieval from the MODIS LST: two SM estimation approaches based on the ATI method are compared and the results are validated using the *in-situ* measurements and rainfall data, and are compared with the WRF SM simulations.

6. Adjustment of the AMSR-E SM using the MODIS LST: AMSR-E SM is validated based on rainfall data and the WRF model simulations, and the MODIS LST is applied to improve AMSR-E SM over spatial and temporal domains.

7. Summary, conclusion and outlook: summary of the key findings from four major chapters, discussion of the main results, conclusion of the research and the outlook for future research are presented in this chapter.

Chapter 2

Theoretical background, data and methods

2.1 LST retrieval from remotely sensed observations

2.1.1 Electromagnetic radiation in remote sensing

The electromagnetic radiation (EMR) energy in specific spectral ranges is used by various remote sensing instruments for observation of certain groups of earth features. These sensors are designed based on the applications of the observed data. Three common subdivisions of the EMR energy are identified for earth remote sensing purposes which include the visible, infrared (IR) and the microwave (MW) regions (Table 2.1). The IR region itself is subdivided into the near-IR (NIR), middle-IR (MIR) and the thermal-IR (TIR) regions (Lillesand et al., 2008). Other classifications also exist in the literature (e.g., Elachi and Van Zyl, 2006), where the middle part of the IR region is classified as shortwave IR (SWIR), the TIR region is identified as MIR and anything beyond TIR is classified as far IR. In this research the Lillesand et al. (2008) convention is followed (Fig. 2.1).

The original Level 0 TIR observations from the satellite sensors are organized according to the sensor viewing geometry and pixel size to a set of granules called Level 1A data. The level 1A data are calibrated based on the sensor parameters in the ground receiving stations into the Level 1B product. The processing of level 1B product differs slightly by the provider, but it usually contains geolocation fields (Latitude and Longitude) of each pixel on the ground. The calibrated level 1B product for the TIR bands is converted to the top of the atmosphere (TOA) radiance, followed by the TOA brightness temperature (T_b) using inverse Planck's law (Kerr et al., 2000). In order to

Table 2.1: Subdivisions of the EMR energy used in remote sensing (after Lubin and Massom (2006))

Spectrum	Wavelength (μm)	Wavenumber (cm^{-1})	Frequency (THz)	Measured-quantity
Visible	0.4 – 0.7	25000 – 14286	750 – 428	Reflectance
Blue	0.4 – 0.5	25000 – 20000	750 – 600	Reflectance
Green	0.5 – 0.6	20000 – 16667	600 – 500	Reflectance
Red	0.6 – 0.7	16667 – 14286	500 – 428	Reflectance
Infrared (IR)	0.7 – 15	14286 – 667	428 – 20	Ref. + emis.
Near-IR	0.7 – 1.3	14286 – 7692	428 – 231	Reflectance
Mid-IR	1.3 – 3.0	7692 – 3333	231 – 100	Ref. + emis.
Thermal IR	3.0 – 15.0	3333 – 667	100 – 20	Emission
Microwave	10^3 - 10^4	10 - 1	0.03 - 0.30	Ref. + emis.

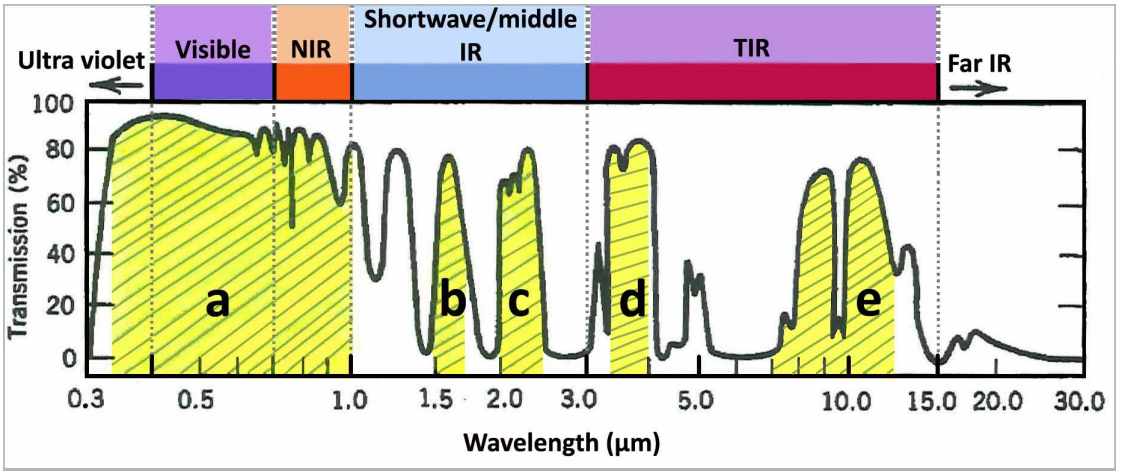

Figure 2.1: Visible and near-infrared (a), shortwave (or middle) infrared (b & c) and thermal infrared (d & e) atmospheric windows (after Elachi and Van Zyl (2006)).

convert the TOA T_b into the surface T_b, it is necessary to consider the atmospheric effects on the radiance. Finally, the surface T_b is converted into surface temperature after taking into account the surface emissivity and directional effects (Kerr et al., 2000). In practice, atmospheric correction, emissivity and directional effects are coupled and these modulating factors cannot be approached independently (Kerr et al., 2000). For the same reason, the subject of LST retrieval from level 1B data in the literature is discussed equally under the atmospheric correction or retrieval models and algorithms (see Kerr et al., 2000; Rees, 2001, pg. 157 sec. 6.3.6). In view of this, the following section provides a general discussion about the existing atmospheric correction models and algorithms used in remote sensing and singles out those which are specifically used for the retrieval of LST from the TIR observations.

2.1.2 Atmospheric correction of remotely sensed data

Correction of the atmospheric effects requires inputs that describe the variable constituents which influence the signal measured at the TOA, as well as a proper modelling of the atmospheric scattering and absorption (Vermote et al., 1997). In addition to absorption and scattering, the atmospheric effects also include upward atmospheric emission and the downward atmospheric irradiance which are originated from surface reflection (Dash, 2005). The objective of the atmospheric correction algorithms, therefore, is to adjust satellite observations for these effects. Special algorithms are designed for the correction of the imagery according to which part of the EM spectrum (visible, NIR and TIR) is used by the sensor. The specific focus in this section is on the algorithms used for the correction of data acquired in the TIR region.

Since the wavelength of the infrared radiation in TIR region is longer than the circumference of the air molecules, the effects of scattering is negligible (see Wallace et al., 2006, pg. 134 section 4.5.3) and, therefore, is generally ignored (Dash et al., 2002). The effects of absorption and emission by the atmospheric constituents, on the other hand, are dominant in TIR region. Water vapour (H_2O), CO_2 and O_3 are the three most radiatively active atmospheric greenhouse gases. The other lesser important greenhouse gases affecting the sensor reaching radiance include O_2, CH_4 and N_2O (Vermote et al., 2006). These gases absorb radiation by rotational changes caused by the weaker frequency EMR energy in the TIR and microwave range (Vermote et al., 2006). CO_2 and O_2 mixing ratios are almost constant and their densities can be determined with the knowledge on the atmospheric pressure and temperature (Wan, 1999). CH_4 and N_2O are uniformly distributed in the troposphere and stratosphere and vary slowly in time (Liou, 2002; Dash, 2005; Vermote et al., 2006). However, H_2O and O_3 concentrations are variable with respect to both time and geographical location (Liou, 2002; Vermote et al., 2006), but one must note that O_3 is only of local importance (Dash et al., 2002; Dash, 2005). The influence of aerosols is generally an order of magnitude smaller than molecular effects, except when the atmosphere is hazy (Price, 1983). As a result, only H_2O (i.e., water vapour) is the main concern in the TIR region (Price, 1983; Rees, 2001; Liou, 2002; Dash, 2005; Wallace et al., 2006).

Errors of up to 3 °C can be attributed to the atmospheric water vapour content under the clear sky conditions (Byrne et al., 1979). Satellite sensor channels avoid the molecular absorption bands (Vermote et al., 2006), which includes water molecules as well. Water vapour absorbs thermal infrared radiation in the 1200 to 2000 cm^{-1} (5.0 - 8.33 μm) region[1], while in the 800 to 1200 cm^{-1} (8.33 - 12.5 μm), except for

[1]Physical discussion of absorption involving water molecules in the TIR window is provided in Liou

the absorption by O_3 in the 9.6 μm, the atmosphere is relatively transparent (Price, 1983; Liou, 2002). These transparent regions are known as *atmospheric windows* (Prince et al., 1998), and the latter window is largely used in thermal remote sensing (Fig. 2.1). The objective of the atmospheric correction algorithms, therefore, is to remove the effects which cannot be avoided even in these windows.

2.1.3 Algorithms for the atmospheric correction

A review of the atmospheric correction algorithms is provided by Gao et al. (2006). The algorithms for the correction of the atmospheric effects traditionally have been based on the radiative transfer (RT) equation, in which the description of the atmospheric state (atmospheric profiles of pressure, temperature and relative humidity) must be given either by satellite sounding or conventional radiosonde (Price, 1983; Becker and Li, 1990; Wan and Dozier, 1996). Given that the longer wavelengths of the EM radiation (such as TIR) are less affected by the atmospheric effects, the majority of the RT codes are designed for the visible and the near-infrared region (approximately 0.4 to 2.5 μm). However, for spaceborne observations where the full effect of the atmosphere is felt, errors in temperature retrievals from thermal data due to the atmospheric effects (mainly by water vapour) can be as large as 10 K, hence correction is generally necessary (Rees, 2001, pg. 157).

The algorithms available for the atmospheric correction of TIR data can be categorized in three major groups (Rees, 2001; Dash et al., 2002):

1. Physical modelling based on RT equation (single channel approaches)
2. Split Window Technique (SWT) based on two TIR channels
3. Multiple view-angle technique

2.1.3.1 Radiative transfer algorithms

Because the main correction is due to the water vapour, physical modelling is rather unsatisfactory unless a detailed characterization of the atmosphere is available (Rees, 2001). Physical modelling algorithms are solutions of the RT equation, therefore, they have been known as RT algorithms. These algorithms are used for the correction of the visible as well as IR (including TIR) data. The RT method takes the TIR measured by satellite sensor in one channel, generally chosen in an atmospheric window, and corrects it from residual absorption in which the atmospheric state must be given either

(2002).

by satellite vertical sounders, climatological data or by atmospheric radiosoundings (Becker and Li, 1990). Since no single-channel TIR data is used in this research, readers are referred to the existing research for further details about RT algorithms and computation equations (see Li et al., 1999; Jiménez-Muñoz and Sobrino, 2003; Elachi and Van Zyl, 2006; Jiménez-Muñoz et al., 2009; Coll et al., 2010; Wang et al., 2011).

2.1.3.2 Split window algorithms

Split window algorithms, or SWTs, are based on the brightness temperature of the target measured in two closely spaced spectral bands (Rees, 2001). The SWT was originally developed to derive sea surface temperature (SST) from multi-channel TIR observations based on the differential absorption in two adjacent spectral windows (Becker and Li, 1990). Since the emissivity of water is relatively homogeneous, this algorithm used a constant value (normally 1) as the emissivity of water. However, such a method did not work over land surfaces, mainly because the emissivity is not equal to 1 and depends on the spectral band and the surface LC type (Becker and Li, 1990). Therefore, an extension of this method to apply on land surfaces was developed by Becker and Li (1990), which takes the emissivity of the surface types into account. Becker and Li (1990) described the SWT to derive LST from two adjacent TIR channels of the NOAA Advanced Very High Resolution Radiometer (AVHRR). This technique was explained by Wan and Dozier (1996) as a new algorithm called generalized split-window (GSW), which was later used to derive LST from the MODIS TIR observations in channels 31 (10.780–11.280 μm) and 32 (11.770–12.270 μm) with a consideration of satellite viewing angles. Details of derivation and validation of the MODIS LST product using the GSW algorithm has been explained in a series of research published by the MODIS science team (Wan et al., 2002a,b, 2004; Wan, 2008; Wan and Li, 2008). Another method to derive LST from the MODIS observations was a physics-based algorithm developed by Wan and Li (1997) for simultaneously retrieving surface band-averaged emissivities and LST from day/night pairs of MODIS data in seven TIR bands (i.e., bands 20, 22, 23, 29, 30, 31 and 32). They used a set of 14 nonlinear equations in the algorithm to solve with statistical regression and the least-squares fit method.

Land SWT uses the brightness temperature from two closely spaced spectral bands (T_{b1} and T_{b2}), usually one centred at 11 μm and another at 12 μm (Rees, 2001). LST is then calculated by Eq. 2.1 (Becker and Li, 1990; Rees, 2001; Dash et al., 2002; Coll

et al., 2005):

$$\mathrm{LST} = a_0 + a_1 T_{b1} + a_2 T_{b2} \tag{2.1}$$

where the coefficients a_0, a_1 and a_2 are determined empirically using a least squares fit. This equation is a simplified form of SWT. More complex forms of SWT also exist in the literature, which are developed to be used with data from different sensors.

Generalized SWT: The Generalized SWT (GSW) is developed by Wan and Dozier (1996) and is used to derive the MODIS LST daily product.

$$\begin{aligned}\mathrm{LST} =& C + \left(A_1 + A_2\frac{(1-\epsilon)}{\epsilon} + A_3\frac{\Delta\epsilon}{\epsilon^2}\right)\frac{T_4 - T_5}{2} \\ &+ \left(B_1 + B_2\frac{(1-\epsilon)}{\epsilon} + B_3\frac{\Delta\epsilon}{\epsilon^2}\right)\frac{T_4 - T_5}{2}\end{aligned} \tag{2.2}$$

where A_i, B_i and C are empirical coefficients provided by look-up tables (LUTs) and depend on viewing zenith angle, column water vapour and air temperature (Wan and Dozier, 1996; Wan, 1999). A_i and B_i are obtained from regression analysis of the MODIS simulation data created by MODTRAN4 atmospheric RT code in wide ranges of surface and atmospheric conditions and C is derived using NDVI values of the area (Wan and Dozier, 1996):

$$C = \frac{\mathrm{NDVI} - \mathrm{NDVI}_{bs}}{\mathrm{NDVI}_v - \mathrm{NDVI}_{bs}} \tag{2.3}$$

where NDVI_{bs} is the minimum value of NDVI in the area over bare soil and NDVI_v is the maximum NDVI of the area over vegetation cover.

2.1.3.3 Multiple view-angle algorithms

Multiple view-angle (or too-look) technique uses observations of the same surface from two view angles (Rees, 2001). It is based on the differential absorption due to different atmospheric path length (Becker and Li, 1990). One of these views is usually nadir whereas the other view is oblique. The distance between the target and the sensor from an oblique view is longer than the nadir view (Eq. 2.4), which means that the brightness temperature of the oblique view has been subject to more atmospheric effects (Rees, 2001). As a result, the difference in the brightness temperatures of these two view angles is used to estimate the atmospheric contribution.

$$\Delta d = cos(\theta_{nadir})/cos(\theta_{oblique}) = 1/cos(\theta_{oblique}) \tag{2.4}$$

where Δd is the coefficient of difference in distance between the target and the sensor from a nadir and an oblique view angle (θ_{nadir} is considered equal to 0, $\theta_{oblique}$ is relative to θ_{nadir}). Therefore,

$$d_{oblique} = \Delta d \times d_{nadir} \tag{2.5}$$

where $d_{oblique}$ is the distance between the target and the sensor from an oblique and d_{nadir} is the distance between the target and the sensor from a nadir view angle, respectively[2].

2.1.4 *Uncertainty in LST retrievals*

The two principal sources of uncertainty in the temperature observing systems are atmospheric attenuation and thermal emissivity (ϵ) of the terrestrial surface (Taylor, 1979). Other sources of error include directional or view angle effects (Kerr et al., 2000; Dash, 2005), and to a lesser extent, the spatial/temporal variability (Coll et al., 2005), state of the surface (roughness, surface type, moisture, vegetation cover) and height of the instrument above the surface (Jin, 2004).

The total uncertainty in the temperature measurement for each radiometer, $\sigma(T)$, is given by the combination of the three sources of error: calibration (or atmospheric effects), emissivity correction and spatial/temporal variability (Coll et al., 2005):

$$\sigma(T) = \left[\sigma(cal)^2 + \sigma(em)^2 + \sigma(var)^2\right]^{1/2} \tag{2.6}$$

where cal is calibration, em is emissivity and var is spatial/temporal variability. Eq. 2.6 is especially useful for differentiating the amount of uncertainties due to the emissivity and the atmospheric effects, and can be helpful to estimate the uncertainties if the available data from one of these parameters seems erroneous. A generalized equation to estimate sensitivity of the derived LST (δLST) for each of the individual sources of error in given by Jiménez-Muñoz and Sobrino (2003):

$$\delta\text{LST} = |LST(x - \delta x) - LST(x)| \tag{2.7}$$

where δLST is the error in the LST, x is the parameter for which the sensitivity analysis is performed (e.g., emissivity, directional effects, etc.) and δx is the error in this parameter.

[2]For $\theta_{oblique} = 30°$, Δd will be 1.155 and if the satellite is orbiting at 800 km altitude (i.e., $d_{nadir} = 800$), $d_{oblique}$ will be 924 km which is longer than d_{nadir}.

The effects due to the atmospheric attenuation, sometimes classified as a calibration error (e.g., Coll et al., 2005), can be as high as 10 K (Rees, 2001, pg. 157). Since atmospheric effects were discussed above (Section 2.1.2), this section is focused on the remaining sources of uncertainties. Spatial/temporal variability depends on the ground track of the sensor. In this sense, with a large ground track both geometry and illumination of the sensor footprint will be various depending on the curvature and local solar time on the surface. Since polar orbiting satellites generally view a pre-defined swath at local solar overpass time, such effects seem to be minor. More important sources of error, *i.e.*, emissivity and the view angle effects are discussed in more detail below.

2.1.4.1 Emissivity effects

Emissivity of the surface varies with surface vegetation density, soil chemical components, soil physical conditions (such as grain size, moisture content), view angle (Jin, 2004) and spectral wavelength (Kant and Badarinath, 2000). From the latter perspective, the broad-band thermal emissivity values vary from narrow-band values for the same surface (Kant and Badarinath, 2000). The emissivity of terrestrial objects can vary greatly according to the texture, mineral composition and moisture content of the surface (Taylor, 1979). Emissivity can vary over the same surface type with a change in the spectral wavelength, however, the spectral emissivity characteristics of various LC types in 10–12.5 μm atmospheric window is relatively stable (Wan, 1999).

Emissivity error in the SWT, where two bands are involved, is given by Becker and Li (1990) as below:

$$\Delta T = 50\frac{(1-\epsilon)}{\epsilon} - 300\frac{(\epsilon_1 - \epsilon_2)}{\epsilon} \tag{2.8}$$

where $\epsilon = (\epsilon_1 + \epsilon_2)/2$.
For an uncertainty of 0.01 in emissivity, errors of up to 1.6 K in LST retrievals from the θ-independent GSW algorithm can be expected (Wan and Dozier, 1996). These errors can be reduced to 0.37 K over well known land surfaces in the θ-dependent GSW algorithm (Wan and Dozier, 1996).

2.1.4.2 View angle effects

Directional effects increase with an increase in the viewing zenith angle (θ) of the instrument. However, θ effect may be ignored when the angle is less than 45° (Jin, 2004). θ is the angle covering the instantaneous field of view (IFOV) of the satellite. θ is different than the satellite or local zenith angle, which is expressed by θ_s. θ_s is

relative to the Nadir zenith line and varies over the pixels in the scene with an increase towards pixels off nadir (Fig. 2.2), which is related to θ with Eq. 2.9,

$$sin(\theta_s) = (R + H) / R.sin(\theta) \tag{2.9}$$

where R is the Earth's radius and H is satellite height (or orbiting altitude) relative to the Earth (Sun and Pinker, 2003).

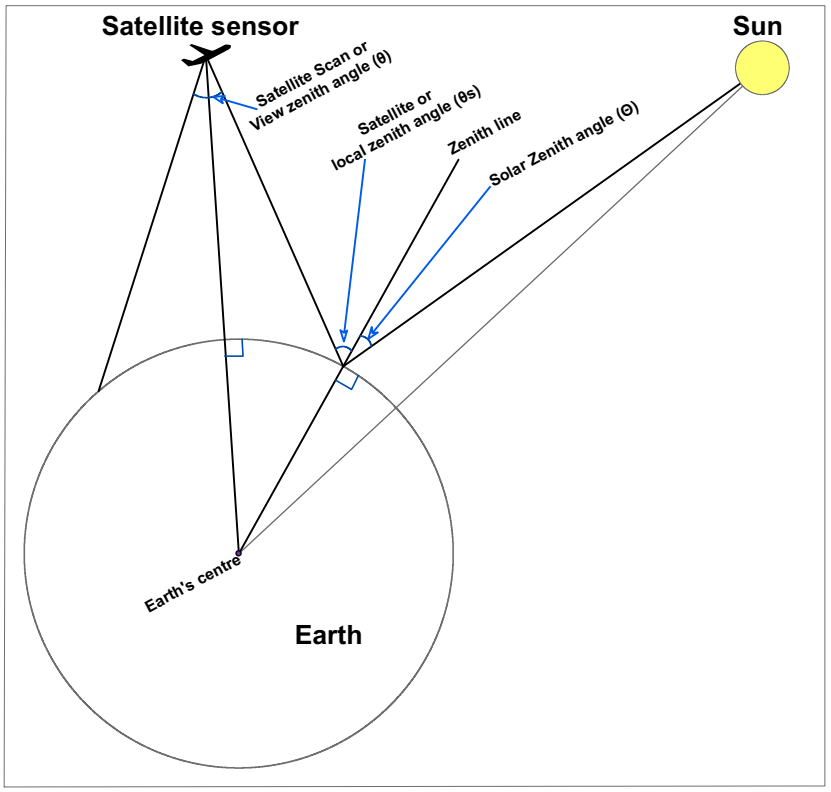

Figure 2.2: Schematic diagram of Sun, Earth and Satellite geometries and Zenith angles [after: http://www2.ncdc.noaa.gov/docs/podug/html/c1/sec1-1.htm, accessed 15 March 2012]

Variations in θ can affect ϵ as well (Wan, 1999, pg. 6). Over vegetation, in addition to the angular effects in the emissivity, the emitted radiation varies with the viewing angle due to the angular effect in canopy temperature (Wan, 1999, pg. 6). The LST product from MODIS is produced by a θ-dependent SWT algorithm, where individual viewing angles are considered to retrieve LST at an accuracy of 1 K for the whole scan swath range (Wan and Dozier, 1996). Considering Terra and Aqua orbiting altitude ($H \approx$ 700 km) and Earth's radius ($R \approx$ 6400 km), θ_s is given based on Eq. 2.9 for a number of angles[3] viewed from the East or West of nadir in Table 2.2.

[3]Example: for H = 700 km, R = 6.4 x 10^3 km and $\theta = 55°$, θ_s will be 65.33°

Table 2.2: MODIS Terra/Aqua θ and θ_s equivalents based on Eq. 2.9

θ	θ_s	$sin(\theta)$	$sin(\theta_s)$
15°	16.69°	0.26	0.29
25°	27.96°	0.42	0.47
35°	39.52°	0.57	0.64
45°	51.67°	0.71	0.74
55°	65.33°	0.82	0.91

2.1.5 Validation versus inter-comparison

Validation is defined as assessing the uncertainties in the remotely sensed products through comparison with *in-situ* ground measurements (Garrigues et al., 2008). It is an important and particularly challenging task due to the disparity in spatial scales between satellite and *in-situ* observations (Jackson et al., 2010). It must be noted, therefore, that ground-based validation is a close approximation and not an absolute verification due to the following issues (Sapiano and Arkin, 2009; Jackson et al., 2010):

1. Disparity of pixel to point assignment
2. Ambiguities in satellite footprint and pixel-size variations
3. Variability of surface conditions over time
4. Accessibility of parts or all of the footprint for ground measurements
5. Temporal disparity between the energy recorded by the *in-situ* instrument and instantaneously observed by the satellite
6. Uncertainties due to instrument calibration and/or measurement set-up

On the other hand, evaluating the temporal and spatial consistency of satellite products over a large area can be easily achieved by inter-comparison of different datasets (Garrigues et al., 2008) from satellites or from other sources, such as numerical model simulations. Since *in-situ* measurements as the highest quality field data are not usually employed in an inter-comparison, the uncertainty assessment results based on this approach are generally inferior when they are weighed against the results of a direct validation. In this research, direct validation is employed when *in-situ* measurements are available (Chapter 3, 4 and 5) and an inter-comparison is practiced when there are no direct ground measurements available for a certain period of time (Chapter 6).

2.2 Numerical modelling of land surface parameters

This section provides a brief introduction about numerical modelling of surface parameters with the WRF model, which will be used in this research. This model is used in

hindcasting mode for simulations of T_a and SM. The WRF is a numerical weather prediction and atmospheric simulation system suitable for both research and operational applications (Skamarock et al., 2008). Developed by the National Center for Atmospheric Research (NCAR), the WRF model is a limited-area, nonhydrostatic, terrain-following sigma-coordinate[4] model designed to simulate or predict regional weather and climate (Jin et al., 2010; Maussion et al., 2011). The WRF model is suitable for use in a broad range of applications across scales ranging from metres to thousands of kilometres (Hong et al., 2009; NCAR, 2011).

2.2.1 *Components of the WRF modelling system*

Two packages of programs are available in the WRF modelling system for simulations:

(*i*) the WRF Preprocessing System (WPS) and

(*ii*) the Advanced Research WRF (ARW) dynamic solver

(*i*) The WPS is for preparation of the model domains, integration of terrestrial data and interpolation of the global meteorological data into defined model domains. It is a set of programs that takes terrestrial and meteorological data (typically in GriB format) and transforms them for input to the ARW pre-processor "*Real*" program (Fig. 2.3) for real-data cases (Skamarock et al., 2008). Terrestrial data (including the local LC) are integrated by the *"Geogrid"* component of the WPS into the 2-dimensional static fields. Global meteorological data are ingested by the *"Metgrid"* component of the WPS into the 3-dimensional atmospheric fields. Each of the static and atmospheric fields contain various terrestrial and atmospheric information about the target area for the simulation (see Skamarock et al., 2008, for a list and details of these fields). Global meteorological data are available from the National Centers for Environmental Prediction (NCEP) analysis data. The output from WPS contains 3-dimensional fields (including the surface) of temperature and the 2-dimensional static terrestrial fields of albedo, terrain elevation, vegetation greenness factor (Fg) and LC type (Skamarock et al., 2008, p. 43). It also contains the 2-dimensional time-dependent (non-static) fields of skin temperature, layers of soil temperature and soil moisture (*Ibid.*).

(*ii*) The ARW dynamical solver uses the output from the WPS to produce simulations for the area specified by the user in a file called 'namelist'. The model uses

[4] A sigma coordinate system conforms to natural terrain, which allows a better depiction of continuous fields such as temperature advection and winds (Allen et al., 2002).

terrain-following, dry hydrostatic-pressure vertical coordinate and the Arakawa-C horizontal grid (Skamarock et al., 2008). The model supports one-way, two-way and moving nest options (http://www.mmm.ucar.edu/wrf/users/model.html). Most of the simulations in this research were produced in two-way nesting with smoothing for the nested domain.

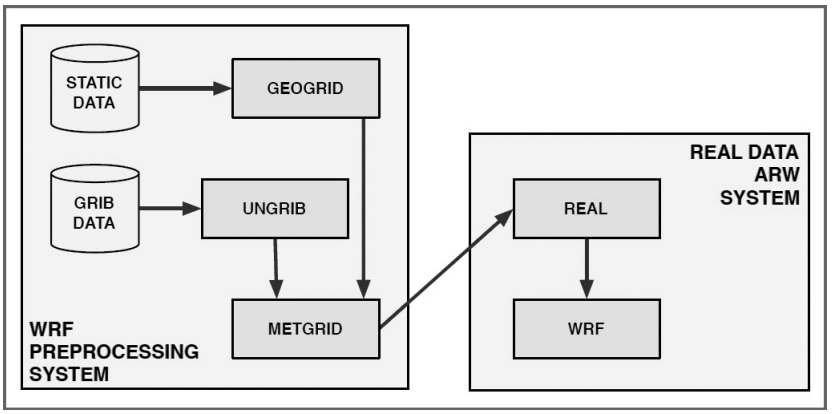

Figure 2.3: WPS components in the WRF modelling system

2.2.2 *WRF physics*

LST in the WRF model is derived based on the allocation of the net radiation (or flux) to latent and sensible heat fluxes (Eq. 2.10). This is determined by the radiation and land surface schemes used in the physics options of the model.

$$Q^* = (Q_{S\uparrow} - Q_{S\downarrow}) + (Q_{L\uparrow} - Q_{L\downarrow}) = Q_G + Q_E + Q_H \tag{2.10}$$

where Q^* is the net radiation (same as Eq. 1.1), $Q_{S\uparrow}$ is the upward shortwave radiation, $Q_{S\downarrow}$ is the downward shortwave radiation, $Q_{L\uparrow}$ is the upward terrestrial longwave radiation, and $Q_{L\downarrow}$ is the downward longwave radiation (Rigo and Parlow, 2005, 2007).

In this research, the Rapid Radiative Transfer Model (RRTM) scheme will be used for computation of the longwave radiation within the model (*"ra_lw_physics"* option). The RRTM is an accurate scheme using lookup tables for efficiency and accounts for multiple bands, trace gases, and microphysics species (NCAR, 2011). For the computation of the shortwave radiation (*"ra_sw_physics"* option), the Dudhia scheme is used, which is a simple downward integration allowing efficiently for clouds and clear-sky absorption and scattering (NCAR, 2011). The rest of the parameters used in the physics options of the WRF are listed in Table (2.3), where the explanations of the options are based on the ARW Userguide Version 3 (NCAR, 2011).

Table 2.3: WRF physics options used for T_s simulations

Parameter name	Param. longname	Opt. code	Option explanation
mp_physics	Microphysics	7	Goddard microphysics scheme. A scheme with ice, snow and graupel processes suitable for high-resolution simulations
ra_lw_physics	Longwave Radiation	1	RRTM scheme: Rapid Radiative Transfer Model. Accounts for multiple bands, trace gases, and microphysics species
ra_sw_physics	Shortwave Radiation	1	Dudhia scheme: Simple downward integration allowing efficiently for clouds and clear-sky absorption and scattering
sf_sfclay_physics	Surface Layer	1	MM5 similarity: Based on Monin-Obukhov with Carslon-Boland viscous sub-layer and standard similarity functions from look-up tables
bl_pbl_physics	Planetary Boundary layer	1	Yonsei University scheme: Non-local-K scheme with explicit entrainment layer and parabolic K profile in unstable mixed layer
cu_physics	Cumulus Parameterization	2	Betts-Miller-Janjic scheme. Operational Eta scheme. Column moist adjustment scheme relaxing towards a well-mixed profile

2.2.3 WRF Land surface schemes

2.2.3.1 NOAH land surface model

NOAH[5] land surface model (or Noah LSM) is a scientific and operational land surface scheme of both NCEP and NCAR and can be used to describe the land surface processes either in a stand-alone (e.g. NLDAS, GLDAS, LIS etc) or in the coupled land-atmospheric model system (e.g. WRF, GFS) (Sultana, 2011). For land surface scheme (*"sf_surface_physics"* option), which is the most important parameter in the T_s simulations, the Noah LSM scheme is used in this research. This scheme has four layers and includes soil temperature and moisture, fractional snow cover and frozen soil physics (Jin et al., 2010; NCAR, 2011). Studies have shown that this model performs well and, therefore, it is refined and implemented in the NCEP's regional and global coupled weather and climate models such as the WRF (Patil et al., 2011).

[5]NOAH stands for N: NCEP, O: Oregon State University, A: Air Force and H: Hydrologic Research Lab http://www.emc.ncep.noaa.gov/mmb/gcp/noahlsm/Noah_LSM_USERGUIDE_2.7.1.htm

2.2.4 Spatial analysis of the WRF simulations

Based on defined conditions for each simulation, there is the possibility to tune the model to split the output file into several files each of which holding a defined number of time-steps from simulations, rather than writing the entire simulation output to a single file. This can facilitate handling of large simulation ouputs. Every grid point in the model output is mapped to an xy coordinate. Based on these coordinates, the outputs of the model can be overlaid on the other spatial data, such as the MODIS LST dataset. Using spatial rules, such as nearest neighbour, the grid points from the model output can be related with the pixels of the MODIS LST grid.

2.3 Geostatistical methods

Most of spatial data, such as the LST dataset used in this research, are usually collected from a set of neighbouring elements in two-dimensional space (usually represented by pixels). Each of these elements are usually specified by a pair of indices as geographic coordinates, or simply the location of the elements in the matrix of the given dataset (Haining, 1990). Such a dataset is defined as spatial point process data, which means that the data consist of the actual locations of the points of the process within a designated study region (Gelfand et al., 2010)[6]. These data are also called *in-situ*, referring to the location of the individual points on the spatial domain (Gelfand et al., 2010). If the relationship between these elements is considered, spatial statistical methods are used. In this case data from the set of the neighbouring pixels are usually given in a two-dimensional matrix and displayed as an image. Each element of the matrix, which is also equivalent to a pixel in the image format, is considered one element often shown with two-dimensional indices ($X_{i,j}$), and the entire image as one variable (or image band). Spatial statistical methods attempt to find the variability inside this two-dimensional matrix (i.e., image band) based on each element (pixel) relative to the neighbouring elements (pixels). More variables will be available for the analysis if more than a single image band with a similar acquisition time is available (such as multispectral and hyperspectral satellite observations). Multispectral image classification and advanced statistical methods such as principal components analysis (PCA) can be applied when multiple image bands are available. However, when the time dimension is considered, each of these pixels from multiple images of the same

[6]Since pixels in imagery data are located in a uniform grid, they do not follow non-uniform pattern of spatial point process data, however, the actual parameter measured by the image (e.g., LC types), do follow the spatial point pattern [more information on this is available in spatial point patterns analysis (spatstat) project by Prof. Adrian Baddeley].

area over time become temporal variables with their own time-series. The value of any given element (or pixel) in any given time can be shown by a third index, $X_{i,j,z}$, where subscript $_z$ indicates the time dimension (Haining, 1990). A large number of time-series, each representing one pixel, will be available for analysis. The methods used for the analysis of time-series from spatial data, therefore, will depend on the objective of the analysis. If both spatial and temporal variations are important for the analysis, time-series of all pixel will be needed. On the other hand, if only temporal variations are the objective of the analysis (i.e., the spatial variations can be ignored), a spatially averaged time-series representing coincident observations from all pixels in the area of interest will be the possible solution.

The advantage of the first approach is to preserve spatial information in the dataset, which enables comparison of temporal profiles of neighbouring pixels. The issue with this approach, however, is the amount of data to be stored, which can also lead to complexities in the analysis. Possible autocorrelation existing in the neighbouring pixels also can lead to a redundancy in the stored dataset. To overcome this issue, image classification techniques are used to store limited number of digital values representing classes of spatial variability over the input image.

The second approach is useful if the overall variations of the variable in time is important. This approach will be even more realistic if another dataset from the same area (e.g., measurements over a single point and remotely sensed LST) must be used in the analysis. However, if the spatial variations of the variable in the area is also important for the analysis, this approach cannot be used.

A third approach is to group the pixels in the study area at first into a number of defined isotropic clusters using classification methods. Spatial averaging is then conducted only for each cluster so that more than one time-series is available from the study area. Pixels inside the study area are grouped according to variations of the spatial variable (e.g., LST) across the two-dimensional space. Temporal variability of the variable (e.g., LST) is then analysed inside each cluster and sometimes compared with that of the other clusters. LC classification is one example of this approach. This approach is used in this research to classify LC types and analyse temporal variations of LST inside each class, as well as comparison of LST variations over different LC classes over time.

2.4 Statistical methods

To draw quantitative conclusions from the analysis, statistical methods are applied in this research. These methods are identified as parametric and non-parametric methods

in statistical textbooks.

Parametric statistical methods follow certain assumptions called *parameters* (Corder and Foreman, 2009). These methods assume that our data (Corder and Foreman, 2009):

- is randomly drawn from a normally distributed population,
- consist of independent observations, except for paired values,
- consist of values on an interval or ratio measurement scale[7],
- are adequately large (n $>$ 25) and
- approximately resemble a normal distribution.

Non-parametric statistical methods are also known as exploratory data analysis (EDA) techniques. Since these methods are solely based on the inherent variations within and between the existing variables in the dataset, no prior assumptions are made on the dataset when doing the analysis. The drawback with these methods is that they tend to be conservative and wasteful of data, losing much in efficiency relative to parametric methods if distributional assumptions hold (Haining, 1990).

In parametric methods, *Parameter*s are measures computed from all the observations in a population, such as the mean (μ) and the standard deviation (σ), while *statistic*s are measures computed from a sample acquired from the population, in order to estimate parameters (Robson, 1994). These concepts are used interchangeably in the current research, mainly because the only available data are sample datasets. Parametric statistical models are based on a few assumptions on the data, such as randomness, normality, having an interval or ratio and adequate size of data (Manly, 2001; Corder and Foreman, 2009), which were listed above. Examining the data gathering method, scale type and size of sample is fairly straightforward, however, examining a data sample's normality and randomness involves more analysis (Corder and Foreman, 2009). Visual inspection of the data for normality in a graphical representation, such as a scatterplot or a stem-leaf-plot can reveal normality of the dataset (Corder and Foreman, 2009). For the univariate spatial point process data the uniform Poisson point process model is used in which Complete Spatial Randomness (CSR) is tested (Gelfand et al., 2010). A detailed description of methods to test data for normality and randomness is given by Corder and Foreman (2009).

To ensure randomness of the time-series as a prerequisite for parametric methods, *Control-charts* method (Guh, 2005) of test for randomness is used in this research. This method requires the series to be within the limits of $\pm 3\sigma$ above/below μ of each

[7] i.e., data are not classification of qualitative attributes (such as: good, average, weak, poor).

dataset, where μ is the mean and σ is the standard deviation of that dataset. If the series are within $\pm 3\sigma$ control limits around μ of the series, randomness rule holds on the time-series in question, and the parametric statistical techniques can be used. As an example, considering MODIS LST time-series for May 2011 ($\sigma = 4.33$, $\mu = 6.98$ in Table 3.3), the valid range to ensure randomness of this dataset will be -6.01 to 19.97; any value out of this range will be violating randomness of the series, in which case parametric methods cannot be used.

Other methods to ensure the randomness of the series include construction of $\bar{x}$-chart, which is also known as Shewhart control charts (Manly, 2001). Similar to the test for randomness method discussed above, $\bar{x}$-chart uses a control chart to ensure the data are in a range around the μ of the series. The rationale behind constructing the $\bar{x}$-chart is to find out whether the changes in the sample are too large to be due to normal random variation in the series (Manly, 2001).

Regression coefficient of determination, R^2, is a parametric measure which states the degree of agreement between the dependent and independent variables. R^2 is the square of the Pearson's r correlation coefficient ($R^2 = r^2$). For a limited sample population the value of r can be calculated using Eq. 2.11:

$$r = \frac{\sum_{i=1}^{n} \left(X_i - \bar{X}\right)\left(Y_i - \bar{Y}\right)}{\sqrt{\sum_{i=1}^{n} \left(X_i - \bar{X}\right)^2} \sqrt{\sum_{i=1}^{n} \left(Y_i - \bar{Y}\right)^2}} \tag{2.11}$$

where n is the number of observations, $\bar{X}$ and $\bar{Y}$ are the mean values of X and Y variables.

In regression analysis R^2 is an indicator of the magnitude of residual errors against the total variation in the explained variable. Therefore, it can be derived from the regression results calculated using a least squares linear model. In that sense R^2 is the ratio of regression sum of squares and the total sum of squares (Eq. 2.12).

$$\mathrm{R}^2 = SSR/SST = 1 - SSE/SST, \qquad SST = SSR + SSE \tag{2.12}$$

where $SSE = \sum_{i=1}^{n} (y_i - \hat{y}_i)^2$ is the sum of squares of residuals (or errors), $\hat{y}_i$ is the modelled value corresponding to i^{th} obsevation, $SSR = \sum_{i=1}^{n} (\hat{y}_i - \bar{y})^2$ is the sum of squares accounted for by the regression and $SST = \sum_{i=1}^{n} (y_i - \bar{y})^2$ is the total sum of squares, which is the measure of the total variation in the explained variable y (Manly, 2001). Squared error of each point explains how far that point is from the regression line and is calculated from the difference between the observed and the corresponding

predicted value given by the regression model ($y_i - \hat{y}_i$).

Analysis of variance (ANOVA) is a parametric statistical method which can help to provide more information about the agreement between the explained and explanatory variables. One of ANOVA measures given alongside regression results is F-statistics. Despite the fact that R^2 is a unitless coefficient, there is no standard to declare a correlation is significant solely based on this value. However, any F-value of greater than 4 in ANOVA is considered statistically significant, hence correlation must have been significant. Therefore, F-value is also presented in most of the regression results in this research. The residual standard error (σ) of the regression model (Eq. 2.13), which is an unbiased value equal to the root-mean-squared error (RMSE) adjusted for the degrees of freedom of residuals (DFE $= n - p - 1$), is another output from the regression model. If the value of RMSE is given, which is a biased estimate of the errors of the regression model, σ can be calculated by removing the bias via multiplying RMSE by n/DFE (in all cases $\sigma >$ RMSE).

$$\sigma = \sqrt{\frac{\sum_{i=1}^{n}(y_i - \hat{y}_i)^2}{n-p-1}} = \sqrt{\frac{SSE}{n-p-1}} \tag{2.13}$$

where p is the number of parameters which is equal to the number of response variables (Manly, 2001). $p = 1$ when only one response variable is used.

2.5 Data used in this research

2.5.1 Remotely sensed data

Two main satellite datasets are used in this research:

1. The MODIS LST product (Sections 3.4, 4.4.1, 5.4 and 6.4).
2. The passive MW SM product from AMSR-E (Section 6.4).

MODIS LST: MODIS acquires data in 36 spectral bands onboard Terra and Aqua satellites and the LST product is derived from TIR bands 31 (10.78–11.28 μm) and 32 (11.77–12.27 μm) with 1 km spatial resolution[8]. MODIS-Terra was launched to the orbit on December 18, 1999 with a descending equatorial overpass time in the morning (10:30 AM). Data acquisition from the sensor became available from early 2000. MODIS-Aqua was launched to the orbit on May 4, 2002 with an ascending equatorial overpass in the afternoon (1:30 PM). Data acquisition from this sensor became available since mid 2002 (`http://modis.gsfc.nasa.gov/about/design.`

[8]For full spectral bands of MODIS see Sohrabinia and Khorshiddoust (2007).

php). The MODIS LST product was chosen to be used in this research due to its higher temporal frequency (four observations per day, Table 2.4) and, at the same time, an adequate spatial resolution for the purposes of this research compared to other available LST datasets. Ease of access to this product via NASA's online tools, such as Reverb, is also another advantage of this dataset.

AMSR-E SM: AMSR-E is another sensor onboard Aqua satellite and, hence, was launched at the same time with MODIS-Aqua in 2002. The global SM product from this sensor is available since June 2002, however, the sensor stopped operating on October 4, 2011 due to a technical fault (http://wwwghcc.msfc.nasa.gov/AMSR/). The spatial resolution of this product is 25 km and the temporal frequency of the product is two daily (a daytime and a nighttime) observations (http://nsidc.org/data/docs/daac/ae_land3_l3_soil_moisture.gd.html). The advantage of AMSR-E is that this sensor is on the same platform as MODIS-Aqua, which facilitates combined analysis of the two datasets. The AMSR-E SM product also provides equally the same or higher spatial and/or temporal resolution (Table 2.4) among the available satellite MW SM datasets[9].

Table 2.4: Specifications of satellite data used in this research

Sensor	Data	Spatial resolution	Temporal resolution	Availability dates from	to
MODIS	LST product	1 km	4 obs./day	2000	–
AMSR-E	SM product	25 km	2 obs./day	2002	Oct 2011
MODIS	Albedo product	1 km	8-daily	2002	–

Additionally, the MODIS Albedo product (Section 5.4) and Landsat imagery (Section 3.3 and 4.4.3) are also used in this research.

2.5.2 Ground measurements

Ground measurements used in this research include:

1. The ground surface temperature (GST) at ∼2 cm depth, as equivalent to remotely sensed LST (Sections 3.4 and 5.4).
2. The near-surface SM measurements at 20 cm and 2–5 cm depth (Sections 5.4 and 6.4).
3. T_a measurements at standard meteorological station (Section 4.4.2).

[9] A list of other remotely sensed SM products can be found in http://www.falw.vu/~jeur/lprm/; see also http://www.ospo.noaa.gov/Products/land/spp/index.html and Merlin et al. (2008, 2013)

2.5.3 Model simulations

Using the WRF model coupled with the Noah LSM, the following variables were simulated to be used in different parts of this research:

1. Simulations of the surface skin temperature, or T_s, which is the equivalent parameter to the *in-situ* measured GST and remotely sensed LST (Section 3.4).
2. Simulations of SM for the top-soil (0–5 cm depth) layer (Sections 5.4 and 6.4).

Chapter 3

Validation of the MODIS LST over the study area

3.1 Preface

As the first step for this research, which was outlined in the objectives, this chapter presents the results from two field campaigns for validation of the MODIS LST product over the study area.

The *in-situ* measurements of LST over a flat valley in the Waimakariri River basin, which is located in the Southern Alps of New Zealand, were collected during a measurement campaign in May 2011. This site was chosen after consideration of logistical issues, access permissions and the size of the site with respect to the MODIS LST pixel size. A second objective of this measurement campaign was to assess the quality of the WRF model simulations on this test-site based on the *in-situ* measurements. Land-cover types of the test-site were first assessed based on Landsat 5 imagery and the Google Earth. In order to cover various land-cover types, a lattice of 3x3 plus 1 points was designed on the field with at least 250 m distance between the points. Meanwhile, to match up the pixel-size of MODIS with the WRF model simulations, the model grid resolution in the second domain was set to to 1 km. Results from this field experiment provided an insight on the quality of the MODIS LST product over mountainous parts of the study area. These results were published in a peer-reviewed journal paper (Sohrabinia et al., 2012) and are presented with no change in the 1st part of this chapter. Additionally, results from a second validation experiment, which was conducted in the flat parts of the study area in the Canterbury Plains, are presented in the 2nd part of this chapter.

Part 1: Validation of the MODIS LST in Cass test-site

NOTE:

Part 1 is published as a paper in the journal of ***Remote Sensing*** (Sohrabinia et al., 2012, DOI: 10.3390/rs4113501, 27 pages) under the title:

Analysis of MODIS LST Compared with WRF Model and *in situ* Data over the Waimakariri River Basin, Canterbury, New Zealand

M. Sohrabinia, W. Rack, P. Zawar-Reza

Abstract. In this study we examine the relationship between remotely sensed, *in situ* and modelled land surface temperature (LST) over a heterogeneous land-cover (LC) enclosed in alpine terrain. This relationship can help to understand to what extent the remotely sensed data can be used to improve model simulations of land surface parameters such as LST in mountainous areas. LST from the MODerate resolution Imaging Spectro-radiometer (MODIS), the modelled surface skin temperature by the Weather Research and Forecasting (WRF) mesoscale numerical model and the *in situ* measurements of surface temperature are used in the analysis. The test-site is located in a mountain valley in the Southern Alps of New Zealand. Geospatial analysis in GIS is used to relate pixels, grid-cells and points from the MODIS LST, model simulations and the *in situ* data, respectively. Differences between LST from MODIS, the WRF model and the *in situ* data are presented with respect to surface LC at different times of day. Initial results from regression analysis of the three datasets showed a goodness of fit R^2 coefficient of 0.77 for the model simulations and 0.35 for the MODIS LST. These values improved significantly when time-lags were considered and the few outliers were removed, giving R^2 values of 0.80 for the model and 0.73 for the MODIS LST. These results show that the WRF model correlates better with the *in situ* measurements over various LC types in this region compared with the MODIS LST. Longer time-series, however, are required to draw more robust conclusions about the applicability of the MODIS LST product for improving WRF simulations over alpine complex terrain.

Keywords. MODIS; land surface temperature; LST; WRF; mesoscale model; *in situ* data; iButtons; Waimakariri

3.2 Introduction

The importance of the land surface temperature (LST) in surface-based bio-geophysical processes and land-atmosphere interactions is well documented in the literature (Wan

and Dozier, 1996; Jin, 2004; Coll et al., 2005; Trigo et al., 2008; Tang et al., 2008; Neteler, 2010; Ghent et al., 2010; Trigo et al., 2011). In complex terrain, meteorological stations and ground surveys are usually sparsely and/or irregularly distributed (Neteler, 2010), hence, remotely sensed LST can be a critical source of data for the study of land surface processes. Skin temperature (in particular, its diurnal cycle) is needed in calculating sensible and latent heat fluxes; specifically, sensible heat flux is determined by the instantaneous difference between the near-surface air temperature (T_a) and LST (Jin, 2004). LST also determines the amount of thermal heat that is vertically transported into the ground. LST is routinely retrieved from remote sensing satellite sensors such as the MODerate resolution Imaging Spectro-radiometer (MODIS), providing reasonably good resolutions in space (1 km) and time (approximately 4 observations per day) at a regional scale.

As an attribute of the land surface, LST is influenced by the local land-cover (LC). Therefore, the quality of LST retrievals from satellite observations over various LC types needs to be assured in order to use this data source in the above applications.

Comparative analysis of LST from remote sensing data and modelling approaches in the existing research can be categorized into four groups. The first group attempt to improve LST retrievals via modelling complex LC and terrain features. These studies have examined LC for the purpose of a better approximation of surface emissivity, which rely on vegetation fraction of the surface cover (Dash et al., 2005; Trigo et al., 2011). The second group have attempted to use remotely sensed thermal and LC data to improve atmospheric models for simulation of land surface parameters (Huang et al., 2008; Sheng et al., 2009; Meng et al., 2009; Ghent et al., 2010). The third group have used remotely sensed LST to study the near-surface T_a (Mostovoy et al., 2006; Colombi et al., 2007; Zhang et al., 2011a) or surface soil moisture (Wang et al., 2004; Hain et al., 2011). Some of these studies have related LC indirectly to T_a looking at LST as the intermediate link (Cheng et al., 2008). Finally, the last group of the published research have used modelling and *in situ* measurements for validation of the MODIS LST (Wan et al., 2004; Coll et al., 2005; Wan, 2008; Wan and Li, 2008; Kabsch et al., 2008; Trigo et al., 2008; Coll et al., 2010; Niclòs et al., 2011).

The focus of the first group is physical modelling of the parameters involved in measurement of LST, including the sensor, the atmosphere in between and the properties (such as emissivity) of the target area. The second group attempt to improve accuracy of numerical models through assimilation of satellite observational data into the models. Both of these groups focus on producing or using satellite derived data often without comparison with a similar database. The third and the last group, on the other hand, are usually concerned with validation of satellite observations based

on ground-truth data. Other works in the literature, which are concerned with both LC and LST, have exploited the inverse relationship between LST and surface vegetation density (e.g., Karnieli et al., 2010), some of which have tried to account for the sub-pixel variations in LST based on higher resolution LC data (e.g., Mostovoy et al., 2008).

Despite numerous research conducted on the validation of remotely sensed LST from various sensors, such as MODIS (e.g., Wan et al., 2002b, 2004; Wan and Li, 2008), Landsat (e.g., Coll et al., 2010) or a combination of sensors (Coll et al., 2005; Trigo et al., 2008) in different parts of the world, a study of LST variations over different LC types is missing in the literature. LST itself is used to derive other surface parameters, such as the near-surface soil moisture (SM). The near-surface SM is a function of soil temperature (Huang et al., 2008), therefore, remotely sensed LST is widely used to study it under different soil conditions (e.g., Wang et al., 2004; Hain et al., 2011). Each LC type has its own unique thermal properties with daily cycles of heating and cooling, hence, the near-surface SM derivations can also be affected by LC types of the surface. As a consequence, characterization of LST variations over different LC types is equally critical in SM derivations. Apart from the *in situ* data, weather models also can be used to analyse the effects of LC types on LST, as well as the near-surface SM. Being able to provide high-resolution data temporally and spatially, computational models of climate and weather provide an opportunity for understanding of LST over a heterogeneous land. Since LST is a key computed variable in the model schemes based on heat fluxes, it is readily available. The spatial distribution of energy and heat fluxes can only be taken into account with remote sensing methods or numerical models (Rigo and Parlow, 2007). However, research on quality of the computed values using remotely sensed data as a basis is limited and does not include a comprehensive analysis over various LC types.

The objective of this paper, therefore, is to examine the relationship between LST observations from MODIS with the modelled dataset and the *in situ* measurements over various LC types in the study area. Taking the *in situ* measurements as reference, the aim of the study is to find out if the MODIS LST product is applicable to improve surface skin temperature simulations from the Weather Research and Forecasting (WRF) model over a valley in alpine terrain. There are very few climate stations in mountain valleys such as the one that we have studied; consequently, satellite data and numerical modelling are the only feasible solutions currently available for long-term environmental and climate studies in these areas. Nevertheless, such a terrain poses complexities on both numerical models and the retrievals from satellite observations.

The paper is organized as follows. The study area and the used datasets (*in situ*,

MODIS, WRF) are described in Sections 3.3 and 3.4, respectively. This is followed by a description of pre and post-processing methods with a focus on the effects of MODIS viewing angles and surface emissivities in Section 3.5. Results are provided in Section 3.6, where in Section 3.6.1, time-series of all three datasets are used as input to a correlation analysis, without looking at the spatial heterogeneity of LC types. In Section 3.6.2 a LC type specific correlation analysis between the three datasets is provided, and in Section 3.6.3 correlations characterizing day and night time-series over different LC types is presented. The interpretation of the results is discussed in Section 3.7, before the summary and conclusion are drawn in Section 3.8.

3.3 Study Area

The study area is located in a valley of the Waimakariri River basin in the Southern Alps of New Zealand (171°45'29"E, 42°59'39"S). The area is relatively flat with an average elevation of 550 m above sea level (a.s.l.), however, high-rise mountains border the area just to the North and to the South (Figure 3.1). The river's braided channel is more than a km wide, whereas the active riverbed is dynamically shifting the braids across the channel, leaving behind barren river banks on the sides. The LC types of this region are predominantly grasslands, mixed grass and tussock, a mixture of Matagauri bush with other scrubs and native forest with Beech trees as the dominant species. The spatial extent of these LC types were interpreted from a Landsat TM 5 image (acquisition date 28 March 2011, 43 days before the field experiment) and were visually checked on the ground during the field experiment. Since the area is free of farming and agricultural activities, the natural landscape is intact with a relatively stable canopy. In mid-Autumn, the season when the field experiment was conducted, vegetation on the site maintained their leaves, and the seasonal variation of the LC types were negligible. As a result, this site provides diverse LC types and adequate spatial extent so that the LST variations over LC types can be differentiated. The rational for choosing this test-site was to collect measurements over a relatively flat land of the mountain valleys in this region, while at the same time to avoid rugged terrain and significant elevation variations to be able to compare the measurements with satellite observations.

The climate of the study area is alpine with large diurnal temperature differences at day and night and freezing temperatures in winter. Based on climate data from the University of Canterbury Cass (UC Cass) Automatic Weather Station (171°45'34"E, 43°02'05"S, 583 m a.s.l.), which is located 3 km to the South of the study area, long-term average T_a of the area is 9.4 °C (1998–2012). However, monthly minimums and

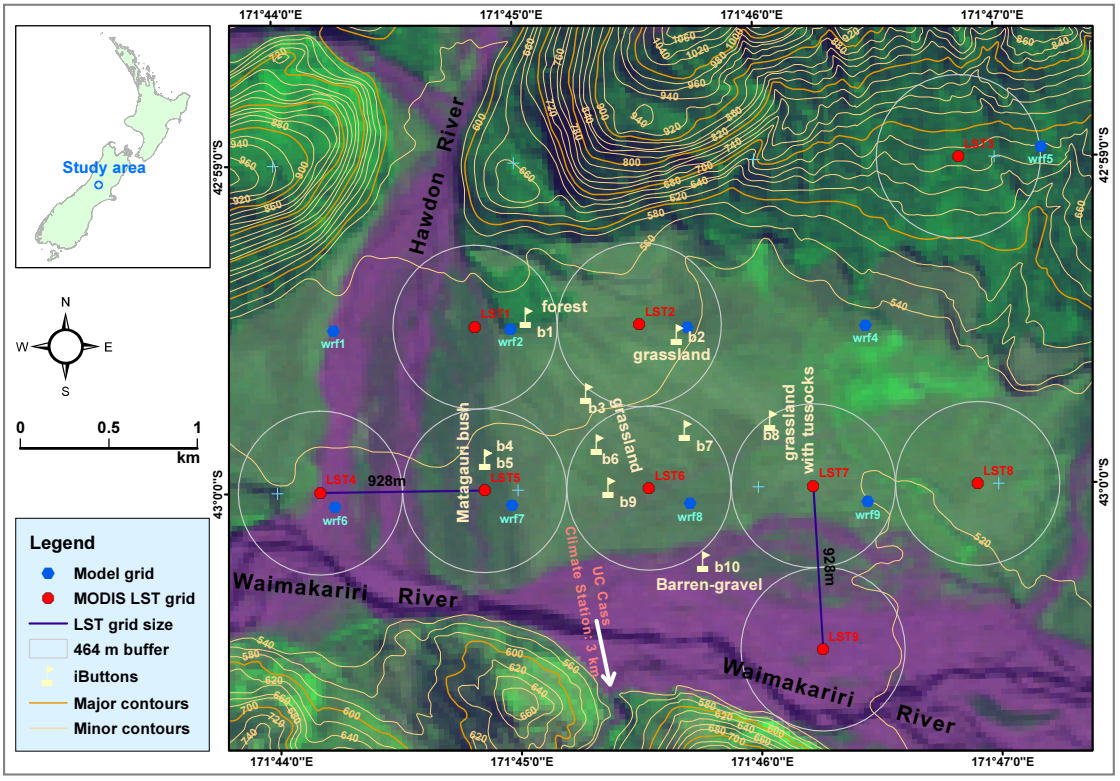

Figure 3.1: *In situ* iButtons (b1 to b10), MODIS grid points (LST1 to LST9) and the WRF model grid points (wrf1 to wrf9) overlaid on a Landsat image (TM5, 28 March 2011) of the test-site and plotted with 20 m topography contours lines.

maximums fluctuate between −10 and 30 °C during cold and warm months of the year, respectively.

3.4 Data

Data analysed in this paper fall into one of three categories: (*i*) *in situ* ground surface temperature (GST) measurements ($\mathrm{LST}_{\mathrm{inSitu}}$); (*ii*) LST retrievals from MODIS thermal infrared (TIR) observations ($\mathrm{LST}_{\mathrm{Modis}}$); and (*iii*) the WRF numerical model outputs ($\mathrm{LST}_{\mathrm{wrf}}$). The first two categories are observational data with different levels of accuracy and precision, while the third category is simulated data generated by the state-of-the-art WRF numerical meteorological model. These data are explained in more detail below.

(*i*) A field experiment for the *in situ* measurements of GST in the study area was conducted over a period of 14 days from May 10 to 23, 2011. Temperature data-loggers known as iButtons (Thermochron® DS1922L iButton, −40 °C to 85 °C sensitivity range, ±0.5 °C accuracy, 0.0625 °C resolution) were used in this experiment to measure GST over five different LC types of the area, allocating at least one iButton for each

LC type (shown as b1 to b10 in Figure 3.1 and described in Table 3.1). These low-cost temperature sensors have already become widely used in geoscience research (e.g., Holden et al., 2011; Fitzgerald et al., 2011; Brooks and Kyker-Snowman, 2008; Gubler et al., 2011). The iButtons were cross-calibrated at indoor conditions before use, and the accuracy of all 10 matched the manufacturer's specification. The sensors were placed over five LC types: grassland, grassland with tussock, forest, barren/gravel and Matagauri bush/scrub. Considering surface conditions and chances of exposure to direct sunlight, more than one sensor was employed over some of the LC types to ensure at least one measurement site with good quality data. The minimum distance between samples was 250 m. Sampling rate for the loggers was set to once every 30 minutes with New Zealand Standard Time (NZST) as reference. NZST is equivalent to UTC+12 hours (centred at 180° longitude), therefore, an offset of −33 minutes needed to be subtracted from NZST corresponding to the longitudinal position of the test site (171.75° E) in order to synchronise the ground measurements with the local solar time provided in the MODIS LST product for every pixel ($171.75° - 180° = -8.25°$ longitude ≈ -33 min in time). Five iButtons were installed over Grassland (b2, b3, b6, b7 and b9), two iButtons on Bush-Scrub (b4, b5) and one iButton over the other LC types, which include Forest (b1), Grassland with Tussock (b8) and Barren-Gravel (b10). All the iButtons but 1 and 5 were placed at a depth of 1–2 cm in the soil for shade and protection against direct sunlight. The Forest LC type is a relatively dense canopy of native Beech trees. For a better approximation of the temperature on top of the forest measured by satellites, iButton 1 was fixed on a tree inside the forest at about 4 m height. The bush-scrub LC type is a sparse canopy of Matagauri native bush with about 50% density. To account for the temperature on top of the bush, as well as on the open ground within the bush canopy, iButton 4 was buried in the soil while iButton 5 was fixed on top of a bush, shaded from direct sunlight. We used the data collected over grassland to examine the spatial heterogeneity of GST, and to determine whether one iButton was able to representatively measure the surface temperature over a single LC type. Difference among 5 iButtons at similar times was less than 2 °C for most of the measurement period. Few exceptions were observed during early morning and around noon (such as 22 May 2011 11:00 AM) when the differences exceeded 4 °C (Figure 3.2). This indicates that one iButton could be able to capture GST over Grassland with an accuracy of ±1 °C for most of the period. Nevertheless, due to larger canopy height and complexity over Forest and Bush-Scrub, we estimate the magnitude of the uncertainty over these LC types to be higher than ±1 °C. A single averaged time-series of GST from the 5 iButtons over Grassland was also compared with the measurements from other LC types (Figure 3.3). Apart from

the iButton on top of the bush (BushT), the range of GST over the LC types has been less than 5 °C for most of the measurement period. At warm hours the range has increased up to about 10 °C. Due to sheltering by the canopy, GST time-series from the iButton buried in the ground among the bush (BushG) showed less sensitivity for day and night extremes.

Given the shallow depth of installations, these iButton measurements are used as a proxy to compare with the MODIS LST. Although this should be presumably a good approximation, we conducted a time-lag analysis to account for the differences depending on the soil heat capacity and LC type. Besides the iButton point measurements, we also used the model simulations (explained further below) as an independent variable, which is also gridded data with a cell-size similar to the MODIS pixel spacing.

Table 3.1: Specifications of iButton measurement sites. All iButtons were buried at a depth of 1–2 cm in the soil except iButtons 1 & 5.

iButton	LC type	Description
b1	Forest	Dense native Beech trees with ≈10 m canopy height
b2	Grassland	Native grass-turf with ≈5 cm height
b3	Grassland	"
b4	Matagauri bush/scrub	Native bush with ≈50% density and ≈1.5 m height
b5	Matagauri bush/scrub	" (this iButton was fixed on top of the bush)
b6	Grassland	Native grass-turf with ≈5 cm height
b7	Grassland	"
b8	Grassland with tussocks	" mixed with native tussock with ≈20 cm height
b9	Grassland	Native grass-turf with ≈5 cm height
b10	Barren-gravel	Bare soil with gravel on the inactive river banks

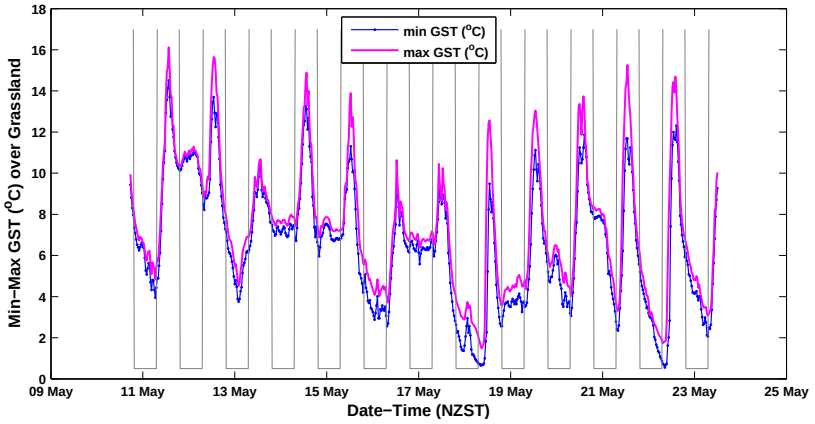

Figure 3.2: Minimum and maximum ground temperature measurements from 5 iButtons over Grassland LC type (30-min rate, May 2011). Night observations (7 pm–7 am) are distinguished by the grey-line overlaid on the plot.

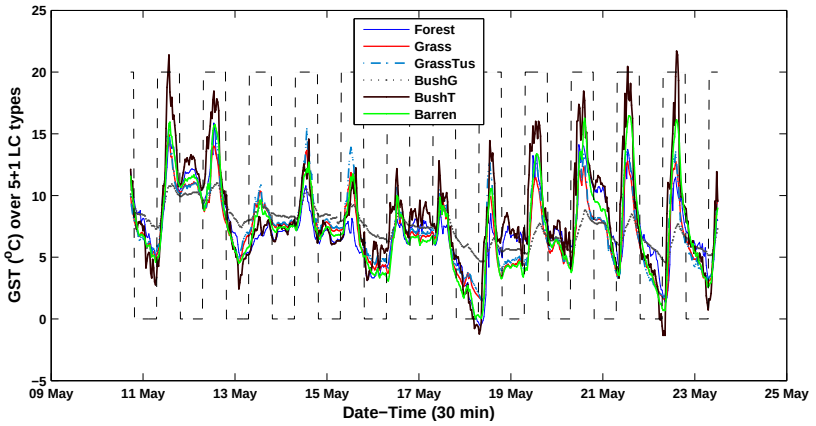

Figure 3.3: Comparison of GST time-series measured over 5 LC types plus the iButton on top of the bush (30-min data, May 2011). The broken grey-line is overlaid on the plot to distinguish day and night measurements; it is assigned 0 for night (7 pm–7 am) and 20 °C for day (7 am–7 pm).

(*ii*) MODIS LST product level 3, collection 5 (V5) archived in hierarchical data format (HDF) with approximately 1 km spatial resolution is used in this paper. This product is retrieved from the MODIS TIR observations in 10.78 to 12.27 μm range (bands 31 & 32) using the generalized split window (GSW) algorithm (Wan and Dozier, 1996; Wan, 1999; Wan et al., 2002a,b, 2004; Wan, 2008; Wan and Li, 2008). This dataset contain TIR observations for both day and night overpasses of MODIS-Terra at ≈10:30 (descending) and 22:30 (ascending) and MODIS-Aqua at ≈13:30 (ascending) and 1:30 (descending) local solar time. Therefore, four observations are available for each day from a combination of the two sensors and day and night overpasses of each sensor in ideal conditions (e.g., no cloud-cover). Because TIR signals cannot penetrate clouds, pixels contaminated with cloud have already been skipped in the LST processing using a cloud mask, so that LST is not mixed with cloud-top temperature (Wan et al., 2004; Wan, 2008), and are assigned a fill value in the LST product (Wan, 2009). The level 3 V5 product is derived in clear-sky conditions at ≥95% confidence defined in MODIS cloud-mask (MOD35) product over land with ≤2,000 m elevation a.s.l. (Wan, 2009). This leaves the possibility of TIR observations suspected to be cloud contaminated with <5% confidence to be skipped from cloud masking. Inside each HDF dataset, the first and fifth data-fields are TIR observations for day and night, respectively. Digital data storage precision of the product is 16-bit unsigned, with a scale factor of 0.02 to produce temperature values in Kelvin (K) after scaling (Wan, 2009; Wolfe and Saleous, 2006). This allows for a quantization precision (or radiometric resolution) of 0.02 K for the LST product at data management and conversion stage. The original values of LST product were first scaled based on the product's documentation (Wan, 2009) using the corresponding attribute fields. Dealing with a large number of LST data from MODIS-Terra and MODIS-Aqua for day and night

over the study area, a code was written to perform radiometric scaling automatically. This code used the corresponding attribute of each field for day and night in each HDF file to produce time-series of LST for each LC type scaled to K. Spatial locations of pixels from this dataset are marked by LST1 to LST9 on the map of the study area (Figure 3.1).

(*iii*) WRF simulations for *land surface skin temperature* in Kelvin (abbreviated as TSK in the WRF model outputs) were produced for the corresponding period of the field measurements. We used version 3 of the WRF modelling system for this work. WRF is a state-of-the-art community atmospheric model, which is suitable for use in a broad range of applications across scales ranging from metres to thousands of kilometres (NCAR, 2011). A detailed description of the WRF modelling system can be found in NCAR (2011); Skamarock et al. (2008). The static geographic data, which include MODIS-based 20-category LC classification at 1-km resolution (available from NCAR) are used by the model to interpolate terrestrial static fields to the prescribed domains (see Skamarock et al., 2008). National Centers for Environmental Prediction (NCEP) Final Operational Global Analysis (known as FNL) data with 1.0x1.0 degree grid resolution and six hourly frequency (see `http://rda.ucar.edu/datasets/ds083.2`) were used as input for initialization and boundary conditions of the 3-dimensional atmospheric fields (see also Maussion et al., 2011). Terrestrial data (including the local LC) are integrated by the Geogrid component in the 2-dimensional static fields and global meteorological data are ingested by the Metgrid component into the 3-dimensional atmospheric fields of the model. Each of the static and atmospheric fields contain various terrestrial and atmospheric information about the target area for the simulation, including (but not limited to) skin temperature (K), layers of soil temperature (K), vegetation/land-use type, vegetation greenness fraction (VGF), relative humidity, soil moisture and annual mean temperature (see Skamarock et al., 2008; Jin et al., 2010, for a complete list and details of these layers). The spatial resolution of the default USGS 24-category land-use data available in the static layers is relatively coarse, therefore, we used NOAH Land Surface Model (LSM) scheme with higher resolution MODIS LC categories for the best compatibility with the spatial resolution of the MODIS LST. NOAH LSM uses four soil layers (of temperature, water+ice, water) (Skamarock et al., 2008), one vegetation type in each grid cell without dynamic vegetation and carbon budget (Jin et al., 2010), and predicts soil moisture and temperature in four layers. Ground heat budget in NOAH LSM is calculated using a diffusion equation for soil temperature and the surface skin temperature is determined using a single linearized surface energy balance equation (Chen and Dudhia, 2001a). The input physics parameters in this scheme include Rapid Radiative Transfer Model

(RRTM) for longwave (Skamarock et al., 2008) and Dudhia scheme (Dudhia, 1989) for shortwave atmospheric radiation (see also Jin et al., 2010). The first domain of the simulations covered the entire South Island of New Zealand centred on the study area. The nested domain covered the study area and the surrounding region. Considering the spatial resolution of the LST product and observation timing of MODIS, grid-size of the nested domain and the interval of the model output were set to 1 km and 30 minutes, respectively. This produced 48 values with 1 km spatial resolution for each day. Duration of the simulations covered one day before till the end of the field experiment. The first 24-hours (or 12-hours as used in the literature) is the spin-up time required by the model to reach a balanced state with the boundary conditions (Maussion et al., 2011). These settings facilitated comparisons of the model TSK with the MODIS LST. The outputs of the WRF model were in netCDF (Network Common Data Form) format. Since TSK is the simulated parameter equivalent to LST from MODIS, it will be referred to as $\mathrm{LST}_{\mathrm{wrf}}$. Spatial locations of the grid-points from this dataset are marked by wrf1 to wrf9 on the map of the study area (Figure 3.1).

3.5 Methods

3.5.1 LST Pre-Processing

We used raster image analysis in order to overlay the MODIS LST with the LC data from the study area. A certain number of pre-processing steps were required to convert the original LST product in HDF format to raster layers with a versatile projected coordinate system. First of all, raster subsets of the LST product were extracted based on the boundary extent of the study area. LST L3 product is gridded in the global Sinusoidal projection, and the grid containing data for the study area is located at column 30 (h30) east-west and line 13 (v13) north-south. However, in this projection New Zealand falls in the lower-right corner with distortion along east-west direction. Using ESRI ArcGIS projection conversion utilities, "New Zealand Transverse Mercator 2000" coordinate system (Spheroid GRS 1980, Datum: NZGD 2000) was applied on the LST raster subsets. With spatial overlay in GIS, coordinates of LST pixels for each LC type in the study area were determined. These coordinates were used in a code to read LST values from the entire HDF files covering the period of field experiment and constructing LST time-series for each LC type. Data for observation times affected with cloud-cover were automatically filtered out by the code using fill-value attribute of the LST product. Quality control field for each observation helped to determine the level of accuracy of that observation.

3.5.2 Spectral Unmixing

The linear mixing model is used for unmixing the LST pixels with mixed LC types in the study area (Equation 3.1). The linear mixing model assumes that the observed reflectance spectrum of a given pixel is generated by a linear combination of a small number of unique constituent deterministic spectral signatures (Averbuch and Zheludev, 2012). This model calculates the final LST values of each pixel based on the fractional abundance of each LC type (or endmember) in that pixel. This model was applied on the correlation analysis between Forest, Bush/Scrub and Barren-gravel, which are measured by b1, b4/5 and b10 *in situ* iButtons, respectively (Figure 3.1).

$$x = \sum_{i=1}^{M} a_i s_i + w \tag{3.1}$$

where M is the number of endmembers, a_i (i from 1 to M) is the fractional abundance vector, w is the additive observation noise, x is the value of the pixel after unmixing (Keshava and Mustard, 2002; Pu et al., 2008; Averbuch and Zheludev, 2012). x is calculated through summation of the weighted values of the endmembers ($s_{i=1}^{M}$) using fractional abundance values ($a_{i=1}^{M}$) and adding the noise term. This method was applied on the LST pixels with a mixing of 5% or more, using fractional abundance vectors of each pixel (Table 3.2). Values of pixels with a homogeneous LC and less than 5% mixing have been used as the endmember (s_i) to calculate the unmixed value of each target pixel. LST5 representing LC type Bush-scrub was an exception, for which there was no ideal homogeneous pixel, hence a weighted value based on LST5 (representing 50% Bush-scrub) and LST6 (representing 40% grassland) was used. For those endmembers that $a_i = 0$, s_i will be 0 too, however, sum of fractional abundance values in each a_i vector must be equal to 1. Since we had only five pixels representing five LC types, which were validated on the ground, $w = 0$ has been assumed in the unmixing process. Equation (3.1) is useful for a single-band or thematic image, but can be expanded to multi-band imagery (see Souza-Jr et al., 2003; Wang and Uchida, 2008)).

3.5.3 Spatial Overlay of MODIS LST, WRF Simulations and in situ Points

We defined the WRF model domain's central point in a way that model grid-cell centres were located as close as possible to the LST pixel centres. Subtle tuning of the model domain's central point moved coordinates of the model grid points close

Table 3.2: Fractional abundance vectors (a_i = LST1, LST4, *etc.*) and endmembers (s_i) used in spectral unmixing.

LC-Types	LST1	LST4	LST5	LST6	LST7	s_i
Barren-gravel	0.35	0.70	0.10	0.15	0.10	LST9
Bush-scrub	0.25	0.05	0.50	0.00	0.05	LST5-6
Forest	0.25	0.00	0.00	0.00	0.00	LST3
Grassland	0.15	0.20	0.40	0.85	0.10	LST2
Grass-Tussock	0.00	0.05	0.00	0.00	0.75	LST8

to the corresponding coordinates of LST pixel in the study area. However, due to the difference in the pixel-size of the MODIS LST (928 m) with the grid cell-size of the model (1 km), a difference of about 100 to 300 m in the positions of the grid cells and LST pixels was inevitable (blue and red points in Figure 3.1). We used a nearest neighbour approach confined with a 462 m proximity rule (white circles in Figure 3.1) for the comparison. Any points (or WRF grid-centres) out of this proximity distance were not spatially related to the MODIS LST centroids (e.g., b3 in Figure 3.1). The distance used in the proximity rule is equal to one-half of the pixel-size of the MODIS LST and almost one-half of the model grid's cell-size for the nested domain. This technique was necessary in order to relate the pixels of $\mathrm{LST}_{\mathrm{Modis}}$, point layers derived from $\mathrm{LST}_{\mathrm{wrf}}$, and *in situ* measurement points. There was no LST pixel with similar LC type within the 464 m buffer of the iButton over "Barren-Gravel" LC type (b10), therefore, time-series of this iButton were related to a LST pixel (LST4) which is outside the defined buffer but has a similar LC type.

3.5.4 View Angle and Emissivity Analysis

Since LST is affected by viewing angle (θ) and the emissivity (ϵ) of surface LC types, we needed to analyse these parameters prior to LST correlation. Every scan of MODIS-Terra and Aqua covers a field of view extending $\pm 55^{\circ}$ from the perpendicular to the surface NADIR zenith line. The actual local view angle extends further to $\pm 65^{\circ}$ due to curvature of the Earth's surface (Wan, 1999). Viewing angle for all pixels of the study area at a single overpass were identical (it could vary if the study area was larger than one degree in the across-track direction of the MODIS ground field of view, or more than $2330/130 \approx 18$ km wide). Retrieved emissivities for each pixel in bands 31 and 32 (emis31 & emis32 fields in the LST product) showed that the emissivities of each LC type varies over time (Figure 3.4), where the amount of standard deviations (σ) from the mean is larger for some LC types (especially in band 31, Figure 3.4(a)).

The mean emissivities of "Forest" were higher than all other LC types from both bands 31 and 32 over the period of field measurements (Figure 3.4). Despite the expected lower values for bare soil, the emissivity fields showed no significant difference between "Barren-Gravel" and other LC types, such as "Bush/scrub" or "Grassland". However, "Barren-Gravel" and "Bush-Scrub" showed the least σ from the mean over the analysed period (this is shown by the upper and lower caps of the error-bars in Figure 3.4). This analysis also showed that the majority of the observations have been viewed from the East (shown with negative values), some exceeding 55° from NADIR (Figure 3.5). On the other hand, θ from the West is under 55° for all cases. We also found that larger variations in ϵ have occurred when θ exceeded $\pm$55° (Figure 3.6).

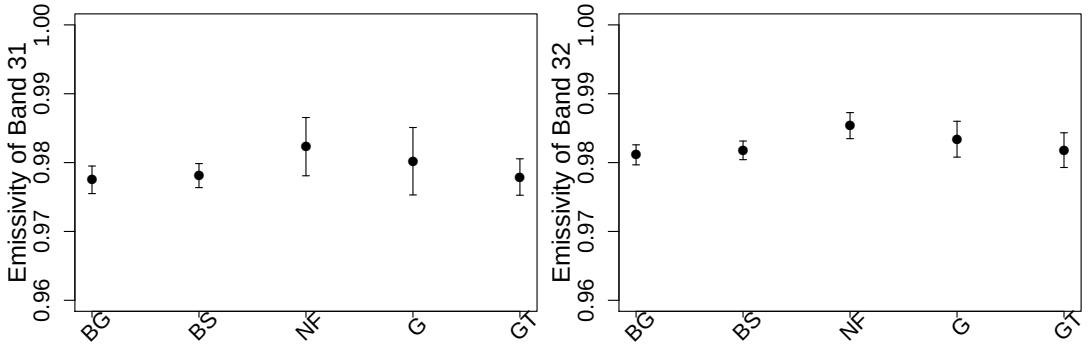

Figure 3.4: The mean (dots) and $\pm 1\sigma$ (bars with caps) from the mean emissivities over the period of 14 days (May 10–23, 2011) in bands 31 & 32 of MODIS over 5 LC types (BG: Barren-Gravel, BS: Bush-Scrub, NF: Native Forest, G: Grassland, GT: Grassland-Tussock).

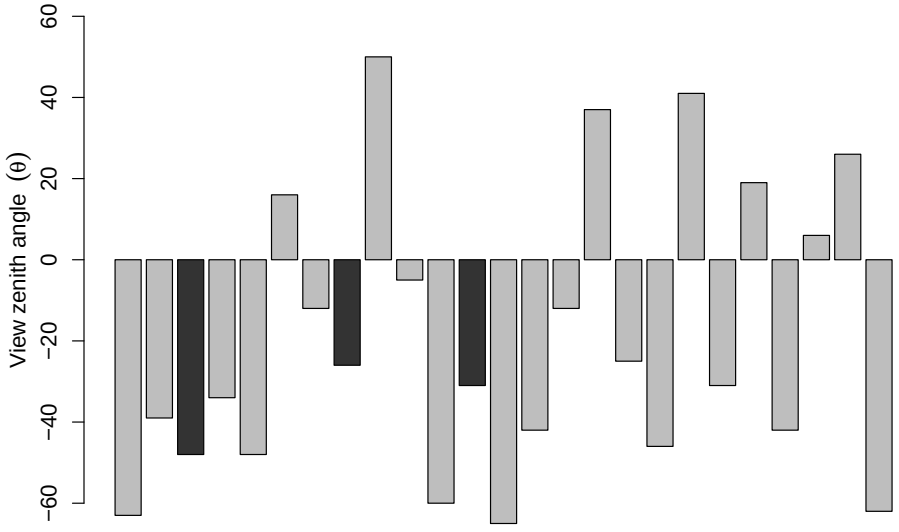

Figure 3.5: View zenith angles (θ) of the MODIS observations: negative values imply view from the east and positive angles are view from the west of Nadir (in total 25 observations in 14 days, dark-grey bars indicate outliers).

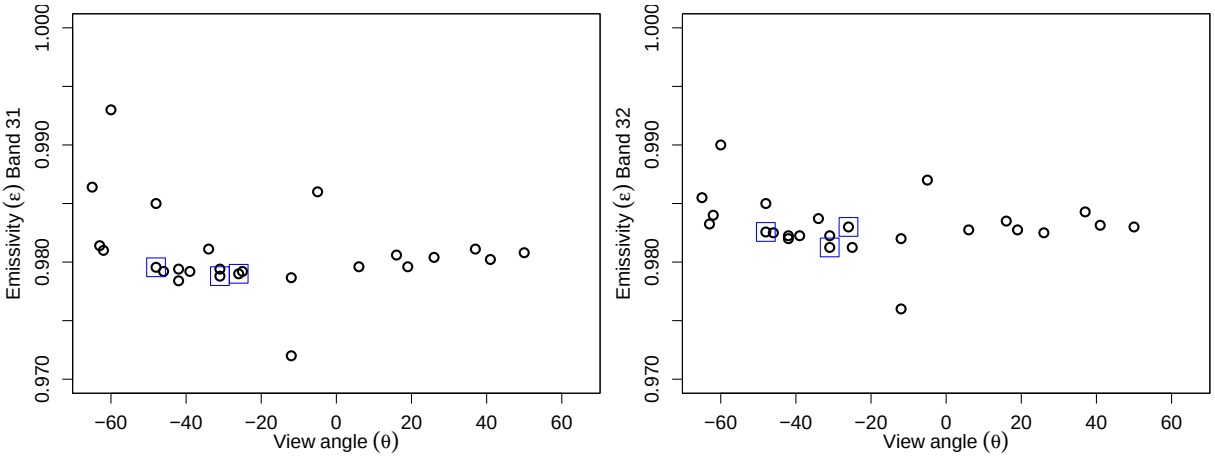

Figure 3.6: View zenith angles (θ) versus emissivities (ϵ) in bands 31 & 32 (outliers are marked by a square).

3.5.5 Geo-Statistical Analysis

Time-series of the input data sources (LST_{Modis}, LST_{wrf} and LST_{inSitu}) were constructed in order to apply correlation and regression analysis on the alternate pairs of the three datasets (listed below). Since the frequency of MODIS observations is limited to four times a day, which is further limited to cloudless days, subsets of the other two datasets were selected accordingly[1]. At least one series from each dataset for each LC type was constructed. Additionally, simultaneous records of all iButtons, MODIS pixels and the WRF grid points over all LC types were spatially averaged to generate three respective time-series (Equation (3.2)).

$$Ts(t) = \frac{\sum_{i=1}^{n} LST(i)}{n} \tag{3.2}$$

where Ts is the spatially averaged time-series of each LST dataset (iButtons, MODIS or WRF), t is time and n is the number of total samples (iButtons = 10, MODIS pixels = 9 and WRF grid points = 9).

Three alternate correlation calculations have been followed in the regression analysis at all times: LST_{Modis} correlated to LST_{inSitu} (denoted as MOD˜*in Situ*), LST_{wrf} to LST_{inSitu} (shown as WRF˜*in Situ*) and LST_{Modis} to LST_{wrf} (shown as MOD˜WRF). The regression coefficient of determination (R^2) was used to show the strength of correlation between each of the two datasets.

We also tested how the removal of possible outliers in the measurements improves

[1]Depending on the latitude, more than four MODIS observations is also possible, but the L3 V5 product contains LST values from only four observations (Wan, 2009).

the correlation results from the regression analysis. A scatter plot by itself is a non-parametric test for the existence of the outliers (Gnanadesikan and Kettenring, 1972; Ben-Gal, 2005). Regression residuals' vector also can be used directly to define a cut-off margin. Any observation outside this cut-off margin is considered as an outlier. The cut-off margin was defined as $\pm 1.5\sigma \approx \pm 5$, where $\sigma = 3.57$, and is the regression's residual standard error when MODIS LST is correlated against *in situ* data (Section 3.6.1). This method, however, cannot determine which of the bivariate dataset was the source of the outliers, unless one or both of those datasets are correlated with a third independent variable. If one of these bivariate datasets shows the same outliers when it is correlated with a third independent variable, outliers can be further investigated in that dataset.

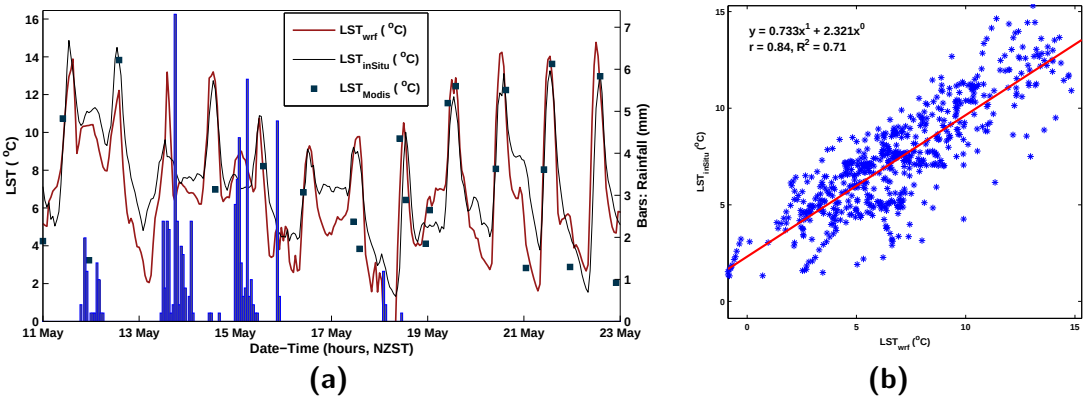

Figure 3.7: (**a**) Spatially averaged time-series produced from the WRF simulations and the *in situ* data (both dataset downscaled from 30-minute to hourly rate) overlaid on hourly rainfall (bars) from the UC Cass climate station; MODIS LST is also plotted as dots for those times when data were available; (**b**) The WRF simulations are correlated *vs.* *in situ* data (30-minute rate, May 2011).

3.6 Results

3.6.1 Time-Series of Spatially Averaged Datasets

In this section, the results from the correlation analysis between the spatially averaged time-series of the three datasets are presented. First, we compared spatially averaged high resolution time-series of the WRF simulations with the *in situ* measurements. Available MODIS LST observations were also overlaid on the *in situ* and WRF series (Figure 3.7(a)). This showed that the WRF and *in situ* datasets have captured diurnal temperature cycle very closely over the measurement period. On the other hand, MODIS LST series have shown larger bias from both WRF and *in situ* series. Hourly rainfall data from the UC Cass climate station was also analysed (Figure 3.7(a)). $\mathrm{LST_{wrf}}$ and $\mathrm{LST_{inSitu}}$ 30-minute data showed a relatively strong ($R^2 = 0.71$) correlation

(Figure 3.7(b)). Afterwards, time-series of the WRF and the *in situ* measurements were filtered according to the available MODIS LST observations. The filtered time-series of the *in situ* data showed highest mean ($\mu = 8.49$) and lowest standard deviation ($\sigma = 3.26$), while the MODIS LST time-series showed the lowest mean and the highest standard deviation (Table 3.3). Comparison of the averaged time-series from the three datasets (which were filtered based on the available MODIS LST observations) revealed the differences in the LST at different dates (Figure 3.8). While model simulations generally follow the *in situ* dataset, the MODIS LST showed some significantly different observations from the *in situ* measurements (such as points 3 and 8 in Figure 3.8). There were a total of 25 coincident measurements over the study period, with 10 measurements over night and 15 measurements during day. During nighttime, 80% of the MODIS observations are lower compared with the *in situ* measurements. During daytime, 73% of the MODIS temperatures are similar or higher and only in 23% of the cases lower than the *in situ* data. This indicates that the lower mean LST from the MODIS time-series (Table 3.3) is mainly due to night-time observations. Correlation with the *in situ* time-series with no time-lag yields $R^2 = 0.35$ for the MODIS LST and $R^2 = 0.77$ for the WRF simulations (Table 3.4(a)).

Table 3.3: Basic statistics from spatially averaged time-series of the three dataset.

Stat.	*in situ*	MODIS	WRF
μ	8.49	6.98	7.99
σ	3.26	4.33	3.63

Time-lags were considered to account for the delay in warming and cooling of the surface as measured by the iButtons 1–2 cm below the surface versus instantaneously observed by the satellite. Taking the MODIS acquisition time as reference, lags of $\pm$100 minute were applied on the *in situ* data iteratively with 1 minute intervals and the regression R^2 values were calculated for each lag. For the correlation of model simulations with the *in situ* data, lags were applied only to the *in situ* measurements. Statistics from 0, 30, 60 and 90 minutes time-lags are given in the results (Table 3.4).

Considering time-lags, correlations were generally deteriorated with lags of more than 90 minutes. The best agreement between the WRF model simulations with the *in situ* data were obtained at 30 minute time-lag while the MODIS LST did so at about 90 min time-lag (Table 3.4(a)). The model simulations also showed the highest agreement with the MODIS LST after adding a 30 min time-lag (Table 3.4(a)). It is noteworthy that the highest correlation between the MODIS LST and the *in situ* data is lower than the smallest value achieved from correlating the model simulations with

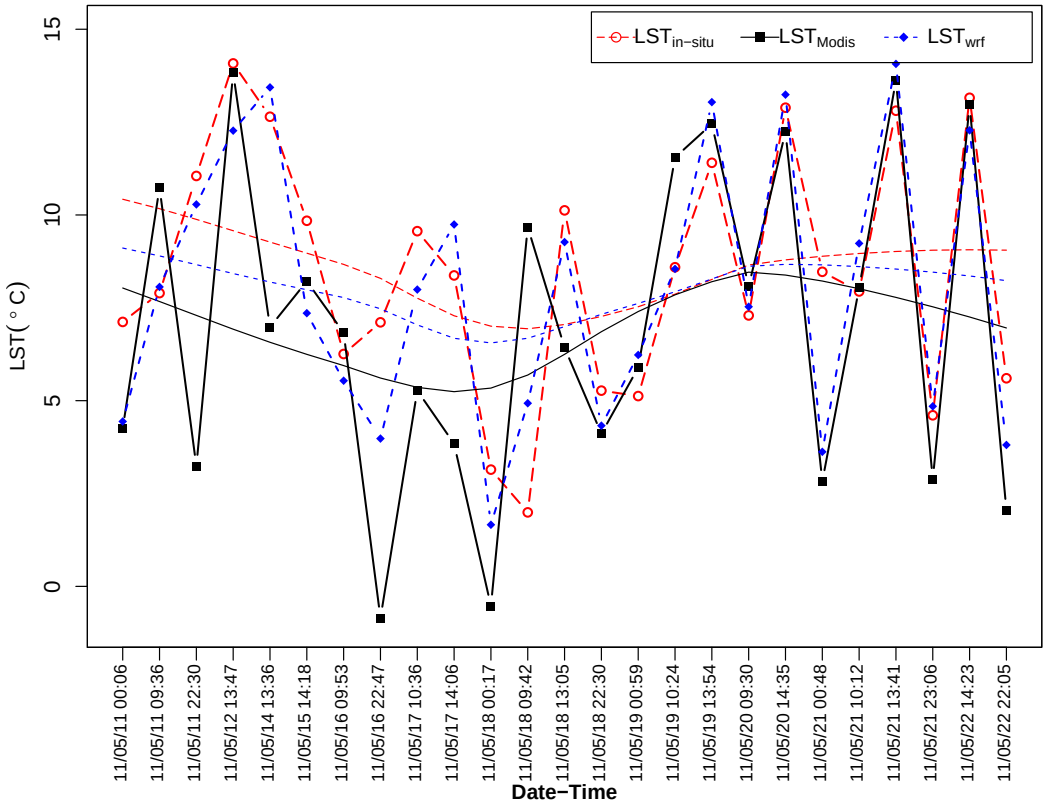

Figure 3.8: Time-series and trend-lines of LST_{inSitu}, LST_{Modis} and LST_{wrf}. Series are produced by spatially averaging points over various LC types in the study area (except for LST3, which is excluded due to its higher elevation, LST1 to 10 in Figure 3.1 are used to calculate the averaged LST_{Modis} series). Series only contain the values from times that were coincident with the MODIS LST observations.

the *in situ* data. Surprisingly, the MODIS LST at all times has correlated better with the model simulations than with the *in situ* data.

Several tests were made to improve the correlation values between the MODIS LST and the *in situ* data by detecting possible outliers based on the regression residuals and the scatter plots of the two datasets. Taking ± 5 ($\approx \pm 1.5\sigma$) as the upper and lower control limits for the regression residuals, three distinct outliers in the MODIS LST time-series appeared likely (Figure 3.9). Since the residuals from the regression between LST_{wrf} and LST_{inSitu} were well inside the cut-off margins, it turned out that the source of the outliers to be in the MODIS LST dataset. The same outliers are also visible in the scatter plots (Figure 3.10(a)). These points are lying farthest from the line-fit in the scatter plots of the two datasets (points bordered by a larger square in Figure 3.10). The first two outliers from MODIS nighttime observations were considerably colder than the measured and modelled data. The third outlier was a MODIS morning observation, which was warmer than the temperatures in the other two datasets.

According to the overpass times (Figure 3.9), all outliers originate from the MODIS-

Table 3.4: Regression statistics from spatially averaged data, with and without outliers. P-values from the correlations between MODIS LST and iButton series are also provided, where the smaller the p-level, the more significant the relationship. (**a**) Regression statistics from original data; (**b**) Regression statistics after removal of outliers.

(a)

	MOD~inSitu				WRF~inSitu		MOD~WRF	
Time-Lag	R^2	σ	**p-val.**	**F-Stat**	R^2	σ	R^2	σ
0min	0.35	3.57	0.0020	12.36	0.77	1.79	0.56	2.92
30min	0.40	3.44	0.0008	15.10	0.80	1.68	0.62	2.73
60min	0.47	3.23	0.0002	20.20	0.79	1.71	0.60	2.80
90min	0.51	3.10	0.0000	24.10	0.67	2.13	0.52	3.06

(b)

	MOD~inSitu				WRF~inSitu		MOD~WRF	
Time-Lag	R^2	σ	**p-val.**	**F-Stat**	R^2	σ	R^2	σ
0min	0.62	2.63	0.0000	32.84	0.77	1.79	0.69	2.38
30min	0.69	2.37	0.0000	45.13	0.80	1.68	0.72	2.26
60min	0.73	2.22	0.0000	54.55	0.79	1.71	0.67	2.47
90min	0.72	2.27	0.0000	51.43	0.67	2.13	0.56	2.83

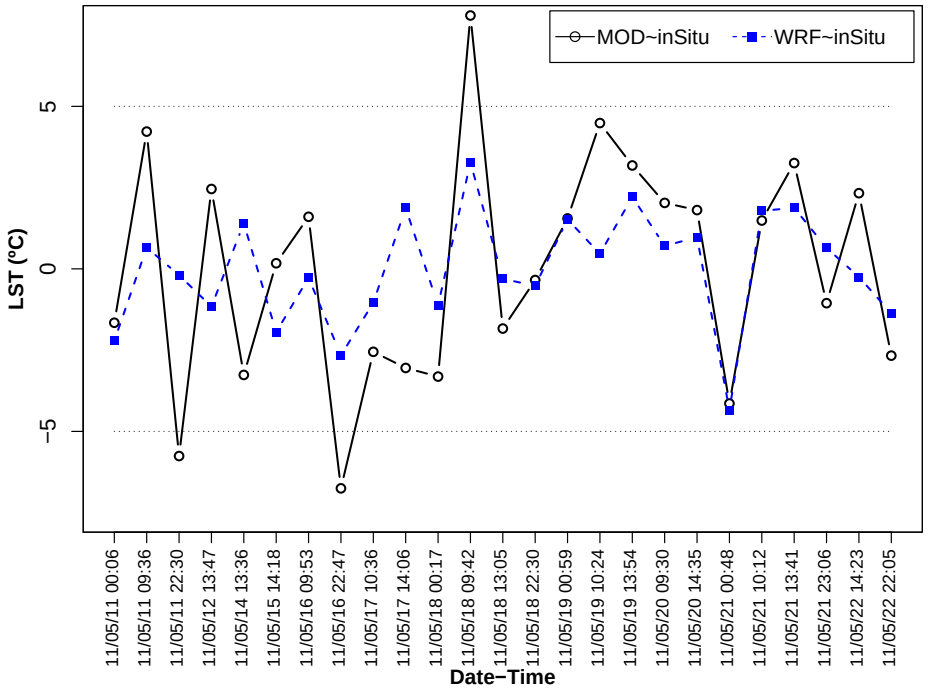

Figure 3.9: Regression residuals' plot revealing the outliers in the MODIS LST dataset (controls are roughly equal to $\pm 1.5\sigma$, where $\sigma = 3.57$ is the residual standard error of regression when the MODIS LST time-series is correlated with the *in situ* measurements).

Terra observations, and have appeared in the first half of the field experiment period. Because the view zenith angles of the outliers (48°, 26° and 31° from the East) are close or within the acceptable range of less than 45° (Jin, 2004), it seems unlikely that the differences are due to unfavourable imaging geometry. Emissivity values of the outliers in both bands 31 & 32 are also within the standard range (Figure 3.6).

We looked at relative humidity (RH) and other parameters from the model, but we did not find any meaningful pattern to explain the reason for the outliers. Since high amounts of atmospheric water vapour limits the accuracy of LST retrievals (Wan, 1999) and, therefore, can be a reason for the outliers, we checked MODIS Total Precipitable Water or Water Vapor (MOD05, level 2, V5.1) product. Both near-infrared (1 km pixel-size, day only) and infrared (5 km pixel-size, day and night) fields were checked, however, there was no data over the study area for those dates when the outliers have occurred. We also checked the outliers against T_a data from the UC Cass climate station. This station is close to our test-site (3 km to the South) and is approximately at a similar elevation (583 m a.s.l.). In all three cases where the MODIS LST shows an outlier, T_a data were closer to the WRF simulations and the iButton measurements. For example, at point 8 (2011/05/16 22:47 in Figure 3.8) the MODIS LST showed -1 °C, while T_a from the UC Cass weather station was 9.3 °C (average daily T_a was 7.9 °C). Also, soil temperature at 10 cm depth recorded in that station was 7.4 °C. These records are much closer to those from the WRF simulations and the *in situ* measurements than to the MODIS LST (Figure 3.8), which affirms the outliers in the latter dataset.

To prevent swamping and masking effects (see Ben-Gal, 2005), outliers were removed sequentially, followed by the calculation of the new R^2 coefficient. Removing the largest outlier (obs. 12 in Figure 3.9) improves R^2 from 0.35 to 0.51, removing the second largest outlier (point 8) improves R^2 to 0.53, and removing the third outlier (point 3) improves R^2 to 0.62 (Figure 3.10(e)). With all the outliers removed, regression statistics were re-calculated for all time-lags (Table 3.4b and Figure 3.10).

3.6.2 Land-Cover Based Time-series

Time-series of the MODIS LST and the model simulations over 5 LC classes were correlated individually versus the corresponding series of the *in situ* data with and without time-lags (Table 3.5). Time-lags with a range of ±100 minute, with 1 minute increments, were applied on the correlations between the MODIS LST and the *in situ* series over all the LC types (Figure 3.11). The five LC classes are Barren-Gravel (BG), Bush-Scrub (BS), Native-Forest (NF), Grassland (G) and Grass-Tussock (GT). For BG

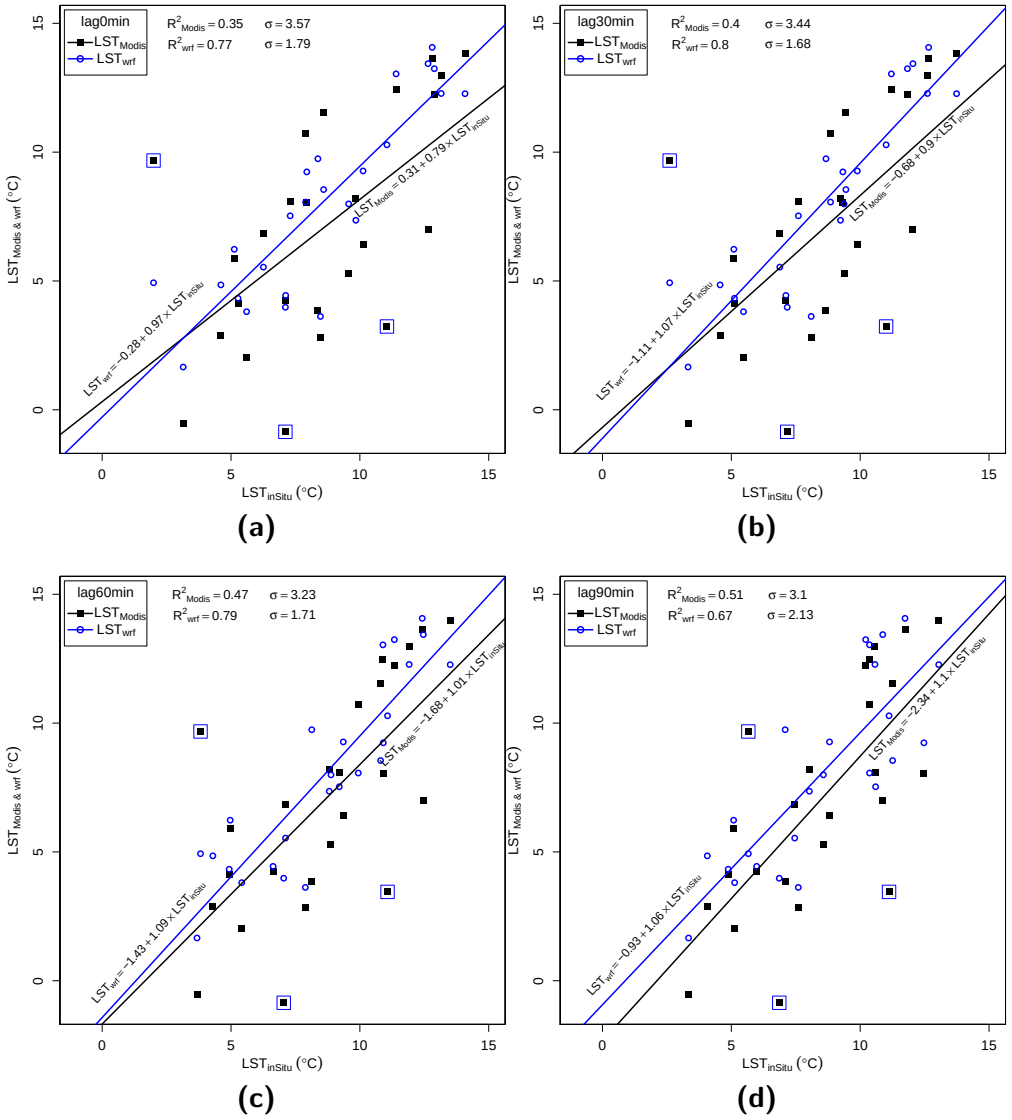

Figure 3.10: Scatterplots with line-fits of $\mathrm{LST_{inSitu}}$, $\mathrm{LST_{Modis}}$ and $\mathrm{LST_{wrf}}$ time-series, first row: all observations (outliers are bordered by a larger square), second row: outliers removed. (**a**) no time-lag; (**b**) 30 min time-lag; (**c**) 60 min time-lag; (**d**) 90 min time-lag; (**e**) no lag, outliers removed; (**f**) 30 min lag, outliers removed; (**g**) 60 min lag, outliers removed; (**h**) 90 min lag, outliers removed.

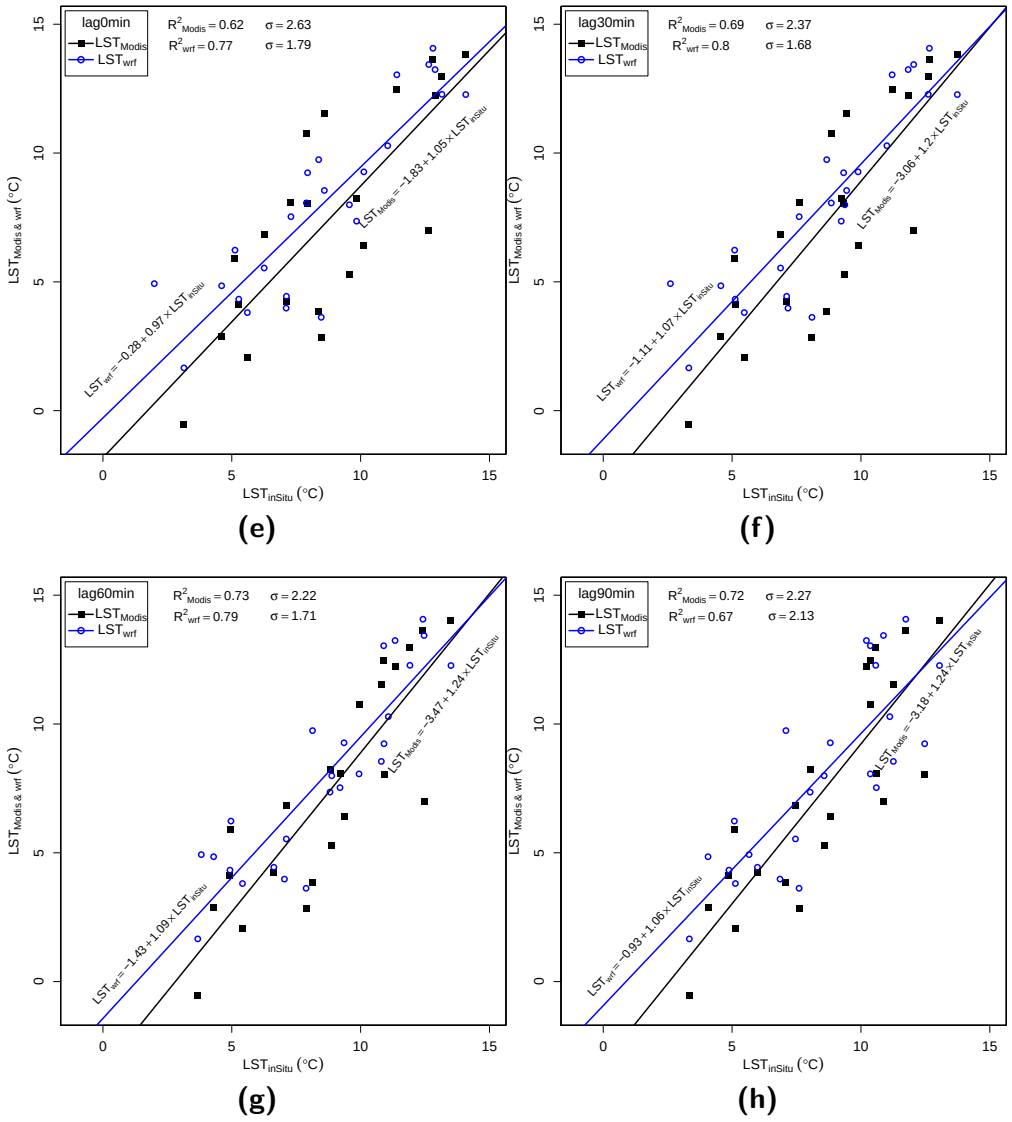

Figure 3.10: *Cont.*

LC type there was no MODIS LST pixel overlapping the *in situ* measurement points, therefore, a non-overlapping pixel with identical LC type has been used in the analysis. The MODIS LST pixel for the LC type NF suffered from high spectral mixing with only 25% fractional abundance (Table 3.2). Another pixel with almost 100% forest cover (LST3), but higher elevation, was used in the spectral mixing of this point (Figure 3.1).

Another point for consideration was the LC type BS. The height of the bush in the area is about 1 to 1.5 m from the base, with a moderate density of the scrub over the surface. Considering this point, the authors were concerned that the values of LST recorded by MODIS observation on this particular LC type are not exactly a representative of the skin temperature of the soil, but rather affected by the temperature near the top of the bush. Although the field experiment was conducted in mid-autumn, the bush

Table 3.5: Regression R^2 statistics over 5 LC types, including the maximum R^2 values achieved with various time-lags (minute). Time-lags were applied in a range of ±100 minutes, with one-minute increments. R^2 results from correlations between MODIS and *in situ* with three lags, plus the lag giving the maximum R^2, are listed in this table. For the other two correlations, only two time-lags are given.

	MOD~inSitu				WRF~inSitu		MOD~WRF	
LC-Type/R^2@lag	0	30	60	best lag	0	30	0	30
BarrenGravel(LST4)	0.42	0.51	0.62	0.68(68)	0.71	0.75	0.73	0.75
BarrenGravel(LST9)	0.38	0.43	0.50	0.56(69)	0.71	0.75	0.43	0.46
BushScrubT(LST5)	0.51	0.62	0.66	0.77(19)	0.67	0.74	0.65	0.67
BushScrubG(LST5)	0.04	0.07	0.09	0.18(74)	0.31	0.33	0.65	0.67
Forest(LST1)	0.21	0.23	0.31	0.47(80)	0.48	0.50	0.64	0.70
Grassland(LST6)	0.42	0.46	0.48	0.61(91)	0.77	0.78	0.69	0.73
GrassTussock(LST7)	0.37	0.39	0.43	0.52(57)	0.81	0.79	0.53	0.62

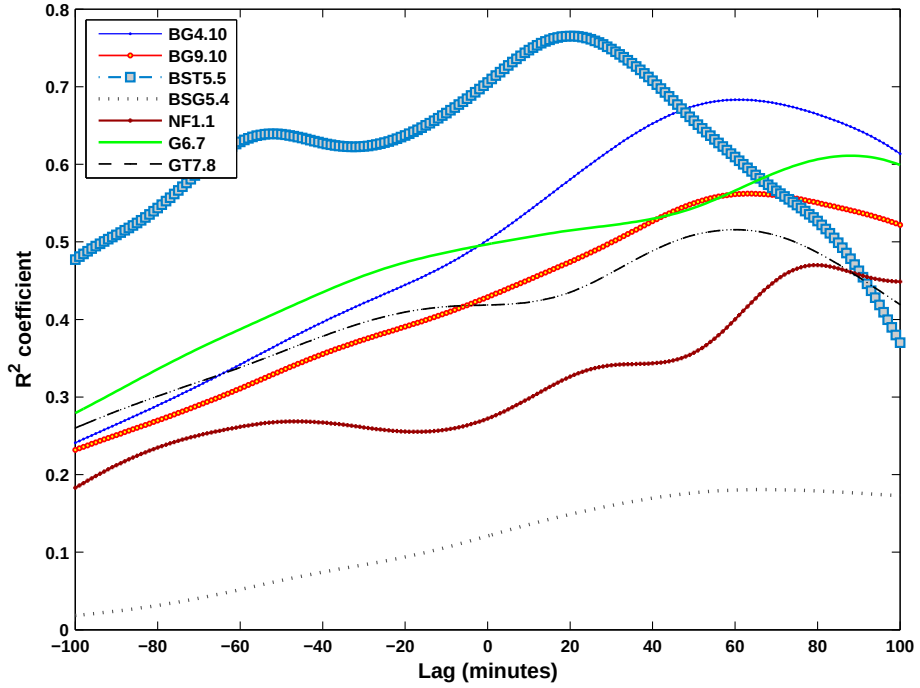

Figure 3.11: Variations of regression R^2 statistics from correlations between iButton GST measurements over 5 LC types and time-series of the corresponding MODIS LST pixels using ±100 minute time-lags (1 min increments). Full names of LC types in this figure are listed in Table 3.5, the first number is for LST pixel and the second number is for iButtons, e.g., BG4.10 stands for Barren-Gravel, LST4 correlated to b10.

maintained considerable foliage, which could have affected temperature measurements as well as solar radiation reaching the ground. Two iButtons were placed at this site, one on top of the bush (b5) and another one on the ground (b4). The corresponding data recorded at this site are referred to as "Bush-Scrub-Ground" (BSG) and "Bush-Scrub-Top" (BST). Correlation of these measurements with the corresponding MODIS LST pixel (LST5) showed higher agreement for BST compared with BSG (Table 3.5). The strongest correlation from BST was observed at 19 min time-lag ($R^2 = 0.77$), with another peak at 60 min, then it dropped significantly when time-lag increased to 90 min (Figure 3.11 and Table 3.5). Also, for other LC classes correlations increased with time-lags between MODIS observations and the *in situ* measurements. For LC type BG two pixels from LST_{Modis} were analysed: LST9 with homogeneous LC and LST4 with mixed LC. Both of them showed highest agreement with the *in situ* data with ≈60 min time-lag; however, except for BST which is affected by the ambient T_a, LST4 showed the strongest correlation ($R^2 = 0.68$) than all LC types at all time-lags (Table 3.5). The maximum improvements in the correlations between LST_{wrf} and LST_{inSitu}, as well as LST_{Modis} with LST_{wrf} were observed when ≈30 min time-lag was applied.

3.6.3 Comparison between Day and Night Measurements

In this section, the results from the regression analysis between the MODIS LST, the WRF model and the *in situ* data are presented by separating day and night observations. This analysis was necessary to discover the difference in time-lags at day/night and any possible anti-correlation due to differing surface temperature on each LC type at day or night.

Correlations between the MODIS LST and the *in situ* data are generally stronger from the night series compared with those from the day series except for LC types GT and BG. LC type BS ("Bush-scrub") showed more complex correlation pattern from day and night observations. During daytime, higher agreement is observed between the MODIS LST and the iButton measurements on top of the bush (BST in Figure 3.12 with $R^2 = 0.63$) compared with the iButton on the ground (BSG in Figure 3.12 with $R^2 = 0.18$), whereas during night a stronger correlation ($R^2 = 0.94$) is observed at the ground (BSG in Figure 3.12). Barren-gravel LC type showed higher correlations over the pixel with higher mixing (LST4) both day and night. Although the other pixel in this LC class (LST9) had less mixing, correlations over that pixel are considerably lower (possible reasons can be shadowing effects of the mountain and contribution of the river water).

On the contrary, the WRF model simulations showed generally higher correlations

with the *in situ* data during day compared to night. Time-lags did not improve correlations between the WRF and the *in situ* day-series (except for few cases with 30 min time-lag), however, some improvements were visible for time-lags of up to 60 min with night-series (Figure 3.12).

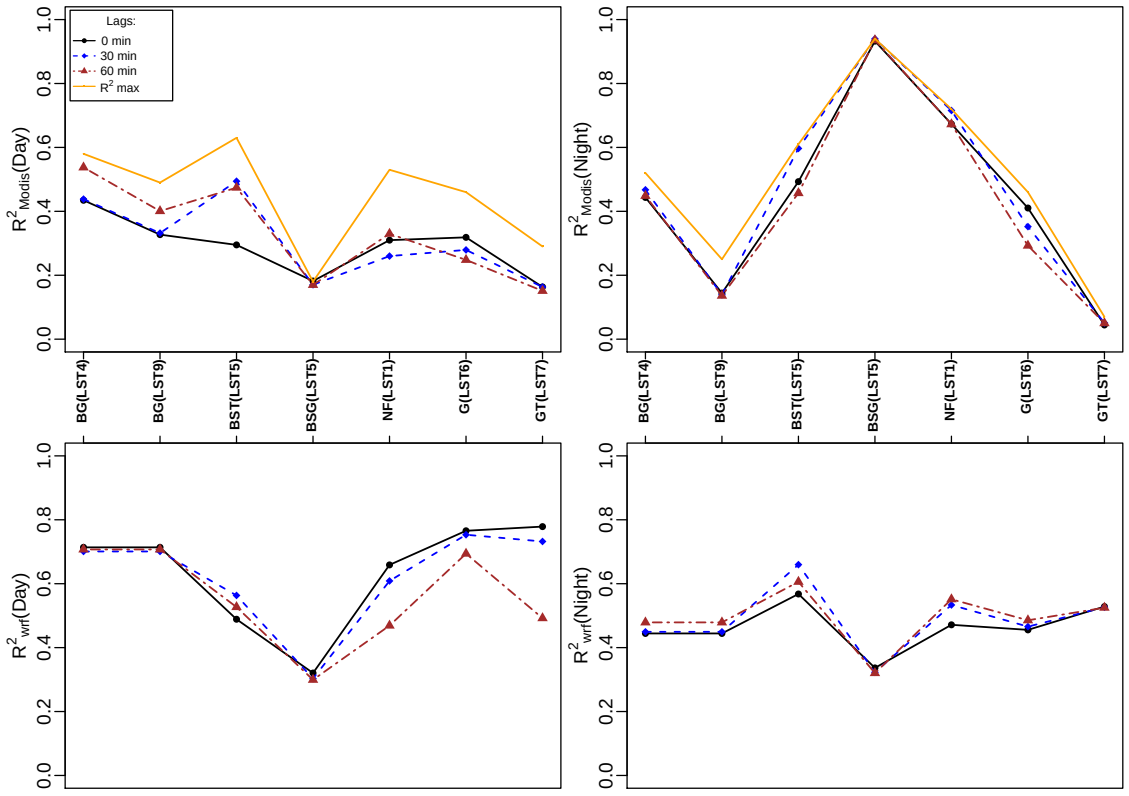

Figure 3.12: Correlations of day and night time-series of the three datasets over various LC types considering different time-lags (BG: Barren-Gravel, BST: Bush-Scrub-Top, BSG: Bush-Scrub-Ground, NF: Native-Forest, G: Grassland and GT: Grass-Tussock).

3.7 Discussion

Although the MODIS LST and the WRF model simulations are both gridded datasets, our results showed that the latter correlates better with the *in situ* measurements. We discuss first the characteristics of the *in situ* data, and then MODIS LST product over the study area as a possible explanation for this result.

3.7.1 Site-Specific Characteristics

The iButtons were buried very close to the surface well shielded from direct radiation. Even though they measure different physical properties, each dataset have already been adjusted to approximate the surface skin temperature. These adjustments include

surface emissivity and directional effects in the MODIS LST product (see Wan, 1999), surface energy balance characterization by the WRF model (Chen and Dudhia, 2001a) and the time-lag analysis on the iButton measurements. Therefore, we were expecting a close correspondence in temperatures between the MODIS LST and iButtons as well as with the model simulations. Warming or cooling at about 1–2 cm below the surface where the iButtons were buried lags behind the surface according to the soil specific heat conduction. The general pattern in the results is confirmed by the time-lag analysis, which showed overall a significant improvement in the correlations. Time-lags improved R^2 values over different LC types at least 14% (such as GT) and up to 26% (such as BG in Table 3.5). Due to higher complexity over NF and BS LC types, more *in situ* measurements at different heights of the forest and bush canopy is needed to characterize the temperature measured by the MODIS from top of the canopy. Such an effort also needs to consider density of the bush and/or the forest, differences in height and even different species of the canopy. As a result, we took a simplistic and practical approach in the field experiment and, therefore, we give higher significance for the results over G, GT and BG LC types.

Consideration of geographic characteristics of the test-site also helps to understand the difference between the MODIS LST and iButton measurements, which is discussed below as how it affects the LST retrieval process.

3.7.2 Issues in LST Retrieval

Uncertainties involved in the retrieval of LST can be related to (*i*) geographic characteristics of the test-site; (*ii*) the emissivity of land surface types and (*iii*) the atmospheric corrections (see Coll et al., 2005). Other sources of uncertainty include view-angle effect (Jin, 2004).

(*i*) The study area is constrained inside a mountainous region, which can be a source of a bias in the MODIS LST at two stages: the initial local effects on the observations upon the sensor's overpass and the second, the effects of local orography on the LST retrieval algorithm. The effects of the rugged terrain on the view angle and multiple scattering on the observations cannot be avoided, so as the effects of local orography and scattered or sub-pixel clouds on the visibility if it is not as strong as to be eliminated in cloud masking. The second outlier in the MODIS LST (point 8 in Figure 3.8), which showed unusually colder value than the other datasets, can be explained as cloud-top temperature skipped during cloud masking. Cloud-top temperatures in the LST dataset typically appear in the negative °C range (see Neteler, 2010). The issue of variability in view angle, as well as overpass time, had been demonstrated in LST-T_a analysis by

Mostovoy et al. (2006). Orography and view angle had been assessed in the cross-sensor analysis of LST in Trigo et al. (2008), where they have identified uncertainties in LST retrievals due to (1) satellite viewing angle (2) surface orography and (3) surface LC types. Synoptic weather effects on LST retrievals can be another source of uncertainties. Based on daily rainfall data from the UC Cass climate station, the first few days of the measurement period has been rainy (Figure 3.7(a)). The agreement between the MODIS LST and the other two datasets during the rainy episode (11–15 May) has been poor (Figure 3.8), while it improves during the subsequent days. The first outlier in the MODIS LST dataset coincides with a moderate rainfall event recorded by the UC Cass climate station, which starts at late afternoon on 11 May and continues till the next morning (Figure 3.7(a)). It is suspected that the rainfall events with higher atmospheric water content and patchy clouds during and shortly after rainy days have affected the accuracy of LST retrievals.

(*ii*) Emissivity and view angle effects: the issues with the accuracy of the model employed for retrieval of LST over regions where the emissivity is highly variable is indicated in the MODIS LST theoretical document (Wan, 1999). Our analysis on the emissivity (emis31 & emis32) and view angle fields, which are accompanied with the LST product, showed that variations in the emissivities of all LC types were less than 0.01 for view angles under $\pm 55^{\circ}$ (for view angles exceeding $\pm 55^{\circ}$ the emissivity variations were higher than 0.01). Although these emissivities are output from (not input to) the retrieval algorithm, it can be interpreted that the emissivity has been well defined prior to the retrieval procedure (see Wan, 1999) for a description of the input emissivities in the GSW algorithm).

(*iii*) Atmospheric effects: with respect to the LST product's algorithm description document, the ultimate quality of the atmospheric adjustments will depend on the quality of temperature and water vapour profile retrievals in the lower troposphere up to 9 km (Wan, 1999). In this respect, we showed that the agreement between the MODIS LST and the other two datasets was poor during and shortly after rainy days. Patchy clouds after intermittent rainfall events, if too small to be detected by the cloud mask, can cause problems in the modelled atmospheric profiles. Input atmospheric profiles used in the V5 LST product include the MODIS Atmospheric Profiles (MOD07) product (Wan, 2008). Information of the atmospheric lower boundary temperature, or T_a, provided in the MODIS atmospheric product is also used to improve LST retrieval accuracy (Wan et al., 2002b). Results from comparison of the MODIS LST with the two iButtons, one on the top of the bush and another on the ground, can be related to the effects of the lower boundary T_a on LST retrievals. It must be noted that the iButton on the bush had been strongly affected by the near-surface T_a. Bush canopy

provides protection against solar heat during day and excess emission during night, hence the iButton on the ground might have been negatively or positively biased at day and night, respectively (this can be interpreted from GST variations measured by BushG iButton in Figure 3.3). When the MODIS LST correlates better with the iButton on the ground protected by the bush, it shows lowest correlation with the exposed BG LC type. It is suspected that strong terrestrial emission occurs from the bare-soil skin at night in mid-Autumn (when field experiment was conducted), while T_a is relatively warmer than the surface skin. Since the MODIS LST correlates better with the warmer temperatures inside the bush at night, it is suspected that the LST product actually has a bias towards T_a at night. Similarly, higher day-time correlations of LST with the iButton on top of the bush, as well as bare-soil (which has faster heating rate), is an indication of the fact that the MODIS LST correlates better with T_a during day.

Consequently, there is the possibility that the algorithm used in the extraction of MODIS LST does not perform well in the mountainous regions, where the solar radiation regimes are different (see Proy et al., 1989), and the atmospheric profiles of temperature and water vapour can vary in short distances.

3.8 Conclusions

The MODIS LST product over a mountainous region in the Southern Alps of New Zealand was analysed in comparison with the *in situ* data and the modelled LST for the same region. Results showed a relatively significant ($R^2 = 0.35$, F-statistics $= 12.36$, p-value $= 0.0020$, 99% confidence) correlation between the MODIS LST and the *in situ* data, while at the same time a relatively strong correlation ($R^2 = 0.77$, 99.9% confidence) between the model simulations and the *in situ* measurements. It also became evident that the MODIS LST over some of the LC types has higher agreement with the *in situ* data, while for the other LC types the agreement is relatively poor. A few outliers in the spatially averaged time-series of the MODIS LST were detected using parametric and non-parametric statistical techniques. When these outliers were removed from the regression analysis, results were significantly improved. Despite these improvements as a result of adding time-lags and outliers removal, model correlations ($R^2 = 0.80$ with 99.9% confidence) were higher than the MODIS LST ($R^2 = 0.73$ with 99.9% confidence). It is, therefore, concluded that the MODIS LST, if assimilated in the WRF model without any prior assessment for the outliers and the local effects, will not provide any improvement for LST simulations over an alpine region. Longer time-series, however, are required to draw more robust conclusions about the applicability of

the MODIS LST product for improving WRF simulations over alpine complex terrain. We suggest outliers in time-series of the MODIS LST to be investigated based on *in situ* measurements (if available) and climate data, especially for areas where the terrain elevation is variable. Rainfall events, and the inherent patchy clouds during and shortly after rainy days, turned out to be the main cause of the outliers. Time-lag between the instantaneous satellite observations and the *in situ* measurements of contact temperature should be also taken into account when the latter is used as reference. In this way, we found that the temperature measured slightly below the surface by iButtons (especially over the grassland) compares well with the model simulations. This suggests that the *in situ* measurements made by these low-cost instruments may serve as a proxy for the remotely sensed and simulated LST after applying a time-lag accounting for the heat capacity of the soil.

Acknowledgments

This research is funded by the University of Canterbury (UC) in New Zealand. We acknowledge free access to the MODIS LST product provided by the US NASA. Warehouse Inventory Search Tool (WIST) and Reverb were used to download the LST product. LC satellite imagery data were obtained from US Geological Survey (USGS) publicly available web resources via Earth Explorer. The authors wish to acknowledge Rob Agnew from the New Zealand Institute for Plant & Food Research for his iButton data-loggers. We also express our thanks to Justin Harrison for his help and expert advice on the field work. We appreciate the valuable comments from four anonymous reviewers, which significantly improved this manuscript.

Part 2: Validation of the MODIS LST over the Canterbury Plains

3.9 Introduction to the second validation campaign

Results from the previous validation site showed that the MODIS LST has some errors over the alpine areas of the Waimakariri river basin, which were mainly due to the rugged topography of that area (Sohrabinia et al., 2012). For this reason, another test-site on the flat lands of the Canterbury Plains was planned to avoid topography effects. Five measurement sites over different land-cover (LC) types were located on this study area (Fig. 3.13). Measurements of the ground surface temperature (GST) and the near-surface soil moisture (SM) were collected on these sites over a period of seven months (24 Sep. 2011 to 06 May 2012) to be used for validation of the MODIS LST product.

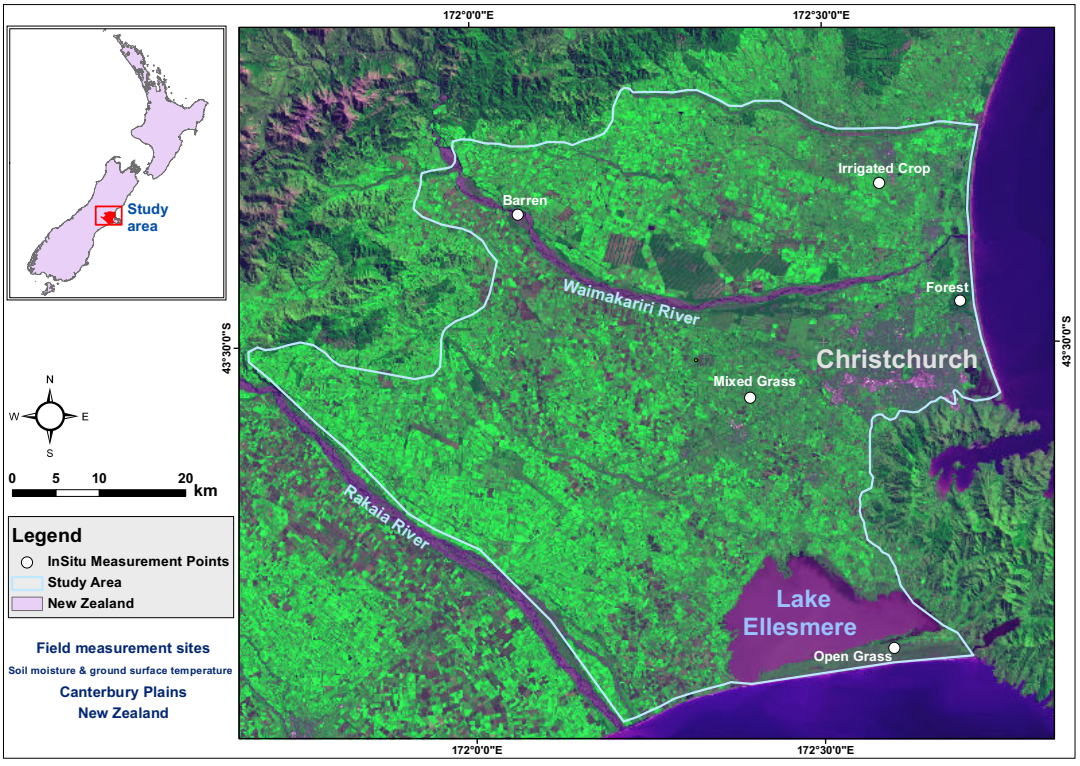

Figure 3.13: Test-sites for the measurements of ground surface temperature and the near-surface soil moisture in the Canterbury Plains, New Zealand.

3.10 Results from the 2nd measurement campaign

The *in-situ* measurements of GST revealed some differences based on LC type. Over some of the sites, such as 'Forest' and 'Irrigated Crop' LC types, the surface had been

cooler (Table 3.6). These differences, however, were not easily detectable from the MODIS LST observations. The MODIS LST series showed higher variance (σ^2) than the *in-situ* measurements over all LC types.

Table 3.6: Basic statistics from the ground surface temperature (GST) measurements and the MODIS LST observations over five land-cover types in the Canterbury Plains.

LC type	Mixed Grass		Barren		Open Grass		Forest		Irrigated Crop	
Stat.	GST	LST	GST	LST	GST	LST	GST	LST	GST	LST
μ	15.84	15.13	17.02	13.15	17.22	14.42	13.55	14.52	13.96	15.24
σ	3.69	8.79	7.28	7.41	6.12	6.68	3.48	6.18	2.53	8.98

Unlike the Cass site, the agreement between the the *in-situ* measurements and the MODIS LST over the Canterbury test-site was relatively high. The highest agreement was obtained over the 'Open Grass' LC type (Table 3.7). Lowest correlation was obtained over the 'Forest' site followed by the 'Irrigated Crop'.

As discussed before (Section 3.4.*ii*), observations from four daily MODIS overpasses were used to build LST time-series. Variations in the ground track of these overpasses caused minor mis-matches in the actual area of the pixel to be related with the *in situ* measurements (Secion 3.5.3). To reduce the uncertainty due to this mis-match at different overpasses, a spatially averaged value at each time from 3x3 pixels (when possible) was applied to build LST time-series. This was not possible on sites with a limited spatial extent (such as 'Open Grass' and 'Barren' sites, Fig. 3.13). Therefore, we conducted most of the analysis on 'Mixed Grass' site, which was located on a vast and homogeneous land. We plotted the *in-situ* measurements over this LC type against the MODIS LST time-series produced from four daily overpasses of the satellite (Fig. 3.14). A maximum of five possible outliers were removed from the MODIS time-series.

Table 3.7: Regression statistics from time-series of the MODIS LST and the ground surface temperature (GST) measurements over five land-cover types in the Canterbury Plains (σ = regression residual standard error & r = correlation coefficient). All correlations were significant at 99% confidence level.

Time-Lag	0 min.			30 min.			60 min.		
LC-type	r	σ	F-stat	r	σ	F-stat	r	σ	F-stat
Mixed Grass	.81	2.17	702	.84	2.06	895	.86	1.95	1054
Barren	.83	4.09	839	.88	3.81	1274	.90	3.55	1655
Open Grass	.85	3.25	1038	.87	3.05	1319	.90	2.89	1650
Forest	.75	2.32	420	.79	2.28	509	.80	2.20	602
Irrigated Crop	.76	1.64	417	.79	1.62	496	.81	1.57	579

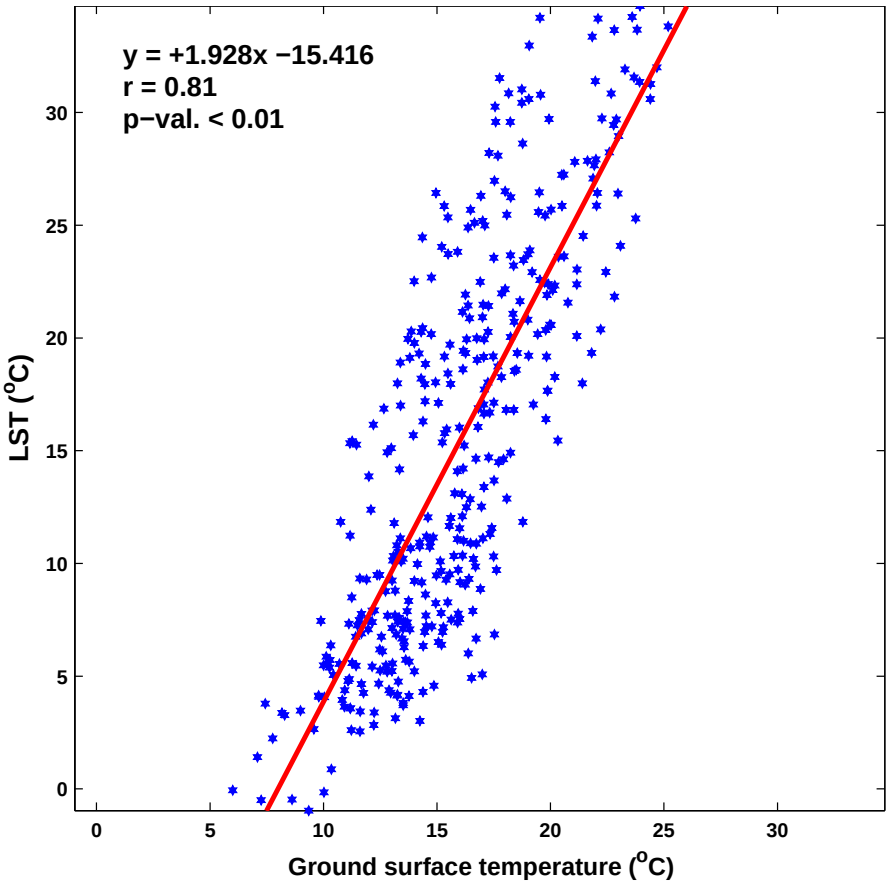

Figure 3.14: Scatterplot of the land surface temperature (LST) from MODIS combined time-series (four observations per day) plotted against the corresponding ground surface temperature (GST) measurements over 'Mixed Grass' land-cover type (24 Sep. 2011 to 06 May 2012).

3.11 Discussion of the results from the 2nd validation campaign

Results from the second validation site located in the Canterbury Plains with a flat terrain showed a good agreement between the *in-situ* GST and the remotely sensed LST. The *in-situ* GST measurements showed clear differences due to LC type, whereas, such differences were not so clear in the satellite observed LST series. Some of these anomalies can be attributed to the conditions of the measurement point. The MODIS LST series showed significantly higher variance than the ground measurements. This indicates that the radiative surface temperature observed by the satellite shows higher diurnal variability than the measurements of a contact instrument buried near to the surface in the ground.

Correlations between the MODIS LST time-series and the *in-situ* GST measurements showed significantly higher agreements than those results we had achieved in the Cass validation site. These results indicate that the issues due to the topography,

which were discussed in Section 3.7, are less effective over the Canterbury Plains with flat land. Since the area is a flat terrain with more homogeneity of the surface LC types (especially over the 'Mixed Grass'), LST retrievals agree better with the *in-situ* GST measurements.

Some of the sites in the Canterbury Plains validation campaign had issues with respect to the spatial size and availability of homogeneous LC over a large area. After initial data processing, it turned out that the measurements over some sites (such as the 'Forest', 'Irrigated Crop' and 'Barren') cannot be related easily to the satellite pixels due to the small spatial size or the localized conditions of the site. Therefore, spatial averaging to reduce mis-matches in the satellite track was not possible on those sites. For example, the 'Barren' site was hardly distinguished in the MODIS LST grid with 1 km spatial resolution. Any variations in the satellite track at different overpasses have possibly introduced uncertainties due to mixing of the adjacent LC types with different emissivity. The 'Open Grass' site is located in between the Pacific Ocean and Lake Ellesmere on a long spit ($\sim$2 km wide) and is highly likely to have been subject to spectral mixing from water. The measurements over 'Forest' site had been made under the forest canopy and relating them with the satellite pixels was a challenging task. Similarly, the 'Irrigated Crop' site, which was located at a cropland in an area with mixed farmlands and croplands, was not clearly distinguished in the satellite data. One of these sites over 'Mixed Grass', however, was located at the inner flat lands of the study area with a homogeneous LC type over a large area. Therefore, the measurements over 'Mixed Grass' site will be used for later analysis in this thesis.

Chapter 4

Air temperature and LST

4.1 Preface

It was shown in Chapter 3 that the MODIS LST product needs a careful pre-processing over an alpine area for detection of cloud-contaminated values and the outliers. Such pre-processing helped to improve the correlation between the MODIS LST and the *in-situ* measurements from $r^2 = 0.35$ to $r^2 = 0.73$. The MODIS LST was also validated over the flat terrains of the Canterbury Plains. Results from the second validation site showed that the MODIS LST product has a considerably higher quality in the flat parts of the study area (Section 3.10). With respect to these results, this chapter attempts to estimate T_a based on the MODIS LST product over relatively flat parts of the study area. The results are tested at four sites across New Zealand. The main question in this process, however, was whether the LST product can be used to estimate T_a on the immediate proximity of the weather station or over a larger area. To answer this question, this chapter investigates the spatial variability of LST-T_a relationship by applying a sliding window of varying size over the MODIS LST grid and distance between different pixels to the weather station where T_a measurements were collected. The whole material in this chapter is submitted for publication and is currently undergoing the peer-review process.

NOTE:

This chapter is under review as a paper in the journal of ***Theoretical and Applied Climatology*** under the title:

Spatio-temporal analysis of the relationship between LST from MODIS and air temperature in New Zealand

M. Sohrabinia, P. Zawar-Reza, W. Rack

Abstract. The ambient air temperature (T_a) is an important environmental parameter which can be estimated from satellite observations of the land surface temperature (LST) using a linear regression analysis. This paper attempts to answer the question of whether the series of a single pixel or a spatially averaged series over several pixels should be used for modelling T_a from remotely sensed LST data. Sensitivity of LST-T_a relationship to the Moderate Resolution Imaging Spectroradiometer (MODIS) window-size, which determines the number of pixels contributed in the correlations, over a number of test-sites in New Zealand was analysed. LST series of a single pixel over a period of 10 years gave a correlation coefficient $r \geqslant 0.80$ with T_a measurements. Bootstrapping by random resampling from seasonal subsets of both time-series was applied to determine seasonal and inter-annual variability of LST-T_a relationship. A fast Fourier filtering was applied for noise reduction and detection of dominant spectra in LST series. Spatially averaged time-series from larger windows, which included more pixels, showed slightly higher agreement with T_a measurements. We considered the effects of wind speed (WS) and wind direction (WD) on the LST-T_a relationship. Highest correlation between T_a and LST time-series was achieved using a 25x25 window at $2 \leqslant WS < 8$ ms^{-1}. No significant effect due to WD was found in the results. MODIS-Terra nighttime ($\sim$10:30 PM) observations showed the highest while MODIS-Aqua nighttime ($\sim$1:30 AM) observations showed the lowest agreement with T_a measurements. These results indicate that the best approach for modelling T_a based on LST observations from MODIS in the long-term is to use a spatially averaged LST series over a window of 5x5 to 25x25 pixels, with a consideration of WS effects and observation times.

Keywords. MODIS LST, air temperature, window-size, spatial averaging, LST-T_a relationship

4.2 Introduction

The ambient air temperature (T_a) in the atmospheric surface layer is an important descriptor of terrestrial environmental conditions and a key element of the regional

climate that influence biogeochemical processes on Earth (Prihodko and Goward, 1997; Mostovoy et al., 2006; Zhang et al., 2011a).

T_a is commonly obtained from the measurements in weather stations in a shelter at ∼2 m height above the surface (Vancutsem et al., 2010; Jin and Dickinson, 2010). Although these stations record data with a reasonably high temporal resolution (1 hour or higher frequency), the number and spatial distribution of these stations are usually insufficient over large areas (Benali et al., 2012). As a consequence, standard meteorological observations provide reasonably detailed temporal variations of T_a for the sampled site but may not describe the spatial heterogeneity over larger land areas (Prihodko and Goward, 1997; Sun et al., 2005). On the other hand, remotely sensed land surface temperature (LST) from polar orbiting satellites provides nearly global coverage with high (∼1 km) spatial resolution (Jin and Dickinson, 2010) but with a frequency controlled by the revisit period of the satellite. The US National Research Council and the Intergovernmental Panel on Climate Change (IPCC) expressed the need for long-term remotely sensed LST data in global warming studies to overcome the limits of conventional surface T_a measurements (Jin, 2004). There is an ongoing research for production of multi-decadal LST time-series from multiple geostationary and polar orbiting platforms for use in climate change studies (Vinnikov et al., 2012). As a global dataset, the Moderate Resolution Imaging Spectroradiometer (MODIS) LST product provides a unique database to study the temperature variations with a reasonably acceptable spatial resolution (1 km) over a large area. The MODIS LST daily product is available since early 2000 from MODIS-Terra and mid-2002 from MODIS-Aqua platforms with at least one daytime and one nighttime observation from each sensor in the mid-latitudes. This dataset has been widely used in the study of LST-T_a relationship in different regions. Sun et al. (2005) used this dataset to derive T_a in the mid-latitudes over flat lands of the North China Plain based on thermodynamics. Some authors have used the MODIS LST to derive daily maximum and minimum T_a (Mostovoy et al., 2006; Zhang et al., 2011a; Evrendilek et al., 2012; Lin et al., 2012), or as a source of climatological information (Vancutsem et al., 2010; Jin and Dickinson, 2010; Mildrexler et al., 2011) based on a statistical method over a wide range of latitudes with various environmental conditions regardless of the effects of terrain elevation variability, whereas others (Colombi et al., 2007; Hengl et al., 2012; Hachem et al., 2012) have also considered elevation variability.

It must be noted that LST differs from T_a in its physical meaning, magnitude and measurement techniques (Jin and Dickinson, 2010). LST from remote sensing satellites is a directional radiometric temperature obtained with certain assumptions about the surface emissivity and taking into account the atmospheric contribution (Norman and

Becker, 1995), whereas, T_a is the thermodynamic (or equivalently kinetic) temperature that is measured in a shelter at 1.5–2 m height with sufficient thermal contact with the air (Jin and Dickinson, 2010; Mildrexler et al., 2011). As LST provides additional information about land surface radiation properties (Jin and Dickinson, 2010), monitoring and understanding the trends of T_a and LST are crucial to study regional and global climate change (Yoo et al., 2011). Considering these benefits and due to the need for spatial information, many researchers have looked at remotely sensed LST as a supplementary source of data for T_a estimation (Cresswell et al., 1999; Florio et al., 2004; Mostovoy et al., 2006; Yoo et al., 2011; Benali et al., 2012) and have found a strong relationship between T_a and remotely sensed LST using statistical methods. Satellite viewing angle and overpass time have been considered for a better understanding of this relationship with varying sensor geometry and at different times of the day (*e.g.,* Cresswell et al., 1999; Jin and Dickinson, 2010). In order to extend such a relationship over a large area, however, it is necessary to identify the spatial extent over which LST agrees most with T_a measurements.

Based on our review of the literature, there has been limited research to study the effects of LST grid's window-size on the relationship between these two variables, especially within the New Zealand context, where remotely sensed data have not been fully exploited. As T_a is influenced by both the local radiation budget and air advection from the surrounding areas, a spatial window with varying size can help to determine the size of the area over which T_a measurements relate best with the MODIS LST observations. An understanding of the spatio-temporal variability in LST-T_a relationship is required for a better integration into the atmospheric models as well as a more efficient use of LST as a proxy for T_a in climate studies. The objective of this study, therefore, is to investigate the relationship between time-series of remotely sensed LST areally averaged[1] over multiple windows with T_a measurements at a number of test-sites across New Zealand. A fast Fourier transform (FFT) is applied to extract dominant cyclic signals and to demonstrate the difference in noise amounts in the series of a single pixel compared to the spatially averaged LST time-series from larger windows. It is generally believed that during daytime, LST is usually higher than T_a, and the opposite occurs at nighttime (Cresswell et al., 1999; Benali et al., 2012). We investigate these variations by exploiting four LST daily observations which enables comparison of LST and T_a diurnal profiles.

The results are organized as the following: the relationship between LST series from a single MODIS pixel and T_a time-series over the study area is assessed (Sec-

[1]A detailed discussion about the importance of areally integrated remotely sensed data over point measurements is outlined in Owe et al. (1988).

tion 4.6.1), the effects of LST window-size on the relationship between LST and T_a are presented (Section 4.6.2), effects of distance between LST pixels and the weather station (Section 4.6.3), and finally, effects of LST viewing times (Section 4.6.4) are discussed.

4.3 Study area

This study was conducted over four test-sites across New Zealand, which were selected following the criteria of *(i)* the availability of T_a measurements, *(ii)* sufficient land area and *(iii)* flat terrain. Low to moderate vegetation is the major land-cover (LC) of the country with a dominant farming and agricultural activities (Fig. 4.1). The climate of New Zealand in general is characterized as marine temperate with ∼600 mm or more mean annual rainfall.

Parts of the analysis, such as wind and distance effects are conducted only at two sites over the Canterbury Plains in the South Island. This area is confined by the mountains at the west and North-West and by the Pacific Ocean at the East. At the South-East corner, the area is partially constrained by the Porthills, which are the remnants of a volcanic crater with ∼1000 m elevation at the highest point. Based on wind speed (WS) and wind direction (WD) data recorded over 10 years, dominant winds at Christchurch station are North-Easterlies followed by Easterlies and South-Westerlies (Fig. 4.2a), whereas in Darfield, North-Westerlies have highest frequency and intensity followed by North-Easterlies and South-Westerlies (Fig. 4.2b).

4.4 Data

4.4.1 MODIS LST dataset

The MODIS LST product, which is derived from the sensor's observations onboard Terra and Aqua satellites, is a global operational dataset available from digital archives of the US National Aeronautics and Space Administration (NASA). This dataset covers a period of more than a decade, since 2000 from MODIS-Terra and 2002 from MODIS-Aqua to date (Oct. 2012). We have used the level 3 (L3), version 5 (V5) LST product with 1 km spatial resolution. This product is derived from thermal infrared (TIR) observations of MODIS in bands 31 (10.78–11.28 μm) and 32 (11.77–12.27 μm) using the generalized split window (GSW) algorithm (Wan, 1999; Wan et al., 2002a,b, 2004; Wan, 2008; Wan and Li, 2008). The TIR observations of both MODIS-Terra and MODIS-Aqua have been used to derive the LST product (Wan, 1999, 2009). The

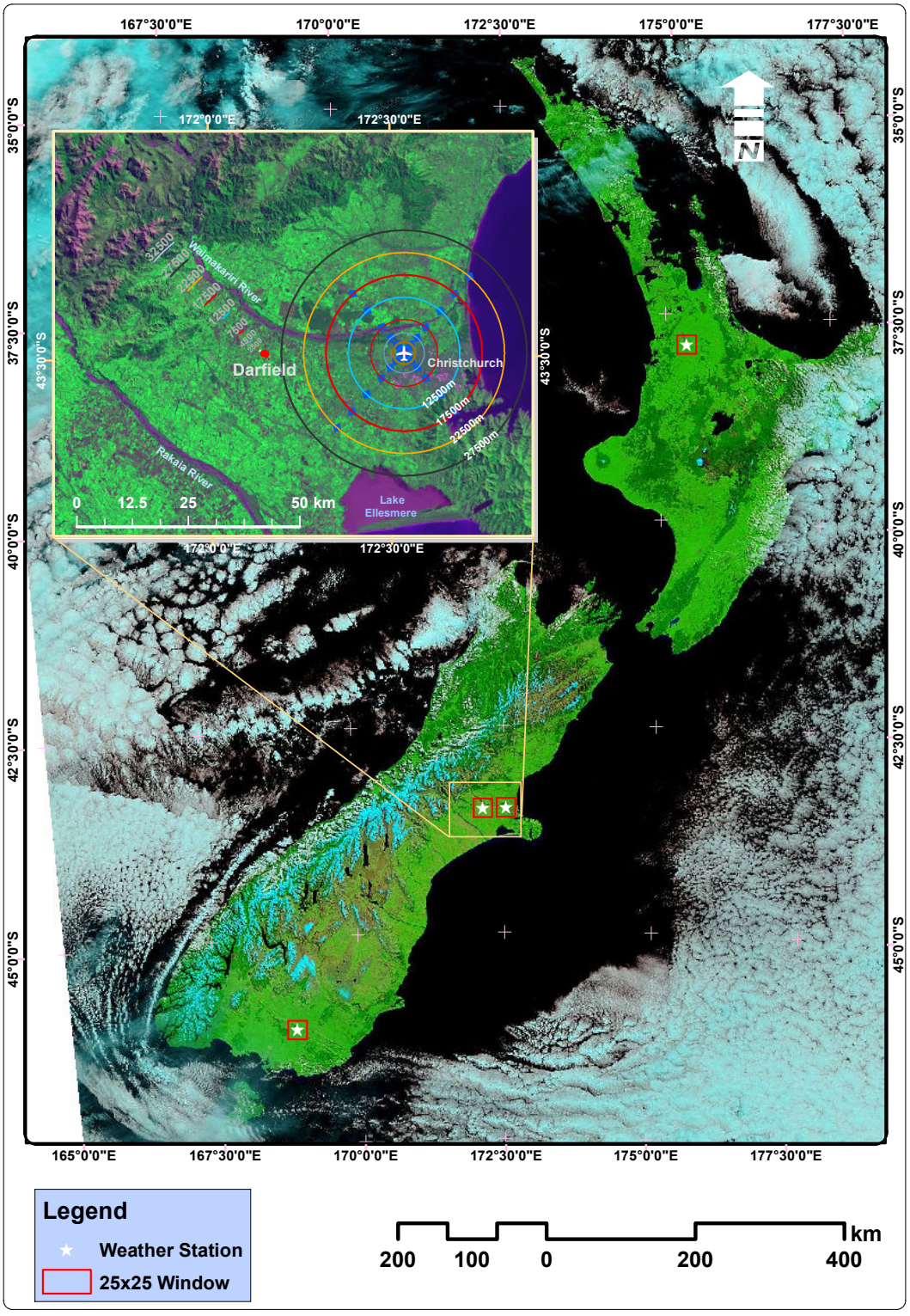

Figure 4.1: Locations of test-sites on a MODIS-Terra false-color (bands 7-2-1) image (acquisition date 18 Sept. 2013) of New Zealand. The enlarged area shown on the top-left is the Canterbury Plains.

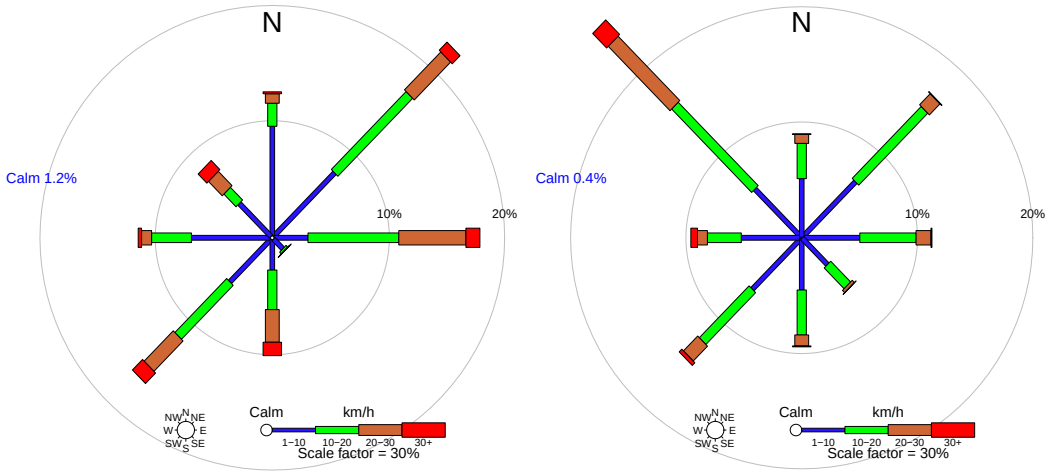

(a) **(b)**

Figure 4.2: Wind directions and speed over the period of 10 years (2002–2012) measured at (a) Christchurch and (b) Darfield permanent weather stations. Length of the wings express frequency (%) and width of the wings indicate categories of speed (km/h).

equatorial local solar overpass times of MODIS-Terra (10:30 descending and 22:30 ascending) and MODIS-Aqua (1:30 descending and 13:30 ascending) can vary depending on the local latitude (Fig. 4.3), and can overlap in high latitudes. The L3 product itself is derived from the Level 2 (L2) product after temporal and/or spatial manipulation (Wan, 2009). For a complete global coverage, the L2 product has been generated from all swaths acquired at day and night, including the polar regions (Wan, 2009). The daily L3 product is then constructed from the L2 product through mapping all pixels in the L2 product onto grids in the sinusoidal projection, where overlapping pixels in each grid are averaged with overlapping areas as weight (Wan, 2009). The entire sequence of the LST L3 composite grid (four grids a day) over the study area (three tiles at: column 29, row 13; column 30, row 13; column 31, row 12), except missing data due to could-cover, from 08 July 2002 to 30 Aug. 2012 (10 years period) were used in this paper.

4.4.2 Meteorological data

Meteorological measurements of T_a at ∼2 m height at Gore (46° 6′ 54″ S, 168° 53′ 13.2″ E, 123 m a.s.l.), Hamilton (37° 51′ 54″ S, 175° 20′ 9.6″ E, 53 m a.s.l.), Christchurch (43° 29′ 35″ S 172° 32′ 13″ E, 37 m a.s.l.), hereafter abbreviated as Chc, and Darfield (43° 29′ 46″ S, 172° 09′ 00″ E, 190 m a.s.l.) weather stations were used in this research. Additionally, WS, WD and rainfall measurements at Chc were used in

the analysis. Data from all stations except one (Darfield) covered 10 years (Jul. 2002 - Aug. 2012). Darfield data were only available for five years (Jul. 2002 - Jun. 2007).

4.4.3 Additional data

Landsat imagery were used for LC classification and detection of major changes in the Canterbury area. Imagery from 02 Oct. 2001 (ETM+), 21 Apr. 2005, 21 Jan 2007 and 28 Mar. 2011 (all TM5) were used for this analysis, which showed no significant change over the analysed period. MODIS imagery from 05 May 2010 (preview; GeoTIFF), 24 Jan. 2012 (preview; GeoTIFF) and 18 Sept. 2013 (preview; GeoTIFF) with 250 m spatial resolution and New Zealand Digital Elevation Model (DEM) were used for LC assessment and selection of suitable sites avoiding rugged terrain.

4.5 Methods

4.5.1 Temporal matching of Ta to LST observations

The temporal frequency of the MODIS LST L3 product is four observations per day (approximately at 1:30, 10:30, 13:30 and 22:30 local solar time) in cloud-free conditions, which are derived from a composite of several MODIS overpasses with different view angles (see Wan, 1999; Zhu et al., 2013). Depending on the local longitude (which results in changes in the sensor's viewing angle) and latitude, the local solar observation times at each pixel can vary up to 120 minutes or more over the repeat cycle (16 days) of the MODIS twin sensors (Fig. 4.3). Other than that, overpass times do not follow a regular time-frame during a day and over the sensor's repeat cycle. On the other hand, T_a data from the weather stations are provided at hourly frequency in New Zealand Standard Time (NZST). This complicates matching the MODIS observation times with T_a time-series. To overcome this issue, T_a time-series were interpolated from an hourly to minute temporal resolution using a spline function. T_a measurement times were adjusted by a negative offset of 19-minute (Hamilton site), 31-minute (Darfield and Chc sites) and 44-minute (Gore site) to convert NZST to local solar time (Sohrabinia et al., 2012). In the next step, each LST record was matched to the closest T_a time in minutes after filtering cloud-contaminated observations based on quality control flags and cloud cover fields.

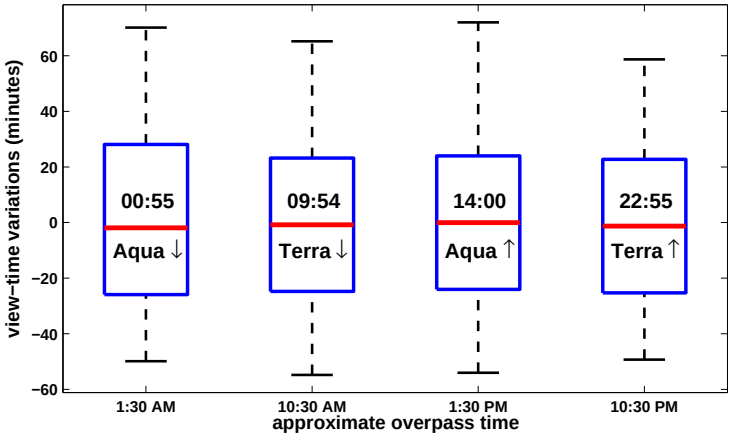

Figure 4.3: Average view-times (local solar) & overpass nodes (shown as labels and arrows), maximum variations from the mean observation times (in minutes shown by lower and upper caps of whiskers), median times (middle line), lower (25^{th}) and upper (75^{th}) quartiles of all observation times (lower and upper edges of boxes) of four overpasses of MODIS (onboard Terra and Aqua, two overpasses each) over the study area over 10 years (2002–2012). The mean local solar observation time of each overpass is subtracted from the series (scaled to 0) but is given as a label on each box.

4.5.2 Multiple LST window-size

To understand the effects of LST window-size on the LST-T_a relationship, we generated areally averaged LST time-series over multiple windows (or kernels) of the MODIS LST grid. At first, time-series of LST from a single pixel (1x1 window-size) overlapping each weather station were used. This was followed by 3x3, 5x5, 9x9, 15x15, 25x25, 35x35, 45x45 and 55x55 pixels, respectively (Fig. 4.1, enlarged area). When window-size was larger than 1x1, mean and median value from the pixels overlapped by each window was calculated to produce LST time-series. The mean (and/or median) of each kernel was derived only for those times when at least two-thirds of the kernel members were valid LST pixels (*i.e.*, no missing values due to cloud mask or water). Using Landsat imagery, the LC classification of the Canterbury Plains showed that the area is predominantly (>80%) covered by low to moderate vegetation, followed by water (Lake Ellesmere, ∼10%) and bare soil. LC classification results also showed that the moderate vegetation class is the dominant LC type (>90%) on Gore and Hamilton sites. Because the emissivity and specific heat capacity of water is considerably higher than vegetation (*e.g.*, Hughes et al., 2007; Benali et al., 2012), pixels over water in the larger windows were removed from the analysis. Spectral mixing of heterogeneous LC types should be minimum for smaller and maximum for larger windows, thus, the smallest window-size is expected to provide the most homogeneous local LC. On the other hand, the measured T_a at the weather station receives convective sensible heat from local features spread over a larger extent than accommodated by a single pixel.

It can be expected, therefore, that the measured T_a in the weather station represents the integrated effects of a larger area than 1x1 km^2 covered by a MODIS pixel. A varying windows-size can help to discover the optimal spatial extent over which LST agrees best with the T_a measurements.

Since a spatial mean or median filter produces a single value from all pixels in the window, it is not possible to identify the effect of distance between the weather station and each pixel in the window on the LST-T_a relationship. To address this issue, we have used time-series of individual LST pixels located at different distances around the Chc weather station. Because T_a is influenced by WS and WD via advection of cold/warm air (see Kawashima and Ishida, 1992; Jönsson and Holmquist, 1995; Hughes et al., 2007; Aikawa et al., 2008; Jiménez-Hornero et al., 2011), we compared correlations from pixels at equal distance but located at different directions to discover any differences due to WD and WS. LST samples were picked along four major WDs and at different distances. Two of these angles were aligned with the dominant WDs in Chc station (NE and SW) while the other two angles were aligned with less frequent winds (Fig. 4.2a). Six to seven samples were selected along each angle at different distances (1.5 to 27.5 km) from Chc weather station (Fig. 4.1, enlarged area).

4.5.3 Day/Night analysis

Apart from spatial variations, observation time can affect the relationship between LST and T_a time-series. To identify any variability in LST-T_a relationship in a diurnal basis, time-series of both variables were separated based on the MODIS overpass times to produce four series. Spatially averaged LST time-series over 25x25 window from MODIS-Terra and MODIS-Aqua day and night overpasses (four in total) were used in this analysis.

4.5.4 Statistical methods

A simple linear relationship is often assumed between LST and T_a in the literature (Brunel, 1989; Mostovoy et al., 2006). In view of this, a univariate linear regression analysis with the MODIS LST as the independent (or explanatory) and T_a as the dependent (or response) variable was applied to analyse LST-T_a relationship. Second and third order polynomial fits were also tested to discover possible non-linearity in the relationship between the two variables. The correlation coefficient, r, is reported as a quantitative measure to evaluate the strength of the agreement between LST and T_a time-series in different steps of the analysis. Significance levels (p-values) are reported

in the results to express how unlikely the given r values would occur if no relationship between the explanatory and response variables did exist, where the smaller the p-level, the more significant the relationship. F-statistic expresses the overall significance of the regression results for $\alpha = 0.05$ and $\alpha = 0.01$. Any correlation with p-value <0.05 is considered significant with 95% confidence, whereas, a p-value <0.01 denotes a 99% confidence level. Errors in the estimation are given by the RMSE (Eq. 4.1) parameter. The mean absolute error (MAE) value (see also Vancutsem et al., 2010; Lin et al., 2012; Zhu et al., 2013) is used to express the long-term mean difference in °C between the two variables (Eq. 4.2).

$$\mathrm{RMSE} = \sqrt{\frac{1}{n}\sum_{i=1}^{n}(\widehat{\mathrm{Ta}}_i - \mathrm{Ta}_i)^2} \tag{4.1}$$

where n is the total number of points and $\widehat{\mathrm{Ta}}$ is a vector of the estimated $\mathrm{T_a}$ values by the regression model.

$$\mathrm{MAE} = \frac{1}{n}\sum_{i=1}^{n}|\mathrm{LST}_i - \mathrm{Ta}_i| \tag{4.2}$$

The abundance of time-points in LST series is controlled by the MODIS overpass times and clear-sky conditions. As a result, LST time-series do not have an equidistant time interval, but rather a sparse and irregular sampling frequency. To find an approximate time-interval for LST series, the total number of points in the series (n = 6188) was divided by the number of days (3694) over the analysed period. As a result, time-interval of LST series (as well as the sub-sampled coincident $\mathrm{T_a}$ series) was an approximate value of 14 hours, which is equal to 1.675 observation points per day or ∼51 points per month (365.25/12*1.675). This is a practical approach to find the time-interval of a non-equidistant discrete sequence in the absence of an equidistant discrete time-series (see also Kerchove et al., 2013).

Bootstrapping with Monte-Carlo resampling (see Efron and Gong, 1983; Haukoos and Lewis, 2005) using r correlation coefficient as sample statistic was applied to identify any seasonal and/or inter-annual variability in LST-$\mathrm{T_a}$ relationship within a confidence interval (CI) of 95% after bias correction (BC). For each bootstrap, n=100 random points were selected from seasonal subsets (365.25/4*1.675 = 153 obs. per season) of each series. The sampling process was conducted with the order of the first seasonal subset to the last and was repeated for a total of 5000 bootstraps.

As explained above, LST series did not have an equidistant time-interval, which means that the series does not follow a regular sinusoidal and some random noise in the series are possible. Therefore, it was difficult to distinguish clear cyclic daily

or seasonal signals in the LST series. A fast Fourier transform (FFT) in frequency (f) domain (Eq. 4.3) was applied to extract dominant cyclic signals from both time-series and filtering possible noise. Dominant amplitudes, or spectral powers (η), were identified in the frequencies of each series according to an arbitrary threshold value (Θ). An inverse FFT (iFFT) was applied to return the series back to time domain (Eq. 4.4) using only the dominant spectral powers ($max(\eta)_i, i = 1, 2, ...\Theta$). The amount of explained variability in the reconstructed LST and T_a time-series was compared using the fraction of explained variability (FEV) value after filtering the redundant spectra from both series. FEV in this analysis is based on the fraction of variability preserved by $\Theta = 50$ largest η in each sequence with respect to the total original variance in the series before FFT (FEV $= var$(reconstructed sequence)$/var$(original sequence)). For an ideal time-series with a few cyclic signals, the reconstructed series using a limited number of dominant η can give FEV ≈ 1. For a noisy series, however, FEV can be considerably lower.

$$X(k) = \sum_{j=0}^{N-1} x(j)\Omega_N^{jk}, \qquad k = 0, 1, 2, ..., N-1 \tag{4.3}$$

where x is an N-point sequence in time domain (N is the total number of points in the series), X corresponds to N samples of the Fourier transform and $\Omega_N = e^{(-2j\pi)/N}$ is the radian frequency (Pei and Luo, 1996).

$$x(j) = A_0 + \frac{1}{N}\sum_{k=0}^{N-1} X(k)\Omega_N^{-jk}, \qquad j = 0, 1, 2, ..., N-1 \tag{4.4}$$

where A_0 is the arithmetic mean (Kerchove et al., 2013) of the original sequence (zero-frequency value given by Eq. 4.3 as the first element of X) and x is the reconstructed sequence from frequency domain back to time domain.

4.6 Results

4.6.1 MODIS LST versus Ta time-series over a single pixel

Before analysing the effects of MODIS window-size, we examine the relationship between LST and T_a over a single pixel co-located at the weather station where T_a data were measured (Fig. 4.4). LST series used in this analysis is a composite time-series which includes four daily LST observations (except for cloudy days) from both MODIS-Terra and MODIS-Aqua day and night overpasses (approximately at 1:30, 10:30, 13:30, 22:30) supplied in the LST L3 product. Long-term correlation between LST and T_a

was relatively strong with a Pearson's correlation coefficient $r \geqslant 0.80$ (Fig. 4.4a). LST values for cold and hot periods have ranged between about -10 to 45 ^{o}C, whereas, T_a range was considerably lower (about -3 to 32 ^{o}C) in all stations (Fig. 4.4). These values indicate that the long-term (10 years) LST range is $\sim$55 ^{o}C compared with T_a range of $\sim$35 ^{o}C. These extremes, however, are based on the series of a single LST pixel. Taking a spatially averaged value from LST pixels over a larger area can give less extremes (Section 4.6.2).

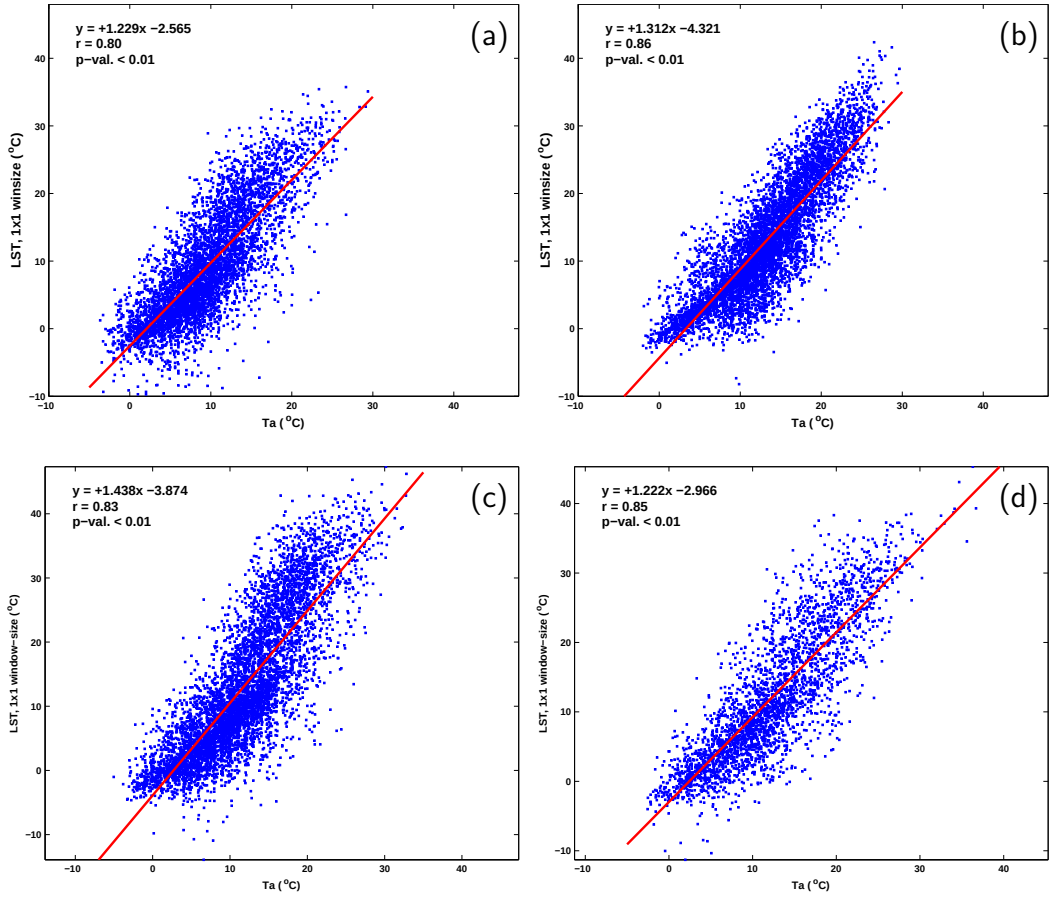

Figure 4.4: Correlation between time-series of LST and Ta over (a) Gore, (b) Hamilton, (c) Christchurch (10 years data: 2002 to 2012) and (d) Darfield (five years data: 2002 to 2007) weather stations.

4.6.1.1 Filtering based on LST viewing angles:

We filtered out the MODIS LST observations from view angles exceeding $\pm 45^{\circ}$ to consider any subsequent improvement in LST-T_a correlation. However, only a slight improvement in r and the MAE values were obtained when LST observations from viewing angles within a range of $\pm 45^{\circ}$ were used in the analysis.

4.6.1.2 Bootstrapping seasonal subsets:

The linear correlation between LST and T_a time-series given above (Fig. 4.4) does not account for possible periodic seasonal and inter-annual variability in the relationship between the two variables (see Benali et al., 2012). Therefore, bootstrapping with sampling design outlined above (Section 4.5.4) was applied to calculate r (Fig. 4.5). Over a 95% CI, the mean values of r were 0.71, 0.82, 0.78 and 0.80 for Gore, Hamilton, Chc and Darfield stations, respectively. The overall correlations obtained from the total LST and T_a series in each station (Fig. 4.4) were more than the mean bootstrapping r values, however, they were within 95% CI of the bootstrapped seasonal correlations at each station. Thus, the LST-T_a relationship varies over a range of about $\pm$10% in different seasons and the mean seasonal relationship is slightly lower than the overall correlations. This indicates that the temporal profiles of LST and T_a have larger differences in some seasons or specific periods over 10 years, which deteriorates correlations in those periods. Such differences can be due to possible noise in LST or T_a time-series. These erroneous observations can be blamed for the less frequent lower correlations extending the lower tails of bootstrap results, causing negatively skewed histograms. When these erroneous values were not picked by chance, correlations have been generally higher, causing a higher frequency for the r values above the mean (Fig. 4.5). These errors are further analysed in the next section.

4.6.1.3 FFT filtering of LST series from a single pixel:

To understand the difference in temporal variability of LST and T_a time-series, FFT filtering in frequency domain was applied. The results of this analysis only on Chc site are reported. Both LST and T_a series have shown a fundamental harmonic (Λ) over a period of approximately 6 days ($f/1.674$, middle panels in Fig. 4.6). The majority of subsequent harmonics in T_a series have appeared over a period of one year, whereas, the subsequent harmonics in LST series suggest a cyclic trend over a period of about three years. Since most of the dominant signals in LST series have stacked at the middle, both six-monthly and yearly signals in this series have appeared at the same harmonic ($\Lambda = 40$). In T_a series, on the other hand, yearly signal ($\Lambda = 24$) was more prominent than six-monthly signal ($\Lambda = 30$).

Using 50 largest η to reconstruct both series (which is how FFT filtering was performed), only FEV $= 0.47$ of the original LST series could be restored, whereas more than 50% of the variability (FEV$= 0.55$) in T_a time-series was recovered. In other words, an unexplained variability ($1-$ FEV) of 0.53 (or 53% loss of detail) has occurred

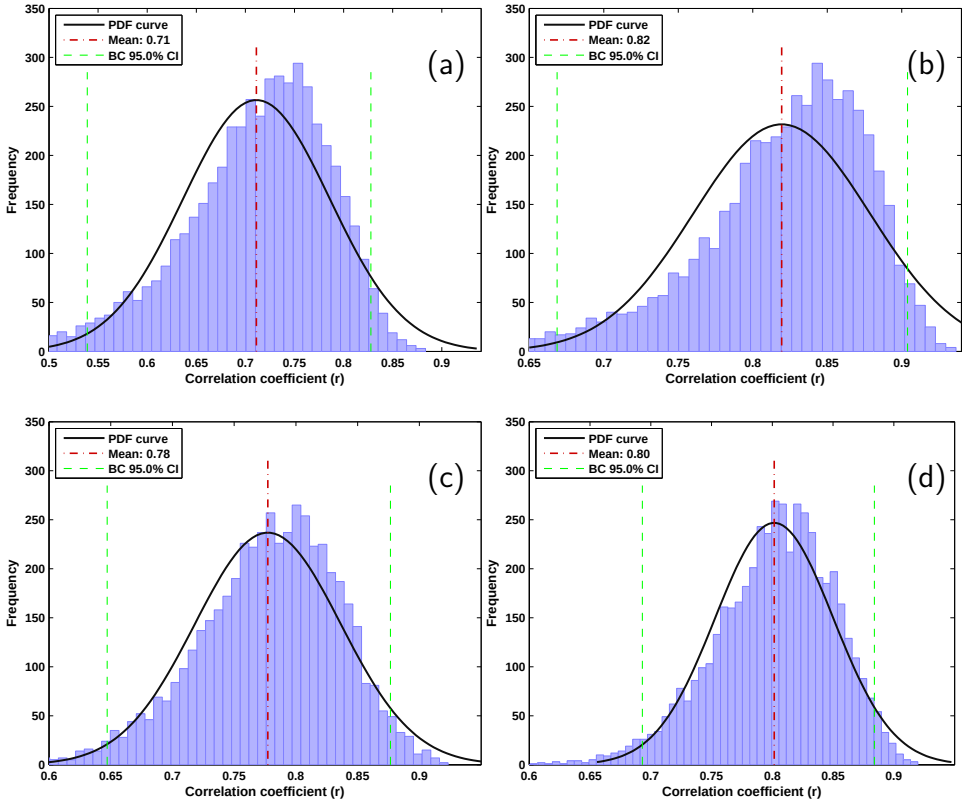

Figure 4.5: Distribution of 5000 bootstrapped r correlation coefficient given by 100 corresponding LST and T_a random samples in each bootstrap over (a) Gore, (b) Hamilton, (c) Christchurch (10 years data: 2002 to 2012) and (d) Darfield (five years data: 2002 to 2007) weather stations. Mean and 95% confidence intervals (CI) are marked on the plots. Normal probability density function (PDF) curve is fitted on the plots to compare distribution of bootstrapped r values with a normal distribution. Bootstraps were bias-corrected (BC).

in the reconstructed LST series compared to only 45% loss of details in T_a time-series. To put the difference into scale, 800 largest η were necessary to retain equal FEV in LST reconstructed time-series compared to only 50 largest η needed to recover the same FEV in T_a series. This analysis showed that LST time-series constructed from a single MODIS pixel contained considerably more variability even in the reconstructed smoothed output. Part of this variability can be due to possible noise, which could be reduced via spatial filters if the neighbouring pixels were also taken into account. This is further examined below by overlapping multiple windows on the MODIS LST grid.

4.6.2 Effects of LST window-size

The first time-series of LST used in this analysis were produced based on LST observations over a single pixel co-located at the weather station where T_a measurements were recorded. Since this time-series is extracted from a single LST pixel, it is referred to as

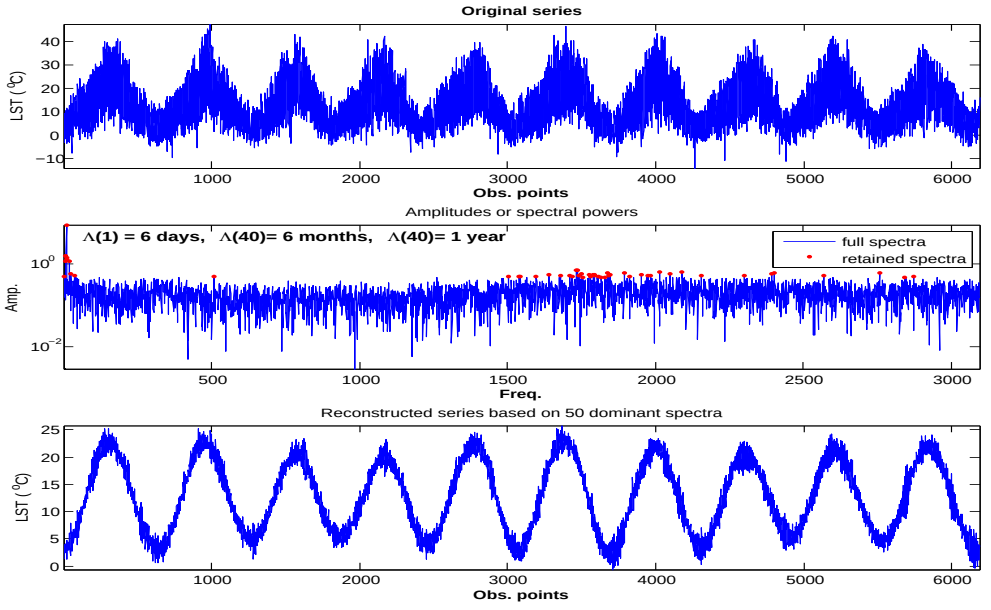

(a)

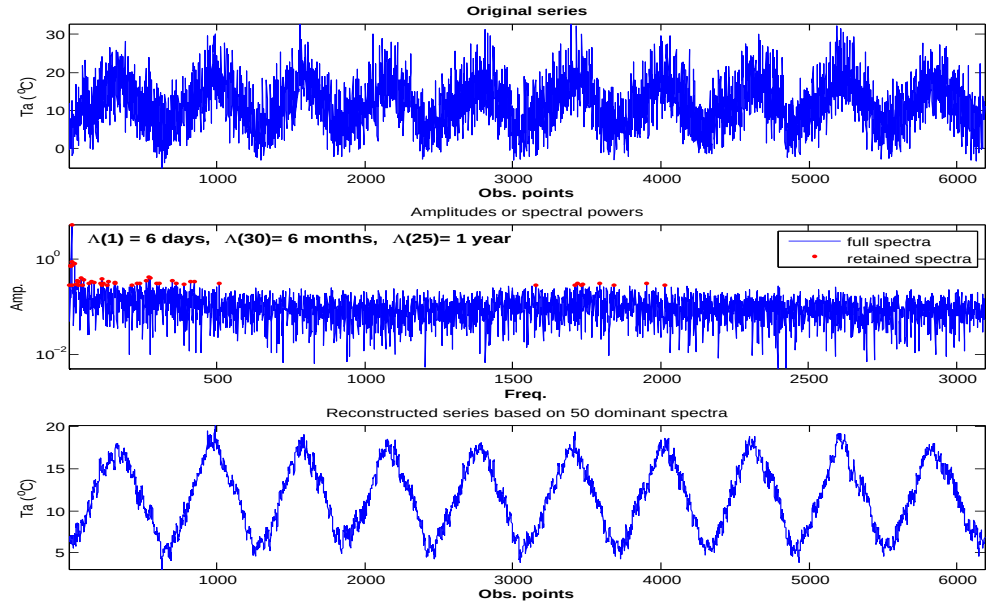

(b)

Figure 4.6: Comparison of (a) LST and (b) T_a time-series in frequency domain over Christchurch station (2002 to 2012 data). The top panels show the original series, the middle panels are the amplitudes of the frequencies from each sequence (scaled to 0-1) and the bottom panels show filtered series. Time-period of the first dominant harmonic (Λ) and harmonic numbers of 6-monthly and yearly signals are given on the middle panels.

1x1 window-size throughout this paper. More LST time-series were produced based on larger windows (Table 4.1 & 4.2), having the first window as the central pixel. Taking the median value in each window also acts similar to a low-pass filter by avoiding the values at either extremes. This can be interpreted from the decreasing trend in the

standard deviations and ranges (minimum to maximum) of the time-series produced from smaller compared to larger windows (Fig. 4.7). Additionally, mean and median filters have reduced both the number and range of outliers in the larger windows. In all cases, the majority of outliers were observed at warmer temperatures. Since warmer temperatures predominantly occur at day-time, outliers are mostly from observations when the surface is heated more rapidly (see also Cresswell et al., 1999; Mildrexler et al., 2011; Zhu et al., 2013) while cooling at night is gradual.

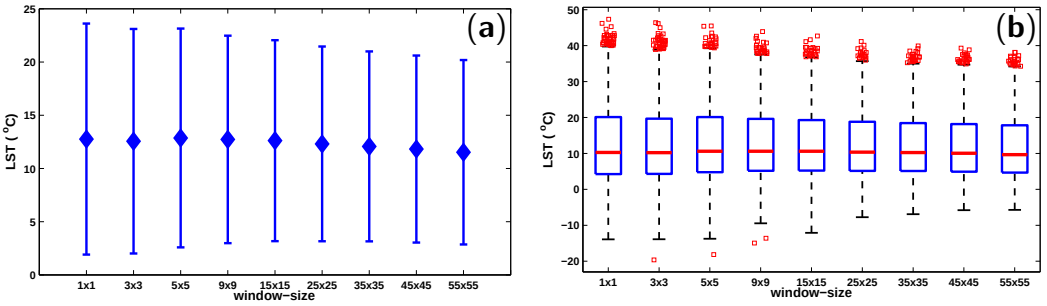

Figure 4.7: (a) Errorbars showing variability of the means (middle diamonds) and ± 1 standard deviation from the mean (lower and upper whiskers) of LST time-series produced from multiple windows; and (b) box-plots showing variability of 25th (Q1) and 75th (Q3) percentiles (lower and upper edges of the boxes), medians (Q2, middle bars), minimums and maximums (lower and upper whiskers) and outliers (points beyond lower and upper whiskers) of LST time-series derived from multiple windows (Christchurch site, 2002 to 2012 data).

Correlations were improved very slightly when the window-size was increased from 1 to 3, 9, 15 and 25 pixels (Table 4.1 & 4.2). Larger windows of up to 55x55 pixels (Fig. 4.1) were also tested. The highest correlation values were achieved with 9x9 (Gore) to 25x25 (all other sites) windows. Significance level of all correlations were found to be at $\alpha = 0.01$ (99% CI), which can be interpreted from p-values (all p-values were <0.01). Considering the degrees of freedom of regression model (DFM $= 1$) and the residual errors (DFE $\geqslant 6187$), the F-statistic far exceeds the F-critical value (6.63) for $\alpha = 0.01$ in all correlations (Table 4.1). The agreements deteriorated when windows larger than 9x9 pixels at Gore and 25x25 pixels at the other sites were used to construct LST time-series. Slight improvements in the correlations were observed when a median filter was applied (Table 4.1, right side). Considering the fact that a mean filter takes the average of all pixels inside each window at each time-point, pixels affected by possible noise have contributed to the correlation results. This is avoided by the median filter.

The MAE value (Eq. 4.2) from most of the windows indicates that the long-term mean value of LST is higher than T_a. The value of MAE is reduced with larger windows. The effect of window-size on the correlations between LST and T_a time-

Table 4.1: Regression statistics and mean absolute error (MAE) values from correlations between LST and T_a time-series in Christchurch station over 10 years (Jul. 2002 - Aug. 2012), where LST series are produced from the MODIS LST grids with varying window-size using mean & median (M&M) filters. P-values from correlations between the MODIS LST and T_a series are also reported to interpret the significance level.

Window	Mean filter				MAE	Median	M&M
size	r	RMSE	p-val.	F-stat	(^{o}C)	filter r	DFE
1x1	.83	3.50	0.00	12870	1.19	.84	6187
3x3	.83	3.49	0.00	13740	1.01	.84	6596
5x5	.84	3.44	0.00	14680	1.06	.85	6667
9x9	.85	3.37	0.00	16230	1.16	.86	6698
15x15	.86	3.34	0.00	16730	1.06	.87	6786
25x25	.87	3.33	0.00	16930	0.76	.88	6794
35x35	.86	3.34	0.00	4505	0.54	.87	6767
45x45	.84	3.36	0.00	16490	0.31	.85	6753
55x55	.84	3.37	0.00	16040	0.03	.85	6671

Table 4.2: Regression statistics and mean absolute error (MAE) values (^{o}C) from correlations between LST and T_a time-series over Gore, Hamilton (10 years data: 2002–2012) and Darfield (5 years data: 2002–2007) sites. LST series are produced from the MODIS LST grids with varying window-size using mean filter.

Window	Gore		Hamilton		Darfield	
size	r	MAE	r	MAE	r	MAE
1x1	.80	1.07	.86	0.74	.85	1.20
3x3	.81	0.91	.88	0.71	.85	1.04
5x5	.83	0.69	.89	0.66	.86	0.92
9x9	.85	0.61	.90	0.62	.87	0.84
15x15	.84	0.55	.92	0.53	.88	0.59
25x25	.82	0.58	.92	0.48	.89	0.40
35x35	.78	0.82	.91	0.44	.89	0.31
45x45	.75	1.03	.87	0.41	.88	0.33
55x55	.72	1.26	.84	0.38	.87	0.34
65x65	.69	1.67	.81	0.39	.85	0.27

series seems minor when r statistic is considered, however, MAE values at all sites improved considerably from $\sim$1 ^{o}C down to $\sim$0.5 ^{o}C when the window-size increased.

4.6.2.1 FFT filtering of LST series from multiple windows.

Using FFT transformation above, we demonstrated that LST time-series extracted from a single MODIS pixel co-located at the weather station contained larger variability than T_a series. Higher variability and possible noise in LST observations can be due to the sensitivity of satellite observed LST to rapid radiant heating and cooling of

the surface, which can also affect the accuracy of GSW (Wan and Dozier, 1996) LST retrieval algorithm. The amount of noise can be reduced by applying a two-dimensional window of varying size on the MODIS grids and producing LST series from the mean or median values of the coincident observations. In the same way, seasonal and annual signals can be better detected when the noise is reduced in the spatially averaged time-series. Comparing the FEV in LST series from different windows, which were all reconstructed based on 50 largest η using iFFT (Eq. 4.4), it turned out that an increase in window-size helps to explain more cyclic variability in the series (Table 4.3). This is due to the noise reduction and smoothing effect of spatial averaging over all pixels inside larger windows.

Table 4.3: Fraction of explained variability (FEV) in LST series (Christchurch site) from multiple windows after reconstruction of each sequence based on 50 largest spectral densities using inverse FFT (10 years data).

Window-size	1x1	3x3	5x5	9x9	15x15	25x25	35x35	45x45	55x55
FEV	0.47	0.49	0.50	0.52	0.54	0.54	0.53	0.51	0.51

4.6.3 Effects of distance

The aim of this section is to identify the effective distance at which LST from a single pixel (at Chc site) relates best with T_a time-series. Additionally, this analysis tries to find out if wind causes any variation in the correlations due to the position of LST samples being upwind or downwind with respect to the weather station but at equal distance (see Jiménez-Hornero et al., 2011). The agreement between T_a and LST pixels along all directions has improved when the distance was increased up to 7.5 km, decreasing again with longer distances (Table 4.4). The highest correlation at all directions was obtained at 2.5 to 7.5 km distance from the weather station. These results indicate that the agreement between T_a and LST series of the pixel co-located at the station is almost similar to the series from pixels at about 12.5 km around the weather station. This distance is equivalent to 25x25 LST window-size (Section 4.6.2). All pixels at equal distance have shown almost similar agreement, regardless of the position of the pixel with respect to WD. However, considerable differences were observed due to the variability in WS. The agreement was lower when time-points only at calm conditions (WS < 2 ms^{-1}) or relatively windy conditions (WS > 8 ms^{-1}) were used in the correlations. This is another interesting result, which indicates that LST and T_a correlate better when there is a light air (approximately $2 <$ WS < 8 ms^{-1} at Beaufort Wind Scale). Windy conditions reduce the agreement

between the two variables while absolutely calm conditions also result in slightly lower correlations. Thus, when distance is held constant, the LST-T_a relationship is affected by WS but not by WD.

Table 4.4: Regression statistics from correlations between LST and T_a time-series where LST series are extracted from pixels at different distances from Christchurch (Chc) weather station along four major wind directions (WDs). The r correlation value is calculated after filtering LST and T_a time-series according to three wind speed (WS) categories to compare the effect of WS on LST-T_a relationship at different distances. The actual WD, or the direction which wind has been blowing from, is neglected in these calculations and the directions given in this table (NE, SE, ...) indicate the location of LST pixels with respect to the weather station.

WS cat.	WS$<$2 ms^{-1}				2$\leqslant$WS$\leqslant$8 ms^{-1}				WS$>$8 ms^{-1}			
dist.\Dir.	NE	SE	SW	NW	NE	SE	SW	NW	NE	SE	SW	NW
Chc	.80	.80	.80	.80	.88	.88	.88	.88	.76	.76	.76	.76
1.5 km	.81	.80	.79	.80	.88	.88	.88	.88	.76	.76	.76	.76
2.5 km	.80	.80	.79	.81	.89	.89	.88	.89	.77	.77	.75	.77
4.5 km	.81	.80	.80	.83	.89	.89	.89	.91	.76	.75	.79	.78
7.5 km	.83	.82	.81	.83	.90	.89	.88	.90	.77	.73	.77	.78
12.5 km	.82	.80	.80	.80	.88	.89	.88	.89	.76	.76	.77	.73
17.5 km	.82	.73	.80	.82	.88	.89	.87	.88	.74	.79	.75	.72
22.5 km	.71	–	.80	–	.81	–	.88	–	.69	–	.74	–

4.6.4 Diurnal differences

To this point, we examined LST-T_a relationship using a composite LST time-series generated from MODIS-Terra and MODIS-Aqua overpasses (total of four) correlated with the T_a measurements at the corresponding times. In this section, daily variability of LST-T_a relationship at Chc site is examined using separate LST series (over 25x25 window) from four MODIS overpasses. This analysis showed that nighttime MODIS-Terra observations have considerably higher agreement with T_a time-series than daytime (Fig. 4.8b,d). On the other hand, daytime MODIS-Aqua observations showed higher agreement with T_a time-series compared to nighttime (Fig. 4.8a,c).

This finding was assessed based on data from other sites as well, where similar results were observed (Table 4.5). Considering the scatterplots of LST-T_a from each MODIS overpass, daytime MODIS-Aqua observations have less scattering while nighttime observations are more spread around the 1:1 line (Fig. 4.8a,c). This indicates that nighttime MODIS-Aqua observations contain more errors than daytime. As a consequence, the relationship between LST and T_a varies at each overpass time with the highest agreement around the evening and the lowest agreement around midnight.

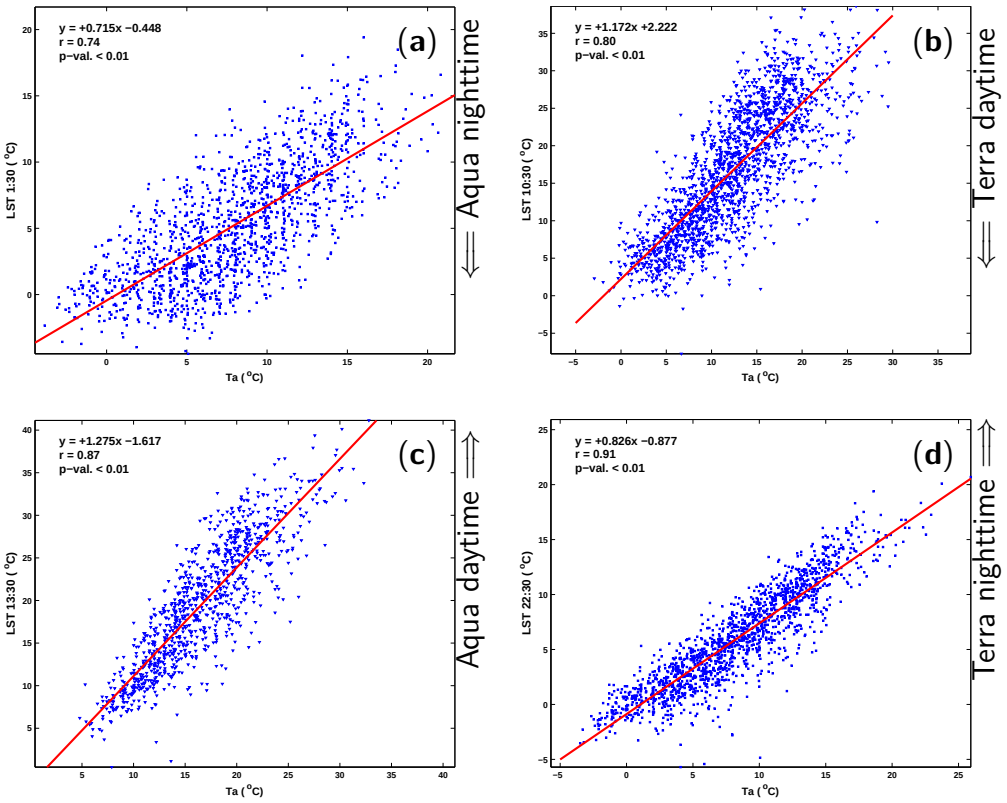

Figure 4.8: Correlations between LST and T_a time-series separated based on approximate overpass times of MODIS-Terra and MODIS-Aqua (10 years data: 2002 to 2012), where each scatterplot shows (a) MODIS-Aqua nighttime, (b) MODIS-Terra daytime, (c) MODIS-Aqua daytime and (d) MODIS-Terra nighttime observations plotted against T_a measurements at the corresponding times.

For further investigation of this finding, we exploited variations in the MODIS daily overpass times to reconstruct the diurnal profile of LST for 10 years and compared it with the mean hourly T_a values calculated from continuous hourly measurements in Chc weather station (Fig. 4.9a). Since LST was not available for all hours (Fig. 4.9b), the missing values were interpolated, hence, some artifacts (*e.g.,* an unusually cold value at 8:00 PM) can be found in the plotted diurnal profile of LST. This analysis showed that the diurnal profile of LST has two cross-overs with that of T_a: once, between 7:00 to 8:00 AM, and the second time between 16:00 to 17:00 in the afternoon. After this time, T_a cools down slower than LST, which leads to a large gap between the two profiles in the late afternoon and the early evening. However, the two profiles become closer again when T_a has also cooled down after sunset in the late evening. This is the time when MODIS-Terra overpasses the study area (21:00 to 00:00, Fig. 4.3), which is why nighttime MODIS-Terra observations showed the highest agreement with T_a measurements. After midnight, LST continues cooling down, while T_a stays warmer. For that reason, larger differences was observed between LST and T_a around midnight.

Table 4.5: Variability of LST-T_a relationship (r) with MODIS overpass time.

Site/Time	∼1:30	∼10:30	∼13:30	∼22:30
Gore	.71	.74	.86	.87
Hamilton	.74	.79	.87	.88
Chc	.74	.80	.87	.91
Darfield	.68	.75	.88	.88

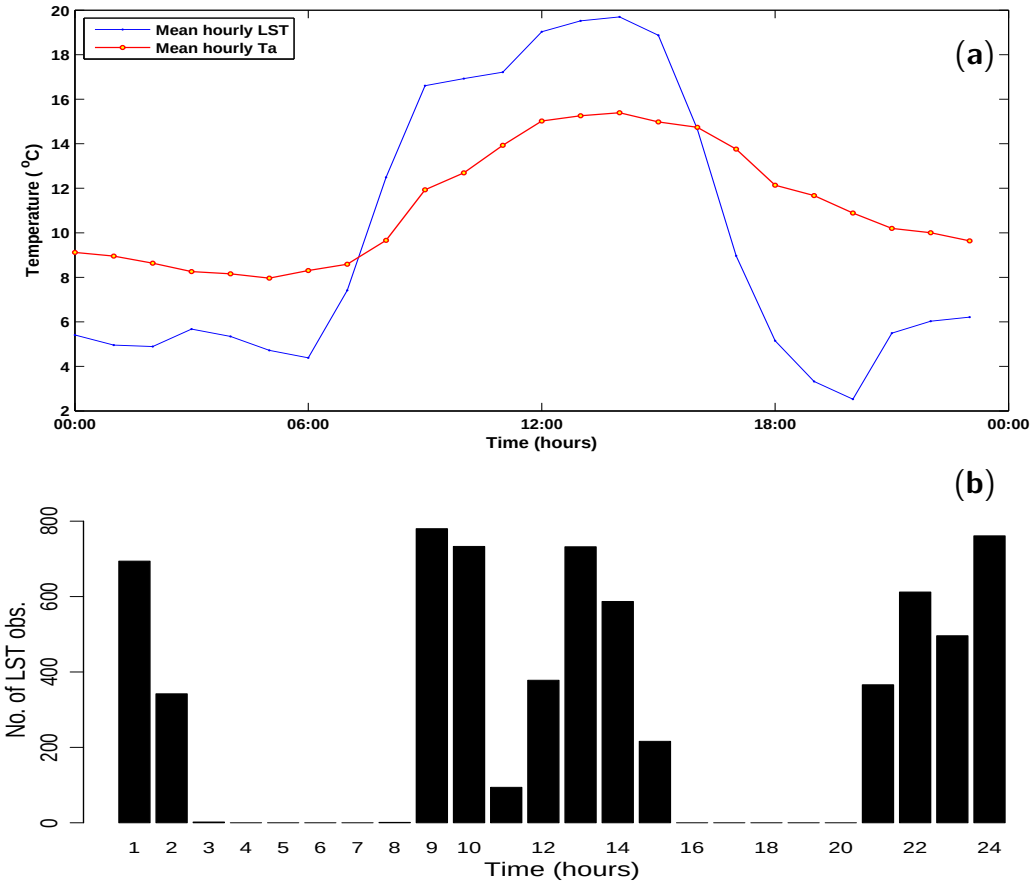

Figure 4.9: (a) Diurnal air and skin temperature cycle based on the mean hourly LST and T_a over 10 years (2002 to 2012) in Christchurch weather station, and (b) the histogram of the available LST observations in the composite time-series from four MODIS overpasses which were used to produce the mean hourly LST values.

4.7 Discussion

Time-series of a single pixel versus multiple pixels. The temporal profile of LST time-series from a single pixel showed higher variability and more noise, which was shown by a FFT analysis. This indicates that the best practice to generate LST time-series from MODIS is to apply a downscaled lower resolution grid rather than the original pixel. Other resources also had taken a similar approach, such as Zhang et al. (2011a), where they had downscaled the MODIS LST grid to 6 km for modelling T_a. We assessed this by applying a varying window on the MODIS LST and found the best correlation by using a spatially averaged series over a 25x25 window. At Gore site, however, correlations deteriorated when the window-size was increased to 15x15 pixels. This was due to the effects of the nearby hills at this site. In general, the highest agreement with T_a measurements is achieved when an adequate area around the site is represented by the LST time-series. Error in T_a estimates from LST were reduced significantly when window-size increased from a single pixel to 5x5 or more pixels. Similar results had been reported by Xu et al. (2012) where they had found that T_a estimation error tends to be lower as spatial window-size increases, suggesting that the model performance is improved by spatially averaging land surface characteristics. Bootstrapping of seasonal subsets from both series showed that the LST-T_a relationship is lower in some seasons. Our sampling design had restricted bootstraps to four seasons of the year. Because cloud contamination in winter, late autumn and early spring is higher in our study area, these differences can be due to the effects of cloud on those seasons. Additionally, cloud patterns can vary at similar seasons in different years in this region due to frontal weather systems, which can explain the inter-annual differences in the correlations. Since LST is basically the directional radiometric temperature of the surface skin (see Norman and Becker, 1995), variability of sun angle over a year can introduce uncertainties in the LST product (Jin, 2004). The latter uncertainty, however, has already been corrected by the GSW algorithm (Wan and Dozier, 1996).

Effects of distance, WS and WD. Our results showed that the LST-T_a relationship stays relatively similar up to distances of 12.5 km from Chc weather station. This indicates that T_a over an area of $\sim$25x25 is relatively homogeneous at this site and the local heat exchange between the surface and the 2 m height does not produce a considerable difference. Although this distance may vary over another site depending on the local conditions, the importance of this finding is that T_a necessarily does not agree best with LST over the closest pixels. A possible explanation for this can be the effects of advection. We found that the LST-T_a relationship is affected by the WS, which is in accord with the previous research (see also Lin et al., 2012), but not by

WD at equal distances. In other words, the effect of WD seems to be similar on all pixels at equal distance around the weather station. These results indicate that LST is better correlated with T_a when a slight instability in the local atmosphere exists, which can strengthen the local turbulent heat fluxes. However, a stable atmosphere with no wind restricts heat exchange (see Pleim, 2006) between surface skin and the near-surface T_a. In a windy atmosphere, on the other hand, T_a is affected more by advection of air coming from the adjacent areas (ocean or mountains, Section 4.3) than the local sensible heat fluxes (see Hughes et al., 2007), which is why it agrees less with LST during stronger winds.

Day/Night differences. Our results showed that the MODIS LST correlates best with T_a measurement around the evening but the strength of correlation deteriorates around midnight. To some extent, this outcome was contradictory to the other works in the literature (*e.g.,* Zhang et al., 2011a; Benali et al., 2012) where they have reported a stronger correlation at nighttime compared to daytime. It must be noted, though, that Benali et al. (2012) used MODIS-Terra but not MODIS-Aqua observations. Variations in the MODIS overpass times in its 16-day repeat cycle enabled us to reconstruct the diurnal LST profile over 10 years. This analysis showed that the gap between LST and T_a temporal profiles vary over a period of 24 hours. Similar profiles had been found previously (Cresswell et al., 1999), but using higher temporal resolution LST data from Meteosat geostationary observations. Although many studies have shown a higher agreement between LST and T_a at night (Zhang et al., 2011a; Benali et al., 2012), this is not the case for all hours of the day or night. At some hours of the night the LST-T_a relationship is weaker than some hours at the day. In particular, when LST diurnal profile changes its slope in the morning and in the afternoon, it can show higher agreement with T_a.

4.8 Conclusion

The relationship between remotely sensed LST and T_a over a period of 10 years in New Zealand was analysed in this paper. Time-series of LST from a single pixel overlapping the weather station, where the T_a measurements were collected, showed a significant correlation ($r \geqslant 0.80$, 99% confidence). After reconstruction of both LST and T_a time-series based on 50 dominant spectra, it turned out that the FEV value in LST series from 1x1 window is considerably lower than that of T_a time-series. FEV values from LST time-series were improved when larger windows over the MODIS LST grid were applied. Smoothing due to averaging in larger windows reduced the

amount of noise in LST series lowering the internal variability in the series, which was shown by FEV values. This was unexpected since the intrinsic heterogeneity of LC over larger windows could possibly lead to more errors. Highest r correlations and lower MAE values were achieved with a 9x9 window-size at Gore ($r = 0.85$, MAE≈0.6 °C) and a 25x25 window-size at Hamilton ($r = 0.92$, MAE≈0.5 °C), Chc ($r = 0.87$, MAE≈0.8 °C) and Darfield ($r = 0.89$, MAE≈0.4 °C) sites, whereas the worst results were obtained from the series of a single pixel co-located at the weather station. Effects of distance between the LST pixels and the weather station, WS and WD on LST-T_a relationship were also considered. LST time-series from sample pixels located at 1.5 to 12.5 km distance from Chc weather station showed almost similar correlations as the pixel co-located at this site. Correlations were improved slightly when LST observations coincident with stable atmospheric conditions (WS < 2 ms^{-1}) and high-speed winds (WS > 8 ms^{-1}) were removed from the analysis ($r = 0.88$, 99% confidence). The MODIS LST, therefore, has a significant agreement with the T_a measurements over a large area around the weather station extending at least across 5x5 and at most 25x25 km^2 area. Beyond that, the agreement gradually deteriorates. Day and night analysis showed that LST and T_a agreement is better in the evening but it deteriorates at midnight.

Consequently, it can be concluded that in relatively calm conditions, T_a can be modelled using the MODIS LST time-series and extrapolated over an area of at least 9x9 to 25x25 km^2 in the study area. The size of window may vary depending on the extent of flat area surrounding the weather station, as well as local LC and topography, nevertheless, the optimal extent seems to be always larger than the area covered by a single MODIS LST pixel. To provide the aggregate effects of the heterogeneous LC, however, the spatial detail in the MODIS LST 1 km^2 grid is essential. Additional local affects such as WS, major topography and water bodies in the area must be considered before construction of LST time-series. A spatial filter (mean or median) over an area which can vary depending on local conditions will be helpful to avoid possible noise. Removing the observations collected from view angles exceeding ±45° from LST time-series (see also Mostovoy et al., 2006) may also improve the results.

Acknowledgements

We acknowledge access to New Zealand's National Climate Database (Cliflo), provided by the National Institute of Water & Atmospheric Research (NIWA), via an online web-based system which we used to download T_a and other climate parameters. Access to the MODIS LST product via Reverb tool from the US National Aeronautics and

Space Administration (NASA) is appreciated. Language editions and proof reading of the paper was done by Caroline Cameron-Blackgrove.

Chapter 5

Soil moisture retrieval from the MODIS LST

5.1 Preface

Results from Chapter 4 showed that the surface skin temperature from MODIS satellite observations relate to the measured T_a over an area of about 25x25 km^2 rather than the exact point where the T_a measurements were recorded. This indicates that the latent and sensible heat fluxes from the surface skin have relatively homogeneous patterns over the flat parts of the study area. Using *in-situ* SM measurements at six sites as reference, this chapter attempts to find out if SM derivations from the MODIS LST are also similar across the Canterbury Plains or a significant difference exists between different LC types. To this end, two ATI methods are used to derive the near-surface SM from the MODIS LST. Quality of SM derivations using both methods is evaluated based on the *in-situ* measurements and rainfall data. Each of these ATI methods use different number of LST observation over a 24-hour period. The first objective of this chapter is to assess the relationship between SM derived from the MODIS LST using the ATI method with the measured and modelled values of this parameter. The second objective is to find out if the ATI method based on more LST observations gives better results. The answer to this question will help to find out if a better representation of the diurnal LST profile leads to a better approximation of the near-surface SM or only two LST observations giving the minimum and maximum daily LST values are sufficient.

NOTE:

This chapter is under review as a paper in the ***Journal of Applied Remote Sensing*** under the title:

Soil moisture derived using two Apparent Thermal Inertia functions over Canterbury, New Zealand

M. Sohrabinia, W. Rack, P. Zawar-Reza

Abstract. The near-surface soil moisture (SM) is an important property of the soil that can be studied from satellite remote sensing observations over a large spatial domain. This research provides an estimate on the accuracy of SM retrieved from satellite land surface temperature (LST) observations over the Canterbury Plains in New Zealand. The apparent thermal inertia (ATI) method with two approaches (ATI1 & ATI2) was applied to derive the near-surface SM from the Moderate Resolution Imaging Spectroradiometer (MODIS) LST product. The *in-situ* measurements of SM and rainfall data at six sites across the study area were used as reference. The analysis was conducted in two temporal scales, a short period of four months and a longer period of three years. SM simulations by the Weather Research and Forecasting (WRF) model was also used in the analysis but only in the short period. Overall, ATI2 showed slightly higher correlation with the *in-situ* measurements ($\bar{\rho} = 0.66$) than ATI1 ($\bar{\rho} = 0.63$). This value was higher from the WRF simulations ($\bar{\rho} = 0.81$). Both functions performed better during summer compared to winter, but even in this season, ATI2 showed less mean errors (ME ≈ -15 m^3 m^{-3}) than ATI1 (ME ≈ -20 m^3 m^{-3}) at most of the sites. Additionally, seasonal variations of SM were detected by ATI2 better than ATI1, and the effects of precipitation were detected on more occasions by ATI2 function. We concluded that ATI2 function can be used to derive the near-surface SM from the MODIS LST time-series in the long-term and the WRF simulations can be applied to fill the gaps in the retrievals due to cloud cover.

Keywords. MODIS; MODIS LST; near-surface soil moisture; rainfall; ATI; WRF; land-cover; time-series

5.2 Introduction

The near-surface soil moisture (SM) affects diurnal change of surface temperature, and is a key variable in computing several parameters of the land energy and water budget (Zhang et al., 2007). Observations of spatially distributed SM are essential for a large range of hydrological, climate and agricultural applications (Pause et al., 2012).

Satellite observations in the visible and near-infrared (VNIR), thermal infrared (TIR) and microwave (MW) regions of the electromagnetic radiation can be used to derive the near-surface SM (Wang and Qu, 2009; Vandoninck et al., 2011) with a varying

depth depending on the surface type and the energy employed by the sensor. Land surface temperature (LST) is the parameter measured by TIR observations. One of the algorithms based on TIR datasets is the Thermal Inertia (TI) method (Price, 1977). The apparent thermal inertia (ATI), a quantification of the effect of soil TI on soil surface temperature, is solely based on remotely sensed observations (Verstraeten et al., 2006; Wang and Qu, 2009; Vandoninck et al., 2011). ATI makes use of the difference between day and night LST as well as surface albedo information derived from VNIR observations (Badarinath and Chand, 2007).

Methods for retrieving the near-surface SM using ATI mainly differ on their approach to estimate the diurnal cycle of LST. Xue and Cracknell (1995) developed a model (known as XC) to derive the real TI from the Advanced Very High Resolution Radiometer (AVHRR) day (14:37 local solar time) and night (04:44) observations in channels 1, 2 and 5 and found that TI is directly proportional to ATI. To compute the real TI, XC method required an extra parameter measured on the ground, which was the time of the maximum temperature in daytime obtained from a meteorological station. Sobrino et al. (1998) developed a method based on three AVHRR LST observations per day (02:30, 7:30 and 14:30 local solar time) to retrieve TI without the need for a ground measured parameter. The same authors developed another model (Sobrino and El-Kharraz, 1999a,b), named FTA (four temperatures algorithm), using four AVHRR thermal observations (02:30, 7:30, 14:30 and 19:30) and compared their method with XC. They found that FTA is better in presenting the diurnal cycle of soil surface temperature as it uses more LST observations over a 24-hour period. Verstraeten et al. (2006) also used two LST observations (day/night) from Meteosat but to estimate ATI rather than TI. They approximated the topsoil saturation index from ATI and scaled it using the maximum and minimum long-term SM measurements on the ground to obtain the near-surface SM content (we will call this ATI1 function). Vandoninck et al. (2011) modified FTA to be applied on the Moderate Resolution Imaging Spectroradiometer (MODIS) LST observations from Terra and Aqua day and night ($\sim$1:30, 10:10, 13:30 and 22:30) overpasses (we will call it ATI2 function).

The LST product is one of many datasets derived from day and night observations of MODIS on-board Terra and Aqua satellites for more than a decade. MODIS BRDF/Albedo product is another dataset which is useful as a necessary input for ATI calculations. As a property of land surface, SM can also be estimated based on surface moisture fluxes, therefore, coupled land-atmospheric models with regional scales are also used to simulate SM across spatial extent. The Weather Research and Forecasting (WRF) community model is a mesoscale regional model which can be used to simulate SM over scales ranging from meters to thousands of kilometers (Hong et al., 2009)

when it is coupled with one of the available land surface schemes in the model. Using numerically modelled SM in combination with a remote sensing approach can be helpful to fill the gaps in the latter due to cloud cover. It also provides the opportunity for inter-comparison of the two outputs over spatial domain. This is critically important on areas where ground truth data are not available (such as rugged alpine or densely forested parts of the South Island of New Zealand).

The objective of this research, therefore, is to assess the relationship between SM derived from the MODIS LST using ATI method, simulated by the WRF model and measured on the ground, and to compare the performance of ATI1 and ATI2 functions. The study is aimed to find out if a more detailed representation of LST diurnal cycle in ATI method leads to an improvement in the near-surface SM retrievals. Based on our review of the literature, there has been limited attempt previously to compare different ATI methods and to evaluate their performance in relation to rainfall events.

5.3 Study Area

The study area is located in the Canterbury Plains in the South Island of New Zealand (Fig. 5.1), approximately at 43° 37′ 48″ S and 172° 11′ 24″ E at the centre. Elevation of the study area ranges from a few metres on the coastal side (East) to about 200 m above sea level (a.s.l.) on the mountainous side (West). The Canterbury Plains is the largest flat land in New Zealand dominated by agricultural and farming land-use. Widespread use of irrigation is an ever increasing need in the region to sustain productivity. For the same reason, studies of soil water content over a large spatial extent is a prime concern in this region. Only satellite data and modelling approaches can provide such an extensive coverage over spatial domain. To obtain consistent results, however, remotely sensed data and modelled parameters need to be validated based on ground measurements.

Measurements of SM at six sites across the study area (Fig. 5.1) were used as reference. The land-cover (LC) types of these sites were dominantly grass mixed with tree, irrigated crop, urban developed area and barren/fallow land (Fig. 5.2 and Table 5.1).

5.4 Data

Data used in this paper include (*i*) the *in-situ* measurements of SM and rainfall, (*ii*) the remotely sensed LST and (*iii*) albedo products, and (*iv*) the WRF simulations.

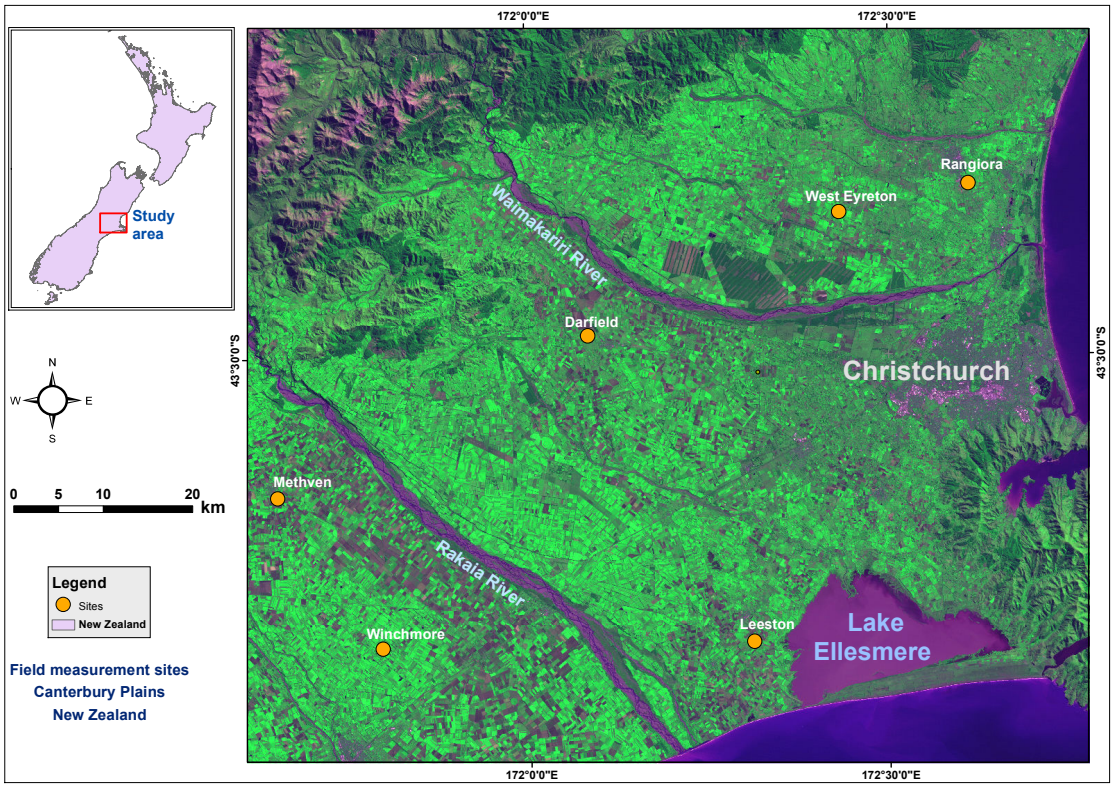

Figure 5.1: *In-situ* soil moisture measurement points overlaid on a false-colour (bands 3,4,1) Landsat image (TM5, 28 March 2011).

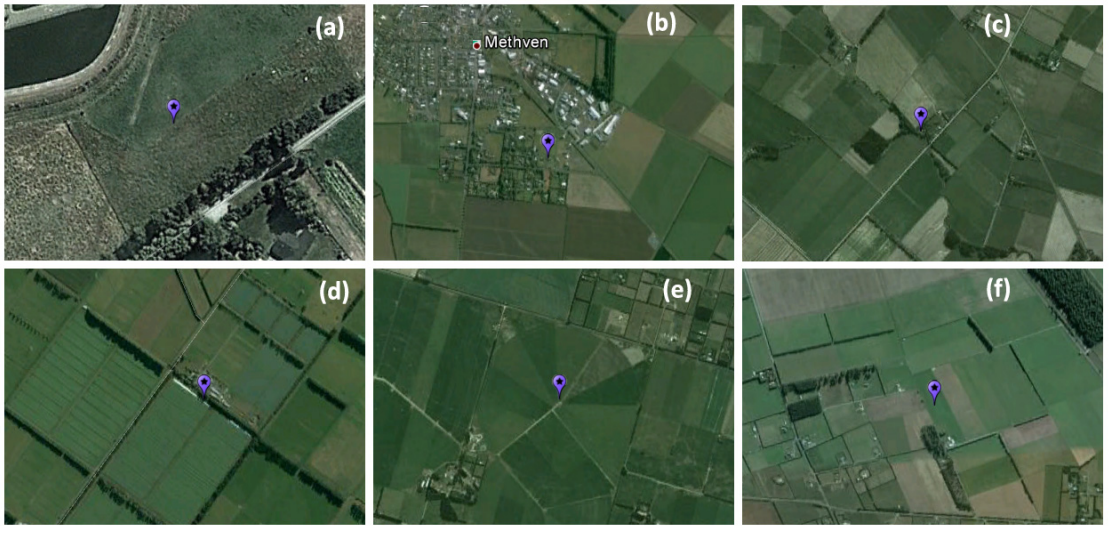

Figure 5.2: Land-cover types of the *in-situ* soil moisture measurement sites at (a) Rangiora, (b) Methven, (c) Leeston, (d) Winchmore, (e) West Eyreton and (f) Darfield (imagery from Google Earth).

Station	Latitude	Longitude	SM_{min}(%)	SM_{max}(%)	Land-cover
Rangiora	-43.3286	172.6110	11	53	Mixed grass & irrigated crop
Methven	-43.6400	171.6521	4	60	Grass mixed with urban
Leeston	-43.7890	172.3116	7	59	Grass mixed with trees
Winchmore	-43.7930	171.7951	1	45	Grass
W.Eyreton	-43.3570	172.4322	11	42	Irrigated grass
Darfield	-43.4800	172.0842	6	59	Grass mixed with barren/fallow

Table 5.1: Geographic coordinates of the *in-situ* soil moisture (SM) and rainfall measurement stations alongside the minimum (SM_{min}) and maximum (SM_{max}) measured SM at each site during the measurement period (three years: Jan. 2010–Dec. 2012), and the dominant land-cover around each site.

(i) In-situ measurements The *in-situ* measurements of SM (20 cm depth) over a period of three years (01-Jan-2010 to 31-Dec-2012) recorded at six automatic stations across the study area (Fig. 5.1) are used in this research. These data were downloaded from the National Climate Database (Cliflo) of New Zealand, which is maintained by the National Institute of Water & Atmospheric Research (NIWA). These data were recorded with hourly rate, but were downgraded to daily rate to match the daily frequency of ATI SM derivations. Daily rainfall data, accumulated over a period of 24 hours, were also downloaded from these stations for the same period to be used in the analysis.

(ii) The MODIS LST product This product is a scientific dataset derived from MODIS thermal observations on-board Terra and Aqua satellites. These observations are collected during day and night overpasses of Terra and Aqua (approximately at 1:30, 10:30, 13:30 and 22:30) with different viewing angles. The LST product is derived from bands 31 and 32, which are observed at 10.78-11.28 μm and 11.77-12.27 μm spectral ranges, respectively. Theoretical background and technical details of the algorithms and the procedure for extraction of LST from MODIS thermal bands is beyond the scope of this paper, but can be accessed in the literature (Wan and Dozier, 1996; Wan, 1999; Wan et al., 2004).

(iii) MODIS combined BRDF/Albedo product Combined albedo product (MCD43B3) is generated from a combination of MODIS-Terra and MODIS-Aqua albedo products (MOD43B3 & MYD43B3) accumulated over a 16-day period. MOD43B3 and MYD43B3 are Level 3 global products with 1 km resolution mapped into Sinusoidal Grid. As a result, MCD43B3 combined albedo product is an 8-daily dataset with the same resolution and geometric specifications (Strahler et al., 1999; BU.edu, 2012) as the two preceding products. This dataset contains two types of albedos: a "black-sky albedo" (BSA), which is the directional-hemispherical reflectance that integrates the

BRDF over the exitance hemisphere for a single irradiance direction, and a "white-sky albedo" (WSA) which is the bi-hemispherical reflectance that integrates the BRDF over all viewing and irradiance directions (Strahler et al., 1996). Data for each of BSA and WSA categories is derived from MODIS bands 1-7. Three more integrated broad-band albedos from the visible (0.3-0.7μm), near-infrared (0.7-3.0μm) and shortwave (0.3-5.0μm) regions (Salomon et al., 2006; BU.edu, 2012) for each of BSA and WSA categories are also provided in this dataset. Broad-band albedo is the ratio of radiant energy scattered upward and away from the surface in all directions to the downwelling irradiance incident upon the surface (Strahler et al., 1996) from all directions. The actual albedo on the ground, or "blue-sky albedo" can be estimated as a sum of black-sky and white-sky albedos weighted by the proportions of direct and diffuse solar radiation arriving at the ground (Salomon et al., 2006). We interpolated both BSA and WSA fields in the 8-daily combined Albedo product to daily values using a linear interpolation function. In the next step, we calculated the blue-sky albedo based on the sum of shortwave broadband BSA and WSA weighted by 0.34 and 0.66, respectively. The advantage of this approach, rather than using a constant value for albedo in ATI calculations (which was practiced by other references (Xue and Cracknell, 1995; Sobrino and El-Kharraz, 1999a)) is taking the seasonal variability of the surface albedo into account.

*(*iv*) WRF simulations* Surface layer SM simulations from the WRF model for a period of four months (31 Jul. till 01 Dec 2010) were used in this paper. We used Noah land surface model (LSM) as land parameterization scheme (Sohrabinia et al., 2012). NOAH LSM is one of multiple land surface schemes coupled with the WRF modelling systemJin et al. (2010). The initial conditions for SM simulations in the model are defined by the National Center for Environmental Prediction (NCEP) global final analysis (FNL) data with a spatial resolution of 1x1 degree (~80x111 km in our study area) and 6-hourly frequency (Hong et al., 2009). The input variables from the NCEP FNL data include (but are not limited to) soil moisture/water content, soil temperature, precipitation, heat flux, humidity, surface winds and land-cover (see `http://rda.ucar.edu/datasets/ds083.2`). The Noah LSM only provides surface heat and moisture fluxes as lower boundary conditions to the coupled atmospheric (i.e., the WRF) model (Chen and Dudhia, 2001b). These fluxes are then transported throughout the boundary layer, and interact with other model physics involving cloud, radiation and precipitation processes (Chen and Dudhia, 2001b). In the Noah LSM, the green vegetation fraction (Fg) parameter, which is defined as the coverage of vegetation over an area-unit or a pixel (Hong et al., 2009), is used to differentiate

moisture flux from vegetation. As a result, the WRF model coupled with the Noah LSM is able to separate soil and vegetation moisture fluxes and also accounts for precipitation effects in SM approximation. To calculate SM, a prognostic diffusion equation for the volumetric SM content is used (Chen and Dudhia, 2001a). Sensitivity of the WRF model to different land surface parameterization schemes, such as the Noah LSM, is discussed in the literature (Hong et al., 2009; Jin et al., 2010), which includes SM simulations. Noah LSM simulates the near-surface SM in four pre-defined layers (from top to down: 0.05, 0.25, 0.70 and 1.5 m depth). Outputs for the top-most layer (5 cm depth) were used in our analysis. The first 24 hours of the simulations were discarded from the analysis as the spin-up period required by the model to reach a balanced state with the boundary conditions. Grid spacing of the simulations was set to 5 km for the first and 1 km for the second domain of the model to match the spatial resolution of the MODIS LST. Time interval of the model outputs was set to 30-minute rate for all simulations.

5.5 Methods

5.5.1 Thermal inertia approach for SM estimation

Thermal inertia (TI), defined as the resistance of a material to change in temperature (Chang et al., 2012), is calculated based on the knowledge of thermal conductivity and density of the near-surface soil layer (Eq. 5.1),

$$\mathrm{TI} = \sqrt{\Lambda \rho C} \tag{5.1}$$

where TI (J m^{-2} K^{-1} sec$^{-1/2}$) is thermal inertia of the soil, Λ (W m^{-1} K^{-1}) is the soil thermal conductivity, ρ (kg m^{-3}) is the soil bulk density, and C (J kg^{-1} K^{-1}) is the soil heat capacity (Pratt and Ellyett, 1979; Wang and Qu, 2009; Minacapilli et al., 2009). Water bodies have a higher TI than dry soils and rocks, and exhibit a lower diurnal temperature amplitude (DTA), therefore, when soil water content increases, DTA of soil will decrease (Verstraeten et al., 2006). This property can be exploited to derive the amount of moisture content in the upper soil from remotely sensed LST. The apparent thermal inertia (ATI) method based on two or more daily LST observations and one daily albedo data, along with a priori knowledge about the acquisition date and the geographic latitude, is used to derive the near-surface SM from remotely sensed observations (Eq. 5.2). ATI is defined as (Verstraeten et al., 2006; Wang and Qu, 2009; Vandoninck et al., 2011; Chang et al., 2012),

$$\mathrm{ATI} = S\frac{1-\alpha_0}{\mathrm{DTA}} \tag{5.2}$$

where α_0 is the broadband albedo, DTA is derived from two or more daily LST observations and S is the solar correction factor defined as,

$$S = sin\vartheta sin\varphi\left(1 - tan^2\vartheta tan^2\varphi\right) + cos\vartheta cos\varphi arccos\left(-tan\vartheta tan\varphi\right) \tag{5.3}$$

where ϑ is the local latitude and φ is the solar declination, which is calculated for each day of the year (Vandoninck et al., 2011).

If only two observations representing coolest and warmest LST values over a 24-hour period are used, DTA will be simply the difference between the diurnal warm and cool temperatures ($\Delta\mathrm{LST}$), defined as (Verstraeten et al., 2006; Chang et al., 2012),

$$\mathrm{DTA}_1 = \mathrm{LST}_{day} - \mathrm{LST}_{night} \tag{5.4}$$

where LST_{day} and LST_{night} are daily LST at peak warm and cool hours, respectively. LST observations from MODIS-Aqua with approximate overpass times at 1:30 am and pm (representing LST_{night} and LST_{day}) have been often used in the literature to calculate DTA (Verstraeten et al., 2006). MODIS-Terra observations with approximate overpass times at 10:30 am and pm (representing LST_{day} and LST_{night}, respectively) were also used by others (Chang et al., 2012).

A second method to calculate DTA is to apply four LST values from a combination of daily MODIS-Terra and MODIS-Aqua observationsVandoninck et al. (2011),

$$\mathrm{DTA}_2 = 2\left(\frac{n\sum_{i=1}^{n} cos(\omega t_i - \psi)T_i - \sum_{i=1}^{n} cos(\omega t_i - \psi)\sum_{i=1}^{n} T_i}{n\sum_{i=1}^{n} cos^2(\omega t_i - \psi) - \left(\sum_{i=1}^{n} cos(\omega t_i - \psi)\right)^2}\right)$$

$$\psi = arctan(\xi) + \pi$$

$$\xi = \frac{(T_1 - T_3)(cos(\omega t_2) - cos(\omega t_4)) - (T_2 - T_4)(cos(\omega t_1) - cos(\omega t_3))}{(T_2 - T_4)(sin(\omega t_1) - sin(\omega t_3)) - (T_1 - T_3)(sin(\omega t_2) - sin(\omega t_4)} \tag{5.5}$$

In Eq. 5.5, $n = 4$ for four MODIS daily observations, $\omega = 2\pi/(24 * 60 * 60)$ rad s^{-1} is the angular velocity of the Earth's rotation, t_i [i = 1, ..., 4] is the overpass time, T_i is the surface temperature (*i.e.*, LST) at each overpass time and ψ is the phase angle.

The near-surface SM can be then calculated from the ATI values for every pixel (Verstraeten et al., 2006) after checking for possible outliers. After calculation of ATI,

Verstraeten et al. (2006) used the minimum and maximum ATI values over each pixel over time (t) to calculate the remotely sensed topsoil saturation index (SMSI_{RS}) using Eq. 5.6:

$$\mathrm{SMSI}_{RS}(t) = \frac{\mathrm{ATI}(t) - \mathrm{ATI}_{min}}{\mathrm{ATI}_{max} - \mathrm{ATI}_{min}} \tag{5.6}$$

where $\mathrm{ATI}(t)$ is the ATI value at time t, ATI_{min} is the minimum and ATI_{max} is the maximum ATI values in the entire time-series of the pixel under analysis.

Finally, Verstraeten et al. (2006) derived volumetric soil moisture content (SMC) based on the SMSI_{RS} values,

$$\mathrm{SMC}(t) = \mathrm{SMSI}_{RS}(t).(\mathrm{SM}_{sat} - \mathrm{SM}_{res}) + \mathrm{SM}_{res} \tag{5.7}$$

where t is time, SM_{res} is the residual volumetric SMC and SM_{sat} is the saturation volumetric SMC. Since SM_{res} and SM_{sat} can only be determined under laboratory conditions, field measurements are unlikely to be equal to extremely high or low laboratory values (Verstraeten et al., 2006). For the same reason, SM_{res} and SM_{sat} in practice are substituted by the minimum (SM_{min}) and maximum (SM_{max}) *in-situ* measurements of SM over the entire period, respectively (Table 5.1).

In this paper, ATI (Eq. 5.2) was calculated with two different approaches: ATI1 using Eq. 5.4 and ATI2 using Eq. 5.5, each of which take a different solution to estimate DTA. In the next step, Eq. 5.6 is used to derive SMSI_{RS} at each site. Finally, we scaled SMSI_{RS} values to the respective SM_{min} and SM_{max} measurements at each site using Eq. 5.7 for a better comparison.

5.5.2 *Multi-temporal time-series analysis of SM from ATI method*

The analysis was conducted in two temporal scales: short-term (four months: 01 Aug. to 01 Dec. 2010) and long-term (three years: 01 Jan. 2010 to 31 Dec. 2012). The first time-scale was chosen to identify the effects of rainfall on ATI SM retrievals, as well as the WRF SM simulations, and to evaluate the difference in seasonal trends in comparison to the *in-situ* measurements. Also, since model simulations of SM with 1 km spatial resolution is time consuming and memory intensive (especially when the time period is longer than a few months), the analysis involving the WRF model was conducted only for the short-term period. The long-term analysis was necessary to evaluate the quality of ATI SM retrievals in different seasons and to find out which ATI function is more able to detect seasonal variability of SM.

5.5.3 Statistical methods

Euclidean distance (d_E) was applied to compare the difference between time-series of SM from ATI functions with the *in-situ* measurements (Eq. 5.8).

$$d_E(ts_1, ts_2) = \sqrt{\sum_{i=1}^{n} (ts_1(i) - ts_2(i))^2} \tag{5.8}$$

where ts_1 and ts_2 are two time-series to be compared (e.g., ATI1 and *in-situ* SM series) and n is the total number of coincident time-points in both series. If ts_1 has less points than ts_2, the extra points in ts_2 (which are not coincident with any point in ts_1) will be excluded from the analysis.

Pearson's correlation coefficient, ρ, is used to express the absolute relationship between any two parameters, without an attempt to predict the future. The value of ρ and d_E averaged over all sites ($\bar{\rho}$ and $\bar{d_E}$, respectively) are also used to express the overall results in the study area. Cross-correlation function (CCF), expressed as Eq. 5.9, is used to find the approximate time-lag between the ATI derivations and the *in-situ* measurements.

$$\mathrm{CCF} = \frac{1}{n} \sum_{t=1}^{n-k} (x_t - \bar{x})(y_{t+k} - \bar{y}) \qquad [k = 0, 1, ..., (n-1)] \tag{5.9}$$

where n is the total number of coincident observations in both series, t is time, k is lag, $\bar{x}$ and $\bar{y}$ are the mean values of x and y input series, respectively (Zhang and Wu, 2006).

5.6 Results

5.6.1 Short-term series: ATI results vs. WRF and in-situ SM

Derived SM from the MODIS LST using ATI method was compared with the *in-situ* and modeled SM at six test-sites for a period of four months (Aug. to Nov. 2010). The accuracy of the WRF simulations is analysed to find out if these simulations can be used to compensate the gaps in ATI derivations. Comparison between the *in-situ* data collected from a singular point in space with the MODIS pixels (or the model's grid-cells) was a major concern. The issue of pixel size versus point measurements, which is already dealt with in the literature (Jackson et al., 2010; Qin et al., 2013), is a well-known problem when it comes to define the relationship between the *in-situ* and remotely sensed gridded datasets. This issue can be partly resolved through

careful selection of the measurement point closest to the pixel centre over a large, flat and homogeneous land area. Although all of our test-sites were located on flat and relatively homogeneous landscape, the *in-situ* SM measurements only represented a fraction of the overlapping pixel or grid from the other two (i.e., ATI and WRF SM) datasets. As a result, a certain level of variation inside each pixel was inevitable. For this reason, a lower agreement between point measurements and gridded data is likely when a 1:1 correlation is applied. Therefore, more emphasis in the results will be given to the temporal profiles, and the correlation coefficient (ρ) values will be given only to provide a quantitative measure of the agreement between the two variables. ρ values were calculated between derived SM (using both ATI1 and ATI2), the WRF simulations and the *in-situ* measurements (Table. 5.2). For most of the sites, ρ values between the WRF and the *in-situ* data have been positive and relatively higher than the ATI SM retrievals. Overall, ATI1 and ATI2 have correlated almost similarly with the *in-situ* measurements.

	ρ			d_E		
Station	ATI1	ATI2	WRF	ATI1	ATI2	WRF
Rangiora	.75	.69	.78	101	69	95
Methven	.78	.74	.82	98	35	75
Leeston	.39	.50	.81	51	45	59
Winchmore	.67	.68	.87	86	35	69
West Eyreton	.57	.62	.80	72	50	70
Darfield	.58	.54	.77	83	26	93

Table 5.2: Correlation coefficient (ρ) and Euclidean Distance (d_E) values between daily soil moisture time-series derived from the MODIS LST (using ATI1 and ATI2) and simulated by the WRF model in one hand and the *in-situ* measurement on the other over the short-term period (Aug. to Nov. 2010).

Although these correlations showed almost similar results, temporal profiles of ATI1 and ATI2 SM retrievals needed to be compared to find out which approach presents a closer trend to the *in-situ* measurements and the WRF simulations. Therefore, temporal profiles of SM derived from both functions, simulated by the WRF model and measured on the ground were overlaid on daily rainfall data (Fig. 5.3). The WRF simulations have shown a close matching with the *in-situ* measurements, and rainfall effects are detected. The declining seasonal trend in SM amount, as observed on the *in-situ* profile, is also detected by the model but is less pronounced. Since ATI1 uses only two MODIS LST observations, there were more points possible to be calculated by this function. On the other hand, ATI2 needs four MODIS LST observations per day, thus, fewer points were possible to be modelled by this function. This is the reason

that at some sites ATI2 has shown weaker correlation (Table. 5.2). However, it appears that ATI2 profile is closer to the *in-situ* measurements than ATI1. Additionally, the declining seasonal trend is detected by the ATI2 function but not by ATI1.

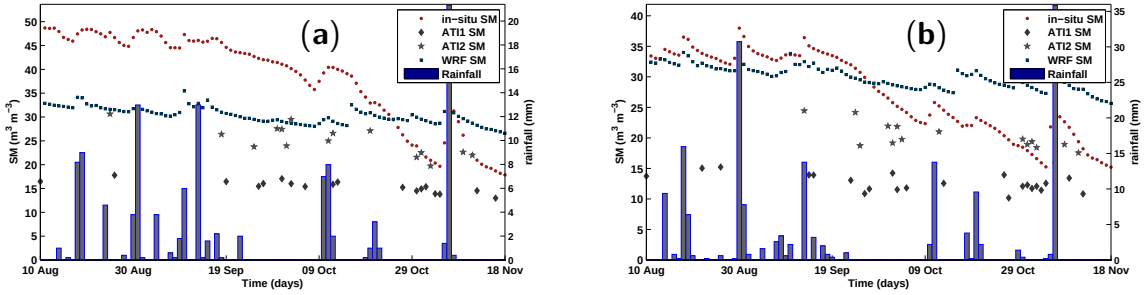

Figure 5.3: Time-series of soil moisture (SM) derived by ATI functions, simulated by the WRF model and recorded by the *in-situ* measurements at (a) Rangiora and (b) Winchmore sites for the short-term analysis (four months: Aug. to Nov. 2010).

There are more points in the later part of the analysed period both in ATI1 and ATI2 time-series. This is due to the higher number of cloudy days in winter than later spring. On the other hand, the model simulations have shown a larger offset with the *in-situ* measurements during the later part of the analysed period. These results show that the ATI method is more useful in less cloudy and warm season, unlike the WRF model, which performs better in colder and wet season of the year. However, a longer period of analysis is required to confirm this finding, which is presented in the next section.

5.6.2 *Long-term analysis: ATI results vs.* in-situ *SM*

The two ATI calculation functions, ATI1 and ATI2, were applied to derive the near-surface SM from the MODIS LST product for a period of three years (01 Jan. 2010 till 31 Dec. 2012). Unlike the short-term analysis, this section will focus only on ATI SM derivations in comparison with the *in-situ* measurements and rainfall data.

Correlations between ATI1, ATI2 and the *in-situ* SM time-series at six sites were calculated (Table. 5.3). Because the *in-situ* measurements were made at 20 cm depth below the surface, time-lags were applied on these measurement before correlating with the derived SM time-series. To discover the best time-lag, the two time-series (i.e, *in-situ* measurements vs. ATI1 or ATI2 SM) were cross-correlated with different time-lags where every step in the lags was equal to one day. The best agreement on most sites achieved when a time-lag of one-day was applied on the *in-situ* measurements. In other words, derived SM from the instantaneously observed LST data agreed best with the *in-situ* SM measured (at 20 cm depth) one day later. The slope of change

in correlations due to time-lags, however, was very gradual with changes of less than 0.03 in ρ values. Thus, the actual time-lag may have been slightly more or less than one day, which could be identified if data with a finer temporal resolution (such as hourly data) was available. However, retrieval of SM from the MODIS LST using ATI method was only possible in a daily basis. Results showed that the correlations from both functions are relatively similar, however, ATI2 provided a better agreement with the *in-situ* measurements at more sites (Table. 5.3).

	ρ		d_E		ME (summer)		ME (winter)	
Station	ATI1	ATI2	ATI1	ATI2	ATI1	ATI2	ATI1	ATI2
Rangiora	0.77	0.76	368	213	-6	-1	-29	-21
Methven	0.67	0.78	251	119	-6	4	-21	-13
Leeston	0.42	0.51	145	82	-1	8	-18	-12
Winchmore	0.69	0.76	274	140	-7	-1	-21	-15
W.Eyreton	0.63	0.66	109	55	-2	5	-15	-10
Darfield	0.57	0.52	276	145	-5	4	-21	-14

Table 5.3: Correlation coefficient (ρ), Euclidean Distance (d_E) and Mean Error (ME) values between time-series of soil moisture derived from the MODIS LST (using ATI1 and ATI2 functions) and measured on the ground at six sites for a period of three years (2010–2012).

As discussed before, although these correlations offer a quantitative measure of how both functions relate to the *in-situ* measurements, they do not provide information about temporal trends of the derived SM with respect to the ground measurements. Therefore, temporal profiles of the derived SM time-series at all sites were compared with the *in-situ* measurements and overlaid on rainfall data. The results from only two sites, Rangioran and Winchmore, are provided (Fig. 5.4). The most striking difference between ATI1 and ATI2 SM retrievals, as shown in the long-term series (Fig. 5.4), is that the latter has detected the annual SM trends better than ATI1. As found in the short-term analysis, both functions have shown a better performance in dry season. The overall bias from the *in-situ* measurements was higher during winter compared to summer. To show this quantitatively, SM time-series from both functions were separated based on winter and summer seasons and then were subtracted by the corresponding *in-situ* measurements at each site. The mean error (ME) values at each site for both seasons were then calculated (Table. 5.3). These values showed that in summer, both functions have a small bias from the *in-situ* measurements. The ME values from the *in-situ* measurements during wet season were considerably higher, especially in ATI1 results (Table. 5.3). Although rainfall effects are not clearly distinguished in this temporal scale, sudden spikes in ATI2 SM are suspected to be due

to rainfall. On the other hand, ATI1 series showed relatively smooth temporal trend with only a few sudden spikes, also suspected to be due to rainfall.

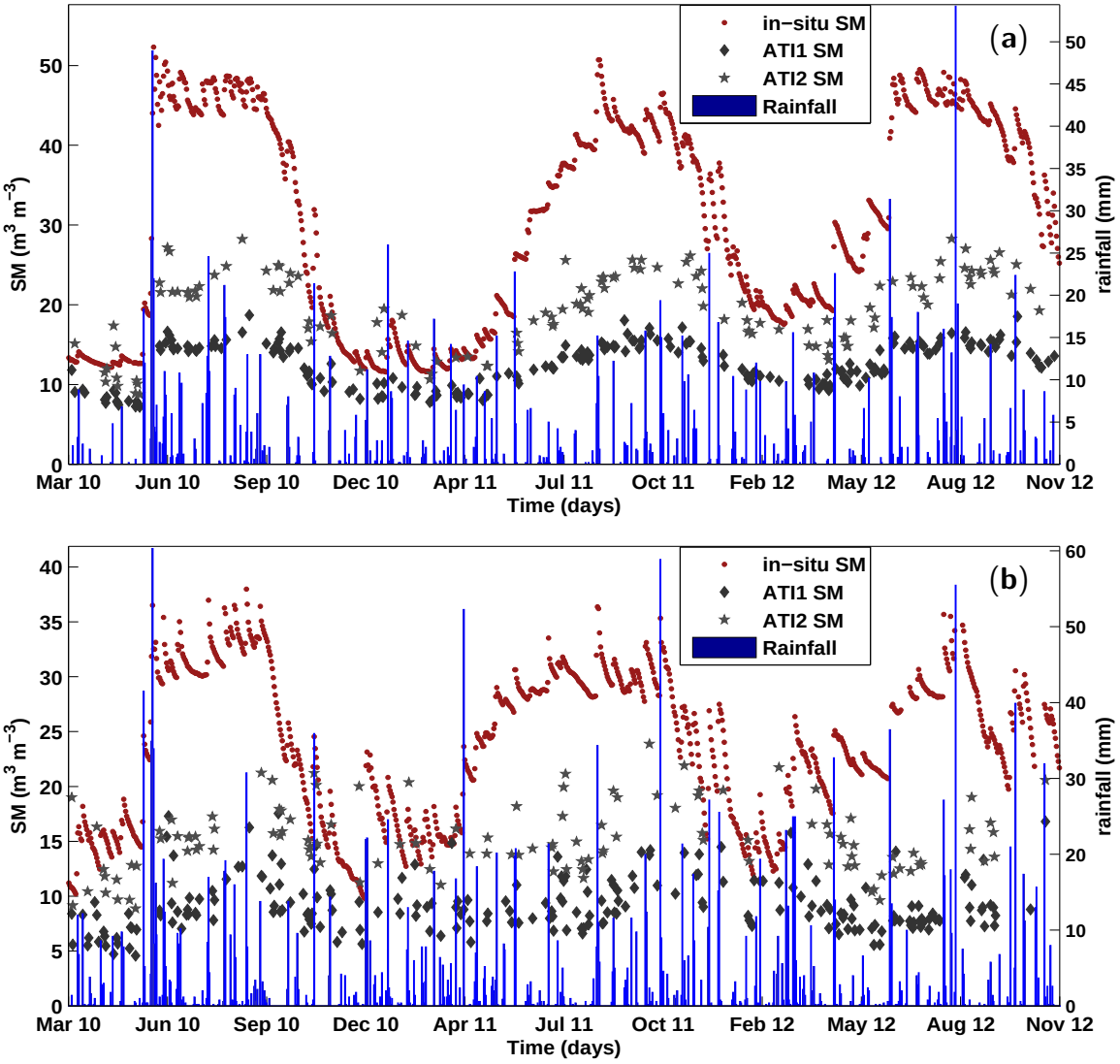

Figure 5.4: Temporal profiles of ATI1 and ATI2 compared with the *in-situ* soil moisture (SM) and overlaid on daily rainfall at (a) Rangiora and (b) Winchmore sites for a period of three years (2010–2012).

Another difference between ATI1 and ATI2 SM retrievals was the long-term offset between the two and the *in-situ* measurements. Although ATI2 temporal trend overlaps the *in-situ* series at summer, both functions have shown a negative offset from the *in-situ* measurements for most of the three years period. To show this quantitatively, d_E was applied. Time-series of SM from ATI1 showed larger difference with the *in-situ* time-series than ATI2 at all sites (Table 5.3). It must be mentioned, however, that these d_E values were calculated based on the absolute SM amount (m^3 m^{-3}) for the whole period, therefore, the one time-series which had more points tends to show more difference. As mentioned before, ATI2 had less points (due to the need for four daily

LST observations) than ATI1 (which only needed two daily LST values). Therefore, larger difference from ATI1 was partly due to more data points it its series. Since the ATI2 function uses both MODIS-Aqua and MODIS-Terra daily LST values, the DTA employed by this function contains more details. As a result, temporal profile of SM derivations from this function is able to provide more details about SM variability in the long-term. On the other hand, since four LST observations are required by ATI2, any missing LST has resulted with no SM retrieval for that day. This effect has been less severe on ATI1 as the possibility of having two cloudless LST per day is higher than four.

We also noticed that the prominent spikes due to rainfall events in ATI series (especially ATI2) have occurred with a slight lag after the rainfall events. This was also shown in the correlations above (Table. 5.3), where the best agreements were achieved when a time-lag of one-day was added to the *in-situ* SM measurements. It indicates that changes in LST due to rainfall, as colder temperatures and smaller diurnal amplitudes, have been recorded by MODIS shortly after rainy days. Any changes in LST during the actual rain events (as a result of higher soil water content) is not available in the LST dataset due to cloud effects. As mentioned above, one way to fill these gaps in ATI SM time-series is to use the model simulations.

5.7 Discussion

Our results showed that the agreement between the *in-situ* measurements at some sites, such as Leeston and Darfield, and the ATI SM retrievals was relatively poor in both short-term and long-term analysis. Leeston site was close to Lake Ellesmere. Thus, it is suspected that the MODIS LST data over this site has been affected by water. This can be partly due to a spatial mis-match between the actual LST pixel overlying on this site and the neighbouring pixels over the lake. However, geometric mis-matching in the MODIS LST grid had been already checked by overlaying this dataset on other spatial data from the study area (such as coastal boundaries and rivers) in a GIS (Geographic Information Systems) environment (Fig. 5.5). Proximity to mountains or local effects (such as irrigation) can be the reasons for the poor correlations from Darfield site. Irrigation is practiced widely during summer to keep the grass growing in the farmlands across the study area. Irrigation effects may have caused higher SM in ATI estimations at those sites for summer season, which can reduce the overall agreement with the ground measurements. Similarly, irrigation can cause anomalies in the *in-situ* data if the measurement site is not well located. It can cause significant divergence from the normal SM trend over a localized small area, which is

not necessarily captured by the satellite observations or computed by the WRF model. Since the *in-situ* measurements were acquired from an already existing online database (Sec. 5.4), it was not possible for the authors to make sure that the measurements were not affected by irrigation. However, a quality check of the SM measurements based on rainfall data demonstrated that there was no external anomalies in the data except for the effects of rainfall. This can be checked in figures 5.3 and 5.4, where the only reasons for changes in SM appears to be due to rainfall and seasonal temperature variations.

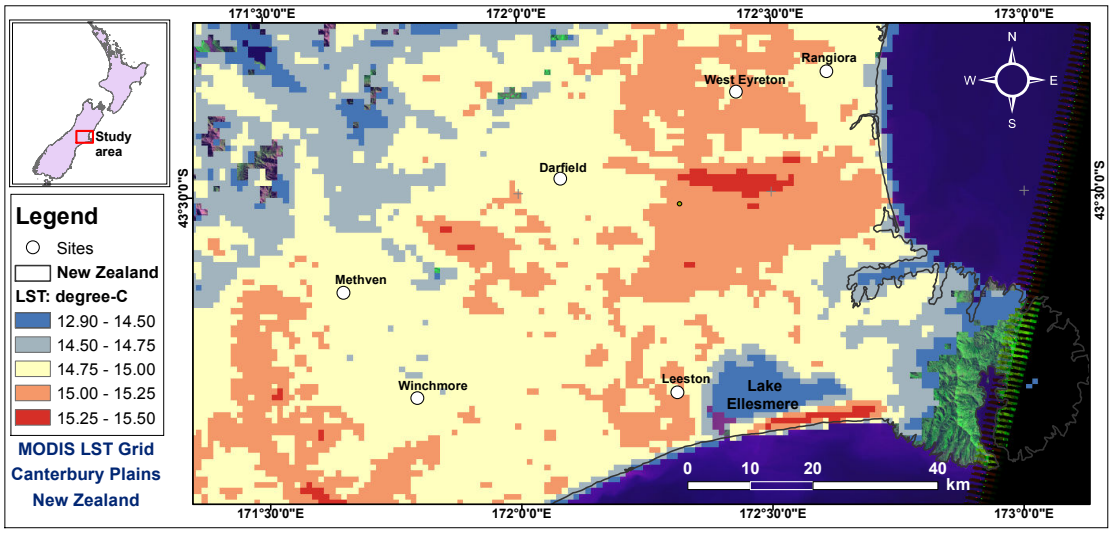

Figure 5.5: Spatial matching between the MODIS LST grid and the coastal boundaries of the study area. Variations of LST over land and lake is also clear on this map.

The results also showed that the WRF model has agreed well with the *in-situ* measurements. Although this analysis was only conducted in the short-term period, these high correlations indicate that the WRF model can be relied also for a longer period. As explained in the paper, the initial conditions for the WRF coupled with the Noah LSM is based on the NCEP reanalysis data. The reanalysis data are produced operationally every six hours by NCEP with 40 km spatial resolution (Hong et al., 2009) based on the upper-air and surface observational data collected from the measurements in the local weather stations via the Global Telecommunications System (GTS). The model also combines land surface parameters, such as the surface LC and vegetation fraction (Hong et al., 2009) to produce simulations. As a result, the ability of the model to incorporate observational data in the land surface parameterization schemes can be the reason for a good agreement with the ground measurements. However, there are two main drawbacks for a modelling system as opposed to a remotely sensed approach. First, the spatial resolution of the model is limited and the uncertainties increase when downscaling to a very fine resolution ($\leqslant$1 km) is required. The second limitation is

	Short-term			Long-term	
Parameter	ATI1	ATI2	WRF	ATI1	ATI2
$\bar{\rho}$	.62	.63	.81	.63	.66
$\bar{d_E}$	82	43	77	237	126
$\bar{\text{ME}}$ (summer)	—	—	—	-4	3
$\bar{\text{ME}}$ (winter)	—	—	—	-21	-14

Table 5.4: Summary table to compare the performance of ATI1 and ATI2 functions for soil moisture derivation from the MODIS LST observations. The mean correlation coefficient ($\bar{\rho}$) and Euclidean Distance ($\bar{d_E}$) values provided in this table are averages of the results from six test-sites.

the computation time and cost for model simulations, whereas, the satellite data are readily available. The WRF model coupled with the Noah LSM, therefore, can be a complementary solution to fill the gaps in SM retrievals from the MODIS LST data.

Although a simple 1:1 correlation helped us to find out which function offers a higher agreement with the *in-situ* SM measurements, comparison of ATI1 and ATI2 temporal profiles enabled us to figure out which function is better able to detect seasonal trends and rainfall effects. Temporal profiles also assisted us with the interpretation of the declining seasonal trend and rainfall effects in the WRF simulations. Overall, the ATI2 retrievals showed a better agreement with the *in-situ* measurements and rainfall events than the ATI1 outputs (Table 5.4). This indicates that using four daily LST from MODIS presents a better approximation of SM rather than two (a minimum and a maximum) LST used by ATI1. This is because more often LST observations enables mapping TI of the surface and interpretation of day–night temperature difference (Price, 1980). However, the drawback of using four daily LST observations is that more uncertainty due to the satellite ground-track variations is introduced into the ATI model. Additionally, using four LST observations in ATI2 results in more missing SM retrievals as opposed to ATI1 which needs only two daily LST values.

The lower correlations at some sites (Leeston and Darfield) and the missing SM values revealed that a remotely sensed approach for SM retrieval is limited to favorable weather conditions and suitable LC types. As the results showed, the accuracy of SM retrievals deteriorate over water, dense vegetation and rugged terrain. Sensitivity of LST to SM differs for the canopy and the soil surface beneath the plants, and is much greater for bare soil than for canopies (Mallick et al., 2009). As a result, the accuracy of the ATI algorithm diminishes over dense vegetation. The retrievals are not possible under cloudy conditions. These limitations indicate that a remotely sensed method for SM retrieval can work only in regions with favorable conditions. Such method, therefore, is not suitable for parts of New Zealand that have dense vegetation and

rugged topography.

5.8 Conclusion

Soil moisture derived from remotely sensed LST, simulated by a numerical model and measured on the ground was analysed in this paper. The objective of the analysis was to understand the potential of the MODIS LST dataset for soil moisture retrieval using ATI method and to compare the accuracy of two ATI functions based on the ground measurements. A land-atmospheric coupled model was also evaluated for potential gap filling of ATI soil moisture retrievals.

Both ATI functions showed almost similar results in the short-term (four months) period but the overall correlation between ATI2 time-series and the *in-situ* measurements was slightly higher ($\bar{\rho} = 0.63$) than ATI1 ($\bar{\rho} = 0.62$). At some sites (such as Leeston), both functions showed relatively poor correlations. It was discussed that the poor results at those sites were due to the effects of the nearby water bodies or mountains. The WRF simulations, on the other hand, showed relatively strong correlations at all sites ($\bar{\rho} = 0.81$). The model simulations also agreed well with the *in-situ* measurements in detection of rainfall effects and the general seasonal trend. Over the long-term (three years), ATI2 showed slightly higher correlation ($\bar{\rho} = 0.66$) than ATI1 ($\bar{\rho} = 0.63$). Temporal profiles of the two functions showed a considerable offset from the *in-situ* time-series in the long-term, however, the overall bias in ATI2 retrievals was lower ($\bar{d_E} = 126$) than ATI1 ($\bar{d_E} = 237$), partly due to the lesser points in its series. To break down this overall bias into seasons, ME values during summer and winter for all sites were calculated. Both functions showed small biases from the *in-situ* measurements in summer ($\sim$5 m^3 m^{-3}), but considerably larger biases in winter with a slightly better result from ATI2 ($\bar{\mathrm{ME}}$ = -14 m^3 m^{-3}) compared to ATI1 ($\bar{\mathrm{ME}}$ = -14 m^3 m^{-3}). ATI2 temporal profile was able to detect seasonal variations of SM better than ATI1. It was discussed that this is due to the more detailed DTA employed by ATI2 compared to the simple DTA of ATI1.

Results of this research indicate that the ATI2 function is more suitable for SM derivations in the study area. Since the MODIS LST product is available for more than ten years and the mission is still continued, long-term series of SM can be derived using the ATI2 function. Considering the well performance of the WRF model, the gaps due to cloud cover in ATI retrievals can be filled by the model simulations.

Acknowledgments

This research is conducted under funding and support of the University of Canterbury in New Zealand. The authors would like to thank Justin Harrison for his help in the field experiment that was conducted for this research. We also acknowledge Graeme Plank from the Physics Department for providing us climate data, as well as permission for setting up our instrument in the Birdlings Flat site. Language editions and proof reading of the paper was done by Caroline Cameron-Blackgrove. We greatly appreciate very useful comments from two anonymous reviewers which helped us in presentation and discussion of our findings. Free access to NASA's MODIS LST and MODIS BRDF/Albedo datasets is also appreciated; we used Reverb tool to download these datasets.

Chapter 6

Adjusting AMSR-E soil moisture using the MODIS LST

6.1 Preface

As the last objective of this research, this chapter attempts to apply the MODIS LST with a higher spatial resolution for adjustment of the AMSR-E SM product in temporal and spatial domain.

Results from the previous chapter showed that the MODIS LST can be used to derive the near surface SM with a reasonably good quality as it was compared with the *in-situ* measurements and the WRF model simulations. It was also shown that using four LST observations per day, as opposed to only two minimum and maximum LST values, gives a better approximation of the nears-surface SM. These results indicate that the diurnal profiles of LST and SM are inversely related. This is an important finding which can be applied to improve the quality of other remotely sensed SM data with lower spatial resolution over the study area. With respect to the above findings, the MODIS LST with 1 km spatial resolution is applied in this chapter to adjust temporal and spatial profiles of AMSR-E SM product, which has a lower spatial resolution of 25 km. Quality of this passive MW SM product will be assessed based on the WRF model simulations and rainfall data before and after adjustment. Results of this chapter are expected to answer the question of whether a linear combination of inverted LST can improve AMSR-E passive MW SM temporally and spatially over the study area with a low to dense vegetation.

NOTE:

This chapter is prepared as a paper to be submitted for publication under the title:

Spatio-temporal adjustment of AMSR-E soil moisture using the MODIS LST in New Zealand

M. Sohrabinia, W. Rack, P. Zawar-Reza

Abstract. The near-surface soil moisture (SM) observed from remote sensing satellites is an important source of data to study the spatial heterogeneity of SM over a large area, which cannot be captured at the same scale from point measurements. A novel approach is presented to adjust SM profiles from the standard NASA SM product derived from the observations of the Advanced Microwave Scanning Radiometer for the Earth Observing System (AMSR-E) over the South Island of New Zealand. *In-situ* measurements in a test-site in the Canterbury Plains and the Weather Research and Forecasting (WRF) model simulations were also used in this study. We used rainfall data to analyse the effect of precipitation on AMSR-E SM time-series. Quality of the WRF simulations was first assessed based on the *in-situ* SM measurements for a limited period. Afterwards, the WRF simulations were compared with AMSR-E SM time-series. Rainfall effects were detected in most of the cases by the WRF model and, after a careful inspection, by the AMSR-E product. However, AMSR-E time-series showed 0.15 m^3 m^{-3} difference in volumetric SM when it was compared with the WRF simulations. Therefore, we used land surface temperature (LST) data from the Moderate Resolution Imaging Spectroradiometer (MODIS) to adjust AMSR-E SM in the spatial and time domain. SM has a strong effect on LST via its influence on emissivity and through the cooling effect which influences the partition of the surface heat fluxes. Seasonal trends were more prominent in the adjusted AMSR-E SM series with a better agreement with rainfall events. Similarly, more detail in the spatial variability of SM from lower flat plains to higher altitudes was found in the adjusted SM grids, which were obscured in the original AMSR-E product.

Keywords. near-surface soil moisture, AMSR-E, MODIS LST, WRF, time-series, spatial domain.

6.2 Introduction

The near surface soil moisture (SM) is an important factor which impacts the exchange of energy and water between land and atmosphere (Shi et al., 2010; Hain et al., 2011; Chang et al., 2012). Defined as the water content of the upper soil (Wang and Qu,

2009), the near surface SM can be interpreted from remotely sensed data which are observed by satellites using the electromagnetic radiation in the visible and near-infrared (VNIR), thermal infrared (TIR), and the microwave (MW) regions (Njoku et al., 2003; Moran et al., 2004; Verstraeten et al., 2006; Hain et al., 2011).

Passive MW remote sensing instruments are able to collect repetitive and large area observations of the near-surface SM (Jackson et al., 1996). The algorithms for SM retrieval based on MW data rely on the dielectric properties of the soil and water (Jackson et al., 1996), which provides a strong response in MW emissivity to variations in soil water content (Hain et al., 2011). The advantage of MW sensors is that the observations are largely unaffected by cloud cover (Njoku and Entekhabi, 1996), which enables more frequent data acquisition. Since the MW instruments operating at longer wavelengths (0.01 – 0.30 m) have fewer problems with the atmosphere and vegetation, they can sense a deeper soil layer and maximize soil moisture sensitivity (Jackson et al., 1996). However, MW sensors offer coarse spatial resolution and reduced SM retrieval ability over moderate to dense vegetation, whereas, TIR observations can provide SM information under vegetation cover and at significantly higher spatial resolution (Hain et al., 2011).

The Advanced Microwave Scanning Radiometer for the Earth Observing System (AMSR-E) is a passive sensor onboard Aqua satellite which measures MW energy radiated from the earth's surface (Yu et al., 2009). The near-surface SM is one of key variables derived from AMSR-E X-band (10.7 GHz) observations as a global land product (Reichle et al., 2007; Njoku, 2008). This dataset is the most extensively validated SM retrieval product derived from passive MW satellite observations (Hain et al., 2011), however, the majority of these validation campaigns have been conducted in the US (Jackson et al., 2010) and the other parts of the world (Choi and Hur, 2012; Gruhier et al., 2008; Zhang et al., 2011b) but none is available in New Zealand. A key issue in the validation of SM products is the disparity in spatial scales between satellite and *in-situ* observations (Jackson et al., 2010). This disparity can be minimized when another grid dataset matching with satellite pixels, such as model simulations, are applied as reference data. Other issues include replication of temporal and spatial variability of SM, heterogeneity of the satellite footprint and variations in footprint size (Jackson et al., 2010). Due to coarse resolution of MW data, SM derivations from these observations include some errors, such as inaccurate evaluations of soil type, surface roughness and vegetation coverage (Shi et al., 2010). Considerable differences between *in-situ* measurements and AMSR-E SM were reported in the literature (-0.10 to -0.17 m^3 m^{-3} bias), which were assumed to be due (in part) to the differences in depth and spatial scaling between point measurements and the AMSR-E gridded

dataset (Choi and Hur, 2012). Other resources, on the other hand, have reported correlations of greater than 0.80 with ground-based data and a strong correspondence with rainfall only after locally normalizing the AMSR-E series to match the mean and variance of the *in-situ* measurements (Draper et al., 2009). The ambiguity in these results can be partly due to the difference in the quality of AMSR-E data over different geographical locations with varying vegetation cover. This is shown in the literature by comparison of the AMSR-E SM derived from different algorithms where each algorithm has performed differently at each site (Jackson et al., 2010). Their results showed that the spatial and temporal variability of SM, the large footprint size and particularly vegetation pose significant problems in AMSR-E SM product. To reduce these anomalies, some resources have combined other data sources, such as rainfall and *in-situ* SM data (Draper et al., 2009), an alternative satellite data[1] (Reichle et al., 2007), the MODIS LST dataset (Kim and Hogue, 2012) or a combination of different SM products from the same sensor (Jackson et al., 2010). The MODIS LST also has been used to improve the spatial resolution or so called 'disaggregation' of other lower resolution datasets such as Soil Moisture and Ocean Salinity (SMOS) L-band SM product (Merlin et al., 2008, 2013). Hain et al. (2011) studied the relationship between SM products from AMSR-E passive MW observations, TIR satellite data and Noah land surface model (LSM) simulations. They suggested filling the gaps in AMSR-E MW data with supplementary information from higher resolution TIR data. In this research, we attempt to use the land surface temperature (LST) product with 1 km resolution from the Moderate Resolution Imaging Spectroradiometer (MODIS) daily TIR observations to adjust AMSR-E SM both temporally and spatially.

Daily variability of SM reflects the impact of precipitation and evaporation (Zhang et al., 2011b), including evapotranspiration from vegetation biomass. Therefore, a warm spot in LST data can be interpreted to have less moisture available, while a colder spot is assumed to have a higher moisture available for evaporation (possibly from rainfall) with less sensible heat flux to be detected by TIR observations. Precipitation can be analysed using daily rainfall data, which are available from weather stations. There are other low-resolution global reanalysis SM datasets, such as the final reanalysis (FNL) dataset from the US National Centers for Environmental Prediction (NCEP), which are generally used as model initial fields (Shi et al., 2010). We have integrated the NCEP FNL data into the Weather Research and Forecasting (WRF) model, coupled with Noah LSM, for SM simulations. LST series were used in this paper for fusion with AMSR-E SM time-series in the frequency domain after a fast Fourier transform.

[1] C-band (6.6 GHz) brightness temperature observations from the Scanning Multichannel Microwave Radiometer (SMMR).

The output SM series were inter-compared with the WRF simulations and evaluated based on rainfall data. The same technique was applied to adjust AMSR-E SM grids over the spatial domain.

6.3 Study area

Our study area is the South Island of New Zealand with a validation site in the Canterbury Plains approximately located at 43.63 S and 172.19 E (Fig. 6.1). This test-site was selected based on a few criteria including relatively homogeneous landscape, flat area with negligible variations in terrain elevation, availability of rainfall data from a nearby climate station (∼15 km to the North) and appropriate distance from large water-bodies (> 25 km) to avoid spectral mixing from water in the AMSR-E pixels.

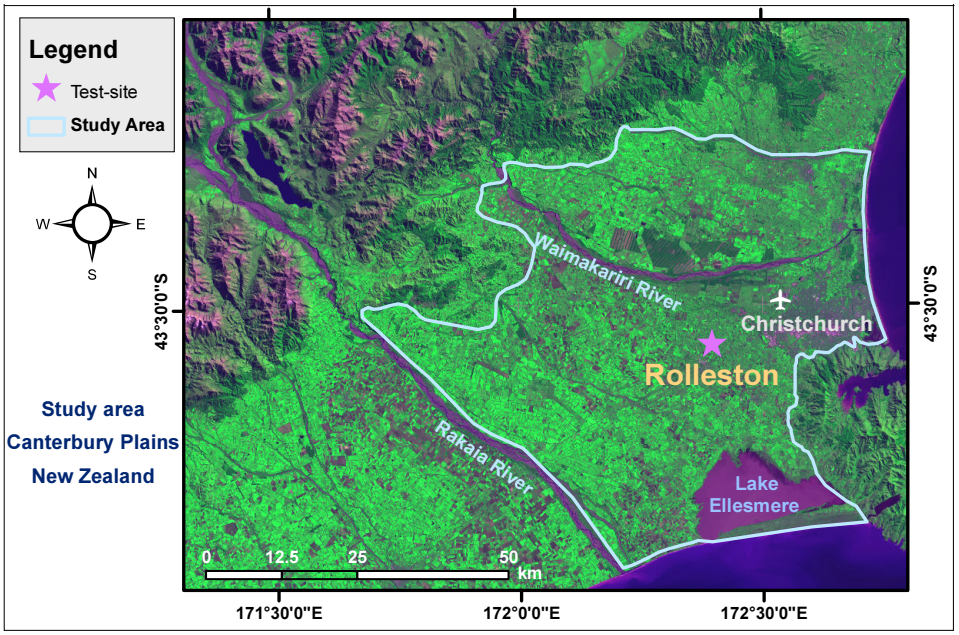

Figure 6.1: The photo-map of the study area with the main test-site overlaid on a Landsat image (TM5, 28 March 2011).

6.4 Data

Four major datasets were used in this paper: *in-situ* SM measurements, passive MW remotely sensed SM from AMSR-E, the MODIS LST product and the WRF model simulations of top-soil moisture. Some additional data are also used which are detailed below.

In-situ SM measurements The *in-situ* near-surface (2–5 cm depth) SM data have been measured over 'Rolleston' test-site, with a dominant land-cover of short grass

(Fig. 6.1), for a period of one month from 30 Oct. till 01 Dec. 2011. These data have been recorded using MadgeTech® digital soil volumetric moisture data loggers known as SMR110®. Frequency rate of the logged data had been set to 30 minute intervals.

AMSR-E SM Soil moisture product (daily, Level-3, Land) from AMSR-E developed by Njoku (2008) and distributed by the National Snow and Ice Data Center (NSIDC) were used in this analysis. AMSR-E measures horizontally and vertically polarized brightness temperature at six MW frequencies in the range 6.9–89 GHz across a single 1445 km swath (Njoku et al., 2003; Song et al., 2009). Data is collected with an ascending orbit at local afternoon (approximately 1:30 PM) and descending orbit at early morning (approximately 1:30 AM) local solar time (Kawanishi et al., 2003; Njoku, 2008). The SM retrievals are based on X-band (10.7 GHz) observations (Reichle et al., 2007). The spatial resolution of SM retrievals is 25 km and the Level 3 (L3) product is mapped to equal area grid (see `http://nsidc.org/data/docs/daac/ae_land3_l3_soil_moisture.gd.html`). Surface type classifications (12 classes) are assigned to indicate low (class 9) and moderate (class 8) vegetation, and retrievals are not performed over dense vegetation (class 7) (Njoku, 2008). Because of a technical failure of AMSR-E, this dataset is only available until 04 Oct. 2011. Some sources have used other data from this region (e.g., Simons and Voogt, 2012), but the authors could not get access to any alternative MW dataset available for New Zealand. Considering the importance of SM in the Canterbury Plains, an assessment of AMSR-E SM quality for the available dates still seems to be useful. Data from 30 Sep. 2006 to 03 Oct. 2011 were used in this paper.

MODIS LST The MODIS LST L3 Version 5 (V5) product, gridded in the Integerized Sinusoidal projection, is used to analyse the effects of the surface temperature on SM profiles. LST product is also used to adjust the AMSR-E SM series for cooling effects due to rainfall. We have used the L3 tile at column 30 line 13 (h30v13), which covers major parts of the South Island of New Zealand. Cloud-contaminated observations were filtered out based on cloud-cover and quality control fields, which are available in the product.

WRF simulations The WRF model simulations of surface SM were produced for a period of four months (30 Jul. to 01 Dec. 2010). Another simulation for a shorter period (31 Oct. till 01 Dec 2011) was also produced for accuracy assessment of the WRF simulations based on the *in-situ* data. The grid cell-size for the simulations was set to 25 km to match the spatial resolution of the AMSR-E SM product and 1 km for the nested domain. The initial conditions in the WRF model are based on the final re-analysis (FNL) data (Hong et al., 2009) with 1.0x1.0 degree grids prepared

operationally every six hours. FNL data include air temperature, wind speed and direction, soil temperature and moisture, sea level pressure and rainfall in global scale (http://rda.ucar.edu/datasets/ds083.2). The model interpolates the FNL data to grid points specified in the input settings, which is controlled by grid dimensions and spatial resolution of the first domain, and the grid-cell size factor of the nested domains.

Additional data Hourly rainfall data from Christchurch Airport Station (43° 29' 34.8" S, 172° 32' 13.2" E, 28 a.s.l.), which is the nearest climate station to the measurement site (Fig. 6.1), are used in SM analysis. The mean annual rainfall map of the South Island (1971 - 2000) from The National Institute of Water and Atmospheric Research (NIWA) is also used in this paper. We have used a Landsat 5 TM imagery to interpret dominant land-cover types of the study area and to choose suitable locations for the test-site so that the *in-situ* measurements represent the most dominant landscape in the area.

6.5 Methods

6.5.1 Statistical methods

Euclidean distance d_E (Buza et al., 2011) is used to approximate similarity between two WRF and AMSR-E SM time-series (Eq. 6.1). d_E is also useful in order to compare AMSR-E SM time-series before and after fusion via multiplication with α weighting matrix (Section 6.5.2).

$$d_E(ts_1, ts_2) = \sqrt{\sum_{i=1}^{n} (ts_1(i) - ts_2(i))^2} \tag{6.1}$$

where ts_1 and ts_2 are two time-series to be merged and n is the total number of coincident time-points in both series.

A fast Fourier transform (FFT) and an inverse FFT (iFFT) are applied to transform time-series from time to frequency domain (Eq. 6.2) and return to time domain (Eq. 6.3), respectively. FFT is used for the fusion of the AMSR-E SM with the MODIS LST dataset in frequency domain.

$$X(k) = \sum_{j=0}^{N-1} x(j)\Omega_N^{jk}, \qquad k = 0, 1, 2, ..., N-1 \tag{6.2}$$

where x is an N-point sequence in time domain (N is the total number of points in the series), X corresponds to N samples of the Fourier transform and $\Omega_N = e^{(-2j\pi)/N}$

is the radian frequency (Pei and Luo, 1996).

$$x(j) = A_0 + \frac{1}{N}\sum_{k=0}^{N-1} X(k)\Omega_N^{-jk}, \qquad j = 0, 1, 2, ..., N-1 \tag{6.3}$$

where A_0 is the arithmetic mean (Kerchove et al., 2013) of the original sequence (zero-frequency value given by Eq. 6.2 as the first element of X) and x is the reconstructed sequence from frequency domain back to time domain.

6.5.2 Mixing matrix

The near-surface SM has a strong effect on LST via its influence on emissivity (Sun and Pinker, 2004) and the cooling effect through partitioning of the surface heat fluxes. A mixing matrix α, designed following Farid and Adelson (1999); Umeyama and Godin (2004), is used in this paper for linear fusion of the AMSR-E SM with the MODIS LST frequencies to adjust AMSR-E SM for diurnal and seasonal variations and rainfall effects (Fig. 6.2). Other methods also exist in the literature, such as the triangle method which uses the MODIS LST, NDVI and Albedo products (Kim and Hogue, 2012). This method, however, is designed only for spatial domain.

$$\alpha = \begin{bmatrix} 0.6 & 0 \\ 0.4 & 1 \end{bmatrix}$$

The first column of α provides weights for the AMSR-E SM series and the second column provides weights for MODIS LST. The output from this mixing matrix is a two-column matrix with the first column having 60% weight from the AMSR-E and 40% weight from the inverted MODIS LST series. The second column is the same as the input MODIS series, which is not needed in the output. The input AMSR-E series is produced over a single pixel and the MODIS LST series are produced by spatially averaging 25x25 pixels overlapping the AMSR-E pixel. This method improves the output SM, where rainfall effects become more evident in the resulting AMSR-E series. To get the original series back, the series can be multiplied by the inverse mixing matrix α^{-1} with the same order as the linear fusion had been implemented.

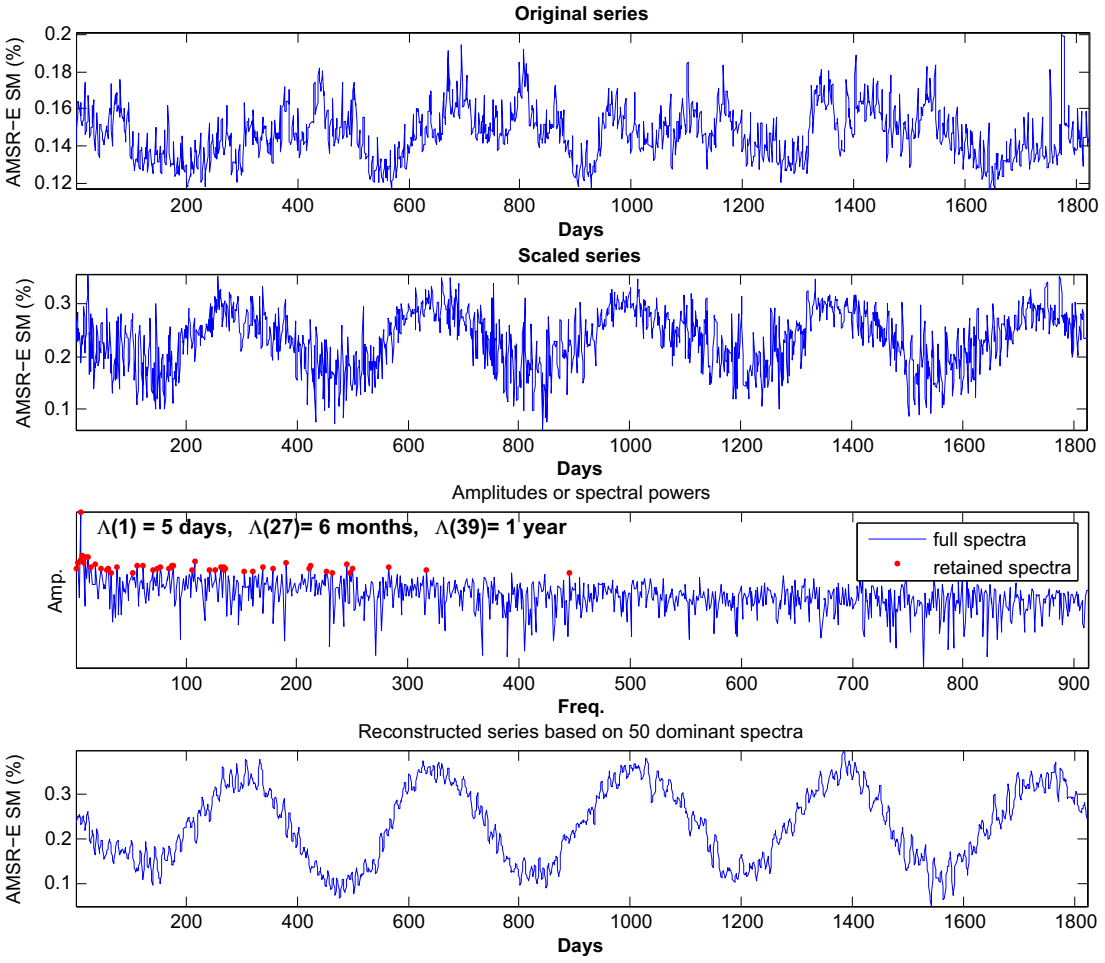

Figure 6.2: Original, scaled by mixing matrix α based on the inverted MODIS LST series, spectral powers of scaled series and filtered series of AMSR-E over a period of five years (30 Sep. 2006 to 03 Oct. 2011).

6.6 Results

6.6.1 Comparison of the WRF simulations with the in-situ SM

The WRF SM time-series from the 2nd domain (1x1 km spatial resolution) were compared with the *in-situ* measurements and overlaid on rainfall data to assess quality of these simulations (Fig. 6.3). This comparison revealed that the model has performed well in detecting the occasional peaks in SM amount due to rainfall. However, a difference of about 0.05 to 0.10 m^3 m^{-3} in normal conditions and up to 0.20 m^3 m^{-3} during rainfall events can be found between the WRF simulations and the *in-situ* measurements ($d_E = 3.8$). The *in-situ* SM values have exceeded 0.65 m^3 m^{-3} after rainfall events. These extremes are partly due to the difference in the scope of point measurements, in contrast to the 1x1 km^2 area covered by the model's grid cells, but also due

to the differences in soil texture used in the WRF model and those actually observed at the *in-situ* site (leading to differences in porosity/field capacity/wilting point). Using d_E to find the absolute difference between temporal trends of the two time-series, it turned out that the lowest distance from the *in-situ* series is achieved when an offset of 0.13 m^3 m^{-3} is added to the WRF simulations (Fig. 6.4). Correlation between the two time-series showed a good (ρ=0.62) agreement.

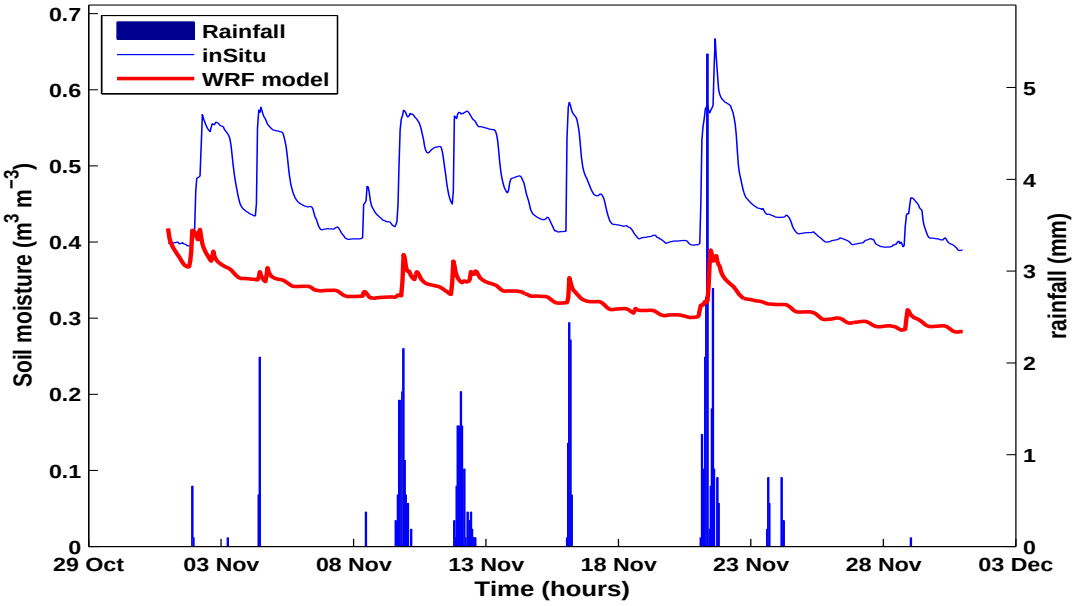

Figure 6.3: Time-series of soil moisture from model simulations (1x1 km grid-size) compared with the in-situ measurements (hourly data, Rolleston site, Nov. 2011)

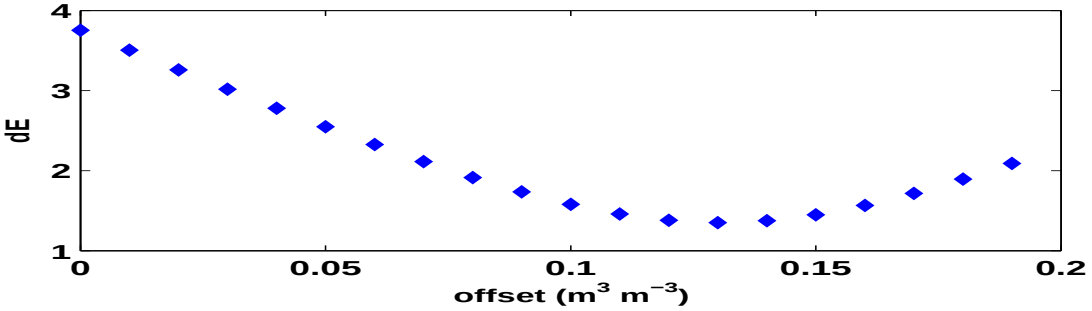

Figure 6.4: Variability of Euclidean distance (d_E) between the WRF (1x1 km grid) and the in-situ SM measurements as a function of different offsets added to the WRF series (Rolleston site, Nov. 2011)

6.6.2 AMSR-E day and night SM time-series

Time-series of AMSR-E SM product for a single pixel located in the centre of the study area (Rolleston site) for a period of about two years (30 Sep. 2009 till 03 Oct. 2011)

were analysed. There is ∼12 hours time difference between the ascending (A) and descending (D) overpasses of the satellite, which take place usually around 13:30 in the afternoon and 1:30 in the morning (local solar time), respectively. Variability of SM over a short period of 12 hours is expected to be within a limited range, except for the occasional rainy days. For this reason, a reasonably high agreement between SM series of the two immediate overpasses of the satellite can be expected. We compared SM series from day and night overpasses of the satellite and calculated the difference between the two series (Fig. 6.5a). Although the long-term mean difference between the two series was negligible (0.004 m^3 m^{-3}), the difference between the two immediate overpasses of the satellite (∼12 hours gap) was considerably higher (∼0.06 m^3 m^{-3}). Correlation between the series of the two overpasses of the satellite was $r = 0.63$ (Fig. 6.5b). This indicates that the agreement between the AMSR-E SM observations with ∼12 hours lag drops significantly. Auto-correlation with 12 hours lag calculated from the continuous SM time-series of both AMSR-E overpasses was even lower ($r = 0.45$). With the same time-lag but over different time periods, we achieved considerably higher auto-correlations from the WRF model ($r = 0.87$) and the *in-situ* series ($r = 0.93$).

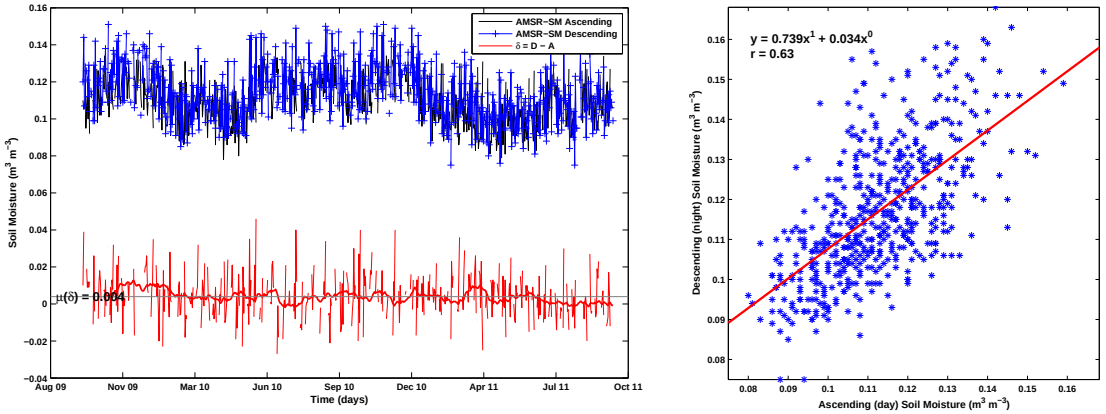

Figure 6.5: AMSR-E daily soil moisture time-series (29-Sep-2009 to 03-Oct-2011) over Rolleston, Central Canterbury, and the differences between ascending (A) and descending (D) overpasses, where **left** panel shows time-series of A (daytime) and D (night-time) observations, the lower part of this figure shows δ = D-A, moving average of δ (bold line) and μ or mean of δ (light-gray straight line); and the **right** panel shows correlation between soil moisture values at day and night.

6.6.3 AMSR-E SM compared with the WRF simulations

Since our *in-situ* measurements were not available before 04 Oct. 2011, which is the date when AMSR-E has stopped collecting data, we could not use the *in-situ* measurements for direct comparison with the AMSR-E SM time-series. On the other hand,

quality of the model simulations were already checked against ground measurements (Sec. 6.6.1). Therefore, we used simulated SM for inter-comparison with the AMSR-E dataset over the study area. Simulations of the near-surface SM for the topmost soil layer (5 cm depth) for a period of four months (from 30 Jul. to 01 Dec. 2010) were produced by the WRF model (25x25 km spatial resolution). Quality of these simulations was assessed based on rainfall data. Time-series of the WRF SM for a single grid-cell over Rolleston test-site was overlaid on the rainfall data. Rolleston test-site is located on a relatively homogeneous and flat land at the centre of the study area, therefore, the effects of elevation and water bodies on the accuracy of the model SM simulations were expected to be small at this site. This analysis revealed that, for the majority of the cases, the model has picked rainfall effects successfully (Fig. 6.6). Moisture fluctuations in the model output fitted well with rainfall events. An overall decline in SM has occurred as the colder and wet season gives way to the warmer months of the year during Southern summer.

To demonstrate the difference in sensitivity of AMSR-E and the WRF simulations to rainfall, we overlaid time-series of SM from both dataset on daily cumulative rainfall measurements (Fig. 6.6). In this analysis, the WRF SM series were downscaled from hourly to daily resolution to match the temporal frequency of the AMSR-E SM observations. This analysis revealed that the AMSR-E dataset have little agreement with the WRF simulations ($dE = 2.2$). Although some of the peaks in the AMSR-E SM coincide with more significant rainfall events, the general agreement is poor with constant offset and no clear trend. Some of the reasons for possible errors in the AMSR-E SM were discussed in Draper et al. (2009), which included errors in the passive MW observations of the surface brightness temperature, as well as the errors introduced by the near-surface SM retrieval algorithm from these observations. AMSR-E SM time-series showed a systematic negative bias of $\sim$0.15 m^3 m^{-3} compared with the model simulations (Fig. 6.6). Since we already noticed that the WRF itself has a negative bias when it was compared with the *in-situ* measurements (Fig. 6.3), we can assume that the bias between AMSR-E and the WRF SM is due to an under-estimation by the AMSR-E product. Differences in soil texture and sensing depth between the model and AMSR-E can also be other potential reasons for this bias. Long-term AMSR-E time-series ranged between 0.08 to 0.15 m^3 m^{-3} (Fig. 6.5a), the WRF simulations for four months ranged from 0.14 to 0.38 m^3 m^{-3} (Fig. 6.6), while the *in-situ* measurements showed a much higher range of 0.40 to 0.65 m^3 m^{-3} over a period of one month (Fig. 6.3). Although the dates of the *in-situ* measurements (Nov. 2011) and AMSR-E time-series (Sep. 2006 to Oct. 2011) do not match, AMSR-E data have not shown similar range as the *in-situ* data or the WRF simulations for the same season in the

previous years (Fig. 6.8). A close inspection of the AMSR-E series, however, showed that SM peaks (at least partly) match with rainfall data (such as 10th Aug., 15th Sep., 7th and 22nd Nov., Fig. 6.6).

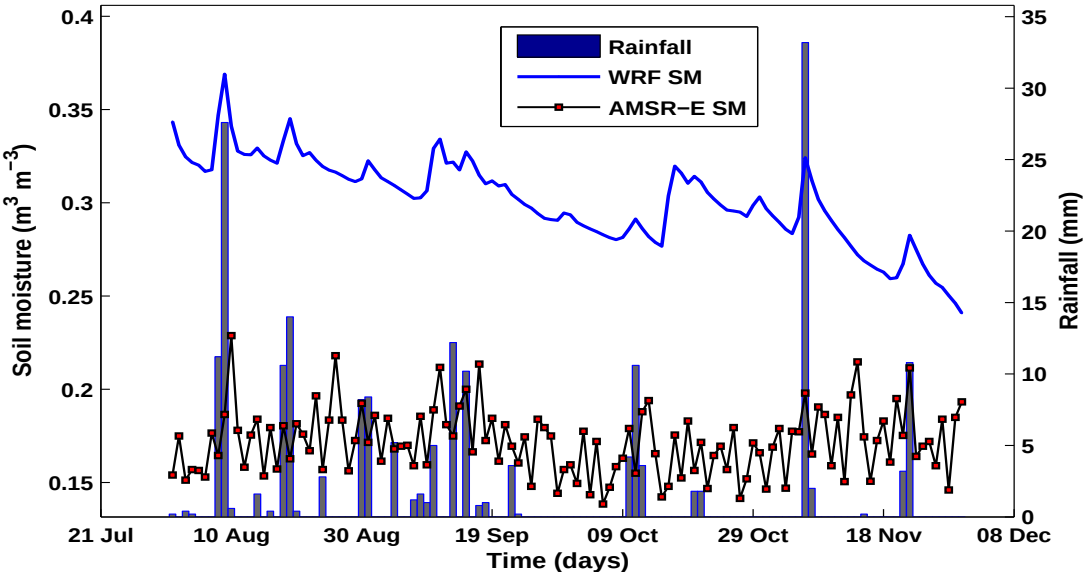

Figure 6.6: Time-series of AMSR-E SM and the WRF simulations overlaid on rainfall data for a period of four months (30 Jul. to 01 Dec. 2010).

We also looked at the quality control flags ('Inversion_QC_Flag' field), which were available in the AMSR-E soil moisture product (see http://nsidc.org/data/docs/daac/ae_land3_l3_soil_moisture.gd.html). Considering data from the four months period, which were used in this analysis, surface type of the AMSR-E pixel over 'Rolleston' test-site was categorized as 'Low Vegetation' (bit 9, Eq. 6.4) in the majority of dates and 'Moderate Vegetation' (bit 8) for some other dates. Hence, the pixel under consideration seems to have the most suitable land-cover type for SM retrieval compared to other possible classes listed in the AMSR-E product's documentation (Njoku, 2008). Ground check of the site during field measurements also confirmed that the land-cover of the area is predominantly short grass with sporadic tree lines as the hedges of the farms. This indicates that the AMSR-E SM time-series over this pixel ideally should meet the specified accuracy of 0.06 m^3 m^{-3} (or 6% volumetric SM) for the product (Njoku, 1999; Njoku et al., 2003). However, the bias from this product relative to the WRF simulations was significantly more than this value (Fig. 6.6). The mean SM from AMSR-E was 0.14 m^3 m^{-3} over the long-term (five years) period and 0.15 m^3 m^{-3} for the four months coincident with the WRF simulations. The mean SM from the *in-situ* data over the measurement period was 0.46 m^3 m^{-3} and from the WRF simulations over the four-month period was 0.32 m^3 m^{-3}.

$$\mathrm{QC} = \sum_{i=1}^{12} b_i \times 2^{i-1} \qquad [i = 1, 2, ..., 12] \tag{6.4}$$

where QC is the given value for quality control flag, $i = 12$ is the number of bits representing possible surface types and b_i is the value of each bit in binary scale (0 or 1).

6.6.4 Adjustment of AMSR-E SM series

It was explained above that although the AMSR-E SM has shown sporadic peaks matching rainfall events, it has significant bias when it is compared with the WRF SM simulations. To improve time-series of SM from AMSR-E, we have incorporated the MODIS LST series using the mixing matrix α (Section 6.5.2). This helps the AMSR-E SM series to be adjusted for the processes captured by LST, such as evaporation and rainfall effects which cool down LST. The MODIS LST series were inverted first so that the warmer spots to become lower and colder spots to show higher values. Both AMSR-E and the MODIS LST series were then transformed to frequency domain using Eq. 6.2. Afterwards, the mixing matrix α was applied to adjust AMSR-E SM for seasonal and rainfall effects. Finally, both series were reconstructed back into time domain based on 50 dominant spectra using Eq. 6.3. The adjusted AMSR-E SM series for four months (30 Jul. to 01 Dec. 2010) was compared with the WRF model simulations and rainfall data (Fig. 6.7). Cooling effect of rainfall, which is provided by the LST series, has clearly helped AMSR-E series to demonstrate a better agreement with rainfall events. The adjusted AMSR-E series also showed a better agreement with the WRF simulations ($dE = 0.9$). Similarly, the adjusted series over five years showed pronounced moist and dry seasons corresponding to the warm and cold seasons of the year (Fig. 6.8). Since only 50 dominant spectra were used for the reconstruction of the series (Fig. 6.2, bottom panel), possible noise in the original series, which appeared as spikes, were considerably reduced in the reconstructed series.

6.6.5 Spatial domain

The adjusted results in temporal domain were derived from a sequence of SM values over a single pixel for a period of five years. In this section, similar method is applied to adjust AMSR-E SM over a larger area covering the entire South Island of New Zealand. As the first step, grids of SM from AMSR-E and the WRF model simulations for the period of 30 Jul. to 01 Dec. 2010 (four months) were used to find the differences in

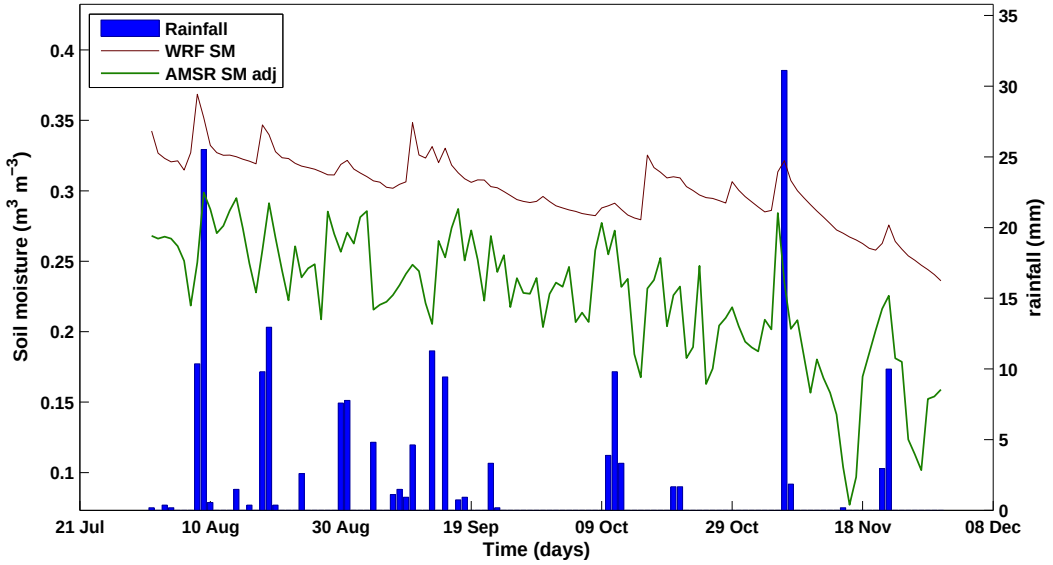

Figure 6.7: Adjusted AMSR-E SM time-series (based on the MODIS LST series) compared with the WRF series and overlaid on rainfall data (30 Jul. to 01 Dec. 2010).

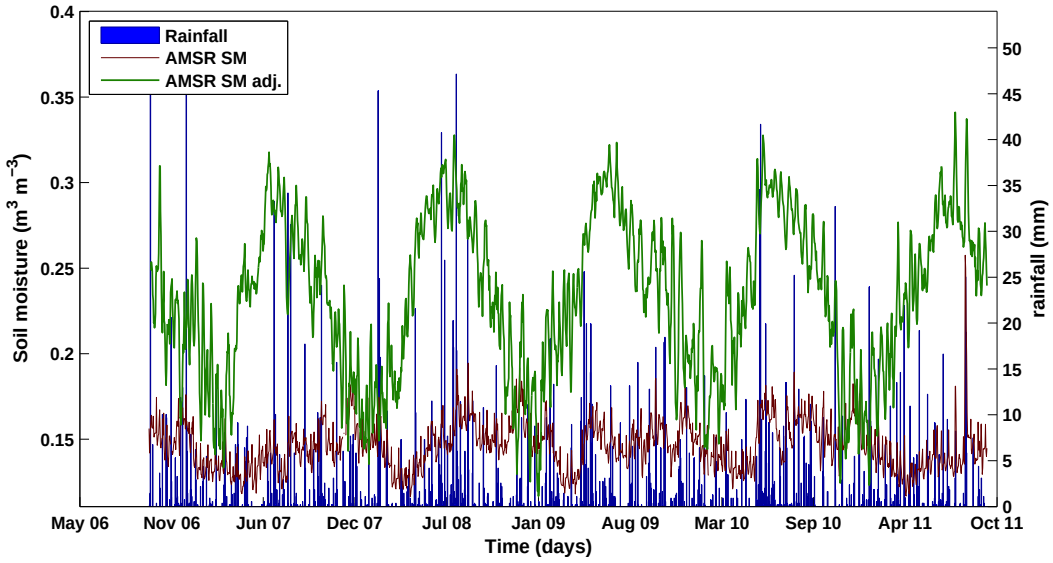

Figure 6.8: Adjusted AMSR-E SM based on the MODIS LST series (30 Sep. 2006 to 01 Oct. 2011).

the variability of SM over the spatial domain. Daily grids were averaged to produce four grids (one grid per month), as well as a single grid averaged over the whole period. These grids were interpolated to a finer resolution of 1x1 km (Fig. 6.9). Comparison of the WRF simulations with the AMSR-E product shows a significant difference in the range and spatial distribution of SM over the South Island of New Zealand for all the months (grids of individual months not shown). Considering the digital elevation model (DEM) of the study area (Fig. 6.10a), the AMSR-E SM have shown a higher moisture amount over the eastern side of the Southern Alps. Similarly, parts of the South Island

on the north-west also have appeared with higher moisture (Fig. 6.9a). The latter areas are covered by dense forests of the Kahurangi National Park, therefore, AMSR-E retrievals on those areas are suspected to be hindered by the forest canopy. We considered rainfall distribution across the South Island using the mean annual rainfall map and the surface temperature using the MODIS LST product. The annual rainfall map of the study area (Fig. 6.10b) showed that the eastern flanks of the Southern Alps in fact receive the lowest rainfall compared to the west coast. Surface temperatures, retrieved from the MODIS LST product (not shown), were higher over the flat plains in the eastern side (i.e., the Canterbury plains) compared to the other parts of the South Island. This means that there is a higher chance for evapotranspiration on the eastern side. As a result, in spite of the values shown by the AMSR-E SM product, lower SM amounts can be expected on the eastern side. These discrepancies can be explained partly due to the problems in SM retrieval under the intensive forest cover, permanent snow and ice and highly rugged terrain on the alpine and the west coast of the South Island. The WRF simulations, on the other hand, have shown higher moisture amounts on the west and south-western parts of the South Island (Fig. 6.9b). The re-analysis data (which include rainfall), used for the model's initial conditions enable the model to predict SM amounts under forest cover. These data also help the model to predict the temporal variability of SM over the study area, whereas, the AMSR-E product showed largely similar values for all months. The overall SM range from AMSR-E retrievals ($\sim 0 - 0.20$ m^3 m^{-3}) were also considerably lower than the corresponding values from the WRF simulations ($\sim 0.10 - 0.35$ m^3 m^{-3}). Considering these results, an adjustment of the AMSR-E SM product seemed necessary in the spatial domain as we did in the time domain. However, the adjustment approach taken in the time-domain, which was suitable for the series of a single pixel, needed to be extended to the whole pixels in the spatial domain. To this end, we used daily LST L3 product from MODIS at 1 km spatial resolution for the period corresponding to the AMSR-E observations. At first, the MODIS LST grids were scaled and inverted based on the long-term maximum and minimum SM values found in the AMSR-E product. Inversion was applied on the basis that the warmer pixels are expected to have more evapotranspiration than colder ones. The mixing matrix α was then applied to merge monthly series of each AMSR-E SM pixel to the corresponding series of the MODIS LST pixel over a period of four month. The spatial extent of the results was determined by the MODIS LST grid which covers a smaller area than the AMSR-E grid. The adjusted SM grids showed a distinctively higher SM amounts on higher altitudes and lower values over flat areas such as the Canterbury plains (Fig. 6.11). There was a gradual decrease in SM values from colder to warmer months of the year. However, there was no distinctive higher SM values on

the west side despite the significantly higher rainfall rates on those parts of the study area (Fig. 6.10b).

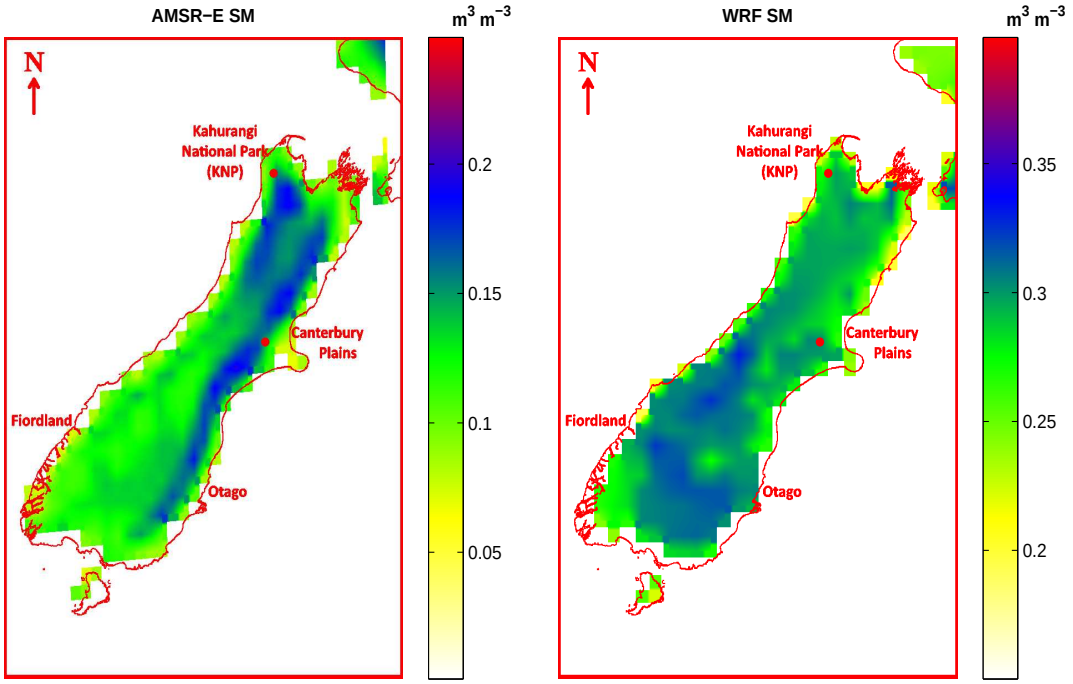

Figure 6.9: (a) AMSR-E and (b) the WRF SM grids over the South Island of New Zealand averaged from daily grids of four months (30 Jul. to 01 Dec. 2010). The display colour-bar of the two grids differ due to a significant difference in their SM range.

6.7 Discussion

The WRF model simulations showed a good agreement with the *in-situ* measurements and a good matching with rainfall events. This is an important result, which indicates that the model simulations can be used in the spatial domain, matching the pixels of satellite data, on those areas where point measurements are sparse or scarce. Simulations of a land-atmospheric model can be superior to interpolation of sparse point measurements in the sense that these models use energy balance characterization based on land-cover data from satellites, as well as atmospheric variables from weather stations, to estimate surface fluxes and SM.

Auto-correlation of AMSR-E SM time-series, which were produced by combining observations from both AMSR-E overpasses, was poor. This indicates that a significant anomaly exists between SM values of two consecutive AMSR-E overpasses. Two reasons can be assumed to be responsible for this anomaly: first, this anomaly is due to the difference in the ground track and sensor viewing geometry of each overpass;

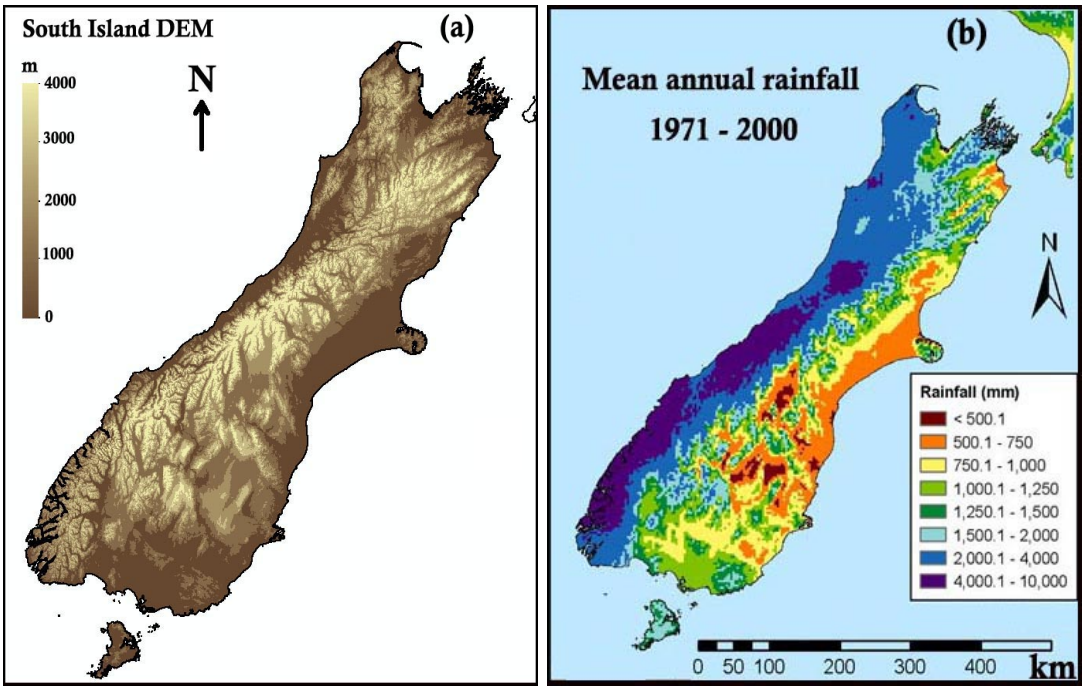

Figure 6.10: (a) The digital elevation model (DEM) and (b) the annual rainfall map of the South Island of New Zealand (from The National Institute of Water and Atmospheric Research–NIWA).

second, it indicates inconsistencies in the SM retrieval process. If the first reason is correct, a higher auto-correlation can be expected from SM series of an individual overpass. To find out, time-series of SM from each overpass were auto-correlated with 24-hour lag. However, these auto-correlations were also poor ($r = 0.42$ & $r = 0.47$). This leaves no explanation for the anomalies except for the second assumption stated above.

Another point for discussion was the lower SM range from AMSR-E compared to the *in-situ* measurements and the WRF simulations. This was shown both in the temporal and spatial domain. The highest SM value from AMSR-E over the South Island turned out to be 0.20 m^2 m^{-3}, which is significantly lower than the similar amount from the WRF grid. On the other hand, it turned out that rainfall effects can be detected in the AMSR-E series after scaling. These results, therefore, indicate that AMSR-E SM product has a negative bias in this region, which can be fixed by a simple scaling function. Since any scaling needs extra information, such as the minimum and maximum SM amounts, another satellite product, such as the MODIS LST, can be an excellent input for this purpose.

Despite the considerable difference in rainfall amounts on the east and the west sides of the South Island, the two sides seemed almost similar in the adjusted AMSR-E SM grids. This can be due to the density of vegetation and forest cover on the west

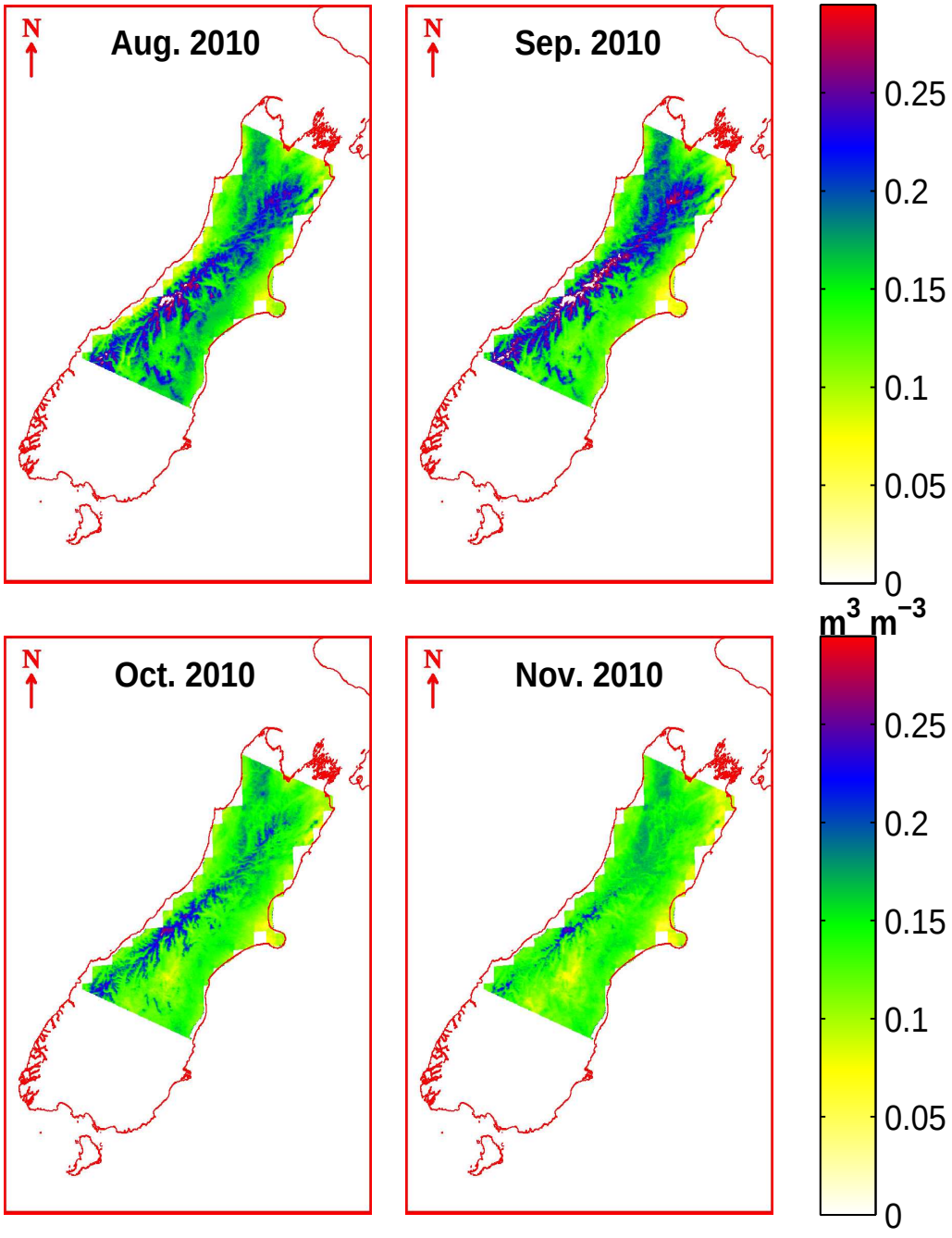

Figure 6.11: Adjusted AMSR-E SM gird for four months using the MODIS LST grid. Both grids are averaged from daily to monthly, AMSR-E grid is interpolated to 1x1 km spatial resolution before adjustment.

side. Dense vegetation and forest on those parts of the study area obstructs detection of higher moisture by AMSR-E MW or MODIS TIR observations.

6.8 Conclusion

The AMSR-E SM product in temporal and spatial domain was analysed in this paper. Soil moisture simulations from the WRF model showed a good agreement with the *in-situ* measurements and rainfall data. An negative offset of $\sim$0.13 m^3 m^{-3} between the WRF simulations and the *in-situ* measurements was found. The WRF simulations, alongside rainfall data, were then used to evaluate the quality of AMSR-E SM time-series. AMSR-E series showed a further negative offset of about 0.15 m^3 m^{-3} from the WRF simulations. Choi and Hur (2012) also had found that the root-mean-square errors (RMSE) in AMSR-E compared to the *in-situ* measurements range between 0.13 to 0.18 m^3 m^{-3} in their study area. Although we did not have access to ground measurements coincident with AMSR-E observations, our results infer a cumulative negative bias of about 0.25 to 0.30 m^3 m^{-3} in the AMSR-E SM series. The MODIS LST time-series were applied to adjust temporal profiles of AMSR-E SM in the long-term. Similar differences were observed when AMSR-E SM grid was compared with the WRF simulations in the spatial domain. Therefore, we applied a similar method to adjust AMSR-E SM grid using the MODIS LST grids for a period of four months over the entire South Island of New Zealand. This produced a more detailed SM map from AMSR-E with a better agreement with rainfall distribution and the DEM of the study area.

Results of this analysis shows that the AMSR-E dataset can be used for SM analysis in the study area only if a pre-processing step based on an alternative dataset, such as the MODIS LST and rainfall data, is applied. This approach can be applied generically on any location with available rainfall data, the MODIS LST product and reanalysis data (such as NCEP FNL) for model simulations to produce adjusted AMSR-E SM in spatial and temporal domain.

Acknowledgment

The authors would like to acknowledge New Zealand's National Climate Database (CliFlo) for granting access to their online database. Access to the NASA's AMSR-E Soil Moisture, MODIS LST and Landsat data are also appreciated; we used the Reverb tool to download these datasets.

Chapter 7

Summary, conclusion and outlook

7.1 Introduction

In this research, remotely sensed land surface temperature (LST) was applied to derive two important land-atmospheric variables, the near-surface air temperature (T_a) and soil moisture (SM). At first, LST observations from the Moderate Resolution Imaging Spectroradiometer (MODIS) were validated over two test-sites in the South Island of New Zealand. The first test-site was located in Cass, a mountain valley in the Waimakariri River basin, and the second test-site was a large flat area in the Canterbury Plains. Results from the second validation site showed that the MODIS LST has a good accuracy over the flat lands of the Canterbury Plains. The MODIS LST product, therefore, was applied to derive the near-surface T_a and SM over this region. Effects of spatial variability in the MODIS window-size, distance between LST pixels and the weather station, wind speed, wind direction and time of the day on LST-T_a relationship were evaluated. To support findings in the Canterbury Plains, T_a was derived at a few additional test-sites with similar land-cover and local topography across New Zealand. The MODIS LST then was applied to derive the near-surface SM using thermal inertia algorithm and to find out if more daily LST observations provide a better SM derivation. Finally, the MODIS LST with a higher spatial resolution was applied for spatio-temporal adjustment of the lower resolution passive microwave (MW) SM product from the Advanced Microwave Scanning Radiometer for the Earth Observing System (AMSR-E).

A summary of key findings, discussion of the overall results, conclusion of the thesis and outlook for future research is provided in this chapter.

7.2 An overview of key findings

The main material in this research was presented in four papers as below:

1. "Analysis of MODIS LST Compared with WRF Model and *in-situ* Data over the Waimakariri River Basin, Canterbury, New Zealand", which is published in the journal of *Remote Sensing* (Sohrabinia et al., 2012).

2. "Soil moisture derived using two Apparent Thermal Inertia functions over Canterbury, New Zealand", under review in the journal of *Applied Remote Sensing*.

3. "Spatio-temporal analysis of the relationship between LST from MODIS and air temperature in New Zealand", under review in the journal of *Theoretical and Applied Climatology*.

4. "Spatio-temporal adjustment of AMSR-E soil moisture using the MODIS LST in New Zealand", to be submitted soon for peer-review.

A summary of key findings from these four papers follows next.

7.2.1 Paper 1. Validation of the MODIS LST over the study area

The *in-situ* ground surface temperature (GST) measurements were collected over the Cass study area during a field campaign in May 2011, which were then used for validation of the MODIS LST. This test-site is located in the Southern Alps of New Zealand on a flat riverbed with relatively homogeneous land-cover types and was chosen after consideration of logistical issues, accessibility and the local conditions required for the validation experiment.

The main concerns were the issue of point-to-pixel assignment, the uncertainty due to the location of the measurement point inside the ground track of a MODIS pixel and spectral mixing over pixels that covered more than one LC type. A grid for measurement points, equivalent to the MODIS LST grid, was defined to solve the problem of pixel-to-point assignment. To quantify the uncertainty due to the location of the measurement point, variability in GST measured by multiple iButton temperature loggers over a similar land-cover type was analysed (Fig. 3.2). A mixing model was applied to estimate spectral mixing due to variability in surface conditions and sensor footprint.

The MODIS LST series were compared with the WRF model simulations and the *in-situ* measurements. This analysis showed that the MODIS LST series have considerable

differences with the *in-situ* measurements ($R^2 = 0.35$) and the model simulations. On the other hand, the WRF model simulations showed a higher agreement with the *in-situ* data ($R^2 = 0.77$). A few outliers were detected and removed from the MODIS LST time-series, which improved the agreements ($R^2 = 0.73$). Possible sources of error in the MODIS LST over the test-site was discussed to be due to the topography and highly variable atmospheric effects over the mountain valleys. It was discussed that the atmospheric correction of LST retrievals from MODIS by the generalized split window algorithm has been possibly subject to some errors due to the rugged terrain and the subsequent variability of the atmospheric water content over the valley. This stresses the need for a thorough quality assessment of the MODIS LST over mountainous areas for detection of cloud-contamination and possible outliers before using the product for further analysis. Based on these results, quality of the MODIS LST over flat parts of the study area, which are not affected by rugged topography, was also checked. Measurements of the *in-situ* surface temperature over several land-cover types in the Canterbury Plains, which is a flat terrain, were collected over a period of seven months and were applied for validation of the MODIS LST (Section 3.8). These results showed that the MODIS LST provides a reasonably acceptable agreement with the *in-situ* measurements ($r \geqslant 0.80$) and the WRF model outputs over the second test-site. As a consequence, the majority of the analysis in this thesis was conducted in the Canterbury Plains, with additional test-sites to support findings in this test-site.

7.2.2 Paper 2. Spatio-temporal variability of air temperature derived from the MODIS LST

This paper explored the relationship between the MODIS LST with 1 km spatial resolution and the ambient T_a using a statistical approach at several sites across New Zealand. The effects of the LST window-size, pixel distance to the weather station, wind speed, wind direction, temporal lags between LST and T_a, overpass time and sensor view angle were analysed to identify their impact on the LST-T_a relationship.

The LST series were produced by combining data from four daily overpasses of MODIS. Results showed that the best agreement between the MODIS LST and T_a measurements at most sites is achieved when a spatially averaged LST time-series over a window of 25x25 pixels is applied. Using LST series from the 25x25 window, the mean absolute difference with T_a measurements over 10 years turned out to be about $\pm$0.5 °C. A Fourier filtering was applied to compare the amount of noise in the series of

LST from a single pixel versus 25x25 window. It turned out that the spatially averaged time-series have less noise amount than the single-pixel LST series. As opposed to the series of a single pixel, where only a single value is available for each time, noise was suppressed by the mean or median filter used by the spatial window.

The diurnal profiles of T_a and LST were found to have two cross-overs; with larger LST at daytime and lower LST at nighttime. The first cross-over occurred around the early morning and the next one was found to be in the late afternoon. The two profiles came close in the late evening but went apart at midnight. It was discussed that due to these changes, the agreement between the MODIS LST time-series and T_a measurements showed the highest correlation in the evening but less agreement at midnight.

It was suggested that the best approach for modelling T_a based on the MODIS LST is to use a spatially averaged LST series over a window of 5x5 to 25x25 pixels with a consideration of wind speed and the local topography.

7.2.3 Paper 3. Soil moisture retrieval from the MODIS LST

In this paper, SM retrievals over the study area using the Apparent Thermal Inertia (ATI) algorithm with two approaches were compared. Both approaches (ATI1 and ATI2) used the MODIS LST product, however, ATI1 was based on two LST observations from MODIS-Terra for day and night while ATI2 used four LST observations from both MODIS-Terra and MODIS-Aqua day/night observations. The objective was to find out if more LST observations used by ATI model leads to a better SM retrieval. It was also aimed to evaluate the potential of the WRF model for filling the gaps in SM retrievals.

SM derivations from the MODIS LST using both ATI1 and ATI2 were validated based on the *in-situ* SM measurements and rainfall data at six sites. The analysis was conducted in two temporal scales, (***i***) over a period four months which also included the WRF simulations and (***ii***) over a longer period of three years which was aimed to compare temporal profiles of ATI1 and ATI2 SM retrievals. Both ATI1 and ATI2 showed relatively similar correlations with the *in-situ* measurements, however, ATI2 showed less offset from the ground measurement. The WRF simulations showed considerably higher agreements with the *in-situ* time-series at all sites. In the long-term, ATI2 showed slightly higher agreement with the *in-situ* measurements ($r = 0.66$) than ATI1 ($r = 63$). On the other hand, temporal profile of ATI2 showed a better matching with the *in-situ* SM and rainfall data. Seasonal effects were also better detected by ATI2. However, both ATI1 and especially ATI2 had suffered from missing values due to cloud

cover. Considering the good performance of the WRF model in the short-term, it was concluded that the model simulations can be used to fill the gaps in ATI SM retrievals.

Limitations of the ATI algorithm was outlined in the discussions, and it was clarified that the ATI information is commonly used to infer the near-surface SM on land, over low vegetation and relatively flat terrain. Sensitivity of LST to SM differs for the canopy and the soil surface beneath the plants, and is much greater for bare soil than for canopies (Mallick et al., 2009). As a result, the accuracy of the ATI algorithm diminishes over dense vegetation. It was concluded that the ATI2 has a better performance for SM retrieval in the study area.

7.2.4 *Paper 4. Adjustment of the AMSR-E soil moisture using the MODIS LST*

A linear fusion method for adjustment of the AMSR-E SM using the MODIS LST is presented in this paper. The *in-situ* measurements of SM were collected over five sites across the Canterbury Plains from early Oct. 2011 to early May 2012. However, due to the failure of AMSR-E on 04 Oct. 2011, it was not possible to directly validate AMSR-E SM with the field measurements. For this reason, the *in-situ* measurements were first used for accuracy assessment of the WRF model SM simulations. In the next step, the WRF SM simulations and rainfall data were used for validation of AMSR-E SM.

The results in this paper showed that the AMSR-E SM product has a significant offset when it is compared with the WRF model simulations. The mean AMSR-E SM series over five years was 0.15 m^3 m^{-3} lower than the WRF simulations and 0.25 to 0.30 m^3 m^{-3} lower than the overall mean from the *in-situ* measurements. Seasonal trends were also not clear in the AMSR-E SM time-series. However, peaks in AMSR-E time-series matched major rainfall events. Similar differences in the range and spatial distribution of SM were observed in the AMSR-E grid when it was compared with the WRF grid. Therefore, the MODIS LST was applied as an indirect parameter to adjust AMSR-E SM for evaporation and rainfall effects. It was discussed that evaporation is controlled by LST, and LST itself if cooled down by rainfall. Adding these information to the AMSR-E SM time-series gave a better agreement with rainfall data. A clear annual cycle was found in AMSR-E adjusted time-series which was obscured in the original series. The same technique was applied in the spatial domain to adjust the AMSR-E SM grids over the South Island of New Zealand. The adjusted AMSR-E grids showed a declining trend in SM amounts from winter to warmer months of the year

with finer detail from higher altitudes to lower flat plains.

7.3 Discussion of the results and limitations

The overall results from the four main chapters of this thesis (papers 1 to 4) and the limitations of remotely sensed data for T_a and SM modelling in New Zealand, which can be generalized to the other regions of the World with similar local conditions, are discussed in this section.

The results from the two validation campaigns (Chapter 3) demonstrated that the MODIS LST product has a better quality over the flat parts of the study area, whereas, over the alpine areas it contains a larger bias. The WRF model's simulations, on the other hand, showed a better agreement with the ground measurements at both sites. What becomes clear from these findings is that the surface temperature in alpine areas is largely affected by the surrounding conditions, such as topography, scattered cloud, water vapour and heterogeneous land-cover. In order to derive LST in alpine areas, therefore, a more sophisticated approach (such as surface energy balance parameterization, which is used by the WRF model) is required rather than using only the instantaneously observed brightness temperature from satellites. As a result, remotely sensed LST over alpine areas should be used only after a rigorous error assessment.

It was shown in the results of paper 2 (Chapter 4) that the MODIS LST product can be used to estimate T_a with a reasonably high accuracy over flat lands. These results also showed that a spatial window provides a better estimation of T_a than a single LST pixel. In all test-sites which were chosen across New Zealand, the modelled T_a based on the MODIS LST showed a strong correlation ($r \geqslant 0.80$) with the measurements in weather stations. However, it must be noted that these sites were chosen over flat areas with a relatively homogeneous land-cover. The quality of the modelled T_a solely based on remotely sensed LST might be lower in mountainous and heterogeneous areas. Over some land-cover types, such as forest, T_a can be highly variable. Such level of variability is not possible to be modelled from remotely sensed LST data.

The results from paper 3 (Chapter 5) showed that the MODIS LST can be applied to derive the near-surface SM using ATI method. These results were validated with the *in-situ* SM measurements and were compared with the WRF model simulations. Two ATI approaches were applied to derive the near-surface SM: ATI1 based on two and ATI2 based on four daily LST observations. Long-term variability of the near-surface SM was better presented when four daily LST values were employed by the ATI model. This is because more often LST observations enables mapping thermal

inertia of the surface and interpretation of day–night temperature difference (Price, 1980). This can partly explain the reason for the better performance of ATI2, which uses four LST observations as opposed to ATI1, which uses only two LST observations. It turned out that the missing LST values for cloudy days pose the major limitation on ATI model, which results in a large number of gaps in SM retrievals. This problem is even more severe with ATI2 approach due to its need for more daily LST values. Since model simulations are available for almost everyday, regardless of cloud effects, it was suggested to fill the gaps in SM derivations using the WRF simulations. This may lead to an argument that why remotely sensed SM derivations with large gaps should be attempted in the first place when the model simulations with no gaps can be used instead. The answer to this question lies in two important points. First, model simulations are made based on certain idealistic assumptions, whereas, remotely sensed observations are real data which have gone through a few pre-processing steps to account for the atmospheric effects. Second, model simulations are time-consuming, require large amount of memory for storage and need several chains of processes. Therefore, a combined approach using remotely sensed data and model simulations, only to fill the gaps, can be better (because it benefits from observational data) and faster (because it uses the model only for cloudy days).

Finally, it was explained in Paper 4 (Chapter 6) that although MW observations do not have the limitations of TIR data due to cloud cover, the spatial resolution of these observations is poor. This research attempted to overcome the spatial limitations of AMSR-E MW data by dis-aggregating the higher resolution (1 km) MODIS LST dataset into AMSR-E 25 km grid. It became evident that the SM product from AMSR-E MW observations over New Zealand suffer from a number of issues, such as dense vegetation over parts of the country (especially over the West-Coast and the Southland in the South Island). These issues were not resolved even in the final product dis-aggregated with the MODIS LST (Fig 6.11). In this final product, the effects of topography overshadows the general spatial trends in SM over the South Island. Therefore, topography and dense vegetation pose limitations on this dis-aggregation approach. One way to overcome this issue can be to mask out high elevation and densely vegetated areas. Only parts of New Zealand meet such criteria. As a result, the dis-aggregation method presented in this thesis can be more suitable for the flat and less vegetated parts of the study area, such as the Canterbury Plains, and similar regions around the world.

Considering the results from the four main chapters, the general conclusion can be that the MODIS LST product has a great potential for T_a and SM modelling in New Zealand. Based on the results, this potential varies according to the local

land-cover and topography and is limited on areas with dense vegetation and rugged topography. As it was discussed in this thesis, SM is of critical importance in agricultural lands, which are often located on flat lands cleared from native forests. SM is also highly variable across spatial extent. Therefore, a remotely sensed approach for SM estimation, which showed a better accuracy over flats lands, can be very useful. T_a, on the other hand, is usually measured in the weather stations and varies less across flat areas. Therefore, a remote sensing-based T_a over flat lands is of minor importance except for the long-term. On the other hand, a remotely sensed approach for T_a estimation can be more helpful in alpine areas with numerous mountain valleys and often no weather stations. Regarding the long-term availability of the MODIS LST (> 10 years), this dataset has the potential for T_a estimation in the long-term. Over mountainous areas, however, it can only be used after rigorous error assessment and detection of cloud-top temperatures.

7.4 Conclusion of the thesis

This thesis dealt with the validation of remotely sensed LST data from MODIS, based on the ground measurements in comparison with a numerical model simulations, and application of this dataset for T_a and SM estimation in New Zealand. It was also aimed to identify the advantages and shortcomings of satellite data in comparison with the WRF model's numerical simulations. Finally, improving spatio-temporal quality of a MW SM dataset over New Zealand based on the higher resolution TIR data from MODIS was explored. Key results can be summarized as below:

- Validation results showed that the MODIS LST product is subject to errors in the alpine areas, such as the Southern Alps in the South Island of New Zealand, one of the case studies in this thesis. It was suggested the LST product over mountainous areas to be rigorously checked for cloud effects and outliers before using the product in any analysis. The LST product was also validated over flat lands of the Canterbury Plains, which, in this case, showed a high agreement with the *in-situ* measurements.

- After validation of the MODIS LST, the product was applied to estimate the near-surface T_a. Results showed that using time-series of a single LST pixel (with 1 km spatial resolution) for T_a estimation is prone to noise and gives lower agreement with the measurements in the weather station. Using a spatially averaged time-series over 25x25 pixels, on the other hand, gave the best agreement with T_a measurements. It was, therefore, suggested to use a spatially averaged LST

time-series over a window of 5x5 to 25x25 pixels rather than the series of a single pixel for T_a modelling.

- The MODIS LST product was also applied to derive the near-surface SM using two ATI functions. The ATI SM retrieval algorithm based on four MODIS observations (ATI2) showed better results than the ATI function which used only two LST observations (ATI1). It was discussed that the better performance of the ATI2 function is due to a better representation of the diurnal SM profile using four (as opposed to two) daily LST values.

- Adjustment of the AMSR-E SM product using the MODIS LST with a higher spatial resolution resulted in a better agreement with the *in-situ* and modelled SM as well as rainfall data. The adjusted AMSR-E showed a higher level of detail in both temporal and spatial domains. Results also showed that the WRF model provides a good agreement with the *in-situ* SM and rainfall data. It was clarified that the advantage of the model simulations is the ability of the model to simulate SM over a large spatial extent, matching the pixels of satellite data. It was discussed that simulations from a land-atmospheric model can be superior to point interpolation methods in the sense that these models estimate surface fluxes by energy balance characterization using land-cover data from satellite observations and atmospheric variables measured in the weather stations.

Based on the results of this research, it can be stated that the satellite observed LST is useful for the estimation of some land surface properties over a long-term period (10 years) and at large spatial domain. This potential is especially more important on those areas where regular measurements are not available due to the lack of permanent weather stations. Considering the results from the first validation site, however, the MODIS LST product over those areas must be checked for possible outliers due to cloud contaminated pixels, which have been skipped during cloud masking process because of sporadic clouds over the rugged terrains. This research clarified that a number of environmental phenomena, such as cloud cover, dense vegetation and rugged topography limit the use of remotely sensed data. It was also found that a land-atmospheric model, such as the WRF coupled with the Noah and surface model, can be applied for filling the gaps due to cloud cover in remotely sensed variables. As the final concluding remark, satellite observed LST has the potential for SM and T_a estimations in New Zealand and other areas around the world with similar land-cover types, topography and climate.

7.5 Outlook for future research

- Results of this research showed that the near-surface T_a can be estimated with an accuracy of about ± 1 °C over a flat terrain, such as the Canterbury Plains, using the MODIS LST. The accuracy of the estimated T_a from spatially averaged LST time-series over 25x25 pixels was even higher. It is important to investigate this finding in other parts of New Zealand with different land-cover types and topography. This can be greatly helpful on those areas where automatic weather stations are sparse or non-existent. Such an effort must consider the fact that a larger spatial window is not feasible over areas where the land is restricted by uneven topography.

- The ATI algorithm to derive the near-surface SM in the study area showed promising results, but needs to be tested on other test-sites in New Zealand. The advantage of using this method is that it can be applied to derive the near-surface SM with a high spatial resolution over a large extent. The approach suggested in this research for filling the gaps in SM derivations using the WRF model simulations can be further investigated. Improvements can be possible by using a higher resolution land model, which can produce SM simulations with finer spatial resolution using the initial conditions based on higher resolution satellite data for parameterization of vegetation and LST.

- The SM product derived from the passive MW observations of AMSR-E has a coarse resolution. As a result, the entire New Zealand with substantial heterogeneity is sampled with a limited number of pixels causing errors in the product, which was shown in chapter 6. It was found that the MODIS LST with considerably higher spatial resolution can be used to improve the spatial and temporal profiles of SM from AMSR-E. However, quality of the improved product needs to be checked on densely vegetated areas. Vegetation and land-cover classification data are necessary to identify these areas and those parts where this adjustment technique can be more efficient. Therefore, it is suggested to produce a detailed land-cover classification over the study area beforehand and, based on that, to remove the areas with dense vegetation and extreme topography from the analysis.

Bibliography

Aikawa, M., Hiraki, T., Eiho, J., and Miyazaki, H. (2008). Role of the wind in the control of the air temperature distribution. *Meteorology and Atmospheric Physics*, 102:15–22, doi: 10.1007/s00703-008-0001-8.

Allen, C., Kramer, D., Smith, R., and Stults, A. (2002). Vertical Resolution and Coordinates. Online at http://atmo.tamu.edu/class/metr452/models/2001/vertres.html(Accessed: 25 June 2012).

Averbuch, A. and Zheludev, M. (2012). Two Linear Unmixing Algorithms to Recognize Targets Using Supervised Classification and Orthogonal Rotation in Airborne Hyperspectral Images. *Remote Sensing*, 4(2):532–560, doi: 10.3390/rs4020532.

Badarinath, K. and Chand, T. (2007). Analysis of apparent thermal inertia over different land use / land cover types using envisat AATSR data. *Journal of the Indian Society of Remote Sensing*, 35:185–191, doi: 10.1007/BF02990782.

Becker, F. and Li, Z.-L. (1990). Towards a local split window method over land surfaces. *International Journal of Remote Sensing*, 11(3):369–393, doi: 10.1080/01431169008955028.

Ben-Gal, I. (2005). Outlier detection. In Maimon, O. and Rockach, L., editors, *Data Mining and Knowledge Discovery Handbook: A Complete Guide for Practitioners and Researchers*, pages 1–16. Kluwer Academic Publishers, url: http://www.eng.tau.ac.il/~bengal/outlier.pdf.

Benali, A., Carvalho, A., Nunes, J., Carvalhais, N., and Santos, A. (2012). Estimating air surface temperature in Portugal using MODIS LST data. *Remote Sensing of Environment*, 124(0):108–121, doi: 10.1016/j.rse.2012.04.024.

Bindlish, R., Kustas, W., French, A., Diak, G., and Mecikalski, J. (2001). Influence of near-surface soil moisture on regional scale heat fluxes: model results using microwave remote sensing data from SGP97. *Geoscience and Remote Sensing, IEEE Transactions on*, 39(8):1719–1728, doi: 10.1109/36.942550.

Brooks, R. T. and Kyker-Snowman, T. D. (2008). Forest floor temperature and relative humidity following timber harvesting in southern New England, USA. *Forest Ecology and Management*, 254(1):65 – 73, doi: 10.1016/j.foreco.2007.07.028.

Brunel, J. (1989). Estimation of sensible heat flux from measurements of surface radiative temperature and air temperature at two meters: Application to determine

actual evaporation rate. *Agricultural and Forest Meteorology*, 46(3):179 – 191, doi: 10.1016/0168-1923(89)90063-4.

BU.edu (2012). MODIS BRDF/Albedo Product (MOD43B) User's Guide. http://www-modis.bu.edu/brdf/userguide/albedo.html (Accessed: 18 June 2012).

Buza, K., Nanopoulos, A., and Schmidt-Thieme, L. (2011). Fusion of Similarity Measures for Time Series Classification. In Corchado, E., Kurzyński, M., and Woźniak, M., editors, *Hybrid Artificial Intelligent Systems*, volume 6679 of *Lecture Notes in Computer Science*, pages 253–261. Springer Berlin Heidelberg, doi: 10.1007/978-3-642-21222-2_31.

Byrne, G., Begg, J., Fleming, P., and Dunin, F. (1979). Remotely sensed land cover temperature and soil water status - a brief review. *Remote Sensing of Environment*, 8(4):291 – 305, doi: 10.1016/0034-4257(79)90029-4.

Carlson, T. (2007). An Overview of the "Triangle Method" for Estimating Surface Evapotranspiration and Soil Moisture from Satellite Imagery. *Sensors*, 7(8):1612–1629, doi: 10.3390/s7081612.

Carlson, T. N., Gillies, R. R., and Perry, E. M. (1994). A method to make use of thermal infrared temperature and NDVI measurements to infer surface soil water content and fractional vegetation cover. *Remote Sensing Reviews*, 9(1-2):161–173, doi: 10.1080/02757259409532220.

Chang, T.-Y., Wang, Y.-C., Feng, C.-C., Ziegler, A. D., Giambelluca, T. W., and Liou, Y.-A. (2012). Estimation of Root Zone Soil Moisture Using Apparent Thermal Inertia With MODIS Imagery Over a Tropical Catchment in Northern Thailand. *Selected Topics in Applied Earth Observations and Remote Sensing, IEEE Journal of*, 5(3):752 –761, doi: 10.1109/JSTARS.2012.2190588.

Chen, F. and Dudhia, J. (2001a). Coupling an advanced land surface-hydrology model with the Penn State-NCAR MM5 modeling system. Part I: Model implementation and sensitivity. *Monthly Weather Review*, 129(4):569–585, url: http://dx.doi.org/10.1175/1520-0493(2001)129<0569:CAALSH>2.0.CO;2.

Chen, F. and Dudhia, J. (2001b). Coupling an advanced land surface-hydrology model with the Penn State-NCAR MM5 modeling system. part ii: Preliminary model validation. *Monthly Weather Review*, 129(4):587–604, url: http://nldr.library.ucar.edu/repository/collections/AMS-PUBS-000-000-000-012.

Cheng, K., Su, Y., Kuo, F., Hung, W., and Chiang, J. (2008). Assessing the effect of landcover changes on air temperature using remote sensing images - A pilot study in northern Taiwan. *Landscape and Urban Planning*, 86(3-4):297–297, doi: 10.1016/j.landurbplan.2007.09.014.

Choi, M. and Hur, Y. (2012). A microwave-optical/infrared disaggregation for improving spatial representation of soil moisture using AMSR-E and MODIS products. *Remote Sensing of Environment*, 124(0):259 – 269, doi: 10.1016/j.rse.2012.05.009.

Coll, C., Caselles, V., Galve, J. M., Valor, E., Niclòs, R., Sánchez, J. M., and Rivas, R. (2005). Ground measurements for the validation of land surface temperatures derived from AATSR and MODIS data. *Remote Sensing of Environment*, 97(3):288 – 300, doi: DOI: 10.1016/j.rse.2005.05.007.

Coll, C., Galve, J., Sanchez, J., and Caselles, V. (2010). Validation of Landsat-7/ETM+ Thermal-Band Calibration and Atmospheric Correction With Ground-Based Measurements. *Geoscience and Remote Sensing, IEEE Transactions on*, 48(1):547 –555, doi: 10.1109/TGRS.2009.2024934.

Colombi, A., Michele, C. D., Pepe, M., and Rampini, A. (2007). Estimation of daily mean air temperature from MODIS LST in alpine areas. *EARSeL eProceedings*, 6(1):38–46, url: http://www.eproceedings.org/static/vol06_1/06_1_colombi1.pdf?SessionID=3a07ce7d4ead4eeaea8ad.

Corder, G. W. and Foreman, D. I. (2009). *Nonparametric statistics for non-statisticians: a step-by-step approach*. Wiley, Hoboken, N.J.

Cresswell, M. P., Morse, A. P., Thomson, M. C., and Connor, S. J. (1999). Estimating surface air temperatures, from Meteosat land surface temperatures, using an empirical solar zenith angle model. *International Journal of Remote Sensing*, 20(6):1125–1132, doi: 10.1080/014311699212885.

Crow, W. T., Kustas, W. P., and Prueger, J. H. (2008). Monitoring root-zone soil moisture through the assimilation of a thermal remote sensing-based soil moisture proxy into a water balance model. *Remote Sensing of Environment*, 112(4):1268 – 1281, doi: 10.1016/j.rse.2006.11.033.

Dash, P. (2005). *Land surface temperature and emissivity retrieval from satellite measurements*. PhD thesis, Karlsruhe Institute of Technology (KIT), Karlsruhe, Germany.

Dash, P., Göttsche, F.-M., Olesen, F.-S., and Fischer, H. (2002). Land surface temperature and emissivity estimation from passive sensor data: Theory and practice-current trends. *International Journal of Remote Sensing*, 23(13):2563–2594, doi: 10.1080/01431160110115041.

Dash, P., Göttsche, F.-M., Olesen, F.-S., and Fischer, H. (2005). Separating surface emissivity and temperature using two-channel spectral indices and emissivity composites and comparison with a vegetation fraction method. *Remote Sensing of Environment*, 96(1):1–17, doi: 10.1016/j.rse.2004.12.023.

Dousset, B. and Gourmelon, F. (2003). Satellite multi-sensor data analysis of urban surface temperatures and landcover. *ISPRS Journal of Photogrammetry and Remote Sensing*, 58(1-2):43–54, doi: 10.1016/S0924-2716(03)00016-9.

Draper, C. S., Reichle, R. H., De Lannoy, G. J. M., and Liu, Q. (2012). Assimilation of passive and active microwave soil moisture retrievals. *Geophys. Res. Lett.*, 39(4):L04401, doi: 10.1029/2011GL050655.

Draper, C. S., Walker, J. P., Steinle, P. J., de Jeu, R. A., and Holmes, T. R. (2009). An evaluation of AMSR-E derived soil moisture over Australia. *Remote Sensing of Environment*, 113(4):703 – 710, doi: 10.1016/j.rse.2008.11.011.

Dudhia, J. (1989). Numerical Study of Convection Observed during the Winter Monsoon Experiment Using a Mesoscale Two-Dimensional Model. *J. Atmos. Sci.*, 46(20):3077–3107, doi: 10.1175/1520-0469(1989)046%2525253C3077:NSOCOD%2525253E2.0.CO;2.

Efron, B. and Gong, G. (1983). A Leisurely Look at the Bootstrap, the Jackknife, and Cross-Validation. *The American Statistician*, 37(1):pp. 36–48, url: http://www.jstor.org/stable/2685844.

Elachi, C. and Van Zyl, J. (2006). *Introduction to the physics and techniques of remote sensing*. Wiley-Interscience, Hoboken, N.J.

Evrendilek, F., Karakaya, N., Gungor, K., and Aslan, G. (2012). Satellite-based and mesoscale regression modeling of monthly air and soil temperatures over complex terrain in Turkey. *Expert Systems with Applications*, 39(2):2059 – 2066, doi: 10.1016/j.eswa.2011.08.023.

Farid, H. and Adelson, E. (1999). Separating reflections and lighting using independent components analysis. In *Computer Vision and Pattern Recognition, 1999. IEEE Computer Society Conference on.*, volume 1, pages 2 vol. (xxiii+637+663). doi: 10.1109/CVPR.1999.786949.

Fitzgerald, W. B., Fahmy, M., Smith, I. J., Carruthers, M. A., Carson, B. R., Sun, Z., and Bassett, M. R. (2011). An assessment of roof space solar gains in a temperate maritime climate. *Energy and Buildings*, 43(7):1580 – 1588, doi: 10.1016/j.enbuild.2011.03.001.

Florio, E. N., Lele, S. R., Chi Chang, Y., Sterner, R., and Glass, G. E. (2004). Integrating AVHRR satellite data and NOAA ground observations to predict surface air temperature: a statistical approach. *International Journal of Remote Sensing*, 25(15):2979–2994, doi: 10.1080/01431160310001624593.

Gao, B. C., Davis, C., and Goetz, A. (2006). A Review of Atmospheric Correction Techniques for Hyperspectral Remote Sensing of Land Surfaces and Ocean Color. In *Geoscience and Remote Sensing Symposium, 2006. IGARSS 2006. IEEE International Conference*, pages 1979 –1981. doi: 10.1109/IGARSS.2006.512.

Garrigues, S., Lacaze, R., Baret, F., Morisette, J. T., Weiss, M., Nickeson, J. E., Fernandes, R., Plummer, S., Shabanov, N. V., Myneni, R. B., Knyazikhin, Y., and Yang, W. (2008). Validation and intercomparison of global Leaf Area Index products derived from remote sensing data. *Journal of Geophysical Research: Biogeosciences*, 113(G2):G02028, doi: 10.1029/2007JG000635.

Gelfand, A. E., Diggle, P. J., Fuentes, M., and Guttorp, P. (2010). *Handbook of spatial statistics*. CRC Press, Boca Raton.

Ghent, D., Kaduk, J., Remedios, J., Ardö, J., and Balzter, H. (2010). Assimilation of land surface temperature into the land surface model JULES with an ensemble Kalman filter. *J. Geophys. Res.*, 115(D19):D19112, doi: 10.1029/2010JD014392.

Gnanadesikan, R. and Kettenring, J. R. (1972). Robust Estimates, Residuals, and Outlier Detection with Multiresponse Data. *Biometrics*, 28(1):81–124, url: http://www.jstor.org/stable/2528963.

Göttsche, F.-M. and Olesen, F.-S. (2009). Modelling the effect of optical thickness on diurnal cycles of land surface temperature. *Remote Sensing of Environment*, 113(11):2306 – 2316, doi: 10.1016/j.rse.2009.06.006.

Goward, S. N., Cruickshanks, G. D., and Hope, A. S. (1985). Observed relation between thermal emission and reflected spectral radiance of a complex vegetated landscape. *Remote Sensing of Environment*, 18(2):137–146, doi: 10.1016/0034-4257(85)90044-6.

Gruhier, C., de Rosnay, P., Kerr, Y., Mougin, E., Ceschia, E., Calvet, J.-C., and Richaume, P. (2008). Evaluation of AMSR-E soil moisture product based on ground measurements over temperate and semi-arid regions. *Geophys. Res. Lett.*, 35(10):L10405, doi: 10.1029/2008GL033330.

Gubler, S., Fiddes, J., Gruber, S., and Keller, M. (2011). Scale-dependent measurement and analysis of ground surface temperature variability in alpine terrain. *The Cryosphere Discussions*, 5:307–338, doi: 10.5194/tcd-5-307-2011.

Guh, R.-S. (2005). A hybrid learning-based model for on-line detection and analysis of control chart patterns. *Computers & Industrial Engineering*, 49(1):35–62, doi: 10.1016/j.cie.2005.03.002.

Hachem, S., Duguay, C. R., and Allard, M. (2012). Comparison of MODIS-derived land surface temperatures with ground surface and air temperature measurements in continuous permafrost terrain. *The Cryosphere*, 6(1):51–69, doi: 10.5194/tc-6-51-2012.

Hain, C. R., Crow, W. T., Mecikalski, J. R., Anderson, M. C., and Holmes, T. (2011). An intercomparison of available soil moisture estimates from thermal infrared and passive microwave remote sensing and land surface modeling. *J. Geophys. Res.*, 116(D15):D15107, doi: 10.1029/2011JD015633.

Haining, R. (1990). *Spatial data analysis in the social and environmental sciences*. Cambridge University Press.

Hashimoto, H., Dungan, J. L., White, M. A., Yang, F., Michaelis, A. R., Running, S. W., and Nemani, R. R. (2008). Satellite-based estimation of surface vapor pressure deficits using MODIS land surface temperature data. *Remote Sensing of Environment*, 112(1):142 – 155, doi: 10.1016/j.rse.2007.04.016.

Haukoos, J. S. and Lewis, R. J. (2005). Advanced Statistics: Bootstrapping Confidence Intervals for Statistics with "Difficult" Distributions. *Academic Emergency Medicine*, 12(4):360–365, doi: 10.1197/j.aem.2004.11.018.

Hengl, T., Heuvelink, G., Perčec Tadić, M., and Pebesma, E. (2012). Spatio-temporal prediction of daily temperatures using time-series of MODIS LST images. *Theoretical and Applied Climatology*, 107(1-2):265–277, doi: 10.1007/s00704-011-0464-2.

Holden, Z. A., Abatzoglou, J. T., Luce, C. H., and Baggett, L. S. (2011). Empirical downscaling of daily minimum air temperature at very fine resolutions in complex terrain. *Agricultural and Forest Meteorology*, 151(8):1066–1073, doi: 10.1016/j.agrformet.2011.03.011.

Hong, S., Lakshmi, V., Small, E. E., Chen, F., Tewari, M., and Manning, K. W. (2009). Effects of vegetation and soil moisture on the simulated land surface processes from the coupled WRF/Noah model. *J. Geophys. Res.*, 114(D18):D18118, doi: 10.1029/2008JD011249.

Huang, C., Li, X., and Lu, L. (2008). Retrieving soil temperature profile by assimilating MODIS LST products with ensemble Kalman filter. *Remote Sensing of Environment*, 112(4):1320–1336, doi: 10.1016/j.rse.2007.03.028.

Hughes, M., Hall, A., and Fovell, R. (2007). Dynamical controls on the diurnal cycle of temperature in complex topography. *Climate Dynamics*, 29:277–292, doi: 10.1007/s00382-007-0239-8.

Hulley, G. C., Hughes, C. G., and Hook, S. J. (2012). Quantifying uncertainties in land surface temperature and emissivity retrievals from ASTER and MODIS thermal infrared data. *Journal of Geophysical Research: Atmospheres*, 117(D23):n/a–n/a, doi: 10.1029/2012JD018506.

Jackson, T., Cosh, M., Bindlish, R., Starks, P., Bosch, D., Seyfried, M., Goodrich, D., Moran, M., and Du, J. (2010). Validation of Advanced Microwave Scanning Radiometer Soil Moisture Products. *Geoscience and Remote Sensing, IEEE Transactions on*, 48(12):4256–4272, doi: 10.1109/TGRS.2010.2051035.

Jackson, T. J., Schmugge, J., and Engman, E. T. (1996). Remote sensing applications to hydrology: soil moisture. *Hydrological Sciences Journal*, 41(4):517–530, doi: 10.1080/02626669609491523.

Jiménez-Hornero, F., Pavón-Domínguez, P., de Ravé, E. G., and Ariza-Villaverde, A. (2011). Joint multifractal description of the relationship between wind patterns and land surface air temperature. *Atmospheric Research*, 99(3-4):366–376, doi: 10.1016/j.atmosres.2010.11.009.

Jiménez-Muñoz, J., Cristobal, J., Sobrino, J., Soria, G., Ninyerola, M., Pons, X., and Pons, X. (2009). Revision of the Single-Channel Algorithm for Land Surface Temperature Retrieval From Landsat Thermal-Infrared Data. *Geoscience and Remote Sensing, IEEE Transactions on*, 47(1):339–349, doi: 10.1109/TGRS.2008.2007125.

Jiménez-Muñoz, J. C. and Sobrino, J. A. (2003). A generalized single-channel method for retrieving land surface temperature from remote sensing data. *J. Geophys. Res.*, 108(D22):4688–9 pp., doi: 10.1029/2003JD003480.

Jin, J., Miller, N. L., and Schlegel, N. (2010). Sensitivity Study of Four Land Surface Schemes in the WRF Model. *Advances in Meteorology*, 2010:167436.1–167436.11, doi: 10.1155/2010/167436.

Jin, M. (2004). Analysis of land skin temperature using AVHRR observations. *Bulletin of American Meteorological Society: BAMS*, 85:587–600, doi: 10.1175/BAMS-85-4-587.

Jin, M. and Dickinson, R. E. (2010). Land surface skin temperature climatology: benefitting from the strengths of satellite observations. *Environmental Research Letters*, 5(4):044004, doi: 10.1088/1748-9326/5/4/044004.

Jin, M. and Shepherd, J. (2005). Inclusion of urban landscape in a climate model - How can satellite data help? *Bulletin of the American Meteorological Society*, 86(5):681–689, doi: 10.1175/BAMS-86-5-681.

Jönsson, P. and Holmquist, B. (1995). Wind direction in Southern Sweden 1740–1992: Variation and correlation with temperature and zonality. *Theoretical and Applied Climatology*, 51:183–198, doi: 10.1007/BF00867279.

Kabsch, E. (2009). *Validation of land surface temperatures from MSG satellite measurements by observations at the ground station near Evora, Portugal*. PhD thesis, Karlsruhe Institute of Technology (KIT), Karlsruhe, Germany.

Kabsch, E., Olesen, F., and Prata, F. (2008). Initial results of the land surface temperature (LST) validation with the Evora, Portugal ground-truth station measurements. *International Journal of Remote Sensing*, 29:5329–5345, doi: 10.1080/01431160802036326.

Kant, Y. and Badarinath, K. V. S. (2000). Studies on land surface temperature over heterogeneous areas using AVHRR data. *International Journal of Remote Sensing*, 21(8):1749–1756, doi: 10.1080/014311600210029.

Karnieli, A., Agam, N., Pinker, R. T., Anderson, M., Imhoff, M. L., Gutman, G. G., Panov, N., and Goldberg, A. (2010). Use of NDVI and Land Surface Temperature for Drought Assessment: Merits and Limitations. *J. Climate*, 23(3):618–633, doi: 10.1175/2009JCLI2900.1.

Kawanishi, T., Sezai, T., Ito, Y., Imaoka, K., Takeshima, T., Ishido, Y., Shibata, A., Miura, M., Inahata, H., and Spencer, R. (2003). The Advanced Microwave Scanning Radiometer for the Earth Observing System (AMSR-E), NASDA's contribution to the EOS for global energy and water cycle studies. *Geoscience and Remote Sensing, IEEE Transactions on*, 41(2):184–194, doi: 10.1109/TGRS.2002.808331.

Kawashima, S. and Ishida, T. (1992). Effects of regional temperature, wind speed and soil wetness on spatial structure of surface air temperature. *Theoretical and Applied Climatology*, 46:153–161, doi: 10.1007/BF00866095.

Kerchove, R. V. D., Lhermitte, S., Veraverbeke, S., and Goossens, R. (2013). Spatio-temporal variability in remotely sensed land surface temperature, and its relationship with physiographic variables in the Russian Altay Mountains. *International Journal of Applied Earth Observation and Geoinformation*, 20(0):4–19, doi: 10.1016/j.jag.2011.09.007.

Kerr, Y. H., Lagouarde, J. P., Nerry, F., and Ottlé, C. (2000). Land surface temperature retrieval techniques and applications: case of the AVHRR. In Quattrochi, D. A. and Luvall, J. C., editors, *Thermal Remote Sensing in Land Surface Processes*, pages 33–109. CRC PRESS, Boca Raton London New York Washington, D.C., doi: 10.1201/9780203502174-c3.

Keshava, N. and Mustard, J. F. (2002). Spectral unmixing. *IEEE Signal Processing Magazine*, 19(1):44–57, url: http://ieeexplore.ieee.org/xpls/abs_all.jsp?arnumber=974727.

Kim, J. and Hogue, T. (2012). Improving Spatial Soil Moisture Representation Through Integration of AMSR-E and MODIS Products. *Geoscience and Remote Sensing, IEEE Transactions on*, 50(2):446–460, doi: 10.1109/TGRS.2011.2161318.

Kumar, P. and Kaleita, A. (2003). Assimilation of near-surface temperature using extended Kalman filter. *Advances in Water Resources*, 26(1):79–93, doi: 10.1016/S0309-1708(02)00098-2.

Lakhankar, T., Ghedira, H., Temimi, M., Azar, A. E., and Khanbilvardi, R. (2009). Effect of Land Cover Heterogeneity on Soil Moisture Retrieval Using Active Microwave Remote Sensing Data. *Remote Sensing*, 1(2):80–91, doi: 10.3390/rs1020080.

Lakshmi, V. and Zehrfuhs, D. (2002). Normalization and comparison of surface temperatures across a range of scales. *IEEE Transactions on Geoscience and Remote Sensing*, 40(12):2636–2646, doi: 10.1109/TGRS.2002.805069.

Li, B., Toll, D., Zhan, X., and Cosgrove, B. (2012a). Improving estimated soil moisture fields through assimilation of AMSR-E soil moisture retrievals with an ensemble Kalman filter and a mass conservation constraint. *Hydrology and Earth System Sciences*, 16(1):105–119, doi: 10.5194/hess-16-105-2012.

Li, F., Crow, W. T., and Kustas, W. P. (2010). Towards the estimation root-zone soil moisture via the simultaneous assimilation of thermal and microwave soil moisture retrievals. *Advances in Water Resources*, 33(2):201–214, doi: 10.1016/j.advwatres.2009.11.007.

Li, Z., Zhao, L., and Fu, Z. (2012b). Estimating net radiation flux in the Tibetan Plateau by assimilating MODIS LST products with an ensemble Kalman filter and particle filter. *International Journal of Applied Earth Observation and Geoinformation*, 19(0):1 – 11, doi: 10.1016/j.jag.2012.04.003.

Li, Z.-L., Becker, F., Stoll, M., and Wan, Z. (1999). Evaluation of Six Methods for Extracting Relative Emissivity Spectra from Thermal Infrared Images. *Remote Sensing of Environment*, 69(3):197 – 214, doi: 10.1016/S0034-4257(99)00049-8.

Lillesand, T. M., Kiefer, R. W., and Chipman, J. W. (2008). *Remote sensing and image interpretation*. John Wiley & Sons, Hoboken, NJ.

Lin, S., Moore, N. J., Messina, J. P., DeVisser, M. H., and Wu, J. (2012). Evaluation of estimating daily maximum and minimum air temperature with MODIS data in east Africa. *International Journal of Applied Earth Observation and Geoinformation*, 18(0):128 – 140, doi: 10.1016/j.jag.2012.01.004.

Liou, K. (2002). *An Introduction to Atmospheric Radiation*. Academic Press, San Diego. CA, 2nd edition edition.

Lubin, D. and Massom, R. (2006). *Polar remote sensing Volume I: Atmosphere and Oceans*, volume 1. Springer, Berlin.

Mallick, K., Bhattacharya, B. K., and Patel, N. (2009). Estimating volumetric surface moisture content for cropped soils using a soil wetness index based on surface temperature and NDVI. *Agricultural and Forest Meteorology*, 149(8):1327–1342, doi: 10.1016/j.agrformet.2009.03.004.

Manly, B. F. (2001). *Statistics for Environmental Science and Management*. Chapman and Hall/CRC, Western Ecosystem Technology Inc. Wyoming, USA.

Matsushima, D., Kimura, R., and Shinoda, M. (2011). Soil Moisture Estimation Using Thermal Inertia: Potential and Sensitivity to Data Conditions. *J. Hydrometeor*, 13(2):638–648, doi: 10.1175/JHM-D-10-05024.1.

Maussion, F., Scherer, D., Finkelnburg, R., Richters, J., Yang, W., and Yao, T. (2011). WRF simulation of a precipitation event over the Tibetan Plateau, China - an assessment using remote sensing and ground observations. *Hydrology and Earth System Sciences*, 15(6):1795–1817, doi: 10.5194/hess-15-1795-2011.

Meng, C. L., Li, Z.-L., Zhan, X., Shi, J. C., and Liu, C. Y. (2009). Land surface temperature data assimilation and its impact on evapotranspiration estimates from the Common Land Model. *Water Resour. Res.*, 45(2):W02421, doi: 10.1029/2008WR006971.

Merlin, O., Escorihuela, M. J., Mayoral, M. A., Hagolle, O., Bitar, A. A., and Kerr, Y. (2013). Self-calibrated evaporation-based disaggregation of SMOS soil moisture: An evaluation study at 3 km and 100 m resolution in Catalunya, Spain. *Remote Sensing of Environment*, 130(0):25–38, doi: http://dx.doi.org/10.1016/j.rse.2012.11.008.

Merlin, O., Walker, J. P., Chehbouni, A., and Kerr, Y. (2008). Towards deterministic downscaling of SMOS soil moisture using MODIS derived soil evaporative efficiency. *Remote Sensing of Environment*, 112(10):3935–3946, doi: http://dx.doi.org/10.1016/j.rse.2008.06.012.

Mildrexler, D. J., Zhao, M., and Running, S. W. (2011). A global comparison between station air temperatures and MODIS land surface temperatures reveals the cooling role of forests. *Journal of Geophysical Research: Biogeosciences*, 116(G3):G03025, doi: 10.1029/2010JG001486.

Minacapilli, M., Iovino, M., and Blanda, F. (2009). High resolution remote estimation of soil surface water content by a thermal inertia approach. *Journal of Hydrology*, 379(3 - 4):229 – 238, doi: 10.1016/j.jhydrol.2009.09.055.

Moran, M. S., Peters-Lidard, C. D., Watts, J. M., and McElroy, S. (2004). Estimating soil moisture at the watershed scale with satellite-based radar and land surface models. *Canadian Journal of Remote Sensing*, 30(5):805–826, doi: 10.5589/m04-043.

Mostovoy, G. V., Anantharaj, V., King, R. L., and Filippova, M. G. (2008). Interpretation of the relationship between skin temperature and vegetation fraction: Effect of subpixel soil temperature variability. *International Journal of Remote Sensing*, 29(10):2819–2831, doi: 10.1080/01431160701395286.

Mostovoy, G. V., King, R. L., Reddy, K. R., Kakani, V. G., and Filippova, M. G. (2006). Statistical Estimation of Daily Maximum and Minimum Air Temperatures from MODIS LST Data over the State of Mississippi. *GIScience & Remote Sensing*, 43(1):78–110, doi: 10.2747/1548-1603.43.1.78.

NCAR (2011). *ARW Version 3 Modeling System User's Guide*. Mesoscale & Microscale Meteorology Division and National Center for Atmospheric Research.

Neteler, M. (2010). Estimating Daily Land Surface Temperatures in Mountainous Environments by Reconstructed MODIS LST Data. *Remote Sensing*, 2(1):333–351, doi: 10.3390/rs1020333.

Niclòs, R., Galve, J. M., Valiente, J. A., Estrela, M. J., and Coll, C. (2011). Accuracy assessment of land surface temperature retrievals from MSG2-SEVIRI data. *Remote Sensing of Environment*, 115(8):2126 – 2140, doi: 10.1016/j.rse.2011.04.017.

Nieto, H., Sandholt, I., Aguado, I., Chuvieco, E., and Stisen, S. (2011). Air temperature estimation with MSG-SEVIRI data: Calibration and validation of the TVX algorithm for the Iberian Peninsula. *Remote Sensing of Environment*, 115(1):107–116, doi: 10.1016/j.rse.2010.08.010.

Njoku, E., Jackson, T., Lakshmi, V., Chan, T., and Nghiem, S. (2003). Soil moisture retrieval from AMSR-E. *Geoscience and Remote Sensing, IEEE Transactions on*, 41(2):215 – 229, doi: 10.1109/TGRS.2002.808243.

Njoku, E. G. (1999). *AMSR Land Surface Parameters: Surface Soil Moisture, Land Surface Temperature, Vegetation Water Content (Algorithm Theoretical Basis Document)*. Jet Propulsion Laboratory, Pasadena, CA.

Njoku, E. G. (2008). AMSR-E/Aqua Daily L3 Surface Soil Moisture, Interpretive Parameters, & QC EASE-Grids. online at http://nsidc.org/data/docs/daac/ae_land3_l3_soil_moisture.gd.html (Accessed: 15 June 2012).

Njoku, E. G. and Entekhabi, D. (1996). Passive microwave remote sensing of soil moisture. *Journal of Hydrology*, 184(1 - 2):101 – 129, doi: 10.1016/0022-1694(95)02970-2.

Norman, J. M. and Becker, F. (1995). Terminology in thermal infrared remote sensing of natural surfaces. *Agricultural and Forest Meteorology*, 77(3–4):153–166, doi: 10.1016/0168-1923(95)02259-Z.

Owe, M., Chang, A., and Golus, R. E. (1988). Estimating surface soil moisture from satellite microwave measurements and a satellite derived vegetation index. *Remote Sensing of Environment*, 24(2):331 – 345, doi: 10.1016/0034-4257(88)90033-8.

Parinussa, R. M., Holmes, T. R. H., Yilmaz, M. T., and Crow, W. T. (2011). The impact of land surface temperature on soil moisture anomaly detection from passive microwave observations. *Hydrology and Earth System Sciences*, 15(10):3135–3151, doi: 10.5194/hess-15-3135-2011.

Patil, M., Waghmare, R., Halder, S., and Dharmaraj, T. (2011). Performance of Noah land surface model over the tropical semi-arid conditions in western India. *Atmospheric Research*, 99(1):85 – 96, doi: http://dx.doi.org/10.1016/j.atmosres.2010.09.006.

Pause, M., Schulz, K., Zacharias, S., and Lausch, A. (2012). Near-surface soil moisture estimation by combining airborne L-band brightness temperature observations and imaging hyperspectral data at the field scale. *Journal of Applied Remote Sensing*, 6(1):063516–1–063516–13, doi: 10.1117/1.JRS.6.063516.

Pei, S.-C. and Luo, T.-L. (1996). Split-radix generalized fast Fourier transform. *Signal Processing*, 54(2):137 – 151, doi: 10.1016/S0165-1684(96)00103-X.

Piters, A. J. M., Buchmann, B., Brunner, D., Cohen, R. C., Lambert, J.-C., Stammes, P., van Weele, M., and Wittrock, F. (2011). Data Quality and Validation of Satellite Measurements of Tropospheric Composition. In Burrows, J. P., Platt, U., and Borrell, P., editors, *The Remote Sensing of Tropospheric Composition from Space*, pages 315–364. Springer Berlin Heidelberg, Berlin, Heidelberg, url: http://www.ppmborrell.co.uk/RemoteSensingBook/07_Remote_Sensing_Validation.pdf.

Pleim, J. E. (2006). A Simple, Efficient Solution of Flux-Profile Relationships in the Atmospheric Surface Layer. *J. Appl. Meteor. Climatol.*, 45(2):341–347, doi: 10.1175/JAM2339.1.

Pratt, D. and Ellyett, C. (1979). The thermal inertia approach to mapping of soil moisture and geology. *Remote Sensing of Environment*, 8(2):151 – 168, doi: 10.1016/0034-4257(79)90014-2.

Price, J. C. (1977). Thermal inertia mapping: A new view of the earth. *Journal of Geophysical Research*, 82(18):2582–2590, doi: 10.1029/JC082i018p02582.

Price, J. C. (1980). The potential of remotely sensed thermal infrared data to infer surface soil moisture and evaporation. *Water Resources Research*, 16(4):787–795, doi: 10.1029/WR016i004p00787.

Price, J. C. (1983). Estimating surface temperatures from satellite thermal infrared data - A simple formulation for the atmospheric effect. *Remote Sensing of Environment*, 13(4):353–361, doi: 10.1016/0034-4257(83)90036-6.

Prihodko, L. and Goward, S. N. (1997). Estimation of air temperature from remotely sensed surface observations. *Remote Sensing of Environment*, 60(3):335 – 346, doi: 10.1016/S0034-4257(96)00216-7.

Prince, S., Goetz, S., Dubayah, R., Czajkowski, K., and Thawley, M. (1998). Inference of surface and air temperature, atmospheric precipitable water and vapor pressure deficit using Advanced Very High-Resolution Radiometer satellite observations: comparison with field observations. *Journal of Hydrology*, 212 - 213(0):230 – 249, doi: 10.1016/S0022-1694(98)00210-8.

Proy, C., Tanré, D., and Deschamps, P. (1989). Evaluation of topographic effects in remotely sensed data. *Remote Sensing of Environment*, 30(1):21 – 32, doi: 10.1016/0034-4257(89)90044-8.

Pu, R., Gong, P., Michishita, R., and Sasagawa, T. (2008). Spectral mixture analysis for mapping abundance of urban surface components from the Terra/ASTER data. *Remote Sensing of Environment*, 112(3):939 – 954, doi: 10.1016/j.rse.2007.07.005.

Qin, J., Yang, K., Lu, N., Chen, Y., Zhao, L., and Han, M. (2013). Spatial upscaling of in-situ soil moisture measurements based on MODIS-derived apparent thermal inertia. *Remote Sensing of Environment*, 138(0):1 – 9, doi: 10.1016/j.rse.2013.07.003.

Rees, G. (2001). *Physical Principles of Remote Sensing*. Cambridge University Press, Cambridge, U.K, 2nd edition edition.

Reichle, R. H., Koster, R. D., Liu, P., Mahanama, S. P. P., Njoku, E. G., and Owe, M. (2007). Comparison and assimilation of global soil moisture retrievals from the Advanced Microwave Scanning Radiometer for the Earth Observing System (AMSR-E) and the Scanning Multichannel Microwave Radiometer (SMMR). *J. Geophys. Res.*, 112(D9):D09108, doi: 10.1029/2006JD008033.

Rigo, G. and Parlow, E. (2005). Measurement and modeling of the ground heat flux in the city of Basel during BUBBLE by different methods. In *ISPRS Intl. Archives of Photogrammetry, Remote Sensing and Spatial Information Sciences*, volume XXXVI PART 8/W27. url: http://www.isprs.org/proceedings/XXXVI/8-W27/.

Rigo, G. and Parlow, E. (2007). Modelling the ground heat flux of an urban area using remote sensing data. *Theoretical and Applied Climatology*, 90:185–199, doi: 10.1007/s00704-006-0279-8.

Robson, C. (1994). *Experiment, Design and Statistics in Psychology*. Penguin Group, Blackwell Publishing, 3rd edition edition.

Salomon, J., Schaaf, C., Strahler, A., Gao, F., and Jin, Y. (2006). Validation of the MODIS bidirectional reflectance distribution function and albedo retrievals using combined observations from the aqua and terra platforms. *Geoscience and Remote Sensing, IEEE Transactions on*, 44(6):1555 – 1565, doi: 10.1109/TGRS.2006.871564.

Sapiano, M. R. P. and Arkin, P. A. (2009). An Intercomparison and Validation of High-Resolution Satellite Precipitation Estimates with 3-Hourly Gauge Data. *J. Hydrometeor*, 10(1):149–166, doi: 10.1175/2008JHM1052.1.

Sheng, J., Wilson, J. P., and Lee, S. (2009). Comparison of land surface temperature (LST) modeled with a spatially-distributed solar radiation model (SRAD) and remote sensing data. *Environmental Modelling & Software*, 24(3):436 – 443, doi: 10.1016/j.envsoft.2008.09.003.

Shi, X., Wen, J., Wang, L., Zhang, T., Tian, H., Wang, X., Liu, R., and Zhang, J. (2010). Regional soil moisture retrievals and simulations from assimilation of satellite microwave brightness temperature observations. *Environmental Earth Sciences*, 61(6):1289–1299, doi: 10.1007/s12665-010-0504-8.

Shi, X. K., Wen, J., Wang, L., Zhang, T. T., Tian, H., Wang, X., Liu, R., and Zhang, J. H. (2009). Application of satellite microwave remote sensed brightness temperature in the regional soil moisture simulation. *Hydrology and Earth System Sciences Discussions*, 6(1):1233–1260, doi: 10.5194/hessd-6-1233-2009.

Simons, G. and Voogt, M. (2012). Refined assessment of soil moisture and water consumption on the irrigated Canterbury Plains. Technical report, Environment Canterbury, Lincoln, Christchurch, New Zealand.

Skamarock, W. C., Klemp, J. B., Dudhia, J., Gill, D. O., Barker, D. M., Duda, M. G., Huang, X.-Y., Wang, W., and Powers, J. G. (2008). NCAR Technical Note: A Description of the Advanced Research WRF Version 3. Technical report, Mesoscale & Microscale Meteorology Division and National Center for Atmospheric Research, Boulder, Colorado, USA.

Sobrino, J. A. and El-Kharraz, M. H. (1999a). Combining afternoon and morning NOAA satellites for thermal inertia estimation: 1. Algorithm and its testing with Hydrologic Atmospheric Pilot Experiment-Sahel data. *Journal of Geophysical Research: Atmospheres*, 104(D8):9445–9453, doi: 10.1029/1998JD200109.

Sobrino, J. A. and El-Kharraz, M. H. (1999b). Combining afternoon and morning NOAA satellites for thermal inertia estimation: 2. Methodology and application. *Journal of Geophysical Research: Atmospheres*, 104(D8):9455–9465, doi: 10.1029/1998JD200108.

Sobrino, J. A., El-Kharraz, M. H., Cuenca, J., and Raissouni, N. (1998). Thermal inertia mapping from NOAA-AVHRR data. *Advances in Space Research*, 22(5):655–667, doi: 10.1016/S0273-1177(97)01127-7.

Sohrabinia, M. and Khorshiddoust, A. M. (2007). Application of satellite data and GIS in studying air pollutants in Tehran. *Habitat International*, 31(2):268–275, doi: 10.1016/j.habitatint.2007.02.003.

Sohrabinia, M., Rack, W., and Zawar-Reza, P. (2012). Analysis of MODIS LST compared with WRF Model and in-situ Data over the Waimakariri River Basin, Canterbury, New Zealand. *Remote Sensing*, 4(11):3501–3527, doi: 10.3390/rs4113501.

Song, Q., Chelton, D. B., Esbensen, S. K., Thum, N., and O'Neill, L. W. (2009). Coupling between Sea Surface Temperature and Low-Level Winds in Mesoscale Numerical Models. *Journal of Climate*, 22(1):146–151,153–159,161–164, doi: 10.1175/2008JCLI2488.1.

Souza-Jr, C., Firestone, L., Silva, L. M., and Roberts, D. (2003). Mapping forest degradation in the Eastern Amazon from SPOT 4 through spectral mixture models. *Remote Sensing of Environment*, 87(4):494–506, doi: 10.1016/j.rse.2002.08.002.

Stisen, S., Sandholt, I., NÃ¸rgaard, A., Fensholt, R., and Eklundh, L. (2007). Estimation of diurnal air temperature using MSG SEVIRI data in West Africa. *Remote Sensing of Environment*, 110(2):262–274, doi: 10.1016/j.rse.2007.02.025.

Strahler, A. H., Muller, J.-P., Lucht, W., Schaaf, C. B., Tsang, T., Gao, F., Li, X., Muller, J.-P., Lewis, P., and Barnsley, M. J. (1999). *MODIS BRDF/Albedo Product: Algorithm Theoretical Basis Document*. Boston University; University College London; Potsdam Institut fur Klimafolgenforschung; Beijing Normal University; University of Wales, Swansea.

Strahler, A. H., Muller, J.-P., Wanner, W., Schaaf, C. B., Li, X., Hu, B., Muller, J.-P., Lewis, P., and Barnsley, M. J. (1996). *MODIS BRDF/Albedo Product: Algorithm Theoretical Basis Document*. Boston University; University College London; Institute of Remote Sensing Application, Chinese Academy of Sciences; University of Wales, Swansea.

Sultana, R. (2011). *Enhancing snow water equivalent estimation in Noah land surface model: Modified approach*. PhD thesis, University of California, Irvine (UCI), United States, California, Irvine.

Sun, D. and Pinker, R. T. (2003). Estimation of land surface temperature from a Geostationary Operational Environmental Satellite (GOES-8). *J. Geophys. Res.*, 108(D11):4326–4341, url: http://dx.doi.org/10.1029/2002JD002422.

Sun, D. and Pinker, R. T. (2004). Case study of soil moisture effect on land surface temperature retrieval. *IEEE Geoscience and Remote Sensing Letters*, 1(2):127–130, doi: 10.1109/LGRS.2004.824749.

Sun, L., Sun, R., Li, X., Liang, S., and Zhang, R. (2012). Monitoring surface soil moisture status based on remotely sensed surface temperature and vegetation index information. *Agricultural and Forest Meteorology*, 166-167(0):175–187, doi: 10.1016/j.agrformet.2012.07.015.

Sun, Y.-J., Wang, J.-F., Zhang, R.-H., Gillies, R. R., Xue, Y., and Bo, Y.-C. (2005). Air temperature retrieval from remote sensing data based on thermodynamics. *Theoretical and Applied Climatology*, 80(1):37–48, doi: 10.1007/s00704-004-0079-y.

Tang, B., Bi, Y., Li, Z.-L., and Xia, J. (2008). Generalized Split-Window Algorithm for Estimate of Land Surface Temperature from Chinese Geostationary FengYun Meteorological Satellite (FY-2C) Data. *Sensors*, 8(2):933–951, doi: 10.3390/s8020933.

Taylor, S. E. (1979). Measured Emissivity of Soils in the Southeast United States. *Remote Sensing of Environment*, 8(4):359–364, doi: 10.1016/0034-4257(79)90035-X.

Trigo, I., Dacamara, C., Viterbo, P., Roujean, J., Olesen, F., Barroso, C., Camacho-de Coca, F., Carrer, D., Freitas, S., Garcia-Haro, J., Geiger, B., Gellens-Meulenberghs, F., Ghilain, N., Melia, J., Pessanha, L., Siljamo, N., and Arboleda, A. (2011). The Satellite Application Facility for Land Surface Analysis. *International Journal of Remote Sensing*, 32(10):2725–2744, doi: 10.1080/01431161003743199.

Trigo, I., Monteiro, I., Olesen, F., and Kabsch, E. (2008). An assessment of remotely sensed land surface temperature. *Journal of Geophysical Research*, 113:D17108, doi: 10.1029/2008JD010035.

Umeyama, S. and Godin, G. (2004). Separation of diffuse and specular components of surface reflection by use of polarization and statistical analysis of images. *Pattern Analysis and Machine Intelligence, IEEE Transactions on*, 26(5):639 –647, doi: 10.1109/TPAMI.2004.1273960.

Vancutsem, C., Ceccato, P., Dinku, T., and Connor, S. J. (2010). Evaluation of MODIS land surface temperature data to estimate air temperature in different ecosystems over Africa. *Remote Sensing of Environment*, 114(2):449 – 465, doi: 10.1016/j.rse.2009.10.002.

Vandoninck, J., Peters, J., Baets, B. D., Clercq, E. M. D., Ducheyne, E., and Verhoest, N. E. (2011). The potential of multitemporal Aqua and Terra MODIS apparent thermal inertia as a soil moisture indicator. *International Journal of Applied Earth Observation and Geoinformation*, 13(6):934–941, doi: 10.1016/j.jag.2011.07.003.

Vermote, E., Tanré, D., Deuzé, J., Herman, M., Morcrette, J. J., and Kotchenova, S. Y. (2006). *Second Simulation of a Satellite Signal in the Solar Spectrum - Vector (6SV) User Guide Version 3*. University of Maryland/Laboratoire d'Optique Atmospherique/European Centre for Medium Range Weather Forecast.

Vermote, E. F., Saleous, N. E., Justice, C. O., Kaufman, Y. J., Privette, J. L., Remer, L., Roger, J. C., and Tanré, D. (1997). Atmospheric correction of visible to

middle-infrared EOS-MODIS data over land surfaces: Background, operational algorithm and validation. *Journal of Geophysical Research*, 102(D14):17131–17141, doi: 10.1029/97JD00201.

Verstraeten, W. W., Veroustraete, F., van der Sande, C. J., Grootaers, I., and Feyen, J. (2006). Soil moisture retrieval using thermal inertia, determined with visible and thermal spaceborne data, validated for European forests. *Remote Sensing of Environment*, 101(3):299–314, doi: 10.1016/j.rse.2005.12.016.

Vinnikov, K. Y., Yu, Y., Goldberg, M. D., Tarpley, D., Romanov, P., Laszlo, I., and Chen, M. (2012). Angular anisotropy of satellite observations of land surface temperature. *Geophys. Res. Lett.*, 39(23):L23802, doi: 10.1029/2012GL054059.

Wallace, J. M., Hobbs, P. V., and Fu, Q. (2006). Radiative Transfer. In Wallace, J. M. and Hobbs, P. V., editors, *Atmospheric Science: An Introductory Survey*, pages 113–152. Academic Press, University of Washington, second edition edition, url: www.elsevier.com/wps/product/cws_home/706883.

Wan, Z. (1999). *MODIS Land-Surface Temperature Algorithm Theoretical Basis Document (LST ATBD)*. Institute for Computational Earth System Science University of California, Santa Barbara, CA 93106-3060.

Wan, Z. (2008). New refinements and validation of the MODIS Land-Surface Temperature/Emissivity products. *Remote Sensing of Environment*, 112:59–74, doi: 10.1016/j.rse.2006.06.026.

Wan, Z. (2009). *Collection-5 MODIS Land Surface Temperature Products Users' Guide*. ICESS, University of California, Santa Barbara, CA 93106-3060.

Wan, Z. and Dozier, J. (1996). A generalized split-window algorithm for retrieving land-surface temperature from space. *Geoscience and Remote Sensing, IEEE Transactions on*, 34(4):892 –905, doi: 10.1109/36.508406.

Wan, Z. and Li, Z. (2008). Radiance-based validation of the V5 MODIS land-surface temperature product. *International Journal of Remote Sensing*, 29:5373–5395, doi: 10.1080/01431160802036565.

Wan, Z. and Li, Z.-L. (1997). A physics-based algorithm for retrieving land-surface emissivity and temperature from EOS/MODIS data. *Geoscience and Remote Sensing, IEEE Transactions on*, 35(4):980–996, doi: 10.1109/36.602541.

Wan, Z., Zhang, Y., Li, Z., Wang, R., Salomonson, V., Yves, A., Bosseno, R., and Hanocq, J. (2002a). Preliminary estimate of calibration of the moderate resolution imaging spectroradiometer thermal infrared data using Lake Titicaca. *Remote Sensing of Environment*, 80:497–515, doi: 10.1016/S0034-4257(01)00327-3.

Wan, Z., Zhang, Y., Zhang, Q., and Li, Z. (2002b). Validation of the land-surface temperature products retrieved from Terra Moderate Resolution Imaging Spectroradiometer data. *Remote Sensing of Environment*, 83:163–180, doi: 10.1016/S0034-4257(02)00093-7.

Wan, Z., Zhang, Y., Zhang, Q., and Li, Z. (2004). Quality assessment and validation of the MODIS global land surface temperature. *International Journal of Remote Sensing*, 25:261–274, doi: 10.1080/0143116031000116417.

Wang, C., Qi, J., Moran, S., and Marsett, R. (2004). Soil moisture estimation in a semiarid rangeland using ERS-2 and TM imagery. *Remote Sensing of Environment*, 90(2):178 – 189, doi: 10.1016/j.rse.2003.12.001.

Wang, L. and Qu, J. (2009). Satellite remote sensing applications for surface soil moisture monitoring: A review. *Frontiers of Earth Science in China*, 3:237–247, doi: 10.1007/s11707-009-0023-7.

Wang, L. and Uchida, S. (2008). Use of Linear Spectral Mixture Model to Estimate Rice Planted Area Based on MODIS Data. *Rice Science*, 15(2):131 – 136, doi: 10.1016/S1672-6308(08)60031-1.

Wang, N., Wu, H., coise Nerry, F., Li, C., and Li, Z.-L. (2011). Temperature and Emissivity Retrievals From Hyperspectral Thermal Infrared Data Using Linear Spectral Emissivity Constraint. *Geoscience and Remote Sensing, IEEE Transactions on*, 49(4):1291 –1303, doi: 10.1109/TGRS.2010.2062527.

Wloczyk, C., Borg, E., Richter, R., and Miegel, K. (2011). Estimation of instantaneous air temperature above vegetation and soil surfaces from Landsat 7 ETM+ data in northern Germany. *International Journal of Remote Sensing*, 32(24):9119–9136, doi: 10.1080/01431161.2010.550332.

Wolfe, R. E. and Saleous, N. (2006). 7 MODIS Land Products and Data Processing. In Qu, J. J., Gao, W., Kafatos, M., Murphy, R. E., and Salomonson, V. V., editors, *Earth Science Satellite Remote Sensing Vol. 1: Science and Instruments*, pages 110–122. Tsinghua University Press-Springer, url: http://www.scribd.com/doc/76129231/6/MODIS-Land-Products-and-Data-Processing.

Xu, Y., Qin, Z., and Shen, Y. (2012). Study on the estimation of near-surface air temperature from MODIS data by statistical methods. *International Journal of Remote Sensing*, 33(24):7629–7643, doi: 10.1080/01431161.2012.701351.

Xue, Y. and Cracknell, A. P. (1995). Advanced thermal inertia modelling. *International Journal of Remote Sensing*, 16(3):431–446, doi: 10.1080/01431169508954411.

Yang, Z.-L. (2004). Modeling land surface processes in short-term weather and climate studies. In Zhu, X., Li, X., Cai, M., Zhou, S., Zhu, Y., Jin, F.-F., Zou, X., and Zhang, M., editors, *Observation, Theory and Modeling of Atmospheric Variability*, pages 288–313. World Scientific, New Jersey, url: www.geo.utexas.edu/climate/research/reprints/yang_land_04.pdf.

Yoo, J.-M., Won, Y.-I., Cho, Y.-J., Jeong, M.-J., Shin, D.-B., Lee, S.-J., Lee, Y.-R., Oh, S.-M., and Ban, S.-J. (2011). Temperature trends in the skin/surface, mid-troposphere and low stratosphere near Korea from satellite and ground measurements. *Asia-Pacific Journal of Atmospheric Sciences*, 47:439–455, doi: 10.1007/s13143-011-0029-4.

Yu, P., Clausi, D., and Howell, S. (2009). Fusing AMSR-E and QuikSCAT Imagery for Improved Sea Ice Recognition. *Geoscience and Remote Sensing, IEEE Transactions on*, 47(7):1980 –1989, doi: 10.1109/TGRS.2009.2013632.

Zhang, L. and Wu, X. (2006). On the application of cross correlation function to subsample discrete time delay estimation. *Digital Signal Processing*, 16(6):682 – 694, doi: 10.1016/j.dsp.2006.08.009.

Zhang, W., Huang, Y., Yu, Y., and Sun, W. (2011a). Empirical models for estimating daily maximum, minimum and mean air temperatures with MODIS land surface temperatures. *International Journal of Remote Sensing*, 32(1):1–26, doi: 10.1080/01431161.2011.560622.

Zhang, X., Tang, B., yuan Jia, Y., and Li, Z.-L. (2007). Estimation of bare surface soil moisture using geostationary satellite data. In *Geoscience and Remote Sensing Symposium, 2007. IGARSS 2007. IEEE International*, pages 1931 –1934. doi: 10.1109/IGARSS.2007.4423204.

Zhang, X., Zhao, J., Sun, Q., Wang, X., Guo, Y., and Li, J. (2011b). Soil Moisture Retrieval From AMSR-E Data in Xinjiang (China): Models and Validation. *Selected Topics in Applied Earth Observations and Remote Sensing, IEEE Journal of*, 4(1):117 –127, doi: 10.1109/JSTARS.2010.2076336.

Zhao, W., Li, Z.-L., Wu, H., Tang, B.-H., Zhang, X., Song, X., and Zhou, G. (2012). Determination of bare surface soil moisture from combined temporal evolution of land surface temperature and net surface shortwave radiation. *Hydrological Processes*, pages n/a–n/a, doi: 10.1002/hyp.9410.

Zhu, W., u, A. L., and Jia, S. (2013). Estimation of daily maximum and minimum air temperature using MODIS land surface temperature products. *Remote Sensing of Environment*, 130(0):62–73, doi: 10.1016/j.rse.2012.10.034.